

(2)



Part 4 of 4

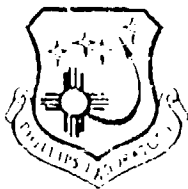
April 1993

DTIC  
ELECTE  
AUG 09 1993  
S A D

Conference Proceeding

APPROVED FOR PUBLIC RELEASE; DISTRIBUTION IS UNLIMITED.

93-18260



PHILLIPS LABORATORY  
Directorate of Space and Missiles Technology  
AIR FORCE MATERIEL COMMAND  
KIRTLAND AIR FORCE BASE, NM 87117-5776

This final report was prepared by the Phillips Laboratory, Kirtland Air Force Base, New Mexico, under Job Order 11050502. The Laboratory Project Officer-in-Charge was Marko M. Stoyanof (VTPT).

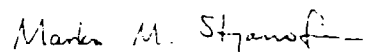
When Government drawings, specifications, or other data are used for any purpose other than in connection with a definitely Government-related procurement, the United States Government incurs no responsibility or any obligation whatsoever. The fact that the Government may have formulated or in any way supplied the said drawings, specifications, or other data, is not to be regarded by implication, or otherwise in any manner construed, as licensing the holder, or any other person or corporation; or as conveying any rights or permission to manufacture, use, or sell any patented invention that may in any way be related thereto.

This report has been authored by employees and contractors of the United States Government and Foreign Governments. Accordingly, the United States Government retains a nonexclusive royalty-free license to publish or reproduce the material contained herein, or allow others to do so, for the United States Government purposes.

This report has been reviewed by the Public Affairs Office and is releasable to the National Technical Information Service (NTIS). At NTIS, it will be available to the general public, including foreign nationals.

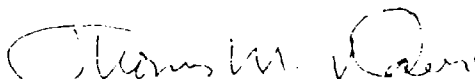
If your address has changed, or if your organization no longer employs the addressee, please notify PL/VTPT, Kirtland AFB, NM 87117-5776 to help maintain a current mailing list.

This conference proceeding has been reviewed and is approved for publication.

  
MARKO M. STOYANOF  
Project Officer

FOR THE COMMANDER

  
ROBERT M. VACEK, GM-14, DAF  
Chief, Thermal Management Br

  
THOMAS M. DAVIS, Lt Col, USAF  
Acting Director of Space & Missile  
Technology

DO NOT RETURN COPIES OF THIS REPORT UNLESS CONTRACTUAL  
OBLIGATIONS OR NOTICE ON A SPECIFIC DOCUMENT REQUIRES THAT  
IT BE RETURNED.

REPORT DOCUMENTATION PAGE			Form Approved OMB No 0704-0188	
<small>Public reporting burden for this collection of information is estimated to average 1 hour per response, including the time for reviewing instructions, searching existing data sources, gathering and maintaining the data needed, and completing and reviewing the collection of information. Send comments regarding this burden estimate or any other aspect of this collection of information, including suggestions for reducing the burden, to Washington Headquarters Services, Directorate for Information Operations and Reports, 1215 Jefferson Davis Highway, Suite 1204, Arlington, VA 22202-4302, and to the Office of Management and Budget, Paperwork Reduction Project (0704-0188), Washington, DC 20503.</small>				
1. AGENCY USE ONLY (Leave blank)	2. REPORT DATE April 1993	3. REPORT TYPE AND DATES COVERED 17-19 Nov 92, Conference Proceeding		
4. TITLE AND SUBTITLE 7th International Cryocooler Conference Part 4 of 4		5. FUNDING NUMBERS PE: 62601F PR: 1105 TA: 05 WU: 02		
6. AUTHOR(S) Several authors				
7. PERFORMING ORGANIZATION NAME(S) AND ADDRESS(ES) Phillips Laboratory Kirtland AFB, NM 87117-5776		8. PERFORMING ORGANIZATION REPORT NUMBER  PL-CP--93-1001		
9. SPONSORING, MONITORING AGENCY NAME(S) AND ADDRESS(ES)		10. SPONSORING, MONITORING AGENCY REPORT NUMBER		
11. SUPPLEMENTARY NOTES Publication of this report does not constitute approval or disapproval of the ideas or findings. It is published in the interest of scientific and technical information exchange. The established procedures for editing reports were not followed for this report.				
12a. DISTRIBUTION AVAILABILITY STATEMENT  Approved for public release; distribution is unlimited.		12b. DISTRIBUTION CODE		
13. ABSTRACT (Maximum 200 words)  The 7th International Cryocooler Conference was held in Santa Fe, New Mexico, on 17-19 November, 1992. Jiri L. Ludwigsen of Nichols Research was the conference chairperson; Capt William Wyche and Marko Stoyanof of Phillips Laboratory served as the program committee chairmen.  The topics included Cryocooler Testing and Modeling, Space and Long Life Applications, Stirling Cryocoolers, Pulse Tube Refrigerators, Novel Concepts and Component Development, Low Temperature Regenerator Development, and J-T and Absorption Coolers.				
14. SUBJECT TERMS Absorption, Cryocoolers, Cryogenic, Low Temperature Heat Exchanger, Pulse Tube Refrigerators, Regenerative, Recuperative, Stirling, Thermal Modeling		15. NUMBER OF PAGES 268		16. PRICE CODE
17. SECURITY CLASSIFICATION OF REPORT Unclassified	18. SECURITY CLASSIFICATION OF THIS PAGE Unclassified	19. SECURITY CLASSIFICATION OF ABSTRACT Unclassified	20. LIMITATION OF ABSTRACT SAR	

*Chairman*

Jill Ludwigsen  
Nichols Research Corporation  
2201 Buena Vista, S.E. #203  
Albuquerque, NM 87106  
(505) 843-7364

*Program Committee*

Capt. Bill Wyche, Co-Chairman  
Marko Stoyanof, Co-Chairman  
Air Force Phillips Laboratory

Ronald White, WRDC/FIVE

Dodd Stacy, Creare

Ron Ross, Jet Propulsion Lab

Al Johnson, Aerospace Corp.

Peter Gifford, Cryomech

*Local Arrangements*  
Peter Jones, Aerospace Corp.

*Advisory Board*

John Barclay  
University of Victoria

Joseph Smith  
MIT

DTIC QUALITY INSPECTED 3

Stephen Castles  
NASA/GSFC

Michael Superczynski  
DTRC

Ray Radebaugh  
NIST

Klaus Timmerhaus  
University of Colorado

Hiroshi Nagano  
Toyama University, Japan

Paul Sheihing  
DOE

Ralph Longworth  
APD Cryogenics

Peter Kerney  
Janis Research

Martin Niseneff  
RL

George Robinson  
Nichols Research Corp.

Accession For	
NIS - DTIC	<input checked="" type="checkbox"/>
DTIC TAB	<input type="checkbox"/>
Unannounced	<input type="checkbox"/>
Justification	
By	
Date	
Availability Codes	
Dist	Availability Codes
A-1	



## FOREWORD

This report contains the proceedings of the Seventh International Cryocooler Conference, held in Santa Fe, New Mexico, on 17-19 November, 1992. Jiri L. Ludwigsen of Nichols Research was the conference chairperson; Capt William Wyche and Marko Stoyanof of Phillips Laboratory served as the program committee chairmen.

The first cryocooler conference held in 1980 was designed to stimulate interest and discussion in the scientific and engineering community about the latest developments and advances in refrigeration for cryogenic sensors and electronic systems. The conference is held every even numbered year and this year over 300 participants attended representing 11 countries.

The technical program consisted of over 100 unrestricted oral and poster presentations. The topics included Cryocooler Testing and Modeling, Space and Long Life Applications, Stirling Cryocoolers, Pulse Tube Refrigerators, Novel Concepts and Component Development, Low Temperature Regenerator Development, and J-T and Absorption Coolers. The proceedings show significant progress in the field of cryocooler technology.

## ACKNOWLEDGEMENTS

The Seventh International Cryocooler Conference Board would like to thank the Air Force Phillips Laboratory for sponsoring the conference and publishing these proceedings. The generous supply of manpower and dedication contributed by Phillips Laboratory was key to the success of the 1992 conference.

The Conference Chairperson would like to express her appreciation to Nichols Research Corporation for providing the support, assets and time required for this effort.

## CONTENTS

TUESDAY SESSION .....	1
SDIO AND AIR FORCE CRYOCOOLER TECHNOLOGY DEVELOPMENTS AT USAF PHILLIPS LABORATORY	
....P. J. Thomas .....	3
JPL CRYOCOOLER DEVELOPMENT AND TEST PROGRAM OVERVIEW	
....R. G. Ross, Jr. ....	14
NASA/GSFC CRYOCOOLER DEVELOPMENT PROGRAM	
....S. Castles, T. Cygnarowicz, R. Boyle, L. Sparr, R. Cory, F. Connors ....E. James, R. Fink, V. Arillo, J. Marketon, C. Lee, and D. Bugby .....	26
DEVELOPMENT AND DEMONSTRATION OF A DIAPHRAGM STIRLING 65 K STANDARD SPACECRAFT CRYOCOOLER	
....D. Stacy, J. McCormick, and J. Valenzuela .....	40
STIRLING SPACE COOLER	
....C. K. Chan, M. Lopez, J. Raab, E. Tward, and G. Davey .....	50
THERMAL, VIBRATION, AND RELIABILITY TEST RESULTS FOR A BALANCED 80 K CRYOCOOLER	
....R. Boyle, L. Sparr, T. Cygnarowicz, S. Castles, ....R. G. Fink, and E. F. James .....	57
SPACECRAFT COOLER CHARACTERIZATION	
....D. L. Johnson, G. R. Mon, and R. G. Ross, Jr. ....	73
PERFORMANCE OF A LONG LIFE REVERSE BRAYTON CRYOCOOLER	
....W. Swift and H. Sixsmith .....	84
SDI CRYOCOOLER PRODUCIBILITY PROGRAM	
....J. Bruning .....	98
MINIATURES PULSE TUBE COOLER	
....C. K. Chan, C. B. Jaco, J. Raab, E. Tward, and M. Waterman .....	113
FLOW PATTERNS INTRINSIC TO THE PULSE TUBE REFRIGERATOR	
....J. M. Lee, P. Kittel, K. D. Timmerhaus, and R. Radebaugh .....	125
EXPERIMENTAL PERFORMANCE OF MODIFIED PULSE TUBE REFRIGERATOR BELOW 80 K DOWN 23 K	
....Y. Ishizaki and E. Ishizaki .....	140

## CONTENTS (Continued)

## PULSE TUBE REFRIGERATOR RESEARCH

...Y. Zhou and Y. J. Han ..... 147

## DEVELOPMENT OF PULSE TUBE REFRIGERATOR WITH LINEAR-MOTOR DRIVE COMPRESSOR

...T. Kuriyama, H. Hatakeyama, Y. Ohtani, H. Nakagome, Y. Matsubara,  
...H. Okuda, and H. Murakami ..... 157

## AN EXPERIMENTAL AND ANALYTICAL INVESTIGATION OF 4 K PULSE TUBE REFRIGERATOR

...Y. Matsubara, J. L. Gao, K. Tanida, Y. Hiresaki, M. Kaneko ..... 166

## A NEW CONFIGURATION FOR SMALL-CAPACITY, LIQUID-HELIUM-TEMPERATURE CRYOCOOLER

...J. A. Crunkleton ..... 187

## ANALYSIS OF A MINIATURE TWO-STAGE CRYOCOOLER

...E. B. Ratts, Dr J. L. Smith, Jr., and Dr Y. Iwasa ..... 197

## POWER, EFFICIENCY, AND OPTIMUM DESIGN OF ELECTROCHEMICAL REFRIGERATORS

...R. T. Ruggeri ..... 213

## LINEARIZED PULSE TUBE CRYOCOOLER THEORY

...H. Mirels ..... 221

## VIBROIMPACT RESONANCE APPLICATION FOR THE DISPLACER MOTION PASSIVE CONTROL IN THE SPLIT CRYOGENIC COOLER

...A. Veprik and N. Purdak ..... 233

## A HIGHLY RELIABLE, MINIATURE STIRLING-CYCLE CRYOCOOLER

...C. S. Keung and G. Esposito ..... 247

## PERFORMANCE TEST RESULTS ON A MINIATURE STIRLING CRYOCOOLER FOR USE IN INTEGRATED DEWAR DETECTOR ASSEMBLIES

...P. Ab-der-Halden ..... 257

## VALIDATION OF THE STIRLING REFRIGERATOR PERFORMANCE MODEL AGAINST THE PHILLIPS/NASA MAGNETIC BEARING REFRIGERATOR

...S. W. K. Yuan and I. E. Spradley ..... 280

## THE MS\*2 STIRLING CYCLE CODE

...M. P. Mitchell ..... 290

## CONTENTS (Continued)

AN INTRODUCTION TO THE LUCAS AEROSPACE THERMODYNAMIC COMPUTER MODEL CMOD ....C. S. Brice. ....	294
THERMOACOUSTIC THEORY FOR REGENERATIVE CRYOCOOLERS: A CASE STUDY FOR A PULSE TUBE REFRIGERATOR ....J. H. Xiao .....	305
SOME PRELIMINARY EXPERIMENTAL RESULTS ON OSCILLATORY HEAT TRANSFER IN A PERIODICALLY REVERSING PIPE FLOW ....X. Tang and P. Cheng .....	321
THERMOELECTRIC COOLERS FOR THE TWS, SFW, WAM AND SADARM PROGRAMS, AND ASSOCIATED MANTECH PROGRAM OBJECTIVES ....W. L. Kolander, B. Morrison, J. Bierschenk, ....J. Fuhrer, and T. Kottak .....	332
CRYOGENIC ATTACHMENT FIXTURE WITH HIGH STRENGTH AND LOW THERMAL CONDUCTION ....P. R. Roach .....	349
HELIUM LIQUID- AND GAS-GAP HEAT SWITCHES ....A. Kashani, B. P. M. Helvensteijn, ....F. J. McCormack, and A. L. Spivak .....	355
A RADIATIVE COOLING SYSTEM FOR THE EOS STRATOSPHERIC WIND INFRARED LIMB SOUNDER ....D. J. Kuyper .....	371
NEW MAGNETIC REFRIGERANTS FOR THE LOW TEMPERATURES REGION ....M. D. Kuz'min, A. M. Tishin, and S. Y. Dan'kov .....	385
WEDNESDAY SESSION .....	387
EXPERIMENTAL INVESTIGATION OF THE REGENERATIVE MAGNETIC REFRIGERATOR OPERATING BETWEEN 4.2 K AND 1.8 K ....S. Jeong, J. L. Smith, Jr., Y. Iwasa, and T. Numazawa .....	389
A 4 K GIFFORD-McMAHON REFRIGERATOR FOR RADIO ASTRONOMY ....R. Plambeck, N. Thatte, and P. Syke' .....	401

## CONTENTS (Continued)

DYNAMIC CHARACTERISTICS OF REGENERATORS USED IN CRYOCOOLERS ....B. J. Huang and C. W. Lu .....	416
REGENERATOR PERFORMANCE AND REFRIGERATION MECHANISM FOR 4 K GM REFRIGERATOR USING RARE EARTH COMPOUND REGENERATOR MATERIALS ....T. Kuriyama, M. Takahashi, H. Nakagome, T. Hashimoto, ....T. Eda, and M. Yabuki .....	429
A STIRLING CYCLE CRYOCOOLER FOR 4 K APPLICATIONS ....D. Stacy, J. McCormick, and P. Wallis .....	444
SUPERFLUID STIRLING REFRIGERATOR WITH A COUNTERFLOW REGENERATOR ....J. G. Brisson and G. W. Swift .....	460
GRADED AND NONGRADED REGENERATOR PERFORMANCE ....W. Rawlins, K. D. Timmerhaus, R. Radebaugh, ....J. Gary, and P. Bradley .....	471
SPECIFIC HEAT DESIGN AND PROPOSAL OF A NEW CUBIC TYPE MAGNETIC MATERIAL FOR A REGENERATOR MATRIX ....Y. Tokai, A. Takahasi, M. Sahashi, and T. Hashimoto .....	484
A COMPACT 150 GHz SIS RECEIVER COOLED BY 4 K GM REFRIGERATOR ....M. Takahasi, H. Hatakeyama, T. Kuriyama, H. Nakagome, R. Kawabe, ....H. Iwashita, G. McCulloch, K. Shibata, and S. Ukita .....	495
DEVELOPMENT OF A PRECISION, SIX-AXIS LABORATORY DYNAMOMETER ....P. J. Champagne, S. A. Cordova, M. S. Jacoby, and K. R. Lorell .....	508
DEVELOPMENT AND DEMONSTRATION OF AN ELECTRONIC CONTROLLER FOR A DOUBLE-ACTING DIAPHRAGM CRYOCOOLER ....C. Konkel, T. Gibborey, L. Van Allen, K. Ha, and R. Beyle .....	526
MAGNETIC NOISE PRODUCED BY GM CRYOCOOLERS ....S. Fujimoto, H. Ogata, and H. Kado .....	560
REGENERATOR TWO-PHASE "SINGLE-BLOW" FOR PERFORMANCE EVALUATION AT SMALL VELOCITIES: ORIENTATION INFLUENCE AT "1g" ....K. V. Ravikumar, R. M. Carandang, T. H. K. Frederking, ....R. Confair, W. Hong, F. Sherman, and C. Toribio .....	569

## CONTENTS (Continued)

OPTIMIZATION ANALYSIS ON A TWO-STAGE AMR HYDROGEN LIQUEFIER ....L. Zhang, A. J. DeGregoria, S. A. Sherif, and T. N. Veziroglu . . . . .	586
SUBMILLIMETER SPACE ASTRONOMY WITHOUT LIQUID HELIUM? ....C. Hagmann and P. L. Richards . . . . .	595
RECENT PROGRESS ON APPLICATION OF HIGH ENTROPY MAGNETIC MATERIAL TO THE REGENERATOR IN HELIUM TEMPERATURE RANGE ....T. Hashimoto, T. Eda, M. Yabuki, T. Kuriyama, and H. Nakagome . . . . .	605
THE EFFECTS OF A LAYERED BED ON ACTIVE MAGNETIC REGENERATOR PERFORMANCE ....S. R. Schuricht, A. J. DeGregoria, and C. B. Zimm . . . . .	614
LONG LIFE STIRLING CYCLE COOLER DEVELOPMENTS FOR THE SPACE APPLICATION RANGE OF 20 K TO 80 K ....B. G. Jones and R. C. Peddle . . . . .	621
STIRLING CRYOCOOLER WITH DUAL OPPOSED DISPLACERS FOR SPACE APPLICATIONS ....P. Arter, D. Berry, W. Gully, and C. Varner . . . . .	644
DEVELOPMENT AND SPACE QUALIFICATION TESTING OF A RANGE OF MECHANICAL CRYOCOOLERS ....C. Weir . . . . .	656
NOVEL LINEAR FLEXURE BEARING ....T. E. Wong, R. B. Pan, and A. L. Johnson . . . . .	675
NASA/GSFC CRYOCOOLER TEST PROGRAM RESULTS ....L. Sparr, R. Boyle, R. Cory, F. Connors, E. James, ....R. Fink, V. Arillo, and J. Marketon . . . . .	699
PERFORMANCE OF THE SIGNAAL USFA STIRLING COOLING ENGINES ....D. Verbeek, H. Helmonds, and P. Roos . . . . .	72
PRESENT LIFE-TESTING STATUS OF "OXFORD TYPE" CRYOCOOLERS FOR SPACE APPLICATIONS ....C. Jewell, T. Bradshaw, A. Orlowska, and B. Jones . . . . .	738

## CONTENTS (Continued)

DESIGN AND TEST OF A COMPREHENSIVE FACILITY FOR LIFE-TESTING  
SPACE CRYOCOOLERS

...R. G. Ross, Jr. and D. L. Johnson ..... 748

## SIMULATION PROGRAM FOR MULTIPLE EXPANSION STIRLING MACHINES

...G. Walker, M. Weiss, R. Fauvel, G. Reader, and E. R. Bingham ..... 759

## COMPUTER MODELING OF STIRLING CYCLE COOLERS

...T. W. Bradshaw, A. H. Orlowska, and J. Heatt ..... 772

DESIGN EQUATIONS AND SCALING LAWS FOR LINEAR COMPRESSORS  
WITH FLEXURE SPRINGS

...E. Marquardt, R. Radebaugh, and P. Kittel ..... 783

NON-REAL TIME, FEED FORWARD VIBRATION CONTROL SYSTEM  
DEVELOPMENT AND TEST RESULTS...R. Boyle, F. Connors, J. Marketon, V. Arillo,  
...E. James, and R. Fink ..... 805DEMONSTRATION OF ACTIVE VIBRATION REDUCTION ON A STIRLING-  
CYCLE CRYOCOOLER TESTBED...B. G. Johnson, D. B. Eisenhaure, F. J. Flynn, M. S. Gaffney,  
...R. L. Hockney, D. L. Johnson, and R. G. Ross, Jr. .... 820

THURSDAY SESSION ..... 829

## EVOLUTION OF THE 10 K PERIODIC SORPTION REFRIGERATOR CONCEPT

...A. L. Johnson and J. A. Jones ..... 831

## DEVELOPMENT OF A PERIODIC 10 K SORPTION CRYOCOOLER

...S. Bard, T. Fujita, L. Wade, J. Rodriguez, and J. J. Wu ..... 854

EVALUATION OF A PROTOTYPE HYDRIDE COMPRESSOR FOR PERIODIC  
HYDROGEN SORPTION CRYOCOOLERS...R. C. Bowman, Jr., B. D. Freeman, D. Labor, F. E. Lynch,  
...R. W. Marmaro, and L. A. Wade ..... 867ASSESSMENT OF A HYDROGEN JOULE-THOMSON EXPANDER AND  
VANADIUM HYDRIDE SORPTION BEDS FOR 20 K CRYOCOOLERS...E. L. Ryba, B. D. Freeman, R. C. Bowman, Jr., R. E. Spjut,  
...E. A. Liu, P. Budic, and C. Okado ..... 886

## CONTENTS (Continued)

DESIGN OF A METAL HYDRIDE SORPTION CRYOCOOLER SYSTEM ...H. J. Strumpf and R. H. Norman .....	898
LINEAR COMPRESSOR FOR JT CRYOCOOLER ...D. T. Kuo .....	921
PROGRESS REPORT ON THE DEVELOPMENT OF THE BALL J-T CRYOCOOLER ... R. Levenduski and R. Scarlotti .....	931
JT CRYOSTAT WITH LIQUID-SOLID CRYOGEN RESERVOIR ...R. C. Longworth .....	958
DESIGN AND OPERATION OF A 30 K TWO-STAGE NITROGEN-NEON J-T COOLER ...W. A. Little, R. Yaron, and C. Fuentes .....	971
DESIGN CONCEPTS FOR A 10 K SOLID HYDROGEN SORPTION REFRIGERATOR ...J. R. Phillips, B. D. Freeman, and R. C. Bowman, Jr. ....	978
EXPERIMENTAL VERIFICATION OF JOULE-THOMSON CRYOCOOLER COOLDOWN PERIOD SIMILARITY RATIOS ...B-Z. Maytal .....	996
BI-MATERIAL CONTROLLED DEMAND FLOW JOULE-THOMSON COOLERS ...G. E. Bonney .....	1003
CONTAMINATION CONTROL IN CLOSED CYCLE JOULE-THOMSON CRYOCOOLERS AND A NEW J-T VALVE ...J. Lester and S. Nieczkoski .....	1012
PHASE EQUILIBRIA IN CRYOGENIC MIXTURES ...L. B. Robinson .....	1025
INCORPORATING A MECHANICAL REFRIGERATOR WITH A REFREEZABLE CRYOGEN IN SPACE APPLICATIONS ...B. G. Williams and J. C. Batty .....	1043
APPLICATIONS AND PACKAGING OF SEMICONDUCTOR DEVICES FOR USE AT CRYOGENIC TEMPERATURES ...K. P. Hyde, J. R. McCoy, and C. S. Naiman .....	1064



## CONTENTS (Concluded)

A METHOD TO ESTIMATE THE PULSE TUBE REFRIGERATOR PERFORMANCES ...M. David, J. Marechal, and Y. Simon .....	1078
CRYOCOOLER TIP MOTION SUPPRESSION USING ACTIVE CONTROL OF PIEZOELECTRIC ACTUATORS ...R. J. Glaser, R. G. Ross, Jr., and D. L. Johnson .....	1086
HIGH TEMPERATURE SUPERCONDUCTING SPACE EXPERIMENT CRYOGENIC SYSTEM OVERVIEW ...T. Kawecki .....	1098
10 K SORPTION CRYOCOOLER FLIGHT EXPERIMENT (BETSCE) ...S. Bard, P. Cowgill, J. Rodriguez, L. Wade, J. J. Wu, ...M. Gehrlein, and W. Von Der Ohe .....	1107
GAS ATOMIZED $\text{Er}_3\text{Ni}$ POWDER FOR CRYOCOOLER APPLICATIONS ...I. E. Anderson, M. G. Osborne, H. Takeya, ...and K. A. Gschneidner, Jr. ....	1120
MAGNETIC NANOCOMPOSITES AS MAGNETIC REFRIGERANTS ...R. D. Shull, R. D. McMichael, J. J. Ritter, ...L. J. Swartzendruber, and L. H. Bennett .....	1133
ENTHALPY FLOW TRANSITION LOSSES IN REGENERATIVE CRYOCOOLERS ...P. Kittel .....	1145
NEODYMIUM REGENERATOR TEST RESULTS IN A STANDARD GIFFORD-McMAHON REFRIGERATOR ...J. Chafe, G. Green, and R. C. Riedy .....	1157
SOLVAY REFRIGERATOR OPERATING AT HELIUM TEMPERATURES ...G. Chen, J. Zheng, F. Zhang, J. Yu, and T. Sun .....	1165

## LINEAR COMPRESSOR FOR JT CRYOCOOLER

DANIEL T. KUO  
BEI ELECTRONICS CO.  
SYLMAR, CA 91342

### INTRODUCTION

BEI is pursuing the development of a reliable, low-cost, closed-cycle JT cryocooler for cooling high temperature superconductor electronics dissipating 5 Watts in the 80-90K range. The closed-cycle JT cryocooler was selected for development because of the promising results obtained with JT cryostats using hydrocarbon mixtures as refrigerant. These mixtures can be formulated with nitrogen and neon to attain temperatures below 80K in a single stage expansion from a high pressure of 50 atm, yielding cooling power of 4 to 10 times greater than nitrogen [1]. The higher cooling power and lower pressures, in principle, promised to mitigate the 2 main shortcomings of closed-cycle JT cryocoolers, i.e., lower efficiency and reliability. The lower operating pressure falls within the operating range of Stirling coolers so that the technology developed for more reliable Stirling compressors could be leveraged. BEI has been engaged in the design and manufacturing of linear actuators for Stirling cryocoolers since the early 1980's.

### DESCRIPTION OF THE COMPRESSOR

The challenge in the implimentation of the JT cycle lies in the design of a low-cost, non-contaminating, and long life compressor. The BEI compressor is a modest step in this direction. It is similar in feature to the linear Stirling cycle compressors, found in tactical IR applications, where the linear drive is employed to mitigate the side loads which lead to wear. The compressor, shown Figure 1, has 2 stages with work equally divided between them. The first and second stage pistons are driven in-line and opposed to minimize vibration with the dynamic elements of the two sides tuned to operate at resonance. Two voice-coil actuators are used to drive these pistons, one for each stage.

The voice coil actuator consists of a magnetic field supplied by permanent magnets in a steel frame and a movable coil within the field. The force produced by the coil is directly proportional to the electrical current flowing through the coil. The direction of the force is determined by the direction of the current flow. This force is sufficient to compress the gas and accelerate the mass of the coil, piston and associated structure. The sophistication in the design of the actuator comes about in producing a linear magnetic field over the length of the stroke, such that the force per unit current is constant. Since the actuator does not position itself, or regulate its speed under load, or automatically reverse, these functions have to be provided for in the compressor drive system.

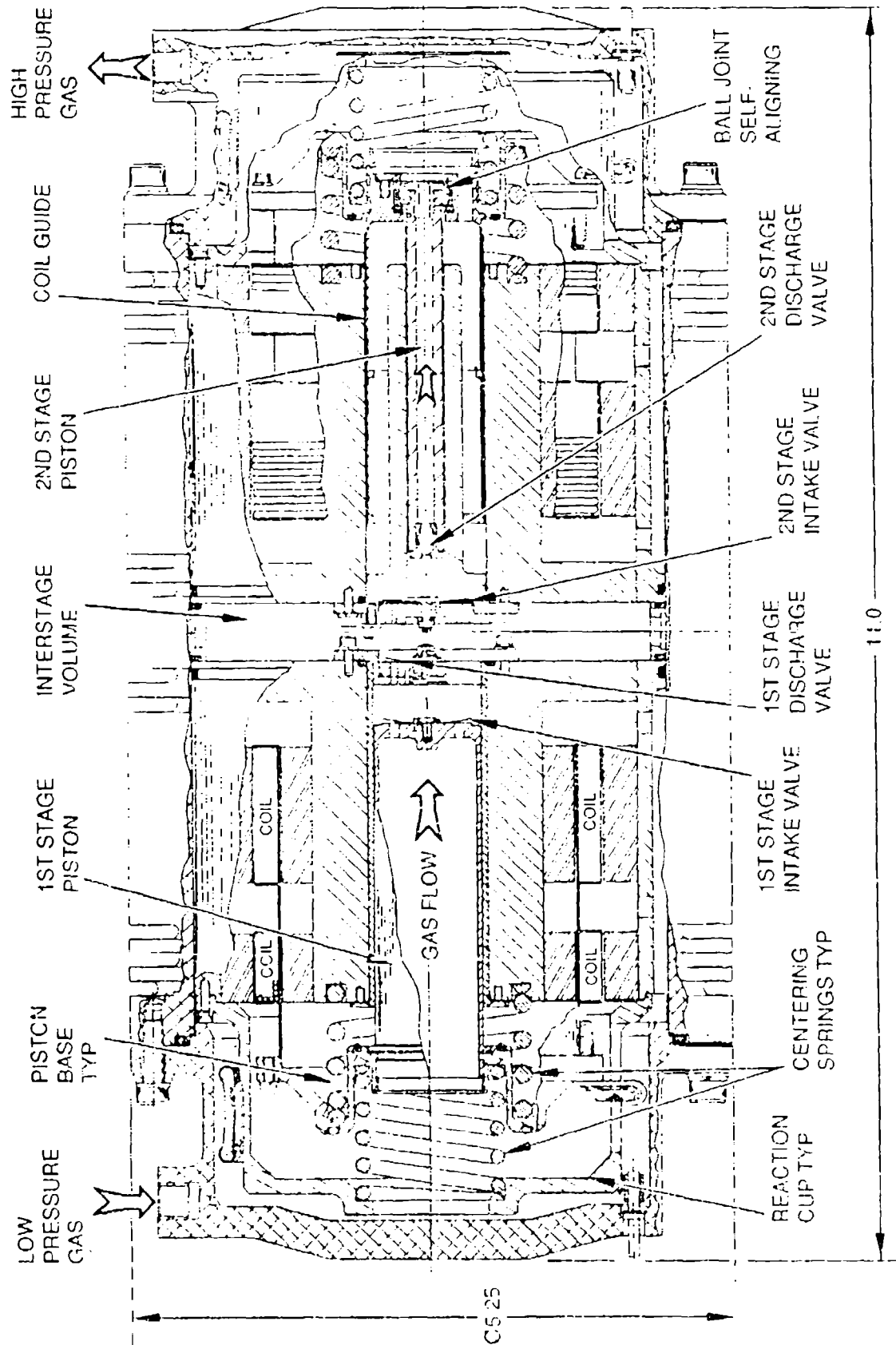


Figure 1. Cross-Section Of The Linear Compressor Assembly

The moving coil's radial clearance relative to the stationary magnet assembly is maintained by the piston on the first stage and a cylindrical guide on the second stage. This guide provides for greater load carrying bearing surface. The second stage piston is self-aligned to its cylinder through a floating spherical joint. Both pistons and the guide are bonded with a thin layer of a self-lubricating composite, which is machined to close tolerances in the case of the pistons to construct a clearance seal. The departure in similarities of this compressor from the Stirling compressor is in the addition of valves. Four valves are required, 2 per stage.

The same clover leaf flapper valve is used at three locations: first stage intake and discharge, and second stage intake. A ball valve assembly that screw into the tip of the piston is used for the second stage discharge to minimize dead volume. The compressor is configured such that the refrigerant is compressed from a low pressure at one end to a high pressure at the other separated by an interstage volume. Both pistons are hollow to allow the axial flow of the refrigerant.

### COMPRESSOR DRIVER

A schematic of the compressor closed loop drive circuit is shown in Figure 2. Piston position feedback is provided by the linear variable differential transformer (LVDT). The major components include an oscillator, servo amplifier, and DC power supply. Adjustments can be made to the oscillator amplitude to boost the drive current and offset to bias the piston in either direction. The PID method of loop compensation is used to stabilize the servo loop. Attachment of the LVDT core to the back end of the piston and the mounting of the coil to an adapter fitting on the cover is shown in Figure 3. Other drive methods investigated are described in a following section.

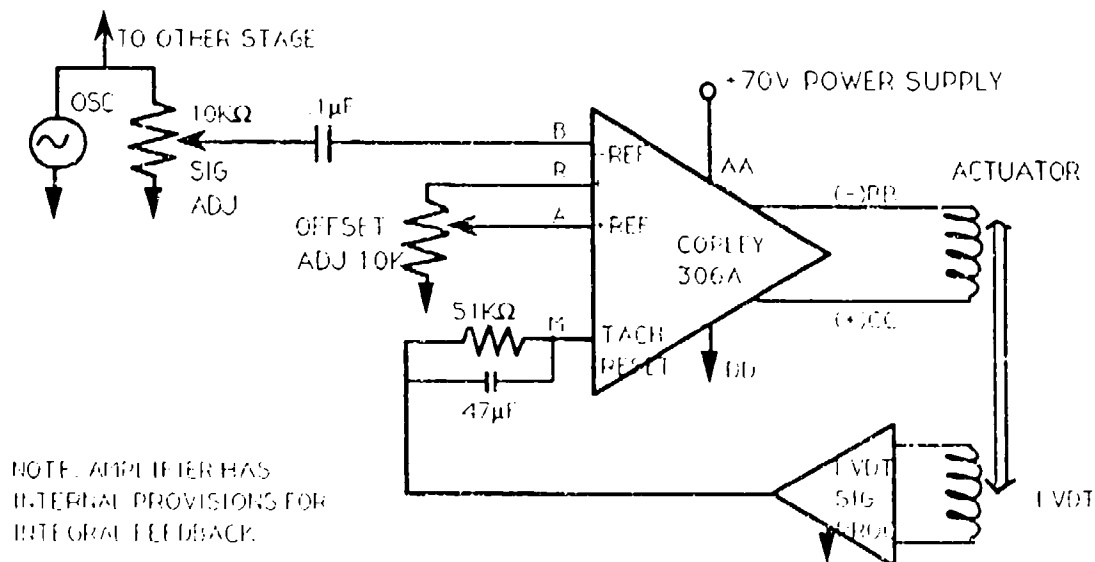


Figure 2. Closed Loop Compressor Drive - One Stage Shown.

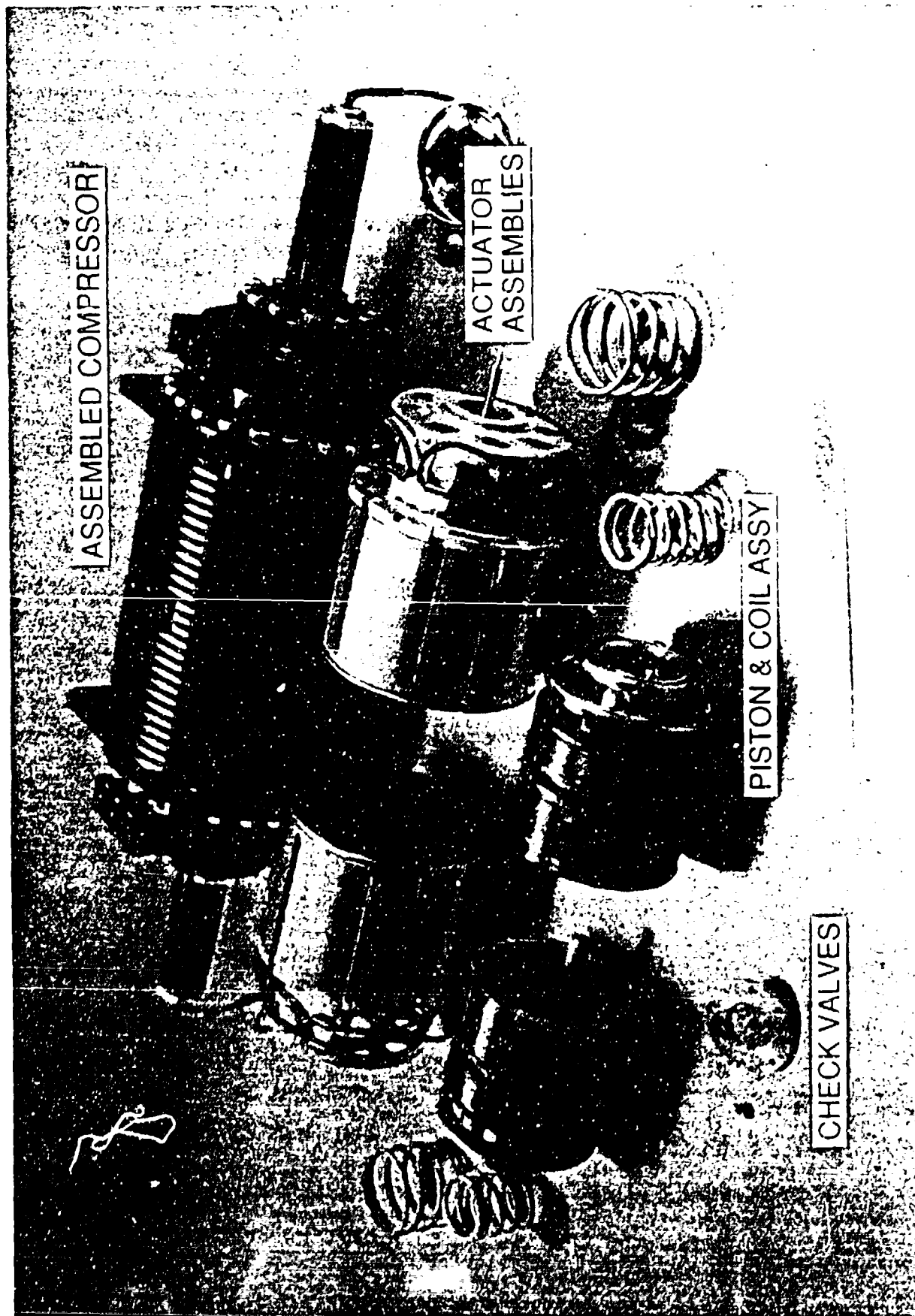


Figure 3. Linear Compressor Assembly

DESCRIPTION OF THE CRYOSTAT

A cross section of the cryostat is shown in Figure 4. The cryostat is a finned metal tube heat exchanger that is wound around a thin wall mandrel. The high pressure refrigerant from the compressor is fed through the finned tube where it is progressively cooled as it is forced to the cold end. The refrigerant is then expanded through a fixed orifice with a fraction liquifying. The low pressure refrigerant lifts the heat load and is then used to precool the incoming high pressure gas before it is returned to the compressor. The return flow path in the cryostat is confined to an annular gap between the mandrel OD and the cold-cylinder ID with the finned tube in between. A dacron sealing thread is used to direct the flow over the fins. Parasitic loads to the cold end is minimized with a vacuum jacket (dewar) enclosure over the cold-cylinder. The instrumentation consists of a diode sensor bonded to the cold tip to measure temperature and a resistor embedded in a flange mounted thermal mass of approximately 2.3 kJ for simulating an active heat load.

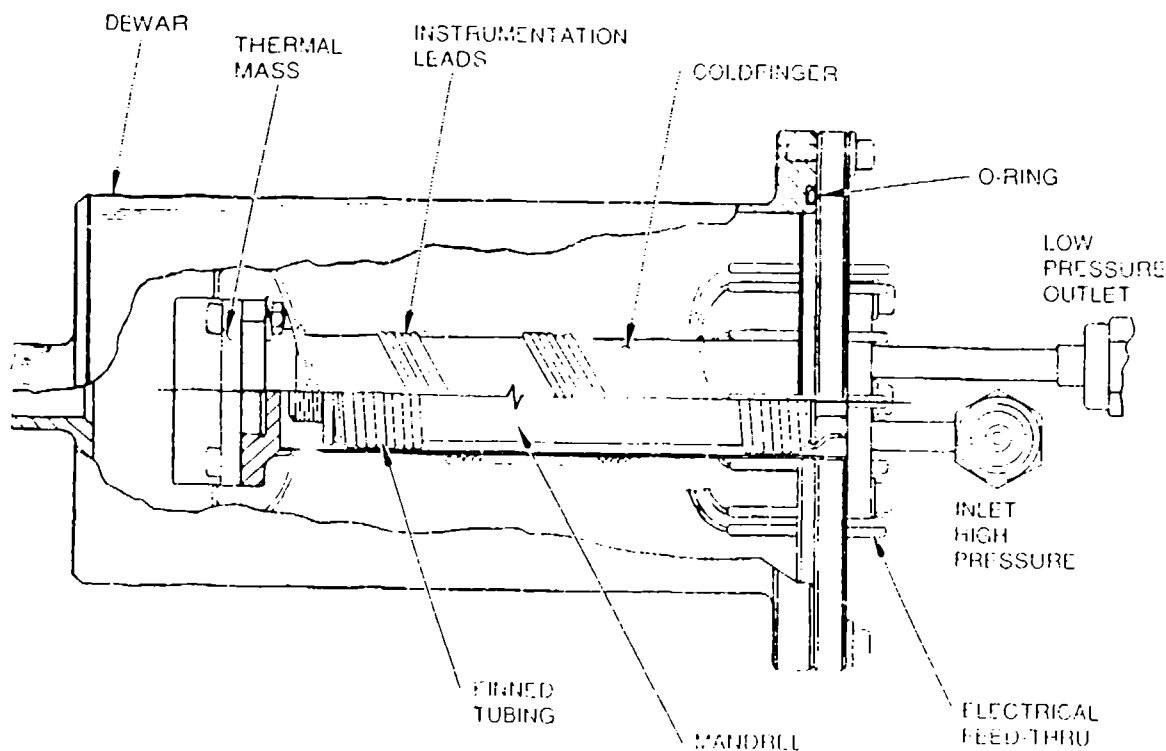


Figure 4. Cross-Section of the Dewar-Cryostat Assembly.

The cooler is designed for 5.5 Watts of gross refrigeration at 80K expanding a hydrocarbon-nitrogen gas mixture from 50 atm to 1 atm. Using the gas mixture property chart [2], the enthalpy drop is approximately 16 L-atm/mol between these pressures. The resulting flow rate requirement is 8.3 L/min (at suction pressure of 10 psia and high ambient temperature of 344K). This is the common point to which both the compressor and the cryostat were sized to.

A compression ratio of 9 per stage was selected for compressing the refrigerant from 10 psia to 90 psia on the first stage and from 90 psia to 810 psia on the second stage of the compressor. Parametric trade-off was performed resulting in the design point for frequency, stroke and volumetric efficiency of 35 Hz, 0.700 inch and 50 %, respectively, with bores sizes at 0.937 inch and 0.312 inch. A contingency for 15% growth in the flow rate was designed in the removable sleeves that fit into the magnet assembly ID. The actuator was specified to 55 lbs., with sufficient force to match the gas force at full compression with a rating of 3.9 lbs/Amp operating at a voltage of 65V. The cryostat size was based on measurements taken on a 0.204 inch diameter cryostat and scaled for the same efficiency, and energy flux using standard finned tubing. The cryostat fits in a 0.490 inch bore and is 2.6 inches long.

### PRELIMINARY TEST RESULTS

The components were tested individually in open-cycle. The dewar parasitic heat load was estimated at 77K by measuring the rate of LN<sub>2</sub> boiloff capturing the radiative and coldfinger conduction losses. This was added to the calculated conduction loss in the cryostat for a total of 0.450 mW. Table 1 shows the fixed-orifice cryostat performance with several fluids.

Table 1. Comparison of cryostat performance vs. JTMIX prediction

Gas Tank @ Room Temperature ~297K High Pressure 800 psig; Low Pressure 0 psig					
(mole fraction) FLUID	(MIN) COOLDOWN TIME TO 90K	(W) GROSS COOLING <sup>1</sup> MEASURED <sup>2</sup> PREDICTED		(K) TEMPERATURE MEASURED <sup>2</sup> PREDICTED	
N <sub>2</sub>	84	0.45	0.4	79	77
.275N <sub>2</sub>	12	2.2		97	
.4CH <sub>4</sub>		1.20		85.5	5.3
.275C <sub>2</sub> H <sub>6</sub>		2.25		unstable	5.3
.05C <sub>3</sub> H <sub>8</sub>					unstable
.085Ne	17				
.4N <sub>2</sub>					
.3CH <sub>4</sub>		2.35	1.80	79	75.6
.14C <sub>2</sub> H <sub>6</sub>					7.6
.075C <sub>3</sub> H <sub>8</sub>					

<sup>1</sup>contains 0.45 W of parasitic load

<sup>2</sup>for hxngcr effectiveness=98%

The nitrogen baseline is in good agreement with the calculations. However, the nitrogen-hydrocarbon mixture yielded less cooling capacity than calculations using the TS diagram based on BWR equations. The desired result is 5 Watts at 80K and 8.3 L/MIN. Instead, the cryostat reached a low temperature of 82 K at zero net cooling and rising to 85.5 K at 0.75 Watt applied load. Flow oscillations leading to blockage occurred with the load set at 1.8 Watts with diverging temperature. Since hydrocarbons normally freeze out around 90K, the solubility of these gases had to be better understood and another source for gas mixture property had to be found for obtaining predictions with greater fidelity. Analysis using DDMIX [3] properties with JTMIX [4] cryostat program resulted in predictions shown in the Table 1. A detailed study was performed to provide a theoretical framework for the selection of mixture components. This study is the subject on another paper presented at this conference [5]. Next, a mixture containing neon was tested with the results shown in the third row. This is a closer match to the design objective for temperature and flow, albeit, approximately half the required cooling capacity.

Several methods were evaluated for compressor drive. These methods are summarized in Table 2.

Table 2. Comparison of compressor drive methods

Drive Method	Compressor Configuration	Comments
1. Open Loop	With resonant spring.	Simple and inexpensive. Resonance is not sharp ( $Q \sim 1.5$ ). Requires manual "twidling" of driver amplitude and offset as the load changes.
2. Closed Loop	Springs removed. Hall switches installed.	Works well at lower frequencies ~10 Hz Excessive piston overtravel at 30 Hz
3. Closed Loop	Springs removed. LVDT position feedback	Servo loop could not be made "tight" (closed loop gain) enough to get full stroke under all pumping load conditions with these amplifiers. Amplifiers go into current limit at high pressure periods. Increasing DC offset required to keep full stroke. Excessive power dissipation.
4. Closed Loop	With resonant springs LVDT position feedback	Most efficient way to drive the compressor. Amplifiers tend to go into current limit. Servo loop needs to be tighter.



Method 4, closed loop servo with mechanical resonance at the frequency required for the design flow rate, seems to be the best solution. However, the servo loop must be further tightened so that manual adjustment during pump-up is not required, and that the amplifiers be large enough so that current limit is not reached. These amplifiers are PWM type with an H bridge (differential output) capable of  $\pm 15A$  continuous and  $\pm 30A$  peak current protection and operate at 75VDC.

The dynamic characteristic of the unloaded compressor is shown in Figure 5. The compressor was operated without valves to estimate the frictional losses and resonance response. Both stages resonated at approximately 30 Hz with a frictional loss of 10 and 20 Watts for the 2nd and 1st stages, respectively. Full characterization of the loaded compressor was limited by the amplifiers.

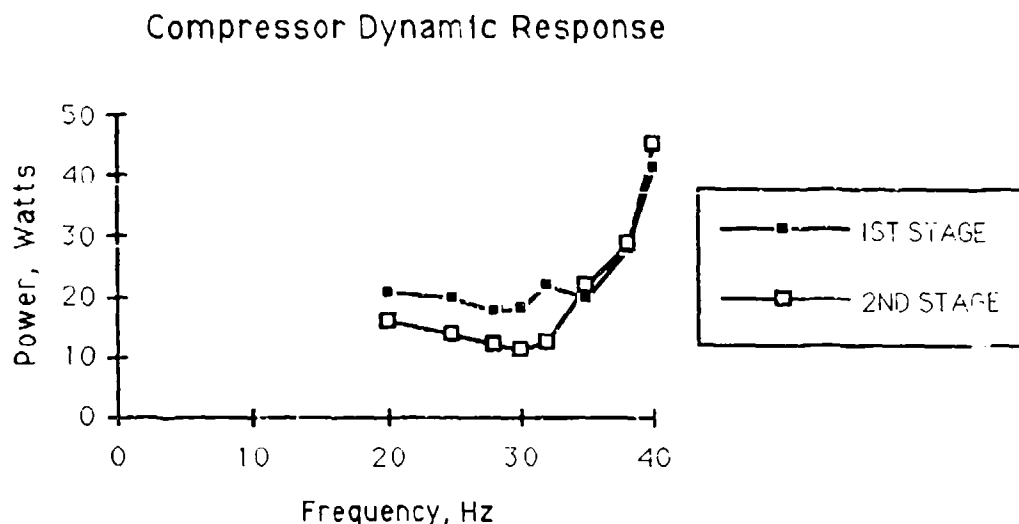


Figure 5. Unloaded compressor input power and resonance point.

Most of the pumping tests were performed with drive method 3, closed loop servo without the resonant springs. This resulted in lower peak current than method 4 and was within the amplifier limit at full stroke. In open-loop, the compressor pumped dry nitrogen from 5 psig to 800 psig, delivering 6-7 L/min.

In closed cycle, cooldown to 79K was reached in 40 minutes. Characterization of the cold end is underway. Fine tuning described in the next section is being carried out to maximize performance.

## REMAINING TASKS AND FUTURE WORK

A great deal of design refinements remains to be implimented. These refinements are designed to increase flow rate, eliminate adjustments to the drive due to varying loads, and wear contamination control.

The increase in flow rate will be accomplished by changing the displacement volume to the maximum allowed for and increasing the operating frequency. A lighter aluminum wire coil will reduce the weight of the moving mass to achieve resonance at 40 Hz. Valves timing, leakage and dead volume has to be quantified so that better volumetric efficiency can be attained.

The twiddling of the controls can be eliminated with tighter servo. This does not appear to be a difficult problem. A more compact LVDT sensor is desirable so as not to project beyond the end-to-end cover dimension of 11.00 inches.

Finally, a very important issue of wear contamination control has to be addressed. Wear from the self-lubricating composite seal will eventually lead to valve failure. Filtering of wear particulate is difficult to impliment especially for the first stage inlet and the second stage discharge valves. Potential solutions include change to hard-on-hard bearing surfaces and if cost and package size were of secondary issues, the compressor piston can be levitated by mechanical springs as in the "Oxford" Stirling cooler. This would eliminate wear.

In conclusion, it's apparent that the closed-cycle JT cooler with linear compressor will not offer a more compact or efficient alternative to the Stirling cycle coolers, however, it may find a niche in applications where a long transfer line is needed, more than 10 feet, and where added premium is placed on having no vibration at the cold head.

## ACKNOWLEDGEMENTS

The author wishes to acknowledge the support of BEI management, the special contribution by D. Haville and the assistance of M. Wu and M. Ritterbush.

## REFERENCES

- [1] Vladimir Nikolavich Alfeev et al, "Refrigerant for a Cryogenic Throttling Unit," British Patent # 1,336,892, November 14, 1973.
- [2] Bill Little, "A Study of the Efficiency and Cooling Behavior of Hydrocarbon-nitrogen Gas Mixtures," Report funded by Systron Donner/Seaton-Wilson, May 1987.

- [3] Ron Ely, "NBS Standard Reference Database 14, DDMIX," National Institute of Standards and Technology, Boulder, Colorado 1988.
- [4] Jack Jones, "Cryogenic Mixed Fluid Application Study and Computer Code," JPL D-7977, June 1989 - December 1991.
- [5] Larry Robinson, "Phase Equilibria in Cryogenic Mixtures," International Cryocooler Conference, November 1992.

## PROGRESS REPORT ON THE DEVELOPMENT OF THE BALL J-T CRYOCOOLER

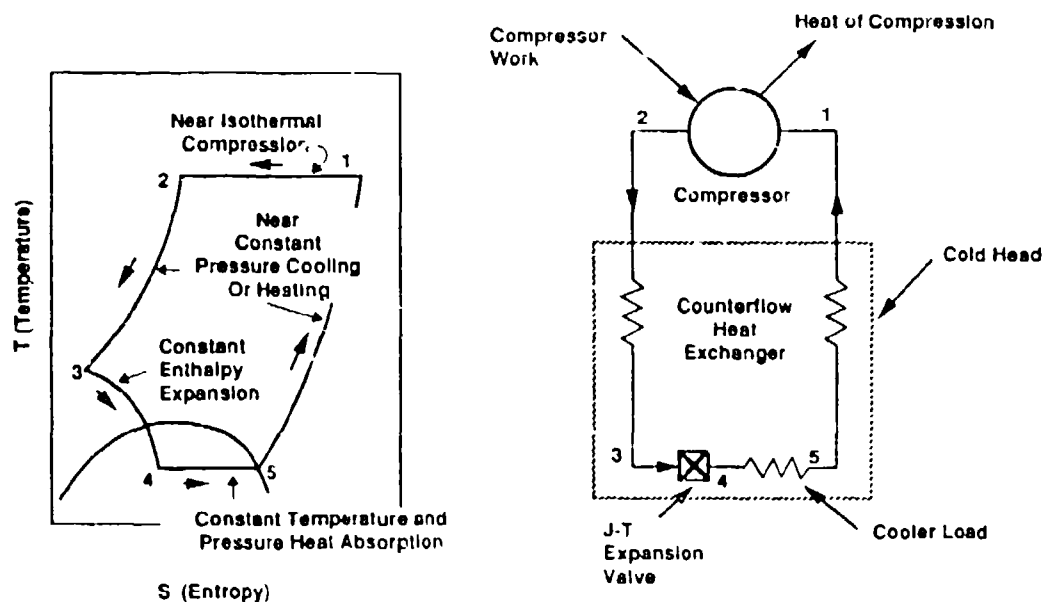
Robert Levenduski, Roger Scarlotti  
Ball Aerospace Systems Group  
Electro-Optics/Cryogenics Division  
1600 Commerce Street  
Boulder, Colorado 80301

### INTRODUCTION

Ball Electro-Optics/Cryogenics Division is developing, through a series of contracts, a J-T cryocooler for space applications. The acronym for the current program is COOLLAR and stands for Cryogenic On-Orbit Long Life Active Refrigerator. The primary objective of COOLLAR is to develop and demonstrate a seven year space flight capable cryocooler that is based on the Joule-Thomson (J-T) cycle. The previous contract, the Advanced Breadboard (ABB), was completed in March of this year. The ABB program successfully demonstrated the solution to the major issues of the J-T cryocooler technology. This paper will report on the results of the ABB program and will present an overview of the COOLLAR program preliminary design.

### J-T CRYOCOOLER BASICS

The basic Joule-Thomson cycle is shown in figure 1. A compressor is used to compress the working fluid in a near isothermal process. We use pure nitrogen as the working fluid to achieve the 65K cooling requirement and compress it from 0.172 to 69 bar (2.5 to 1000 psia). We have used other fluids to achieve different temperatures down to 4.1K. The high pressure gas is precooled by the returning low pressure gas stream in a counter flow heat exchanger. The precooled gas is expanded isenthalpically through a J-T valve. This valve can be as simple as a small hole in a flat plate. The expansion process produces a two phase fluid that absorbs the cooler load at constant temperature. The low pressure gas pre-cools the incoming gas as it returns to the compressor to complete the cycle.



A2074849 014

Figure 1. Basic Joule-Thomson cycle.

A closer examination of the J-T cycle reveals some obvious inherent advantages of this cycle for cryocooler applications. The cold head is for the most part small diameter tubing arranged as heat exchangers and small reservoirs. In addition to the obvious reliability advantage, there are no moving parts to cause vibration or give off electromagnetic interference. Our vibration testing of the cold head recorded vibration outputs that were 3% of our allowable requirement. The small tubing in the cold head between the ambient interface and the application also results in a naturally low parasitic heat leak. For applications that require two cryocoolers for reliability purposes, the low heat leak of the non-operating cooler only slightly increases the cooling requirement of the operating cooler. This heat leak can be so large in other systems that a thermal switch may need to be employed.

The simplicity of the cold head concept allows us to configure it to meet the needs of the application, not the other way around. It can easily be designed to provide uniform cooling to a large surface of any shape without a heavy thermal mass. It can also be

configured to easily replace a cryogenic dewar and the cold finger attachment that is often used. The two cold head designs presented in this paper illustrate some of this design flexibility.

The J-T expansion process produces a liquid which is used to absorb the cooler heat load. Since the liquid is at the saturation point, the heat load can vary drastically without changing the cooling temperature. In our testing we routinely vary the load by more than a factor of five with only a temporary 0.1K temperature change.

Pressure drop between the J-T cold head and the compressor is a minor issue. Consequently, the compressor can be located remotely from the cold head. This allows the compressor to be located in the best possible spacecraft location away from vibration sensitive equipment. Locating it near the heat rejection system would eliminate the need for a heat transfer system. For spacecraft with multiple cooling requirements, it's possible to have one compressor supporting multiple cold heads.

One of the biggest advantages of the J-T cycle is that the working fluid circulates continuously in a closed loop through the cooler. This allows an active contamination control system to be employed which continuously removes contaminants left from fabrication or generated during the cooler's life. Our testing has shown that with the active gas purification system of the J-T cryocooler, the working gas actually gets cleaner with time. A major benefit of an active contamination control system is it allows the J-T cryocooler to use an oil lubricated compressor. This is the conventional approach to achieving a long life compressor.

#### ABB PROGRAM OVERVIEW

The Advanced Breadboard Program began in the summer of 1989 and concluded this spring. The major objective of the program was to advance the technology to the point

that the next phase (the COOLLAR program) could focus on engineering optimization in areas such as weight, size and efficiency. To be at this point, we were required to demonstrate through test, the flight system performance requirements in areas of cooling capacity, temperature stability, and vibration output. During this phase, we developed analytical models that predicted system performance and correlated them to the experimental data. We also conducted several development efforts that addressed critical reliability issues, both at the component and system level.

#### ABB PROGRAM REQUIREMENTS

The major requirements of the ABB program are summarized in the table below.

ABB PROGRAM MAJOR REQUIREMENTS

Cooling Capacity	0.65 W (low load), 3.5 W (high load)
Cooling Temperature	65 +1, -3 K
Temperature Stability	$\pm 0.25$ K, within 30 sec of load change
Input Power	< 100 W/W @ 65 K
Vibration	
Compressor	< 0.133 N (0.03 lb) linear force < 0.035 N-m (0.3 lb-in) rotational force
Cold Head Load Interface	< 0.009 N (0.002 lb) linear force < 0.002 N-m (0.002 lb-in) rotational
Operating Environment	0-g, any orientation in 1-g

ABB SYSTEM DESCRIPTION

## ABB CYCLE DESCRIPTION

We modified the basic J-T cycle to improve the performance of the ABB cryocooler. Figure 2 shows the flow schematic and temperature-entropy diagram for the ABB J-T cryocooler. A dual-pressure hybrid approach was chosen to achieve improved thermal efficiency and to cool loads at 65 K and 100 K.

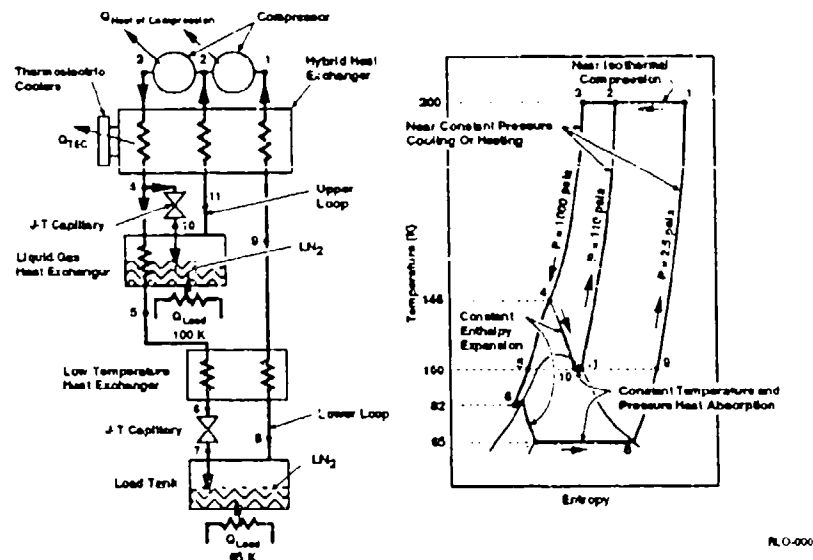


Figure 2.

Low pressure (0.172 bar, 2.5 psia) ambient-temperature gas from the cryocooler's lower loop enters the compressor at state 1. The gas is compressed to state 2, raising its pressure while transferring the heat of compression to the surroundings. It is combined with the intermediate-pressure (7.5 bar, 110 psia) gas returning from the cooler's upper loop and compressed to state 3. The high-pressure (69 bar, 1000 psia) ambient-temperature stream enters the hybrid heat exchanger where it is cooled by counterflow



heat exchange with the two return gas streams and the thermoelectric cooler. The cooling reduces the high-pressure gas temperature to state 4. At this point, the flow is split in a proportion dictated by the downstream restrictions of the two J-T valves. The upper loop flow (90% of flow) is isenthalpically expanded to a two-phase mixture at state 10 and enters the liquid/gas heat exchanger where it cools the lower loop gas flow and provides refrigeration at 100 K. The upper loop flow exits the heat exchanger at saturated conditions (state 11) and is warmed to state 2 as it passes through the hybrid heat exchanger.

The lower loop high-pressure gas enters the liquid/gas heat exchanger at state 4 where it is cooled to state 5 by the upper-loop liquid. It then enters the low-temperature heat exchanger where it is cooled to state 6 by counterflow heat exchange with the low-pressure return stream. The gas is isenthalpically expanded through the J-T valve which creates a low-pressure two-phase mixture at state 7. The mixture enters the load tank where the liquid is used to provide the refrigeration at 65 K. The gas exits the load tank at saturated conditions at state 8. The low-pressure saturated gas enters the low-temperature heat exchanger where it is heated to state 9 and is subsequently warmed to state 1 as it passes through the hybrid heat exchanger.

#### ABB COOLER OPERATION

The Ball J-T cryocooler consists of four subsystems: compressor, cold head, gas purifier, and control electronics. Figure 3 shows the cooler block diagram and figure 4 shows an illustration of the ABB cooler.

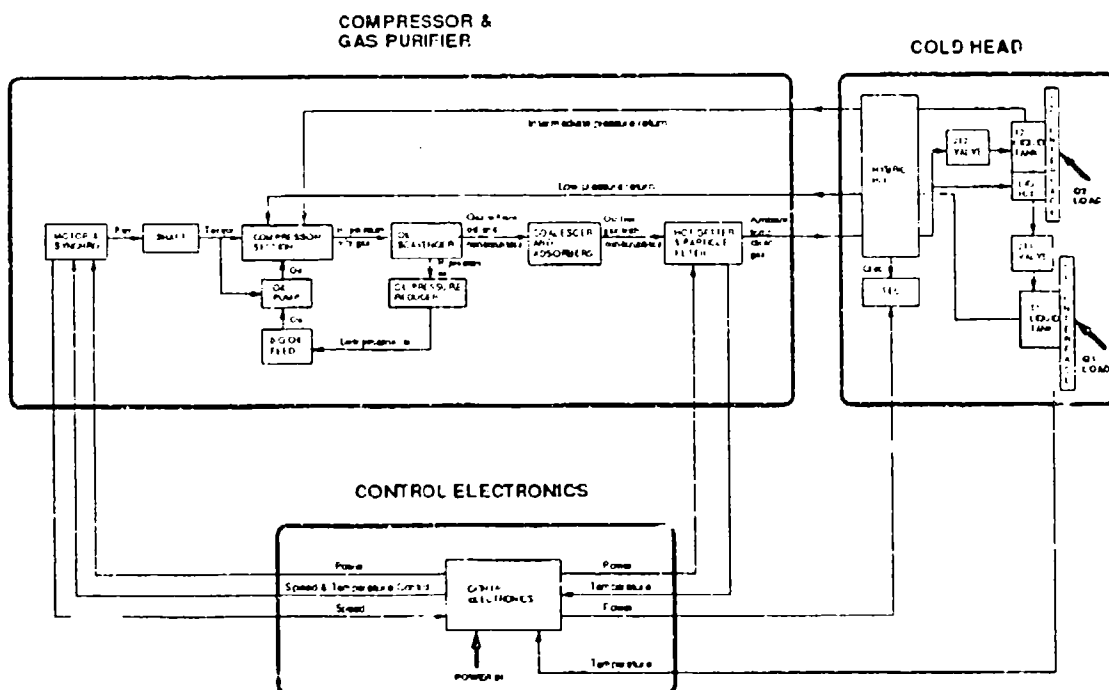


Figure 3.

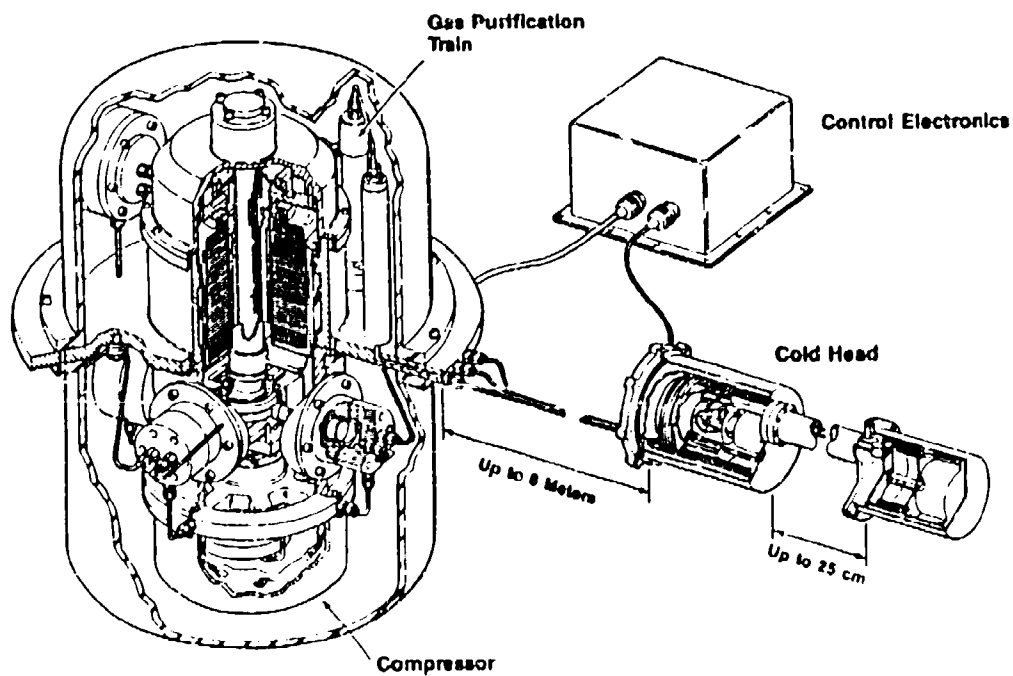


Figure 4.

612: R05:

The four-stage oil lubricated radial compressor produces high pressure gas (69 bar, 1000 psia) and flows the gas into the gas purifier. The first component of the purifier, the oil scavenger, removes 99.997 % of the oil from the gas stream and returns it to the compressor via the oil pressure reducer. The remaining oil and any gaseous contaminants enter the next components of the gas purifier, the coalescer and adsorber. The coalescer removes the remaining trace amounts of oil and the adsorber removes the bulk of the water vapor from the gas stream. The oil-free gas then enters the final component of the gas purifier, the hot getter and particle filter. The hot getter permanently removes the remaining gaseous contaminants and the particle filter prevents particulate contamination from passing the gas purifier.

The ambient temperature clean gas enters the cold head and is cooled by counterflow heat exchange and the TEC in the hybrid heat exchanger. Upon exiting the hybrid heat exchanger, the flow splits into two streams and is expanded to produce cooling at 100 K and 65 K. Each stream returns to the compressor to complete the cycle.

The control electronics provide conditioned power and control functions to the cooler. The control electronics minimizes the rotational vibration of the compressor by maintaining the compressor speed constant within each revolution. This is accomplished with a closed loop speed control servo contained within the electronics. The control electronics also maintains the interface temperature constant. By varying the compressor speed over the range of 2 to 10 rev/sec, the temperature of the liquid in the load tank can be adjusted to maintain the interface temperature constant with varying load. This is accomplished with a closed loop temperature control servo that is also contained within the control electronics.

## ABE TEST RESULTS

The cooler was designed and analyzed with three analytical models: the thermodynamic model, the vibration control model, and the temperature control model. The

thermodynamic model accurately predicted the thermodynamic operation of the cooler during its start up, cooldown, and load profile operating regimes. The vibration control model helped create a speed control servo design that limited compressor speed variations to a level that allowed the compressor to meet the rotational vibration requirement. The temperature control model helped create a temperature control servo design that maintained the interface temperature constant within  $\pm 0.25$  K with varying load.

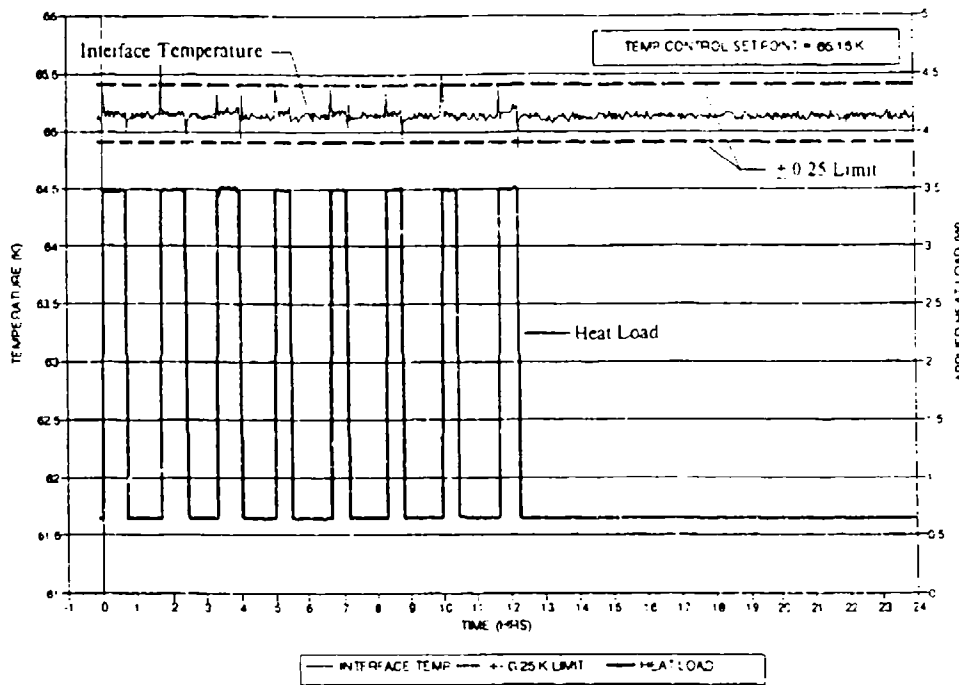
## COOLING CAPACITY & COOLING TEMPERATURE

The cooler demonstrated the required 0.65 W to 3.5 W variable cooling capacity at 65 K. The cooler also demonstrated 1.0 watt of cooling at 100 K while concurrently providing 3.5 watts at 65 K. This was in good agreement with the design point predictions of the thermodynamic model.

## TEMPERATURE STABILITY

The cooler demonstrated the required temperature stability at the load interface. Test data is shown in figure 5 for a 24 hour load profile test and for the interface temperature response during the first high load period. Modeling results and test data for key cold head temperatures are shown in figure 6. This comparison shows the good correlation between the model and test results during the load profile operation.

ABB SYSTEM TEST RESULTS  
LOAD INTERFACE TEMPERATURE STABILITY



SEGMENT #1 RESPONSE

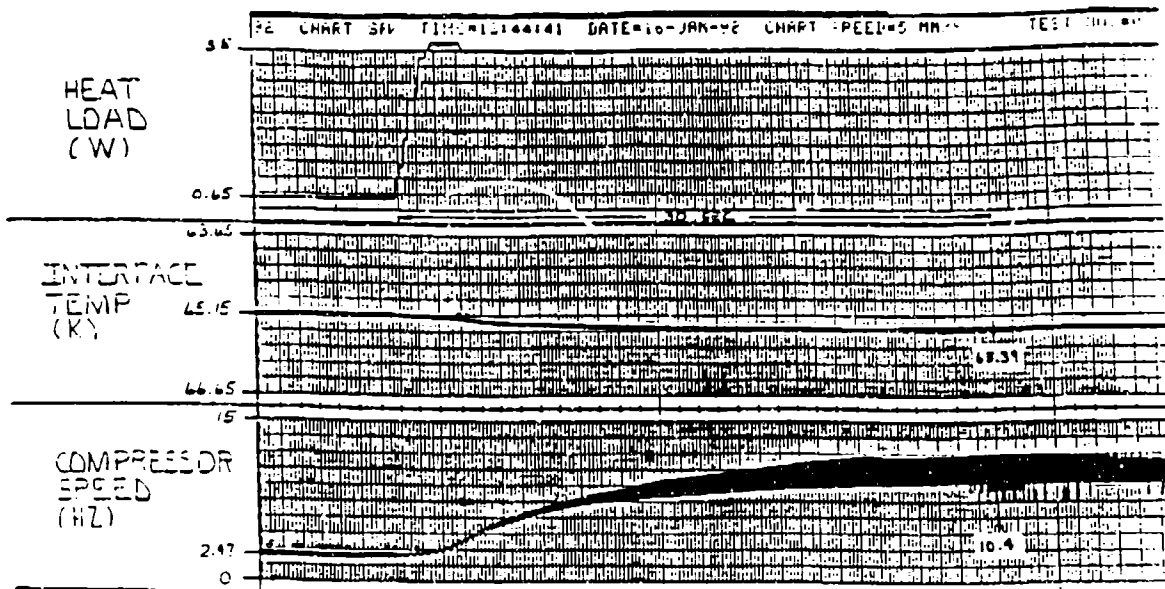


Figure 5.

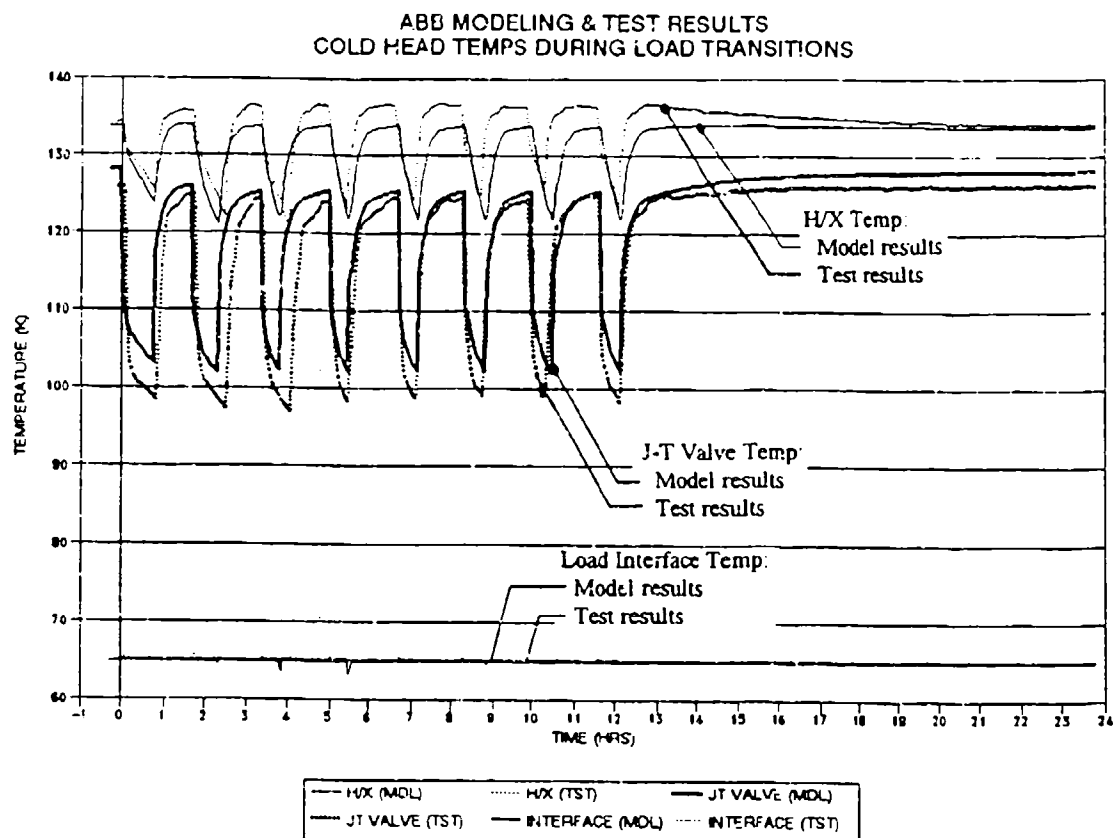


Figure 6.

## INPUT POWER

The cooler demonstrated 3.5 watts of cooling at 65 K concurrently with 1.0 watt at 100 K with a total input power of 295 watts. This equates to 75 W/W at 65 K and 32 W/W at 100 K, or neglecting the upper loop cooling capacity it equates to 84 W/W @ 65 K. The thermodynamic model predicted that the average power budget would be met, but the cooler exceeded that budget by 30%. The power budget was exceeded because the compressor motor efficiency was below the requirement and the electronics were relatively inefficient. Additionally, power was consumed in the test set up electrical cables that was not accounted for in the model. Improving the motor performance and

the efficiency of the electronics along with decreasing the losses in the cables would reduce the input power to within requirements.

## COMPRESSOR VIBRATION

The compressor vibration test set up and test results are shown in figures 7 and 8, respectively. The test results show that the compressor meets the linear vibration requirements at the operating frequency. This is the area in which concentrated effort was directed to minimize vibration from any unbalanced mass. The test results also show that forces at the harmonics of the operating frequency exceeded the requirements. The cause of the force harmonics was a pressure spike in the first stage cylinder that occurred when the piston was at top dead center. The pressure spike caused a temporary load reversal on the scotch yoke which drove the yoke off the cam bearing. When the load reversal ceased, the yoke was driven back on to the cam bearing and the resulting impact "rang" the yoke mechanism. The ringing produced the rich harmonic content seen in the vibration output. The pressure spike, caused by injecting an excessive amount of oil into the cylinder, was eliminated by simply reducing the oil feed pressure. Additional vibration testing is scheduled for early 1993 to confirm the reduction in linear vibration output.

The test results show that with the speed control servo, the compressor also meets the rotational vibration requirements.

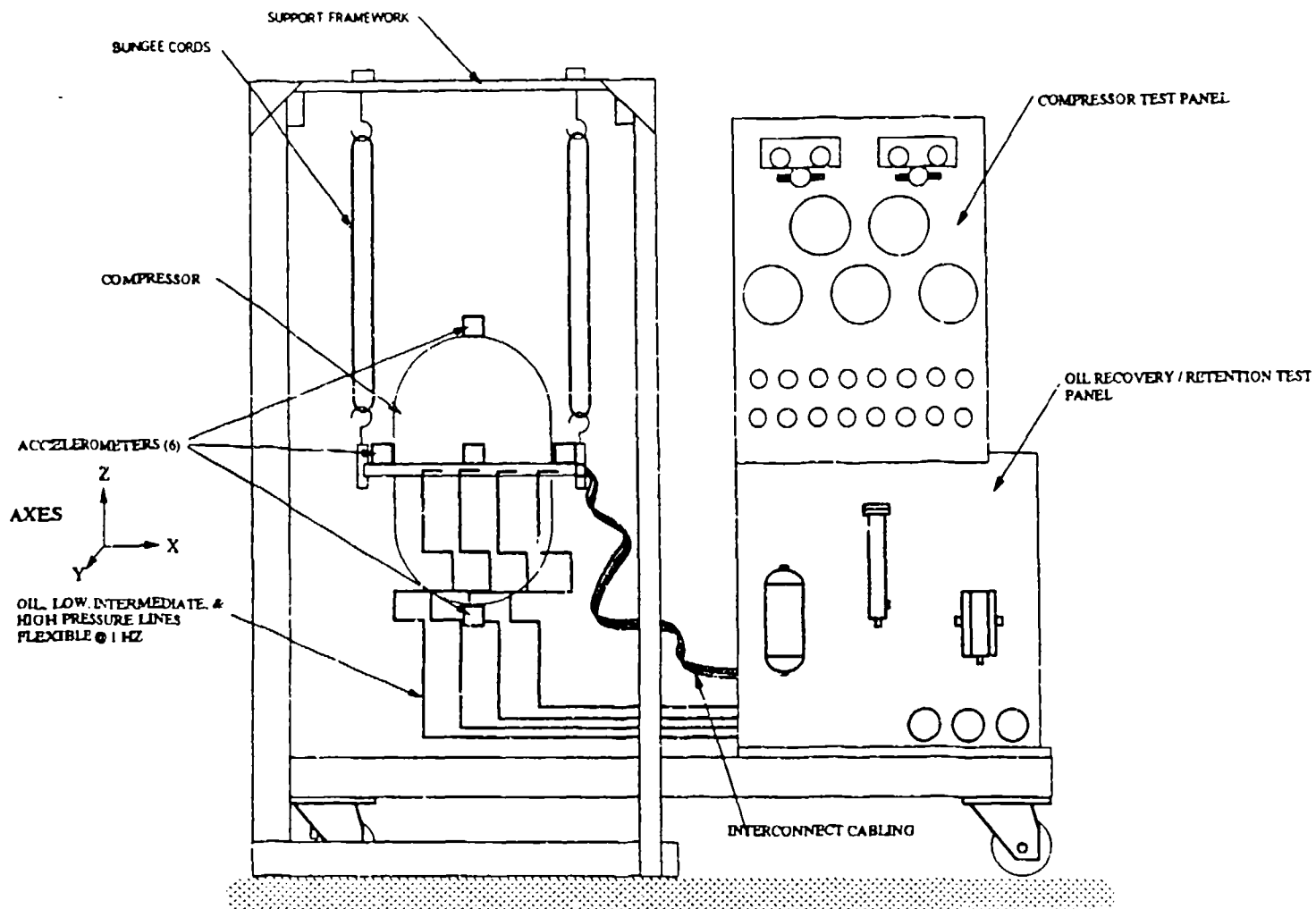


Figure 7.



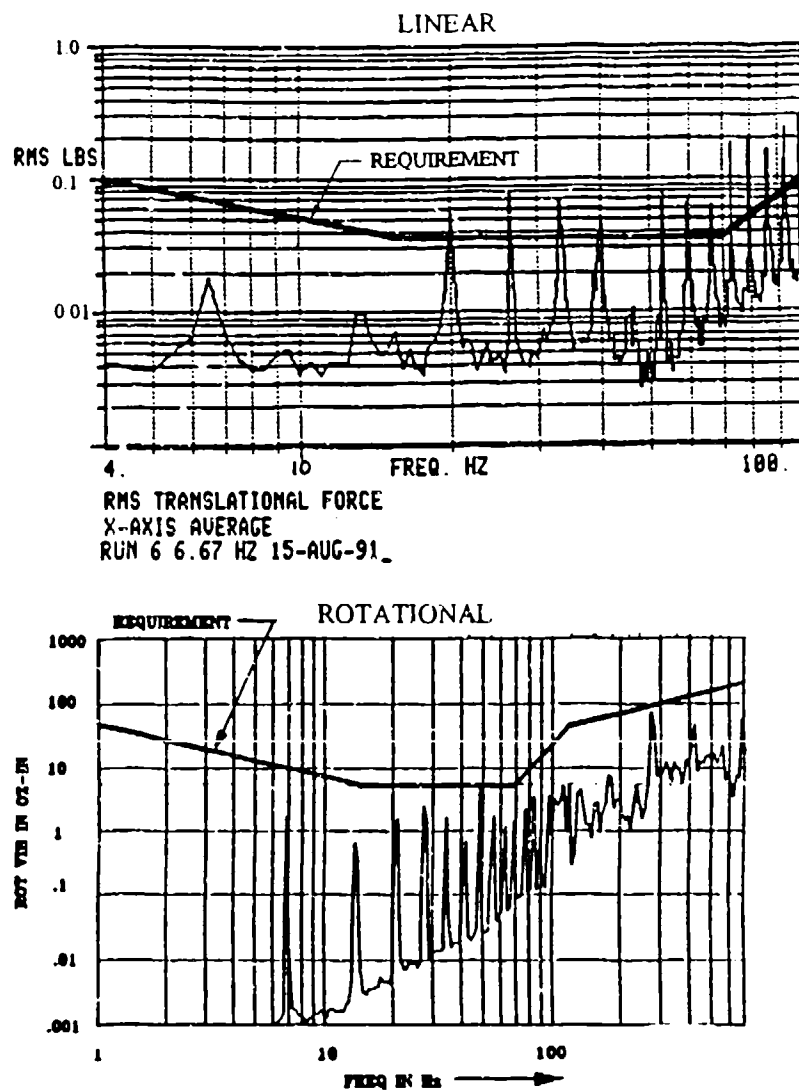


Figure 8.

## COLD HEAD VIBRATION

The cold head vibration test set up and test results are shown in figures 9 and 10 , respectively. The test results show that the maximum vibration at the load interface was  $62 \times 10^{-6}$  lbs (32 times less than the requirement). This is one of the key benefits of the Ball J-T cryocooler.

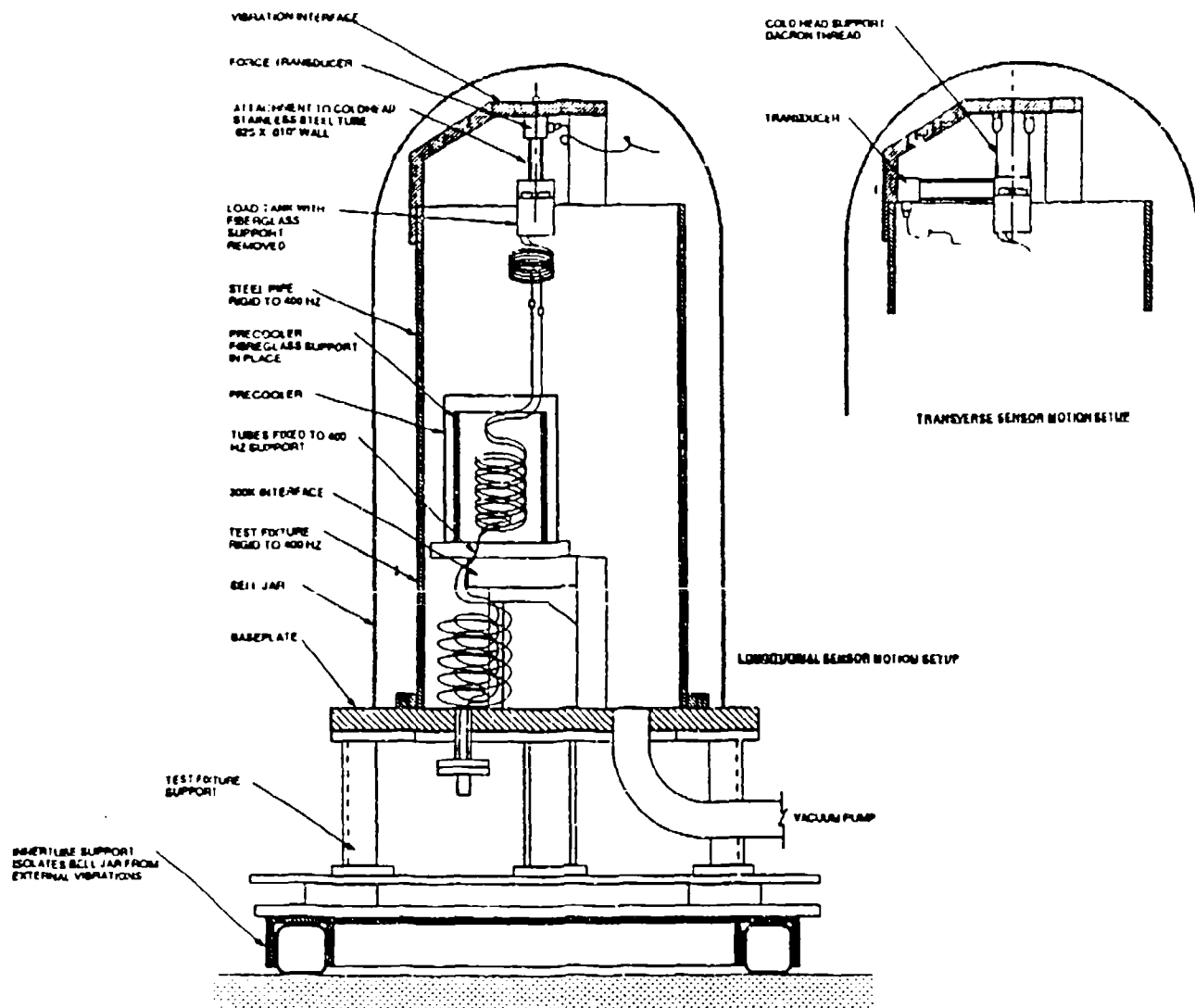


Figure 9.

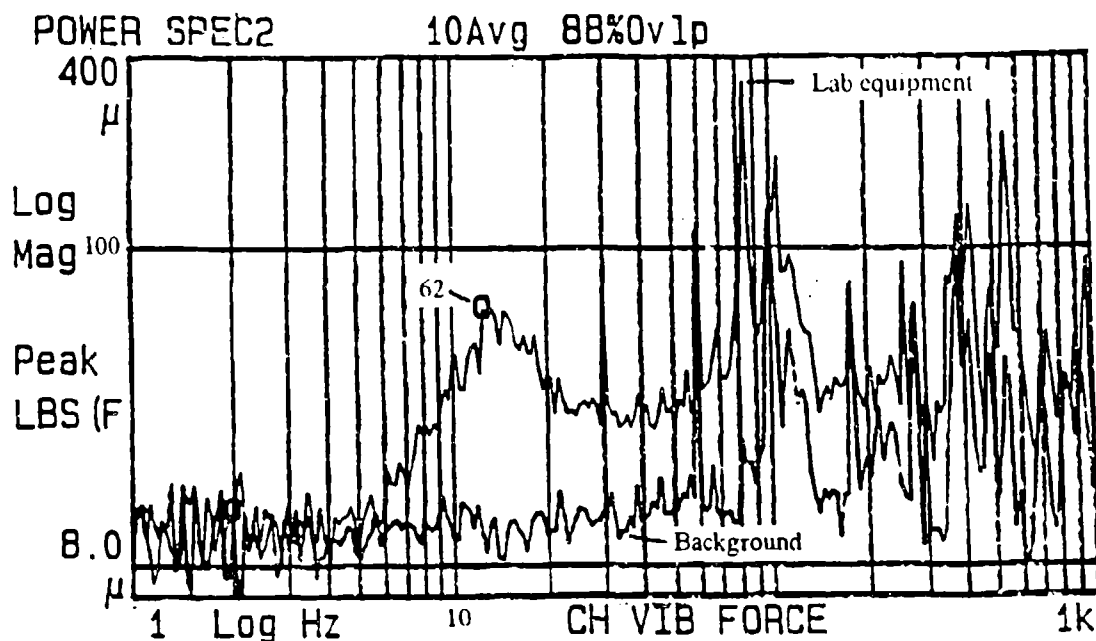


Figure 10.

### ABB COMPONENT TESTING

In addition to the system level testing done on the ABB cryocooler, component and subsystem level development testing was conducted of critical areas. Three of the most significant tests are described here.

Gas Purification Demonstration. Before the ABB program, we designed the gas purification subsystem based on manufacturer's data and test results of our custom components. This data indicated that contamination could be adequately controlled for the required long term operation. A test was set up called the "Gas Purification Demonstration" to prove the capability at the system level. The demonstration consisted of a complete closed-loop J-T cryocooler with instrumentation. We used a commercial diaphragm compressor and a cold head from previous development efforts. For added sensitivity, the J-T valve of this cold head was 50 times smaller than what will be used in

the COOLLAR cryocoolers. The gas purification system was made of commercial and custom breadboard components. A picture of the set-up is shown in figure 10.

We tested the capabilities of the gas purification system by injecting oil into the pure nitrogen gas stream at twice the rate that will be required of the COOLLAR cryocooler. The gas purification system was required to completely clean the gas stream, return the oil to the compressor and permanently retain any contaminants before they reached the 80K cold head.

The test was run for over 3000 hrs before it was terminated. Over this time 11400 liters of oil were scrubbed from the oil by the gas purification subsystem. There was no detectable change in performance of the cold head, indicating the gas purification system worked as expected.

Modified Breadboard Compressor. The only moving parts in a J-T cryocooler are in the compressor. Consequently, this is the only area that will experience wear or fatigue. To uncover any reliability issues with this subsystem we decided to endurance test an early version of the compressor during the design, fabrication and testing activities of the ABB cryocooler. This compressor was called the Modified Breadboard (MBB).

A picture of the MBB compressor is shown in figure 11. At the end of the ABB contract the MBB compressor had run for more than 12000 hours without failure or change in performance. A tear down and inspection of the compressor is planned during the COOLLAR program.

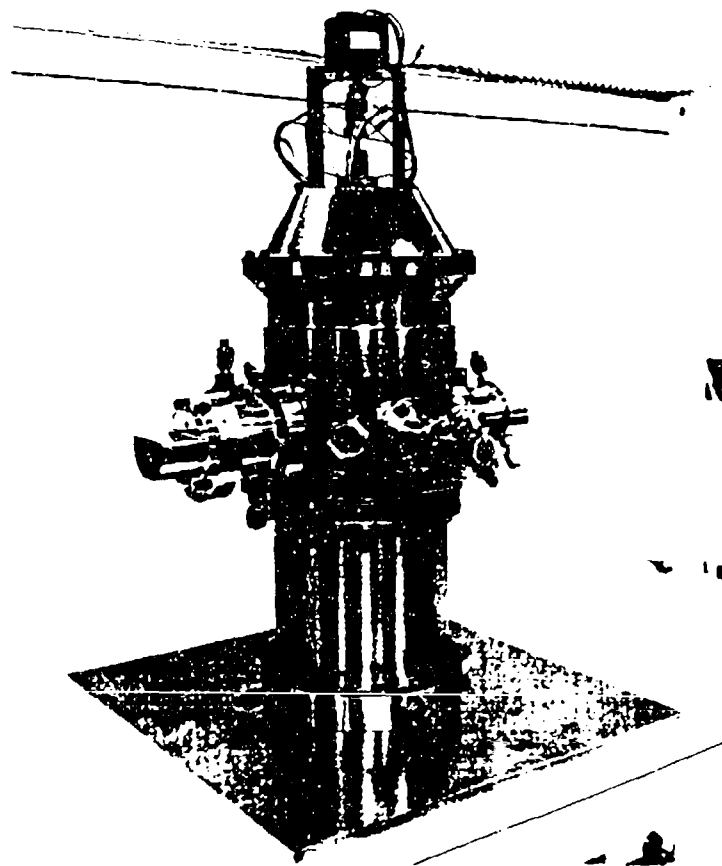


Figure 11.

It should be noted that even though the design of the MBB compressor may be adequate for the eventual flight article, significant reliability improvements have been made to the ABB compressor design to improve reliability even further. For example the drive mechanism was redesigned to reduce piston side loads by 86%. Also bearings were added in the drive train to eliminate sliding forces between the piston rods and cam shaft. We expect that the endurance testing of the ABB will prove that it's reliability has significant margin over the flight requirements.

J-T Valve Development. As we've developed the J-T cryocooler we have continually worked on improving the reliability of the J-T valve. Early models were prone to plugging either from particulate contamination or gases (usually water) freezing in the valve. We have developed our manufacturing processes and the gas purification technology to the point that valve plugging no longer occurs (the ABB cryocooler has never plugged). However, additional advancements have been made to further improve the valve's robustness against plugging. The first advancement was to add a small heater on the J-T valve. This proved to be 100% effective in clearing frozen gases from the valve. We have never had a frozen valve that didn't clear by simply energizing the heater. The process takes less than a minute and does not disturb the performance of the cooler or effect the temperature stability at the load interface.

Our next J-T valve advance was to place fine mesh screens on both sides of the valves that had could filter particles smaller than the size of the valve. We developed the manufacturing processes that allowed us to incorporate these screens in the valve assembly without generating particles in the process. These filters also proved to be a 100% effective. Since their incorporation, we have not had a valve plug with particulate contamination.

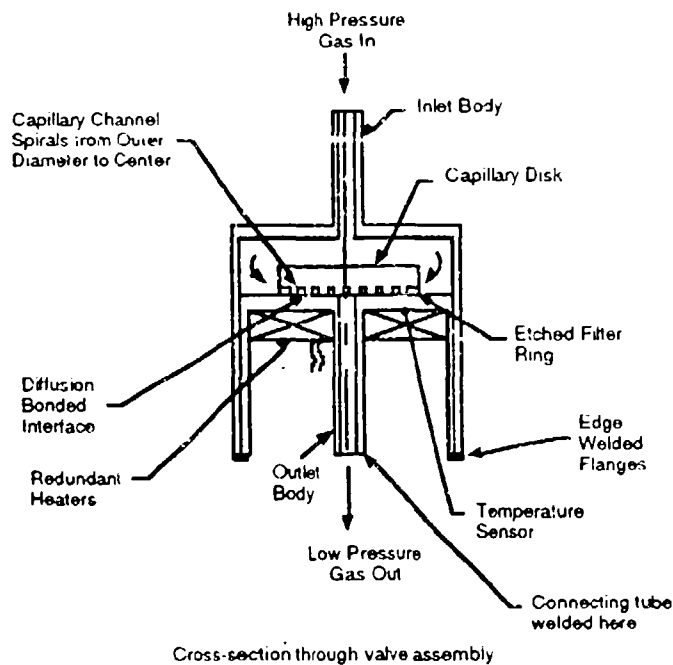


Figure 12.

During the ABB program we have gone one step further. We've developed a capillary J-T valve to get the J-T expansion effect. The capillary flow area is more than 10 times larger than the early flat plate orifice valves. We made the capillary by machining a spiral groove on one circular plate and bonding it to a non-grooved plate. This allows us to completely inspect the inside of the valve for cleanliness, ensuring no contamination is trapped in the valve during the fabrication

process. An illustration of this valve is shown in figure 12.

During the ABB program we ran a test of the advanced J-T valve to verify it's contamination tolerance. We ran the test at both room and liquid nitrogen temperatures. We injected 2 cm<sup>3</sup> of 2 micron particles aluminum oxide particles (a very large amount compared to the cleanliness of the cooler) upstream of the valve. A 5 micron filter was upstream of the valve. The valve had a 50 microns inlet and represents the smallest J-T valve that will be required in the COOLLAR program. Approximately 10,000 particles passed through the valve. The valve never plugged and the flow rate did not change.

### COOLLAR PROGRAM OVERVIEW

The overall objective of the COOLLAR program is to produce a flight worthy design and verify it's capability through testing. The focus will be on optimizing the technology proven during the ABB program with regard to weight, efficiency and size while meeting

all of the technical requirements. An equally important objective will be to continue to develop the reliability of the J-T cryocooler technology and verify the reliability with a robust test and analysis program.

The program is in the preliminary design phase, with the PDR scheduled in early 93. The design will be completed before the fall of 93. Three complete cryocoolers will be fabricated. The first unit will be subjected to full level performance and environmental testing to verify it's capability. After performance testing the first unit will be endurance tested. The second unit will undergo accelerated reliability testing. It will be subjected to conditions beyond normal operation in an effort to uncover any reliability issues remaining in the design. The third unit will be the life test model and will run unattended 5 years.

#### COOLLAR PROGRAM REQUIREMENTS

Additional requirements have been imposed on the cooler that will be developed during the COOLLAR program. The new requirements include a secondary cooling requirement with its associated stability requirement, thermal and vibration environments, and reliability requirements.

The major requirements for the COOLLAR program are summarized in the table below.



## COOLLAR PROGRAM MAJOR REQUIREMENTS

Cooling Capacity	T1: 0.65 W (low load), 3.5 W (high load) T2: 3.0 - 5.0 W
Cooling Temperature	T1: 65 +1, -3 K T2: 100 - 145 K
Temperature Stability	T1: $\pm 0.25$ K, within 30 sec of load change T2: $\pm 4.0$ K
Input Power	T1: < 100 W/W T2: < 40 W/W
Vibration Compressor  Cold Head Load Interface	< 0.133 N (0.03 lb) linear force < 0.035 N-m (0.3 lb-in) rotational force < 0.009 N (0.002 lb) linear force < 0.002 N-m (0.002 lb-in) rotational
Reliability	> 0.99 p for 7 year life, 0.5 confidence no single point failure
Operating Environment Thermal Gravity	255 - 322 K 0-g, any orientation in 1-g

PRELIMINARY DESIGN OVERVIEW

## DESIGN SUMMARY

The cooler developed for the COOLLAR program will be very similar to the proven design of the ABB cooler, but optimized for weight, size, and efficiency. The ABB design, by virtue of the dual-pressure approach, had the inherent ability to accept a

secondary load requirement. All the ABB design attributes are compatible with the 7 year life requirement and will be carried into the COOLLAR design.

The compressor will incorporate the scotch yoke design with refinements to prevent vibration during load reversal. It will also incorporate a speed control servo with improved performance over the ABB servo to add more margin to the rotational vibration output. The intermediate operating pressures of the four stages will change as a consequence of the secondary load, but the high pressure remains at 69 bars (1000 psia). Further refinement of its design may occur as a result of our continuing reliability analysis. An illustration of the COOLLAR compressor is shown in figure 13.

The cold head will be reconfigured to minimize heat leak and optimize weight, size, and efficiency. The operating temperature of the next-generation thermoelectric cooler will be controlled to maintain efficient cooler operation over the full temperature range of the operating environment. The cold head will incorporate the advanced J-T valves that are highly tolerant to gaseous and particulate contamination. Load tanks that have improved 1-g and 0-g performance will also be incorporated. And as with the compressor, further refinement of the cold head design may occur as a result of our continuing reliability analysis. An illustration of the COOLLAR cold head is shown in figure 14.

The gas purifier will feature a more robust version of the oil scavenger and oil pressure reducer and an integrated hot getter and particle filter. Exhaustive testing of the cooler materials will identify and quantify the outgassing products and this information will be used to size the gas purifier components with increased confidence. Also, a new coalescer design will be incorporated that substantially increases the performance of the coalescer.

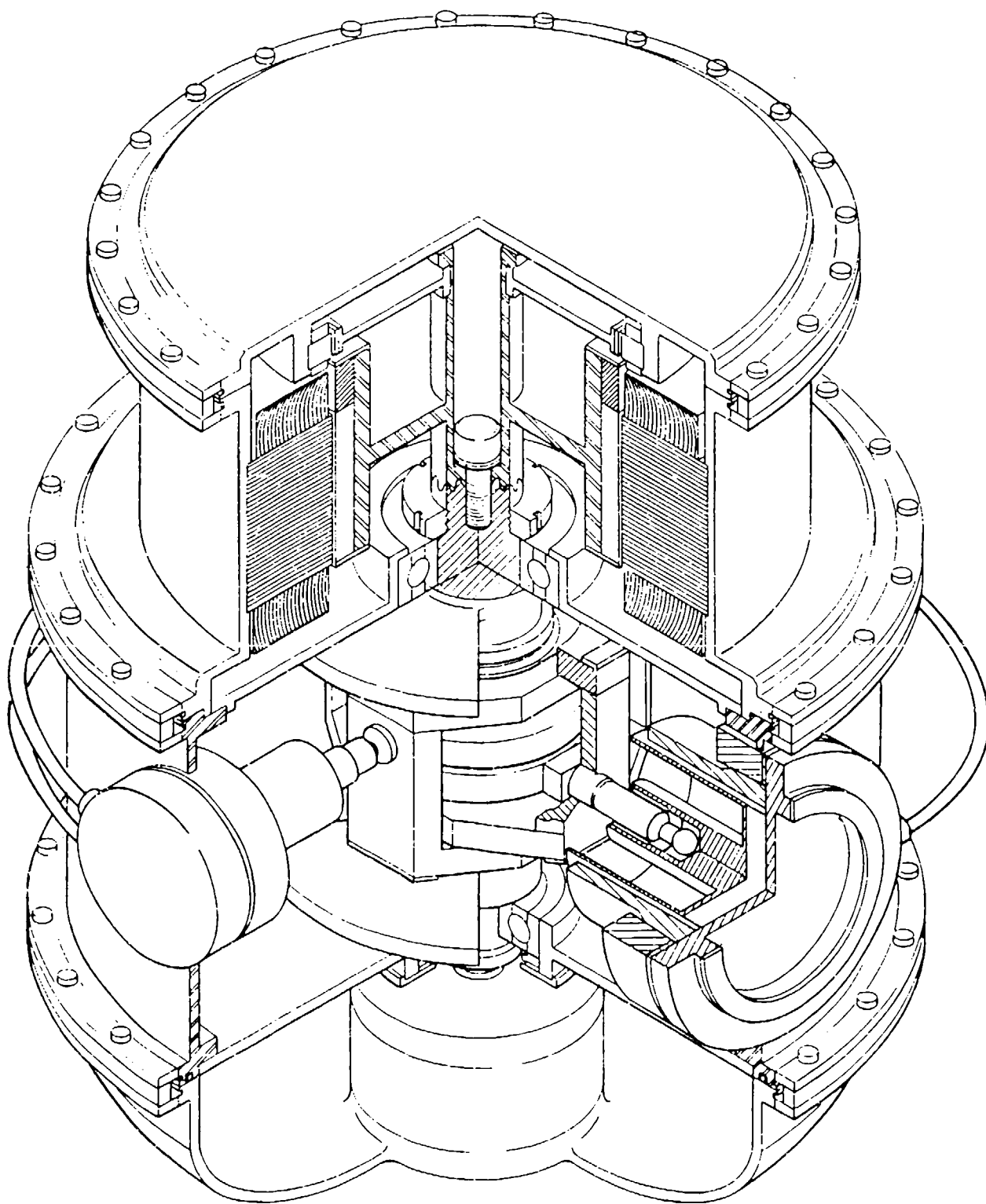


Figure 13.

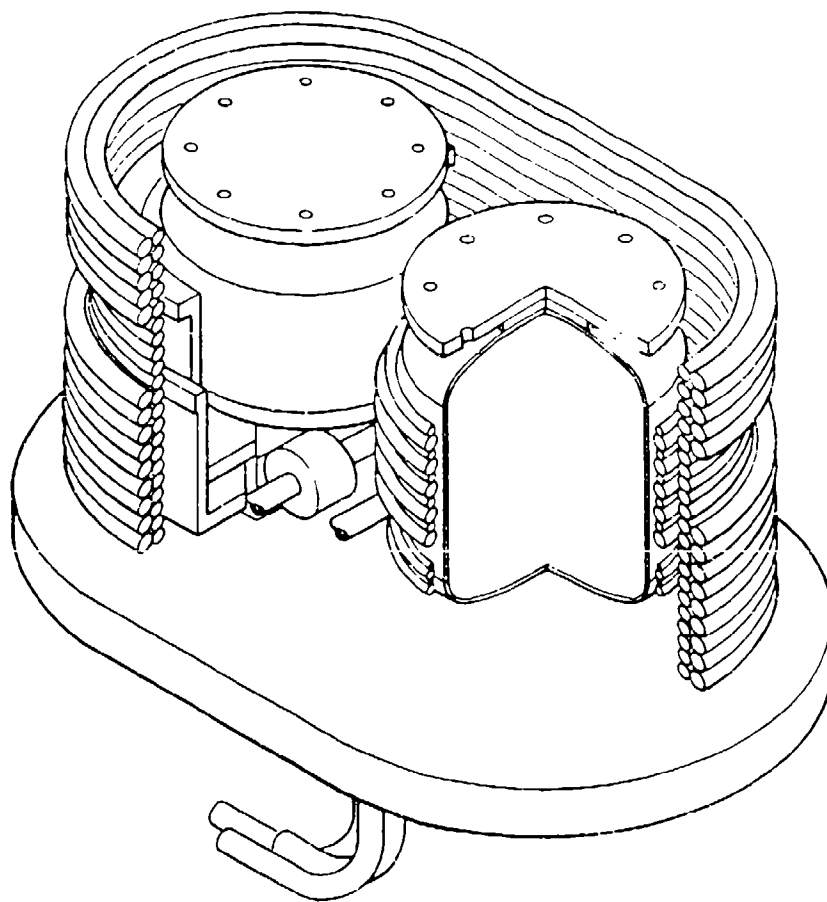


Figure 14.

The COOLLAR control electronics will make use of a microprocessor to provide command and telemetry capability and to add on-orbit adjustment capabilities to key operational parameters. On-orbit adjustments will include: T1 and T2 cooling capacity, T1 and T2 operating temperatures, and control loop performance parameters. The electronics will not be hybridized for flight during this program. Instead, the electronic parts, including the microprocessor, will be selected based on flight qualified availability and heritage. The control electronics will be designed to fit into a standard card cage for this program.

## PREDICTED PERFORMANCE

Based on the test data of the ABB cooler and the models that were developed and correlated during the ABB program, the following performance predictions are made for the COOLLAR J-T cryocooler:

### System

- Efficiency: 60 W/W @ 65 K  
26 W/W @ 120 K
- T1 Temperature stability:  $\pm 0.1$  K within 2 seconds of load change

### Compressor

- Size: 25 cm (10 in) dia, 33 cm (13 in) long
- Weight: < 18 kg (40 lbs)

### Cold Head

- Size: 13 cm X 20 cm X 10 cm  
(5 in X 8 in X 4 in)
- Weight: < 2 kg (4 lbs)

## CONCLUSIONS

The Advanced Breadboard program was successful at demonstrating the capabilities of the J-T cryocooler technology. Critical thermodynamic, vibration and reliability issues have been solved. By demonstrating the flight hardware performance requirements, the COOLLAR program can focus on engineering issues.

## JT CRYOSTAT WITH LIQUID-SOLID CRYOGEN RESERVOIR

RALPH C. LONGSWORTH  
APD CRYOGENICS INC  
ALLENTOWN, PA 18103-4783

### INTRODUCTION

Joule-Thomson cryostats with reservoirs that fill with liquid cryogen have been under development for applications where extended cooling is needed after gas flow has been stopped and for applications in space where the pressure in the reservoir can be reduced to provide temperatures below the triple point temperature of the cryogen. Two methods have been used to fill the reservoir. First is to cool the outside of the reservoir with the JT flow stream and condense gas from a separate supply bottle. Second is to have the JT flow fill the reservoir directly. In order to retain the cryogen in the reservoir and then transfer heat to it with minimum temperature rise, it is necessary to have a special packing in the reservoir.

This paper describes an experimental cryostat which was designed for use with Ar and N<sub>2</sub> that collects liquid directly from the heat exchanger. The packing in the reservoir separates the liquid from the gas as it emerges from the JT nozzle, retains the liquid in wicking material as it is rapidly depressurized, and transfers heat to the liquid or solid cryogen during the hold period with a small temperature rise. Tests were run to simulate its use in a sounding rocket.

### PROCESS

Two basic means have been tried for filling the reservoir with cryogen as shown in Figure 1. The first, Fig. 1a, is to have two separate gas supply bottles, one which supplies gas to the JT heat exchanger at a high pressure, e.g. N<sub>2</sub> or Ar at 40 MPa, and a second which contains the gas that fills the reservoir at a lower pressure, e.g. N<sub>2</sub> at 1 MPa. Cold gas from the JT heat exchanger flows through another heat exchanger on the outside of the reservoir which cools the reservoir and causes the gas in the reservoir to condense until the reservoir is either full or the reservoir bottle pressure has dropped to the saturation pressure corresponding to the reservoir temperature. For example, a JT heat exchanger operating with Ar might cool the reservoir to 95 K corresponding to the Ar pressure in the evaporator being .21 MPa. Thus, if N<sub>2</sub> is condensing in the reservoir, the supply bottle pressure would not drop below .54 MPa. After filling the reservoir with cryogen the JT flow can be stopped and the vent valve on the reservoir opened to a low pressure corresponding to the saturation temperature that is desired in the reservoir. It is important that residual gas in the JT heat exchanger also be vented so that residual gas does not condense and freeze in the evaporator when the reservoir temperature is reduced.

## JT CRYOSTAT WITH LIQUID-SOLID CRYOGEN RESERVOIR

Ralph C. Longworth  
APD Cryogenics Inc  
Allentown, PA 18103

### ABSTRACT

JT Cryostats have been developed which cooldown quickly and collect liquid in a reservoir which can then be vented to vacuum to solidify the cryogen and provide refrigeration at temperatures below the triple point. This paper describes an experimental unit which was designed for use with Ar and N<sub>2</sub> which has a packing in the reservoir that separates the liquid from the gas as it emerges from the JT nozzle, retains the liquid in a wick material as it is rapidly depressurized, and transfers heat to the solid cryogen during the hold period with a small temperature difference.

Examples are given of experiments that simulate a sounding rocket test in which the cryostat is cooled down on the ground and vented to a vacuum pump for pre-launch calibrations, flown into space with liquid maintained by a small on-board tank of gas, then solid cryogen is formed by stopping the JT flow and venting to vacuum.



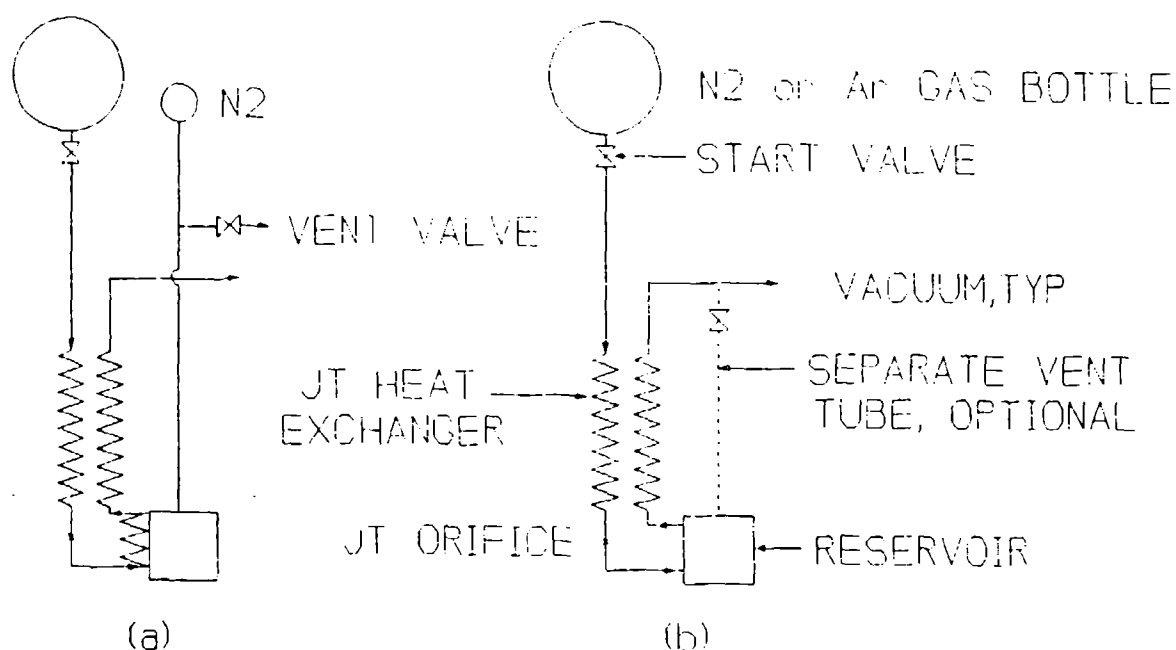


**FIGURE 1** Process Schematics for Two Methods of Filling A Reservoir With a Cryogen Using a JT Cooler.

- (a) Externally-Cooled Reservoir
- (b) Internally-Cooled Reservoir

The packing in the reservoir must consist of an extended surface heat transfer material that can transfer heat from the condensing cryogen in the reservoir to the JT flow in the evaporator and a wicking material that retains the cryogen when the rapid pressure reduction causes violent boiling of the liquid cryogen. Open passages are also needed to let the gas escape without entraining liquid during depressurization. Porous copper and aluminum have been used for this purpose but a better type of packing has been developed as described in [1]. A two-stage  $N_2/H_2$  JT cryostat of this type which used the new packing material to solidify  $H_2$  has been described in [2].

The second method of filling the reservoir, Fig. 1b, is to have cold gas/liquid from the JT heat exchanger flow directly into the reservoir and collect there. The packing in the reservoir for this process must serve as a phase separator to remove liquid from the JT flow which may have a high velocity. Other requirements for the reservoir packing are the same as for the externally cooled reservoir.

The externally cooled reservoir cryostat has the following relative advantages:

- By monitoring the pressure in the reservoir supply tank, it is possible to know when the reservoir is full and how much liquid has been condensed

- A higher temperature gas with higher JT cooling effect such as Ar can be used to condense a lower temperature gas such as N<sub>2</sub>

The internally cooled reservoir cryostat has the following relative advantages:

- The reservoir can be lighter because less heat exchanger surface is needed.
- The reservoir can be lighter because it can be designed for a lower pressure.
- The residual gas in the heat exchanger is vented along with the gas from the reservoir.
- Less cryogen is vaporized to cool the reservoir from the fill temperature to the base temperature because the reservoir is lighter.

When venting to vacuum the minimum temperature that is reached depends primarily on the flow restrictions in the vent path. An internally filled reservoir that is vented through the heat exchanger would not reach as low a temperature as a design that had a separate, less restrictive vent tube with a valve that opens after JT flow has been stopped, ref. Fig. 1b option

#### EXPERIMENTAL CRYOSTAT DESIGN

Figure 2 shows the design of the JT heat exchanger and internally cooled reservoir that was tested. A finned-tube heat exchanger with a central mandrel tube has an extension on the cold end such that the gas/liquid mixture flows out the end of the extension after flowing through the JT restrictor. The heat exchanger slides into a sleeve which has the reservoir connected at the cold end. Adjustments can be made to the JT restrictor by simply removing the heat exchanger.

The reservoir is designed with a thin stainless steel housing and a flat copper end cap that serves as the cold plate where the device being cooled is mounted. The packing in the reservoir consists of alternating layers of porous copper and wicking material which has a very fine pore size. The copper layers are soldered along the bottom edge to the cold plate. Gas from the JT heat exchanger impinges on the back side of the cold plate then flows radially out along the cold plate and back through the porous copper layers before returning to the heat exchanger. This flow path causes the cold plate to cool first and then liquid collects in the packing. Capillary attraction of the liquid in the pores of the wick is high, so that moderate gas velocities through the conductor are possible without blowing liquid out of the wick. Similarly, when the reservoir is depressurized the open structure of the conductor layer allows gas to escape with very little entrainment of liquid. The reservoir was designed to store 460 J of cooling after being filled with LN<sub>2</sub> at 80 K. In cooling to 70 K, 50 J is used to cool the reservoir and the remaining LN<sub>2</sub>. Similarly 105 J is used to cool from 80 K to 60 K, leaving 355 J available for cooling at 60 K.

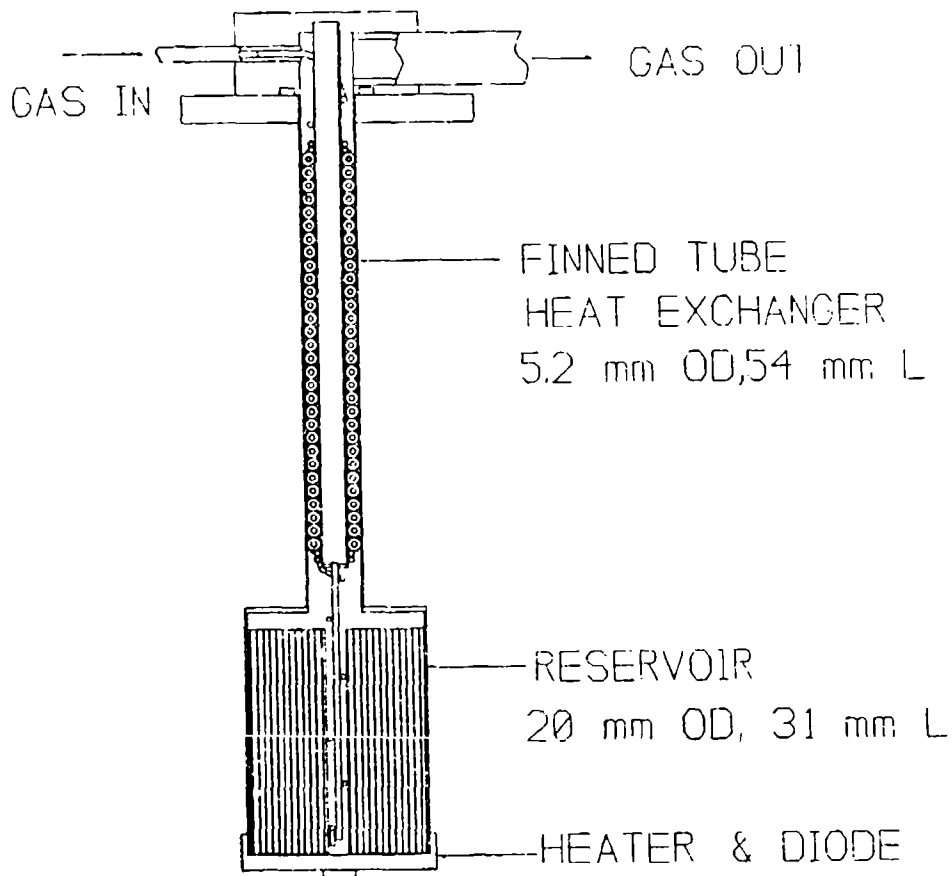


**FIGURE 2** Experimental Cryostat Having a Finned-Tube Heat Exchanger  
Flowing Cold Gas / Liquid Through An Internally-Cooled Reservoir

### TEST ARRANGEMENT

Fig. 3 shows a schematic diagram of the test setup that was used to simulate the operation of the experimental cryostat in a sounding rocket. The mission that is envisioned would occur in the following four phases.

Phase 1 Open V1 & V2. The unit would cool down on the ground with N<sub>2</sub> supplied at constant pressure from a standard cylinder and vacuum provided by a pump, both to be left on the ground. A temperature of about 70K is maintained to do a ground test of the instrument.

Phase 2 Close V1 then V2. Just before launch, the gas supply and vent lines are sealed and disconnected so that during the 2-minute flyout the cryogen in the reservoir is warming and the pressure is increasing

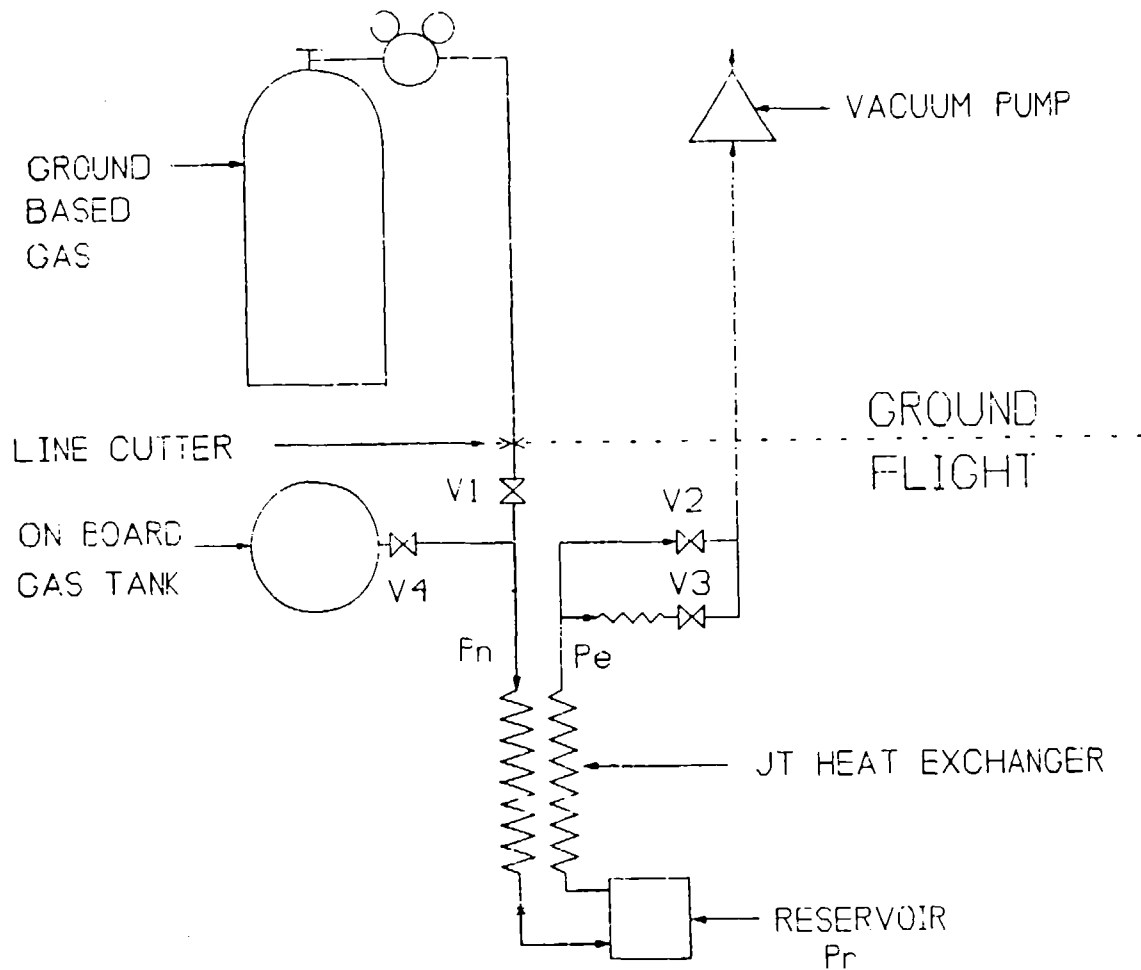


**FIGURE 3** Experimental Test Set Up to Simulate a Space Flight Including Cooling on the Ground From a Large Tank, Cooling in Space From an On-Board Bottle, and Coasting on Cryogen Stored in the Reservoir

**Phase 3** Open V2. When the flight unit has reached a space environment the vent valve is reopened and the valve on the on-board gas supply bottle is opened. The cryostat then returns to the cold operating temperature, which will be the same as on the ground, if a pressure regulator maintains the same supply pressure. The liquid cryogen that boiled off during the flyout is replenished as gas flow continues. If the gas supply line does not have a pressure regulator, then the reservoir temperature will drop as the bottle pressure and gas flow rate drop.

**Phase 4** Gas flow is stopped and cooling is maintained by evaporation or sublimation of the cryogen that has been stored in the reservoir. Stopping the gas flow results in low pressure drop in the heat exchanger, which causes the reservoir temperature to drop if V2 is left open. In order to keep the temperature during the coast period at about the same temperature as when gas is flowing, the vent flow can be redirected to flow through a restrictor by closing V2 and opening V3.

## TEST RESULTS

A liquid nitrogen boiloff test venting to atmospheric pressure was run to measure the static heat loss. It was measured to be 345 mW. For subsequent tests the thermal capacity of the cryogen in the reservoir was calculated as being equal to the applied heat load, plus 345 mW times the coast time.

The following parameters were varied in running the tests:

- a) JT orifice flow rate,  $Co = 5.3, 2.0$  and  $1.0$  L/min at standard conditions,  $N_2$  at 0.8 MPa and  $21^\circ C$
- b) Fill temperature - 66 K to 81 K
- c) Orientation - Up, down
- d) Gas -  $N_2$ , Ar
- e) Vent line pressure -  $< 1$  kPa to 101 kPa

The gas supply was changed from 40 MPa for cooldown to 15 to 20 MPa during the fill period. Temperature during the fill period was dependent on pressure drop in the heat exchanger and the setting of the vent valves.

### Stored Refrigeration Capacity

Initially, the JT restrictor was set with a flow of 5.3 L/min at standard conditions. Fill temperatures for  $N_2$  were in the range of 77 K to 81 K and vent pressures were set so hold temperatures in the range of 60 K to 79 K. Thermal storage capacity for these tests are shown in Fig. 4. Results for the cold end down orientation show results that are comparable to the predicted values. When the unit was oriented cold end up, however, the retained  $N_2$  was only about 60% of the predicted amount.

Two tests were run in which the temperature of the reservoir was reduced to about 70 K by flowing He through the heat exchanger venting to atmospheric pressure rather than using a vacuum pump. Temperature could be changed by changing the He flow rate. The heat exchanger is efficient enough so that there is a relatively small loss of stored cooling in doing this.

The flow in the JT restrictor was reduced to 2.0 L/min at standard conditions and a test was run at the same fill temperature of 80 K, followed by pump down to 69 K in the cold end up orientation. A thermal storage capacity 50% greater than anticipated was measured (plotted in Fig. 4). This indicates that the higher flow rates were causing liquid to be blown out of the wick during the fill period.

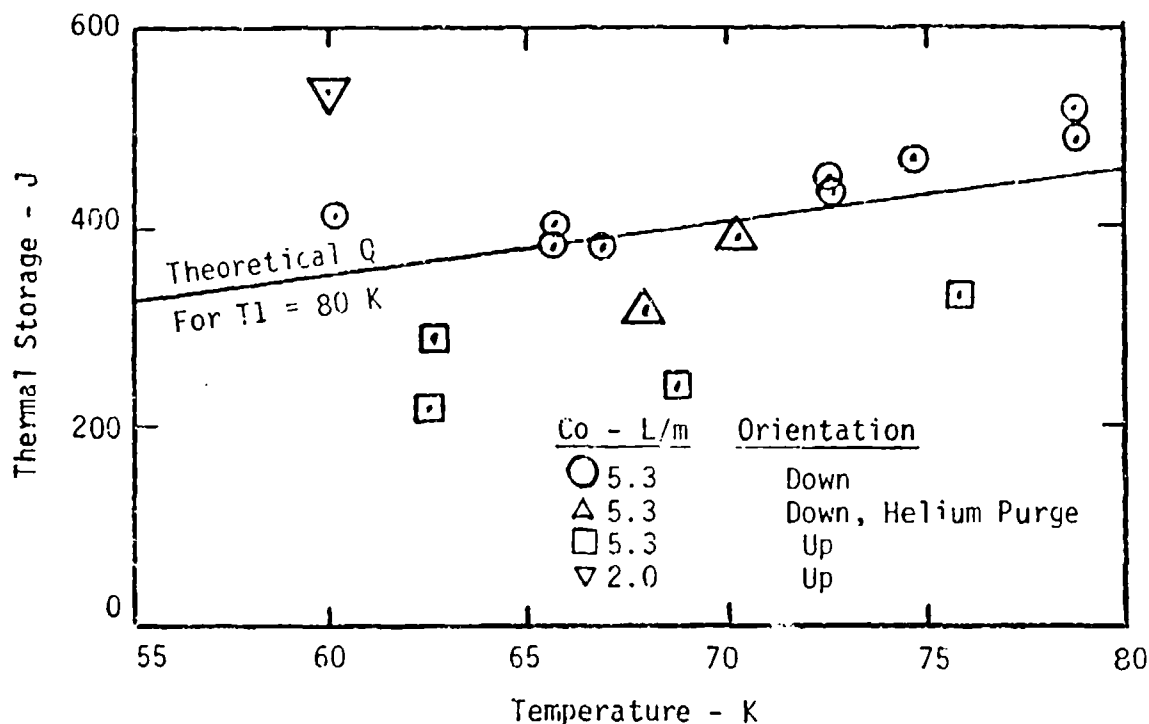


**FIGURE 4** Measured Thermal Storage Capacity for LN<sub>2</sub> Filling the Reservoir at 77 K to 81 K

More tests were run with the JT restrictor set at 2.0 and 1.0 L/min at standard conditions. The lower flow rate resulted in lower pressure drop in the heat exchanger so that the reservoir could be filled at temperatures in the range of 67 to 70 K, for which the reservoir is calculated to retain 520 J of cooling with LN<sub>2</sub>. Results of thermal capacity measurements for this series of tests are shown in Fig. 5. In the cold end up orientation, the stored refrigeration is close to the predicted value, while with the cold end down, the capacity is almost twice the predicted amount.

#### Temperature Change

As heat flows into the reservoir from the cold plate, the cryogen closest to the cold plate vaporizes first. As the cryogen vaporizes, the distance to the remaining cryogen increases and the heat transfer surface area of the cryogen decreases. These two factors cause the temperature difference between the cold plate and cryogen to increase at an increasing rate.

Temperature change versus time for the last 10 minutes of the hold period is plotted in Fig. 6 for a number of tests. All of the tests follow paths that are quite similar. Temperature during the last 2 minutes is seen to increase from an average difference of 1.3 K to an average difference of 3.2 K.

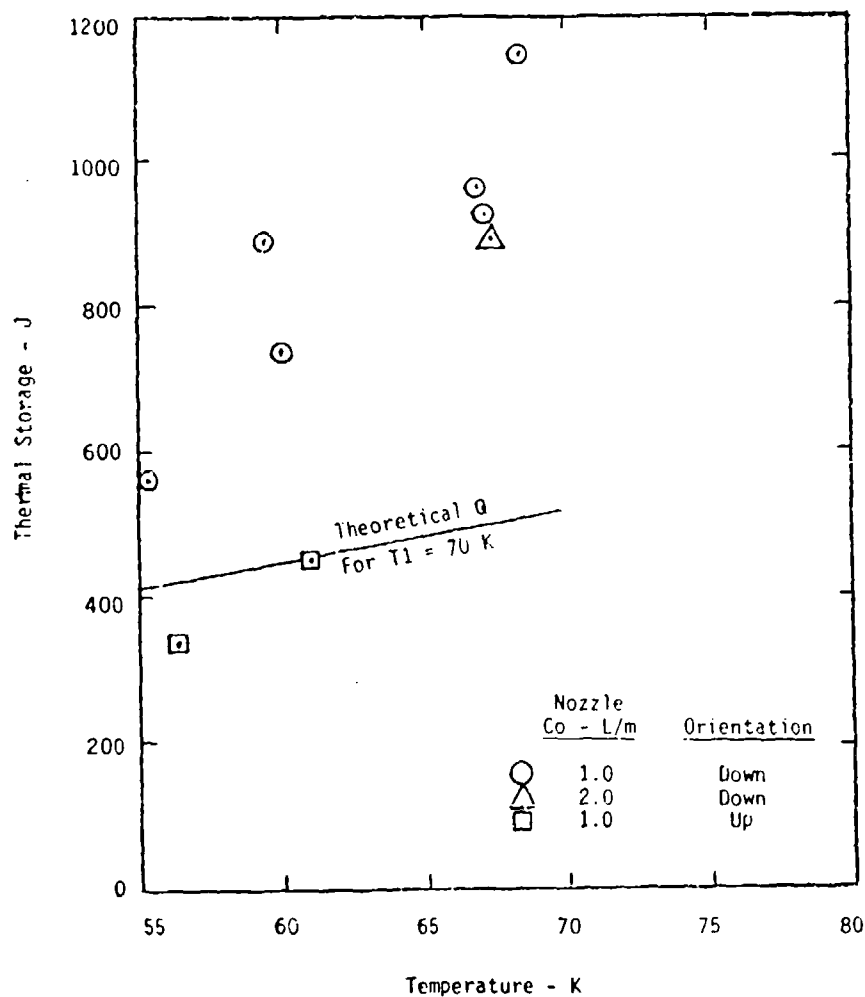


**FIGURE 5** Measured Thermal Storage Capacity for LN<sub>2</sub> Filling the Reservoir at 67 K to 70 K

If an application requires that the temperature be more constant, there are several options, as follows:

- design the reservoir for extra capacity so that only about 80% of the cryogen is vaporized during the period when cooling is needed.
- design the reservoir with a higher ratio of thermal conductor to wick and smaller length to diameter ratio.
- use a variable restrictor in the vent line coupled to a controller to reduce the cryogen pressure and temperature as the  $\Delta T$  increases

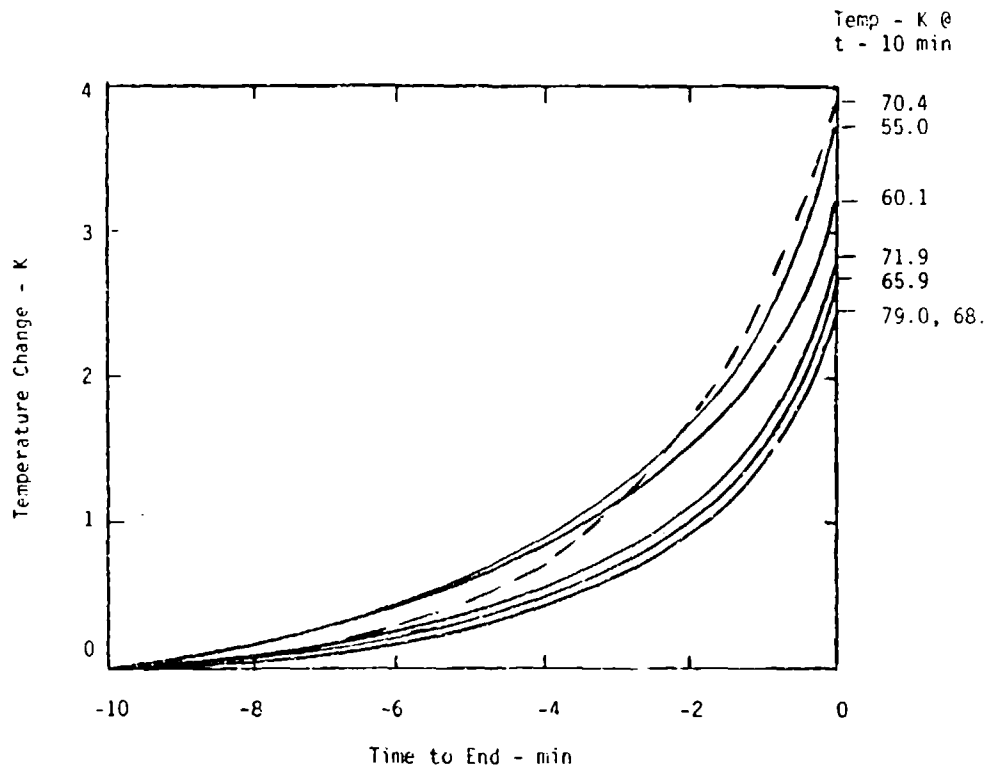


**FIGURE 6** Temperature Rise During the Last 10 Minutes of the Coast Period  
For N<sub>2</sub> \_\_\_\_\_ and Ar - - - - in Test Reservoir.  
250 mW applied Load + 345 mW of Static Load.

### Flight Simulation

Tests were run to simulate cooldown and operation on the ground, launch into space, cooling from an on-board gas bottle, followed by coasting from the stored cryogen.

Fig. 7 shows a plot of a test that was run with the JT restrictor set at 2.0 L/min at standard conditions for which we tried to maintain a temperature of about 70K during the flight phases. This test was run with N<sub>2</sub> in a cold end down orientation, and no additional heat load applied. After cooldown, a temperature of 74 K was held as established by the pressure drop in the heat exchanger and restriction in the vent line, V2 open and V3 closed. Just prior to launch, the gas supply valve is closed and the reservoir allowed to cool to 68 K before closing the vent valves. During the next 120s, the temperature in the reservoir rises back to 74 K. Vent valve V3 is then reopened to vacuum, after which V4 is opened to supply gas to the cryostat. During the period of operation from the .5 L on-board gas bottle, the supply pressure drops from 32 MPa to 10 MPa and the temperature drops from 74 K to 70 K.



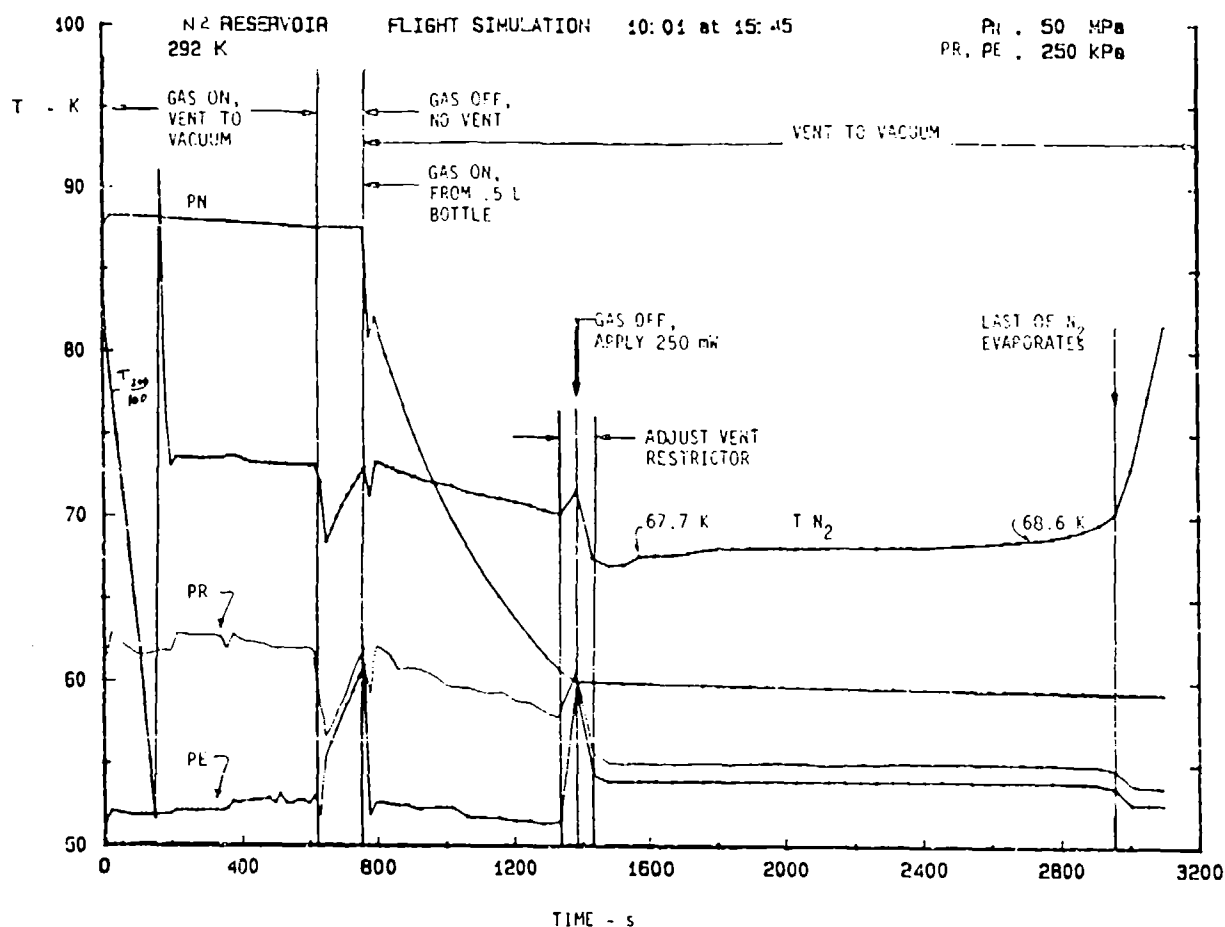


**FIGURE 7** Experimental Flight Test with  $N_2$  in Which the Vent Valves are Adjusted to Maintain a Temperature of About 70 K.

The coast phase is initiated by increasing the restriction in the vent line, opening V3 and closing V2, then closing the gas supply valve V4, and closing V3 at a rate that gets to the desired coast temperature fast without getting too cold. The valve adjustment for this test resulted in a temperature of 67.7 K after the temperature stabilized, rising to 68.6 K when about 85% of the  $LN_2$  had vaporized.

Fig. 8 shows another test for which the JT restrictor flow was 1.0 L/min at standard conditions and the unit was oriented cold end up. Both vent valves, V2 and V3, were set full open during all but the launch phase of the test. This resulted in a temperature of 66 K being held on the ground with no applied heat load, and 67.5 K dropping to 67.0 K when operating with the on-board bottle and 250 mW applied. During the coast phase, the temperature dropped to 56.3 K with 250 mW applied and 55.0 K when the heater was turned off.

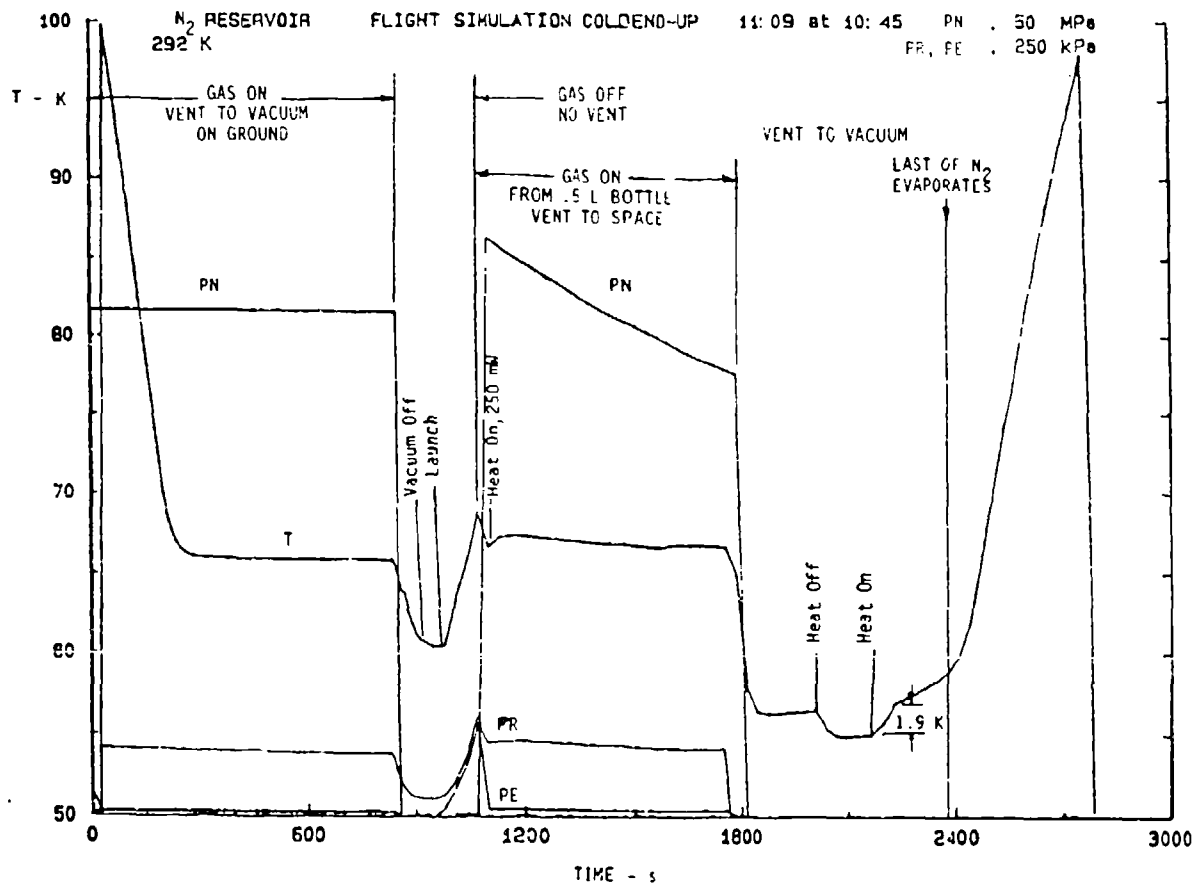


**FIGURE 8** Experimental Flight Test with N<sub>2</sub> in Which the Vent Valves are Fully Opened to Demonstrate Minimum Temperatures.

Similar tests with Ar showed temperatures to be about 10 K warmer than for N<sub>2</sub> and coast times to be longer.

### SUMMARY

A JT Cryostat with an integral reservoir has been built and tested with N<sub>2</sub> and Ar venting to vacuum. The reservoir packing which consists of layers of thermally-conducting porous copper and a non-thermally conducting wick is effective in removing liquid direct from the JT flow stream and retaining it in the wick during the fill period and during the period of rapid depressurization in a cold-end up orientation

Simulation of an experiment that starts on the ground then flies into space showed that when using  $N_2$  it is possible to operate at 66 K while on the ground venting to a vacuum pump and in space venting to vacuum with gas supplied from an on-board bottle. When flow was stopped, the temperature dropped to 55 K then warmed about 1.5 K at the time when 85% of the solid  $N_2$  has sublimed. The temperature difference between the load and the solid cryogen is a function of the heat transfer path and the load. Temperature can be controlled by adjusting a vent line valve which affects the pressure at which the cryogen in the reservoir sublimes.

Argon enables the unit to cool down faster and store more refrigeration than  $N_2$ , but the temperature for comparable conditions is about 10 K greater. The temperature in the reservoir can also be depressed without using a vacuum pump by having He flow through the heat exchanger and stored cryogen.

#### REFERENCES

1. R. C. Longworth, "Cryogen Thermal Storage Matrix" -- U. S. Patent 5,012,650; May 1991.
2. R. C. Longworth, W. A. Steyert and R. L. Pittenger, "J-T Cryostat with Solid Cryogen Storage for Short Missions" -- Proceedings of the Second Interagency Meeting on Cryocoolers -- Easton, MD; September 1986 (Restricted Distribution).

DESIGN AND OPERATION OF A 30K TWO-STAGE  
NITROGEN-NEON J-T COOLER

W. A. LITTLE, RAN YARON, AND CARLOS FUENTES  
MMR TECHNOLOGIES, INC.  
1400 N. SHORELINE BLVD, #A5  
MOUNTAIN VIEW, CA 94043

INTRODUCTION

Miniature<sup>1</sup> and microminiature<sup>2</sup> Joule-Thomson refrigerators operating at 80K and lower have been successfully designed in the past using the thermodynamic and transport properties of the working gas averaged over the temperature distribution of the heat exchangers, and predetermined input and output pressures. This averaging is an approximation to the true state of affairs in the heat exchangers but in many cases has been found to predict the performance of the coolers in close accord with experimental measurements. However, we have recently attempted to design and build some special refrigerators the design of which have presented some special problems. These refrigerators have very small flow rates, or two or more stages for operation at lower temperatures, and where the available volume for the refrigerator was severely restricted. The problems we found could be traced to the drop in thermal conductivity of the heat exchanger matrix at low temperatures, the small surface area over which the heat had to be transferred, and the need for balance in the transfer of heat between the fluids in the different stages. In other cases we have run into similar difficulties in predicting the performance of refrigerators that are designed for use with multi-component gas mixtures where the properties of the mixtures are a strong function of the temperature and pressure.

In an attempt to improve the reliability of the design of such refrigerators we have developed a more detailed treatment of the heat exchangers, and the thermodynamic and transport properties of the gases. We have applied this method to the design of a microminiature, miniflow-rate refrigerator for use with oxygen, and in another case, to the design of a low flow rate, microminiature, two stage, nitrogen-neon refrigerator for operation at 30K. We have obtained remarkably good agreement between the calculated and measured flow-rates, pressures, temperatures and refrigeration capacities of prototypes based on these designs.

The method generates a much more detailed description of the temperature distribution in the heat exchanger, the properties of the gases in the different regions of the exchanger, and, in addition, can alert one to possible problems in a poor design. Yet it is sufficiently tractable

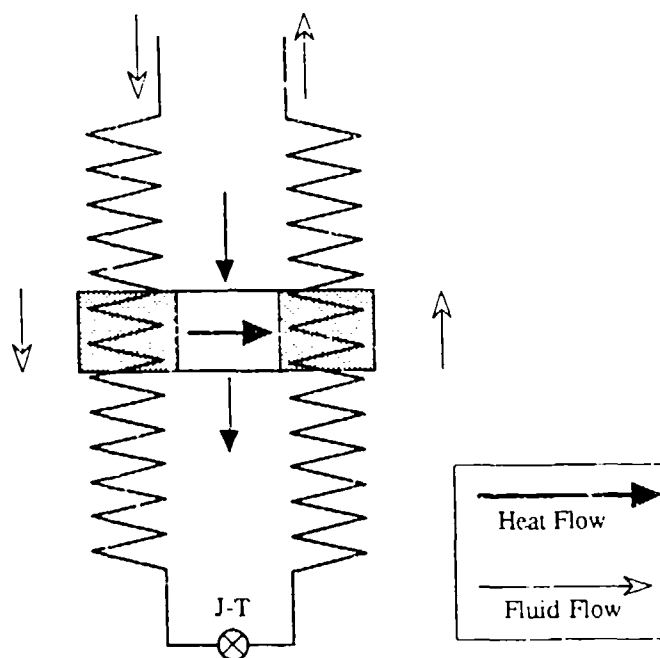


Figure 1. J-T Refrigerator illustrating one element across which heat is transferred between the contra-flowing fluid streams.

that it can be coded in a program that will run on a modest sized personal computer and generate all the needed results in a few hours.

#### SINGLE STAGE, LOW FLOW, OXYGEN REFRIGERATOR

##### METHOD OF CALCULATION.

We illustrate the method of calculation first with the design of a single stage, Joule-Thomson refrigerator for use with oxygen. This was required to operate with a flow rate of 0.07 sl/m, and have a capacity greater than 25mW at 95K. This is a very small flow rate and, in addition, requires an efficiency approaching the maximum attainable for oxygen. The program that was developed to calculate the performance of the refrigerator was based on the division of the refrigerator into a large number of finite elements as illustrated in Fig. 1. Usually about 200 elements were used. Each element consists of a narrow slice across the refrigerator consisting of three portions: the high pressure fluid on one side of the exchanger, the low pressure fluid on the other, and the wall across which the heat flows from one fluid to the other, and down which heat flows from ambient to the cold end. This is illustrated in Fig. 2.

The computer model starts with a given mass flow, a rough estimate of the dimensions of the heat exchanger and flow channels, and a design choice of the temperature and pressure of the saturated vapor at the low temperature inlet to the outflow heat exchanger. The

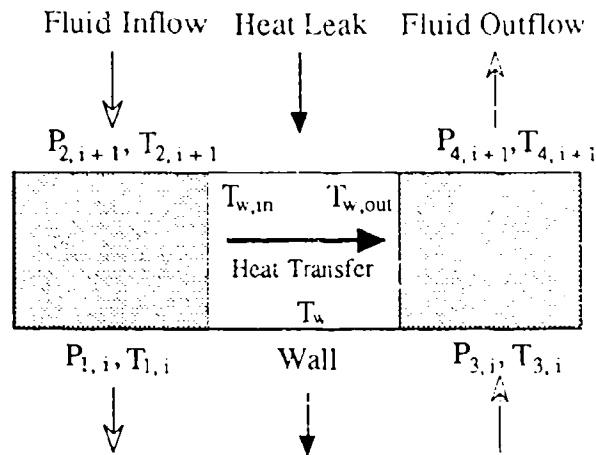


Figure 2. Schematic of Heat and Fluid Transport through one element of Heat Exchanger.

enthalpy of the two phase flow leaving the expander is determined from this after taking in to account the desired heat load. The intersection of this isenthalp with the input isobar provides a first approximation to the temperature of the fluid leaving the cold end of the inflow heat exchanger. These temperatures and pressures provides the input data for the first element at the bottom of the exchanger. The program then computes the thermodynamic and transport properties of the fluid at these temperatures and pressures in both the high and low pressure streams. The calculations were done using analytical expressions for the properties of the fluid taken from published technical data given in William C. Reynolds' compilation, *Thermodynamic Properties in SI*<sup>3</sup>. The transport properties were calculated using data from the 1989 ASHRAE Handbook, *FUNDAMENTALS, SI Edition*<sup>4</sup>. For the given mass flow the pressure drop across each element was calculated for the two streams using published values of the friction factor<sup>5</sup> for these types of channels for the high pressure regime and in-house measurements for the low pressure regime. From these, the input pressures to the next element were determined. Based on an initial guess for the temperature of the walls, the heat transfer to and from the walls were determined, using again, measured data<sup>6</sup> for such channels, taking due account, also, of the heat leak down the refrigerator and the thermal resistance of the material of the exchanger. From these, and the properties of the fluid, the temperature of the fluids leaving each element were next determined. The process was repeated for each element up the exchanger. The final temperature and pressure of the two streams were thus determined at the warm end of the exchanger. In general, these figures would not correspond exactly to the design requirements. The dimensions of the exchanger were then modified to bring these figures closer to the desired values. The process was iterated until the design requirements were met. The print out then gave the detailed temperature distribution down the exchanger.

A prototype of the refrigerator was fabricated using the dimensions determined in the

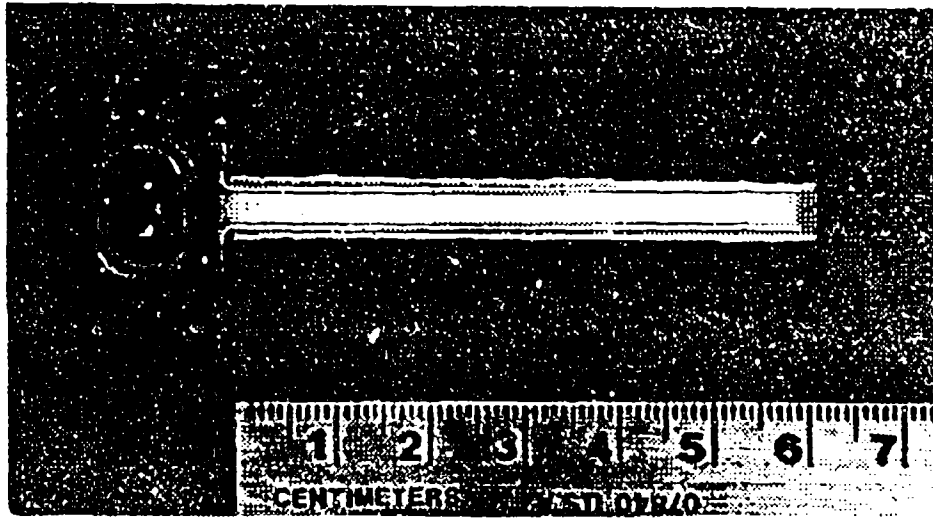


Figure 3. Low Flow Rate Microminiature Refrigerator of operation with Oxygen at 95K

above iterative procedure. This is shown in Fig. 3. In Table I, the calculated performance of this refrigerator is given together with the measured performance. The calculation, design and fabrication were done at MMR, where the refrigerator was pre-tested with nitrogen. The measurements listed, using the design cryogen, oxygen, were made at Boeing Corporation, Seattle. Remarkably good agreement between the computed and the experimental results were obtained. This is all the more satisfying as such low flow-rate refrigerators are particularly difficult to design because of the heat leak down the refrigerator is comparable to the refrigeration capacity of the device itself and can easily slew the temperature distribution in the exchanger and upset the flow rates. The design capacity of this refrigerator is a factor of two smaller than the smallest nitrogen refrigerator built previously<sup>7</sup>.

Table I

Single Stage Oxygen J-T Refrigerator		
	Calculated	Actual
Flow Rate	0.07 sl/m	0.072 sl/m
Temperature	95 K	95 K
Cooling Capacity	36 mW	30 mW

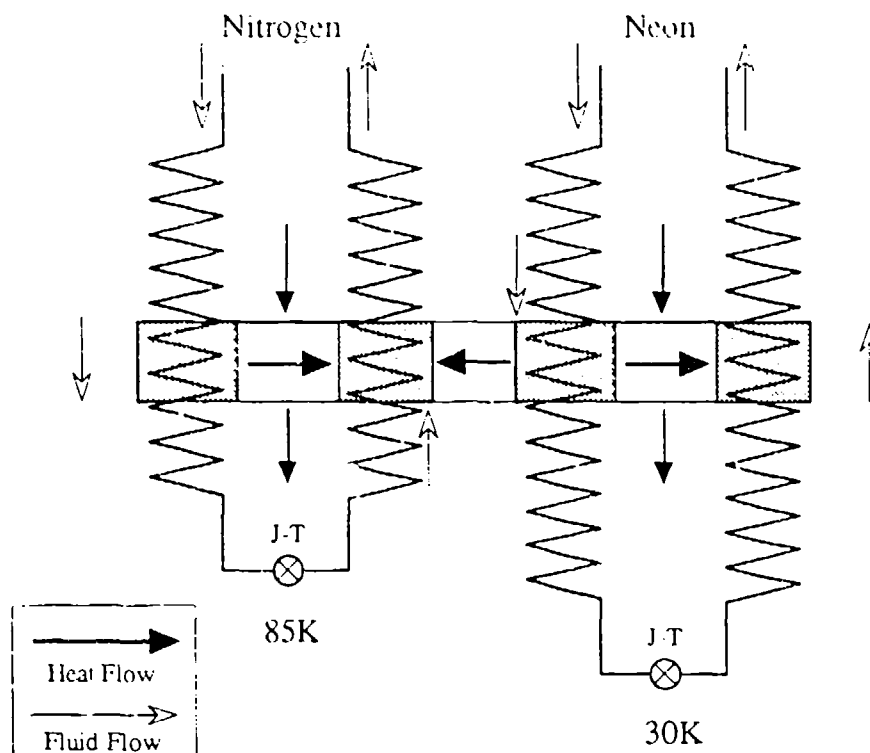


Figure 4. Two Stage J-T Refrigerator illustrating element across which heat is transferred between the two contra-flowing fluid streams.

#### TWO STAGE NITROGEN-NEON J-T COOLER

The design of this class of cooler is somewhat more complicated than that for the single stage, single fluid refrigerator. The nitrogen refrigerator must be designed to have a sufficiently large capacity to pre-cool the neon to 85K or below. At the same time one has to keep in mind the fact that the mass flow of the neon is a strong function of the temperature in the exchanger and will change by a factor of about ten between ambient and the operating temperature. Excess flow in the neon circuit can overwhelm the nitrogen capacity, resulting in unstable or oscillatory operation. In order to meet these demanding conditions we applied the same method developed for the single stage oxygen refrigerator to the design of the two stage devices.

A schematic of the heat exchangers is shown in Fig. 4. In this case one must take in to account the heat flow between the contra-flowing streams in each circuit and, in addition, the heat flow from the neon to the nitrogen stage. The same procedure was used as for the single stage program. The thermodynamic and transport properties of each of the two fluids were calculated in each element in each of the inflow and outflow channels. The various input



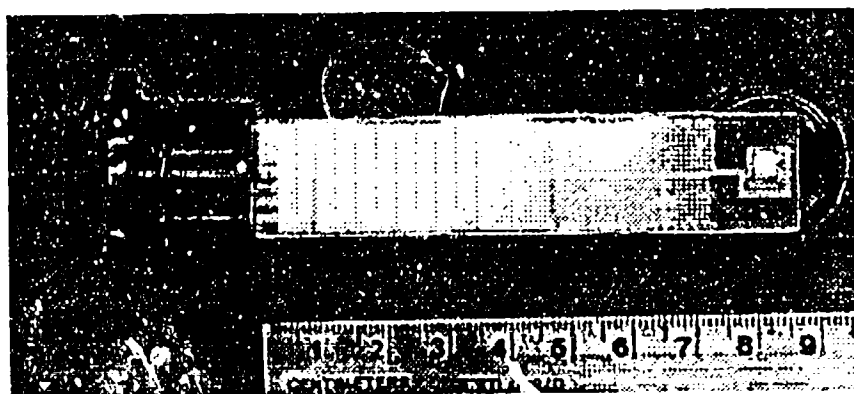


Figure 5. Two Stage Nitrogen-Neon Microminiature J-T Refrigerator  
for operation at 30K

and output temperatures and pressures were then calculated and the process repeated for all the elements of the exchangers. The overall process was iterated a number of times with modifications being made in the dimensions of the various parts of the exchangers. Eventually, the design goals were met, and the dimensions so determined were used for the fabrication of a prototype refrigerator. This prototype is shown in Fig. 5.

The calculated and measured values for the flow rates and temperatures of the nitrogen and neon stages are given in Table II. Again, close agreement is found for the two sets of figures. In this case the observed final stage temperatures were both a little higher than the calculated values. We have now determined the reason for this. It is due to a restriction at the exit port of the refrigerator. A similar problem had been encountered previously in

Table II

Two Stage Nitrogen-Neon J-T Refrigerator				
	Nitrogen		Neon	
	Theoretical	Actual	Theoretical	Actual
Flow rate	1.25 sl/m	1.29 sl/m	1.0 sl/m	0.89 sl/m
Temperature	85 K	89 K	30 K	34 K
Cooling Capacity	1.5 mW			

the design of nitrogen refrigerators, and correcting this problem reduced the operating temperature by 2-3K. Enlarging this hole in these refrigerators should bring the operating temperature to within a degree or two of the design figure. These results have just been obtained and measurement of the capacity of the refrigerator has yet to be made.

## DISCUSSION

The measured performance of two refrigerators, one a single stage low-flow device and the other a two stage, two gas refrigerator, were found to be in excellent agreement with design calculations where in each case the design was based on a multi-element sub-division of the heat exchangers. Within each element, the thermodynamic and transport properties of the gases were calculated and these results were used to calculate the temperature and pressure differences across the element. The procedure was programmed to run on a modest sized personal computer and allowed the design to be completed in a few hours spent in computation, iteration and manual tailoring of the dimensions of the exchanger.

## ACKNOWLEDGEMENTS

We wish to thank Mark Dubois for help with the test measurements and Franz Alkemade for technical assistance. We are indebted to the United States Office of Naval Research for partial support of this work under Contract N00014-91-C-0161.

## REFERENCES

1. J. M. Geist and P. K. Lashmet, in *Advances in Cryogenic Engineering* (Plenum, New York, 1960) **6**, 73.
2. W. A. Little, *Rev. Sci. Instrum.* **55**, 661-680 (1984)
3. William C. Reynolds, *Thermodynamic Properties in SI*, Department of Mechanical Engineering, Stanford University, Stanford, CA 94305
4. 1989 ASHRAE handbook, *FUNDAMENTALS*, SI Edition, American Society of Heating, Refrigerating and Air Conditioning Engineers, Inc., 1791 Tullie Circle, N.E. Atlanta, GA 30329
5. Wu Peiji and W. A. Little, *Cryogenics* **23**, 273 (1983)
6. Peiji Wu and W. A. Little, *Cryogenics* **24**, 415 (1984)
7. S. Garvey, S. Logan, R. Rowe and W. A. Little, *Appl. Phys. Lett.* **42**, 1048-1050 (1983).

DESIGN CONCEPTS FOR A 10K SOLID HYDROGEN  
SORPTION REFRIGERATOR

J. R. PHILLIPS  
DEPARTMENT OF ENGINEERING  
HARVEY MUDD COLLEGE  
CLAREMONT, CA 91711

B. D. FREEMAN AND R. C. BOWMAN, JR.  
AEROJET ELECTRONIC SYSTEMS DIVISION  
AZUSA, CA 91702

ABSTRACT

Three designs are described to produce continuous refrigeration at about 10K through the sublimation of solid hydrogen ( $H_2$ ). Refrigerant compression is achieved with two metal hydride sorption compressors arranged in series. A  $ZrNiH_x$  compressor absorbs low pressure hydrogen at 0.133kPa which corresponds to the solid-vapor equilibrium pressure for n-hydrogen near 10K. A second stage compression of hydrogen to about 10MPa is achieved with a  $VH_x$  compressor. The  $ZrNiH_x$  compressor has been characterized with respect to its energy balance which closed within 1.5% under conditions envisioned for refrigerator operation. The energy balance was achieved by systematic application of carefully assessed thermophysical properties. Idealized designs based upon single and dual stage expansion for continuous production of solid hydrogen have been analyzed. Parametric studies comparing these designs showed that important system variables include refrigerant pressure to the Joule-Thomson valve, precooler temperature, and the intermediate pressure between the  $VH_x$  and  $ZrNiH_x$  compressors. A model analysis is also given for periodic production of solid hydrogen by evaporation of liquid hydrogen starting above the triple point.

INTRODUCTION

Temperatures below 30K have been achieved from closed-cycle cryogenic refrigerators that expand hydrogen gas through a Joule-Thomson (JT) valve and use metal hydride

compressors [1-4]. These cryocoolers produced liquid hydrogen on the low-pressure (i.e., cold) side of the J-T valve. However, Jones [2, 5] has proposed that 10K cryocoolers could be based upon the sublimation of solid hydrogen at 0.0025 atm (2.0 torr) pressure using a suitable low-pressure hydride such as  $\text{PdH}_x$  or  $\text{Mg}_2\text{NiH}_x$ . Recent experiments at the Jet Propulsion Laboratory by Bard, et al [6] have validated this concept with  $\text{ZrNiH}_x$  as the low pressure hydrogen sorbent. The present paper considers in some detail the thermodynamics and performance that can be associated with a two stage 10K hydrogen cryocooler which employs  $\text{VH}_x$  and  $\text{ZrNiH}_x$  in the reversible sorption compressors.

### METAL HYDRIDE PROPERTIES FOR 10K CRYOCOOLERS

#### Thermophysical Properties

Efficient refrigeration by the J-T expansion of  $\text{H}_2$  gas requires [7] an initial pressure greater than 5 MPa (50 atm). A backside pressure of 1.0 atm corresponds to liquid hydrogen at 20K while production of solid hydrogen at 10K needs [2, 5] a nominal 1.0 torr (0.0013 atm) pressure to be maintained in the cold stage. If the practical operating temperature range of the hydride compressor is to lie between 275K and 650K, at least two different sorbents are needed since no metal or alloy can provide the nearly  $10^5$  compression ratio. Furthermore, potential hydride candidates should also have reversible hydrogen storage capacities greater than 0.5 H/M atomic ratios, good intrinsic reaction kinetics, and resist extensive degradation during the absorption/desorption cycling. While previous 20K cryocoolers used  $\text{LaNi}_5\text{H}_x$  or its substitutional alloys [1-4], Bowman, et al. [7, 8] have assessed the favorable potential of  $\text{VH}_x$  for this application.

Figure 1 compares the absorption and desorption plateau pressures for  $\text{VH}_x$  with three low pressure hydrides ( $\text{Mg}_2\text{NiH}_x$ ,  $\text{PdH}_x$ , and  $\text{ZrNiH}_x$ ). Although Jones [2, 5] suggested either  $\text{Mg}_2\text{Ni}$  or Pd for 10K hydrogen sorption refrigerators, both candidates have significant limitations.  $\text{PdH}_x$  has a small capacity of 5.7 mg H/g metal, requires cooling to 254K before reaching a 1.0 torr absorption pressure, and is extremely expensive. While  $\text{Mg}_2\text{NiH}_x$  has excellent capacity at 33 mg H/g alloy as well as favorable equilibrium plateau properties above 500K, its absorption kinetics are exceedingly slow [9, 10] at temperatures below 450K which

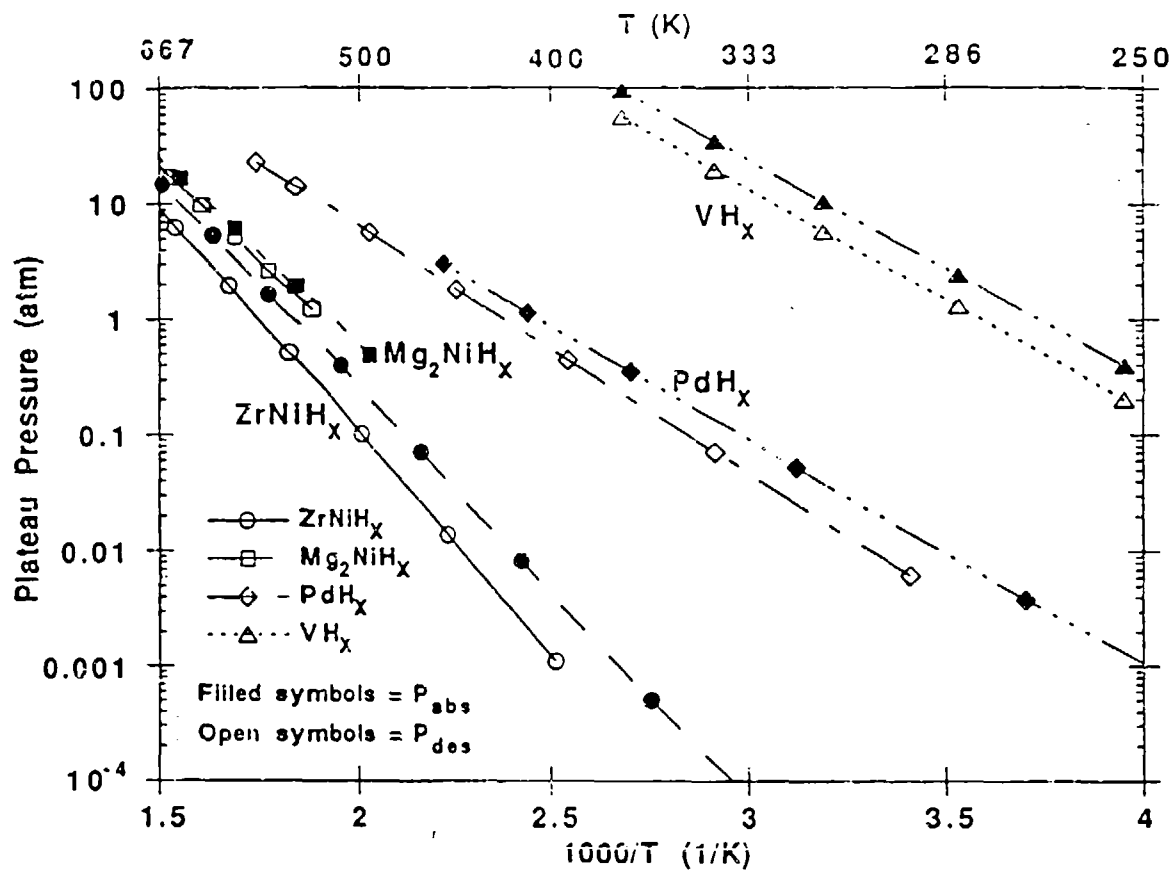
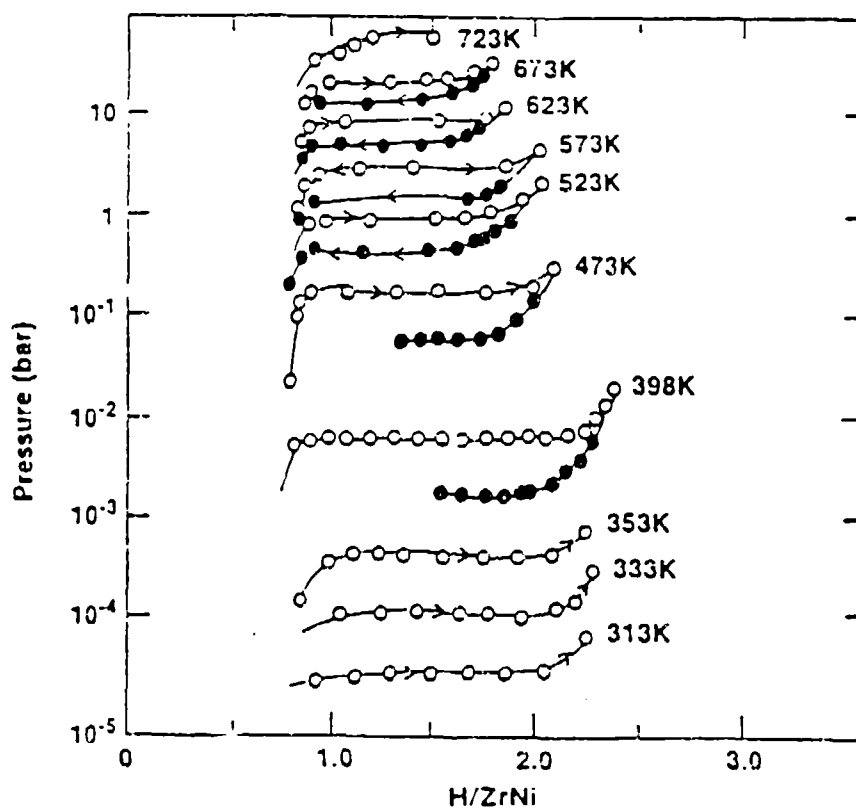


Figure 1. Candidate Hydride Van't Hoff Plots

Figure 2. Isotherms for the  $(\beta + \gamma)$  Plateau of the  $ZrNi-H_2$  System as Measured by Luo, et. al. (13).

prevents it from satisfying the hydrogen absorption conditions [2, 5] needed to generate solid hydrogen.

However, previous investigations of  $ZrNiH_x$  for reversible hydrogen getters [11, 12] strongly indicated very rapid hydrogen absorption occurred at room temperature. Furthermore, the isotherms for  $ZrNiH_x$  in Figure 2, as measured by Luo, et al [13], are most acceptable for the low pressure sorbent bed in a 10K cryocooler. The reversible capacity is 8.7 mg H/g alloy across the plateau region in Figure 2 which is a 53% increase over the marginal capacity of  $PdH_x$ . In addition, Cotts and co-workers [14] have used differential scanning calorimetry to measure the specific heats ( $C_p$ ) for  $ZrNi$ ,  $ZrNiH_{1.01}$ , and  $ZrNiH_{2.7}$  over the temperature range from 100K to 600K. These data are shown in Figure 3 and have been used in the present work to evaluate the energy balance of  $ZrNiH_x$  during the hydrogen absorption-desorption thermal cycles associated with a 10K cryocooler.

An idealized heat balance calculation has been performed for a  $ZrNiH_x$  sorption compressor using an approach similar to our recent analyses [7, 8] of  $VH_x$  compressors. The model compressor element contained 300 grams of  $ZrNi$  which will circulate 2.6 gm of hydrogen during the absorption-desorption cycle. From the bulk alloy density of  $7.42 \text{ g/cm}^3$  and an assumed 40% void fraction in the powder, the bed has  $27 \text{ cm}^3$  of free volume. The absorption conditions are 0.133 kPa (1 torr) at 370K and desorption was set at 101.3 kPa (1.0 atm) at 572K. For this idealized case, heating of the vessel containing  $ZrNiH_x$  powder was not considered. The results of this calculation are summarized in Table I. For the complete cycle,  $\Delta U$  should be zero while the computed difference is 1.9 kJ and corresponds to an energy balance closure within 1.5%. Previous calculations for a similarly ideal  $VH_x$  bed closed within 0.3%. The net work (W) input for the  $ZrNiH_x$  cycle is 2.1 kJ. The calculated heat required for the combined compression and desorption steps of the  $ZrNiH_x$  bed is 51.1 kJ/gH compared to 25.4 kJ/gH for a  $VH_x$  bed [6, 7]. This difference is due to the much larger heat of absorption for  $ZrNiH_x$  [13] compared to  $VH_x$  [15] and also heating of the  $ZrNiH_x$  bed  $200^\circ \text{C}$  compared to only  $115^\circ \text{C}$  for the  $VH_x$  bed.

#### DESIGN DESCRIPTIONS

We have assumed that normal hydrogen properties are appropriate for system design. This is

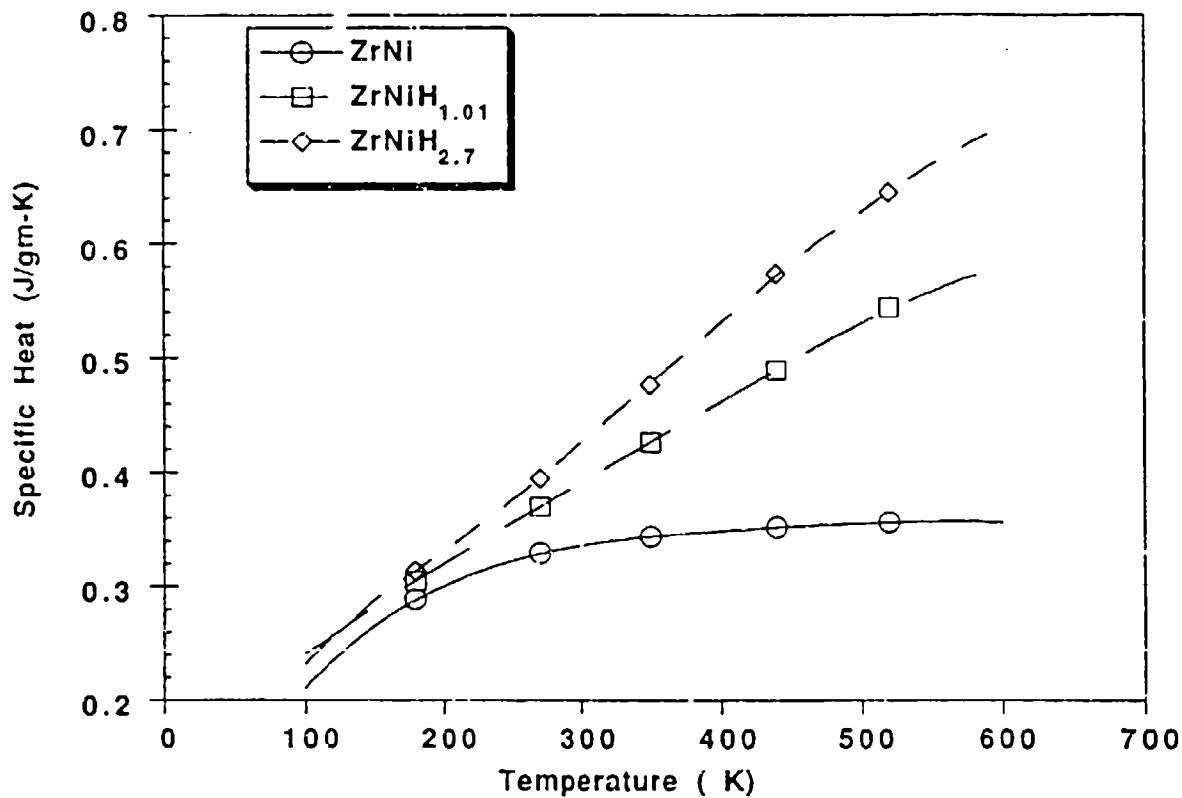


Figure 3. Specific Heat of  $\text{ZrNiH}_x$  From E. Cotts, et. al. (14).

TABLE 1. Ideal Energy Balance Calculation Results for  $\text{ZrNiH}_x$  Compressor

Step	$\Delta U, \text{kJ}$	$Q, \text{kJ}$	$W, \text{kJ}$
Constant Volume Compression	37.15	37.15	0.0
Desorption	89.57	95.71	-6.133
	126.7	132.9	-6.133
Constant Volume Compression	-31.12	-31.12	0.0
Absorption	-93.63	-97.63	4.00
	-124.8	-128.8	+4.00

based on preliminary estimates that little if any ortho to para hydrogen conversion will take place during the refrigeration cycle. Thermodynamic data for n-hydrogen have been derived from Souers (16).

Three different designs were evaluated. Each can produce solid n-hydrogen at 10K on a continuous basis, although Design 3 is a periodic process. The designs have been modelled on an idealized basis: Ideal sorption compressors, ideal heat exchangers, no heat losses, no pressure drop, and fast sorption kinetics. To allow easy comparison all three designs were studied under similar conditions which are shown in Table 2.

#### Design 1 - Single Expansion

Figure 4a shows an ideal schematic diagram for the simplest design envisioned capable of producing refrigeration at 10K on a continuous basis. Also shown is the corresponding pressure-enthalpy diagram for the refrigerant flow (Figure 4b). The precooler is used to provide continuous cooling of the hydrogen to well below its inversion temperature of 202K (2). The load to be refrigerated is applied to the solid hydrogen container after the J-T expansion.

For this design high pressure hydrogen leaves the  $VH'_x$  compressor at  $10 \times 10^3$  kPa and 387.7K and is cooled by a series of coolers and recuperative heat exchangers until reaching point 3. The refrigerant is then expanded to 0.133 kPa, producing a solid-vapor mixture at about 10K. Low pressure hydrogen is heated by exchange to 80K, and again to 370K at which point it enters the cooled  $ZrNiH_x$  compressor. In this compressor, hydrogen pressure is increased to 101.3 kPa (1 atmosphere) by heating to 572K. The desorbed hydrogen must next be cooled to 273.2K and then enters the cooled  $VH_x$  compressor.

As shown in Figure 4b the high pressure hydrogen is cooled to point 3 such that subsequent expansion in the Joule-Thomson valve will initially pass through the two-phase, liquid-vapor dome, then through the triple point (13.96K) and will finally produce a two-phase, solid-vapor mixture at the cold temperature desired. Refrigeration is supplied at constant temperature by sublimation of the solid hydrogen so that the mixture enthalpy increases from point 4 to point 5. Low pressure hydrogen gas then exchanges heat with the incoming refrigerant so that, in



TABLE 2. System Parameters used for Model Analyses

Precooler Temperature	80K
$P_h$ ( $VH_x$ desorption)	$10 \times 10^3$ kPa
$P_l$ ( $ZrNiH_x$ absorption)	0.1333 kPa
$P_i$ (Intermediate)	101.3 kPa
$T_{des} - VH_x$	387.7K
$T_{abs} - VH_x$	273.2K
$T_{des} - ZrNiH_x$	572K
$T_{abs} - ZrNiH_x$	370K

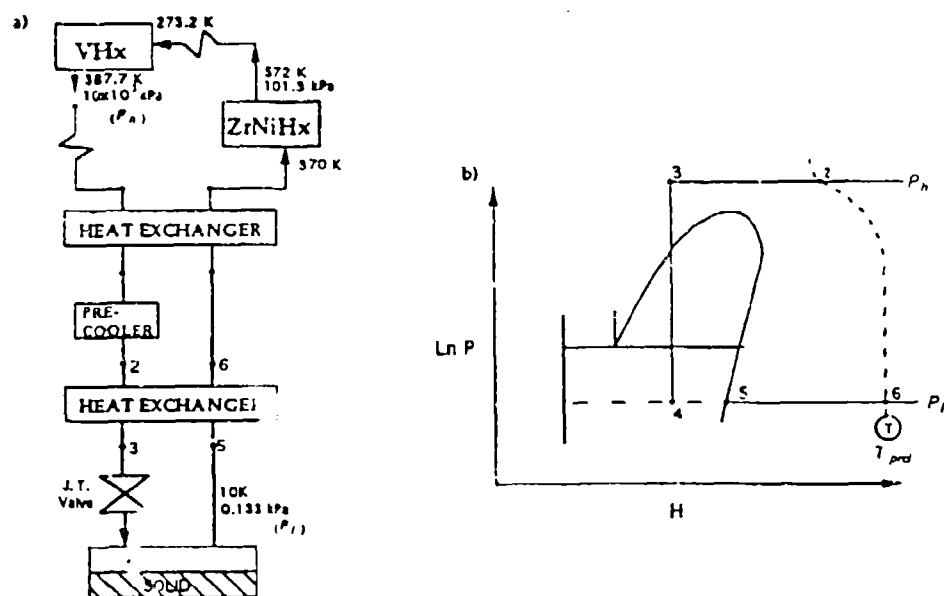


Figure 4. Design 1, One Expansion Method for Solid-Hydrogen Production

the ideal case, 80K is reached at point 6. In this design, the refrigeration provided (i.e., the difference in enthalpy between points 4 and 5) is also given by the difference in enthalpy between points 6 and 2. This is the difference in enthalpy between hydrogen gas at the same temperature (80K) but at significantly different pressures.

To produce 1 w of refrigeration a hydrogen flow of  $5.95 \times 10^{-3}$  g/s is required. The precooler load at 80K is 1.39 w, and a heat input of 304.0 w is required for the  $\text{ZrNiH}_x$  compressor and 151.4 w is required for the  $\text{VH}_x$  compressor. These combine to give a specific power of 455.4 w/w for Design 1.

### Design 2 - Double Expansion

The schematic diagram for Design 2 along with its corresponding pressure-enthalpy diagram for refrigerant flow is shown in Figure 5. This design is different from Design 1 in that a two stage expansion is envisioned. High pressure hydrogen at 80K is cooled to point 3 and then expanded through the first J-T valve to the liquid-vapor, two-phase region at point 10, corresponding to 101.3 kPa and 20.3K. Vapor from point 12 is then heated by exchange to inlet conditions and returned to the  $\text{VH}_x$  compressor (273.2K and 101.3 kPa). Liquid from point 11 is at the same time expanded through a second J-T valve to 0.133 kPa (point 13, a two-phase, solid-vapor mixture). Refrigeration is produced by sublimating the solid hydrogen and increasing the mixture enthalpy to point 5. The low pressure hydrogen is sequentially heated by exchange to 80K, and 370K before it enters the cooled  $\text{ZrNiH}_x$  compressor. After a first compression to 101.3 kPa this hydrogen stream joins the return from the vapor-liquid separator and enters the  $\text{VH}_x$  compressor. Note that the intermediate pressure between the two sorption compressors (101.3 kPa in this case) fixes the temperature of the vapor-liquid separator.

To produce 1 w of refrigeration a total hydrogen flow of  $5.99 \times 10^{-3}$  g/s is required. This is slightly higher than the flow required for Design 1 because of non-ideal gas behavior in the two returning streams. Vapor flow from the vapor-liquid separator is  $3.22 \times 10^{-3}$  g/s, and flow through the  $\text{ZrNiH}_x$  compressor is  $2.77 \times 10^{-3}$  g/s. The precooler load at 80K is 1.38 w. Heat input for the  $\text{ZrNiH}_x$  compressor is 141.6 w and that for the  $\text{VH}_x$  compressor is 152.4 w. The

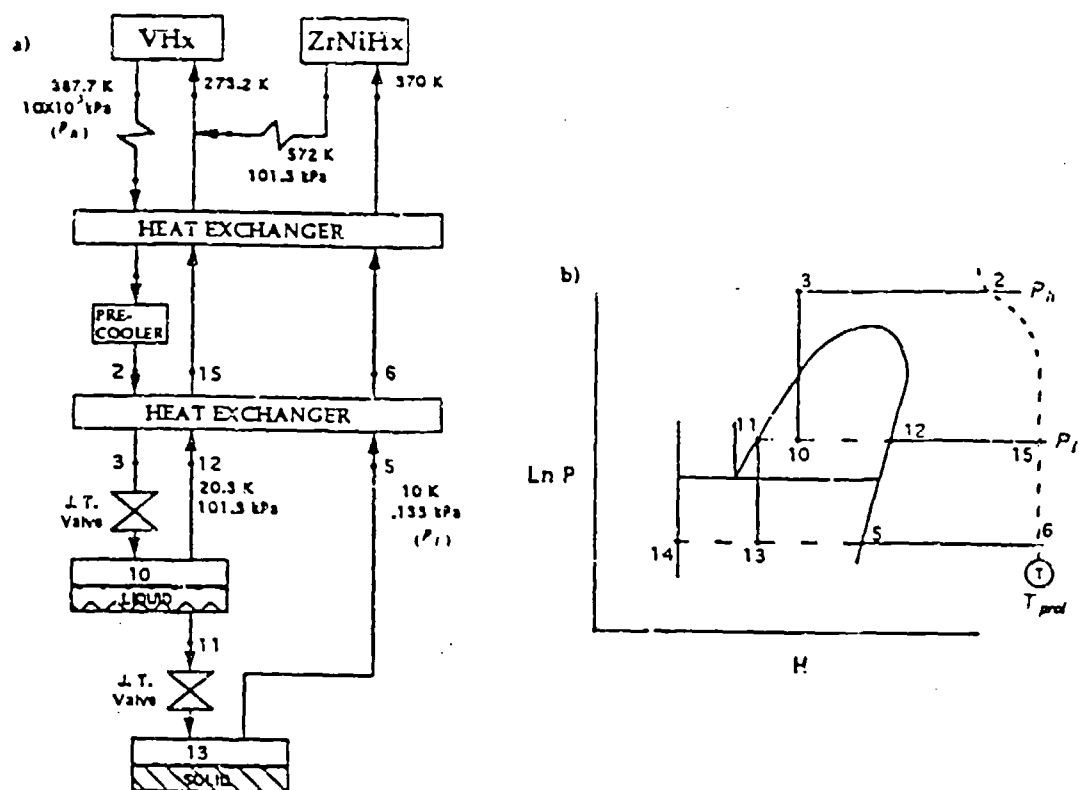


Figure 5. Design 2, Two Expansion Method for Solid-Hydrogen Production

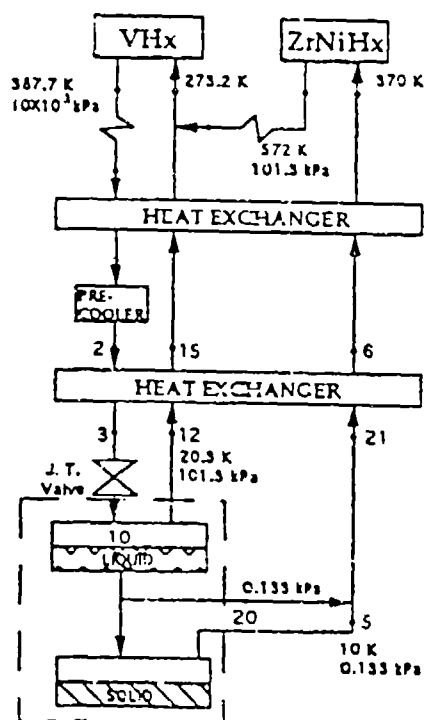


Figure 6. Design 3, Liquid Venting Method for Solid-Hydrogen Production

specific power for this design is thus 294.0 w/w. A significant performance improvement is realized because less hydrogen is required to be compressed in the  $\text{ZrNiH}_x$  compressor. The system is, however, more complicated, with two J-T expansions and special heat exchangers envisioned.

### Design 3 - Single Expansion with Venting

Design 3, which is shown in Figure 6, involves the transient cooling of liquid hydrogen to the solid state by partial evaporation of the initial  $\text{H}_2$  liquid. As such, the process is very similar to the concept for producing refrigeration at 10K initially suggested by Jones (5). Because of the periodic nature of the liquid cooling, one or more additional cold end sections would be required to make the production of refrigeration continuous. Representation of the process on a thermodynamic diagram, such as a pressure-enthalpy diagram, is difficult because of the non-equilibrium nature of the process. That is, the separated liquid at 20.3K loses mass in the process of cooling to and freezing at 10K.

The design is similar to Design 2 up to the point of the liquid-vapor separator. At this point, in Design 2, vapor and liquid are separated in a continuous manner with the vapor then returned to the  $\text{VH}_x$  compressor while the liquid is expanded through a J-T valve to form a solid-vapor mixture at about 10K. In Design 3, liquid at 101.3 kPa and 20.3K is isolated in a closed container while vapor from point 12 is returned to the  $\text{VH}_x$  compressor. In the Design 3 configuration the liquid hydrogen is assumed to be held in a rigid, insulated container. A valve at the top of the container is opened and the resulting vapor is vented to a constant pressure of 0.133 kPa (corresponding to the inlet pressure of the cooled  $\text{ZrNiH}_x$  compressor). The process continues until the pressure in the container falls to 0.133 kPa. At this point, there will exist an equilibrium mixture of solid hydrogen and saturated hydrogen vapor.

Assuming no heat transfer to the tank, the problem is to determine the mass of hydrogen vapor vented and thus the mass of solid hydrogen and saturated vapor that remains. The calculation procedure for this design is based on a method suggested in Smith and Van Ness (17), which is essentially the problem of venting an aerosol container.

The applicable energy balance for this situation is:

$$m_1 u_1 = m_2 u_2 + h m_v \quad (1)$$

where:

$m_1$  = mass initially in control volume  
 $m_2$  = mass finally in control volume  
 $m_v$  = mass vented  
 $u_1$  = specific internal energy initially in cv  
 $u_2$  = specific internal energy finally in cv  
 $h$  = average specific enthalpy of vented vapor

In addition:

$$m_2 = m_1 - m_v \quad (2)$$

The procedure begins by specifying an initial mass of saturated liquid (or solid) and associated vapor at a given temperature and pressure. This fixes  $m_1$ ,  $u_1$ , and  $h_1$ . The next step is to pick a slightly lower temperature that will be achieved by venting vapor. This fixes  $u_2$ , and  $h_2$ , (thus  $h$ ). Recognizing that the relative amounts of liquid (solid) and vapor remaining in the control volume must also satisfy the specific volume requirements of the vapor liquid (solid) mixture,  $m_v$  can be determined from the following derived equation

$$m_v = m_1 - [m_1 (v_L - v_v)(u_1 - h) - (u_L - u_v) \text{Vol}] / [(u_v - h)(v_L - v_v) - v_v(u_L - u_v)] \quad (3)$$

where:

$u_L$  = the final internal energy of the liquid (or solid)  
 $u_v$  = the final internal energy of the vapor  
 $v_L$  = the final specific volume of the liquid (or solid)  
 $v_v$  = the final specific volume of the vapor  
 $\text{Vol}$  = the volume of the control volume

Note that a small step is desirable because of the use of an average value for the enthalpy of the leaving hydrogen vapor.

A result for the calculation procedure described above, for base case conditions, is shown in

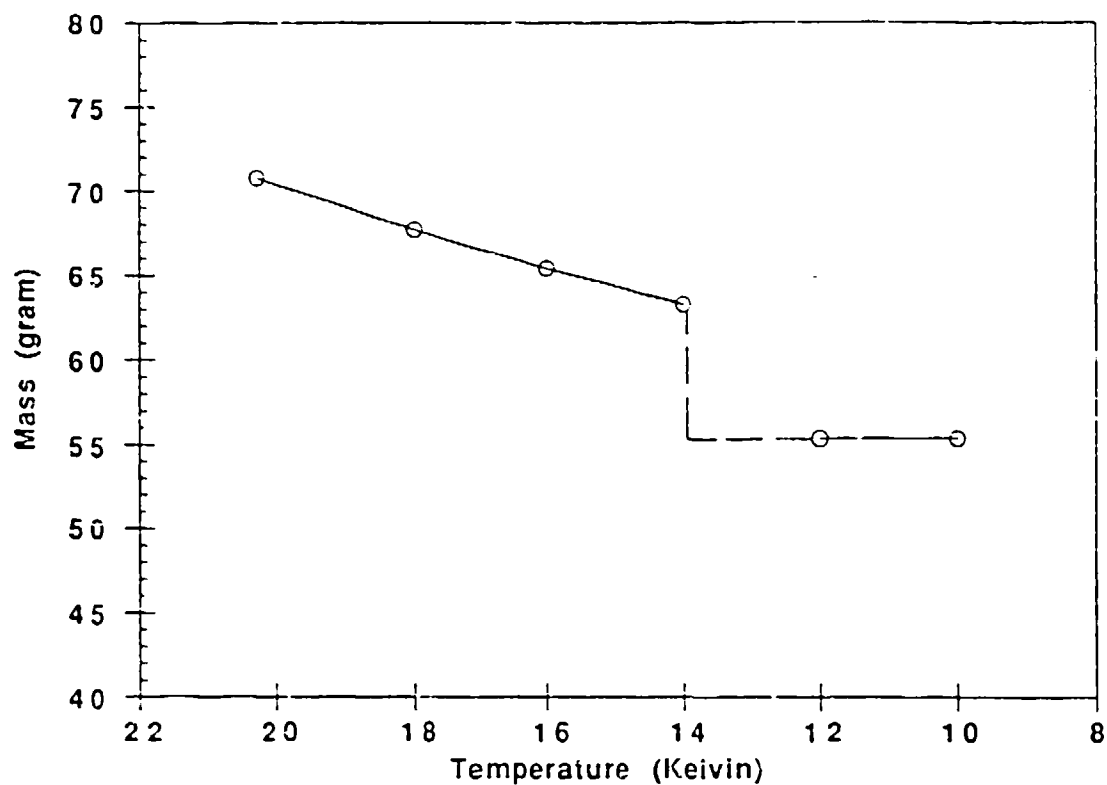


Figure 7. Mass Remaining, For Base Case Conditions for Design 3

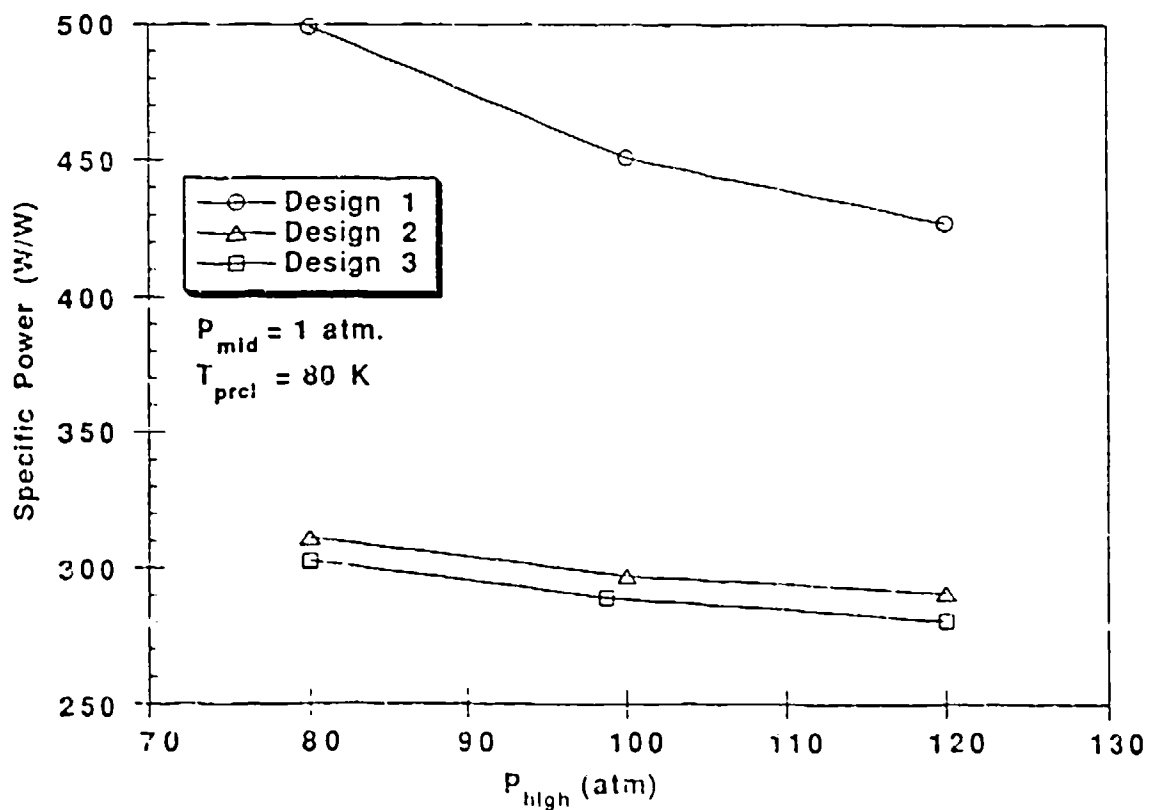


Figure 8. Dependence of Specific Power on System High Pressure for 10K Design Concepts

Figure 7. Here it was assumed that a rigid, insulated container of  $1.0 \times 10^{-3} \text{ m}^3$  initially contained saturated liquid n-hydrogen at 20.3K. The approximate mass of n-hydrogen is 70.3 grams. The calculation proceeded by taking 2°K temperature intervals. The mixture is still liquid-vapor at 14K, but below the triple point (13.96K) the mixture becomes solid-vapor. No calculation was actually done around 13K, so the dashed lines representing the process between 14 and 12K are extrapolations.

In the process of going from liquid at 20.3K to solid at 10K, 21.8% of the initial mass of the liquid is lost through venting. Total flow is about the same for Design 3 as for Design 2 for a given refrigeration requirement. However, more solid hydrogen is formed in Design 3 than in Design 2 for the same original liquid charge, and less vapor is produced after the JT expansion.

For base case conditions, a hydrogen flow of  $5.99 \times 10^{-3} \text{ g/s}$  is required to produce 1 w of refrigeration. The precooler load at 80K is 1.38 w, and a heat input of 137.2 w is required for the  $\text{ZrNiH}_x$  compressor and 152.4 w is required for the  $\text{VH}_x$  compressor. This results in a specific power of 289.6 w/w for Design 3. This is a little less than for Design 2, because of a slightly smaller flow to the  $\text{ZrNiH}_x$  compressor.

### PARAMETRIC STUDIES

Parametric studies of all three designs were made in order to determine the effect on specific power of the most important system variables: refrigerant pressure to the J-T valve; precooler temperature; and intermediate compressor pressure (i.e., the pressure between the  $\text{ZrNiH}_x$  compressor and the  $\text{VH}_x$  compressor). Results are presented in Figures 8, 9, 10.

Specific power as a function of system high pressure (pressure to the J-T valve) is shown for all three designs in Figure 8. The base case described in Table 2 corresponds to a high pressure of 98.7 atm. Other parameters represented in Figure 8 are as stated for the base case.

Over the pressure range investigated, specific power for Design 1 remains significantly

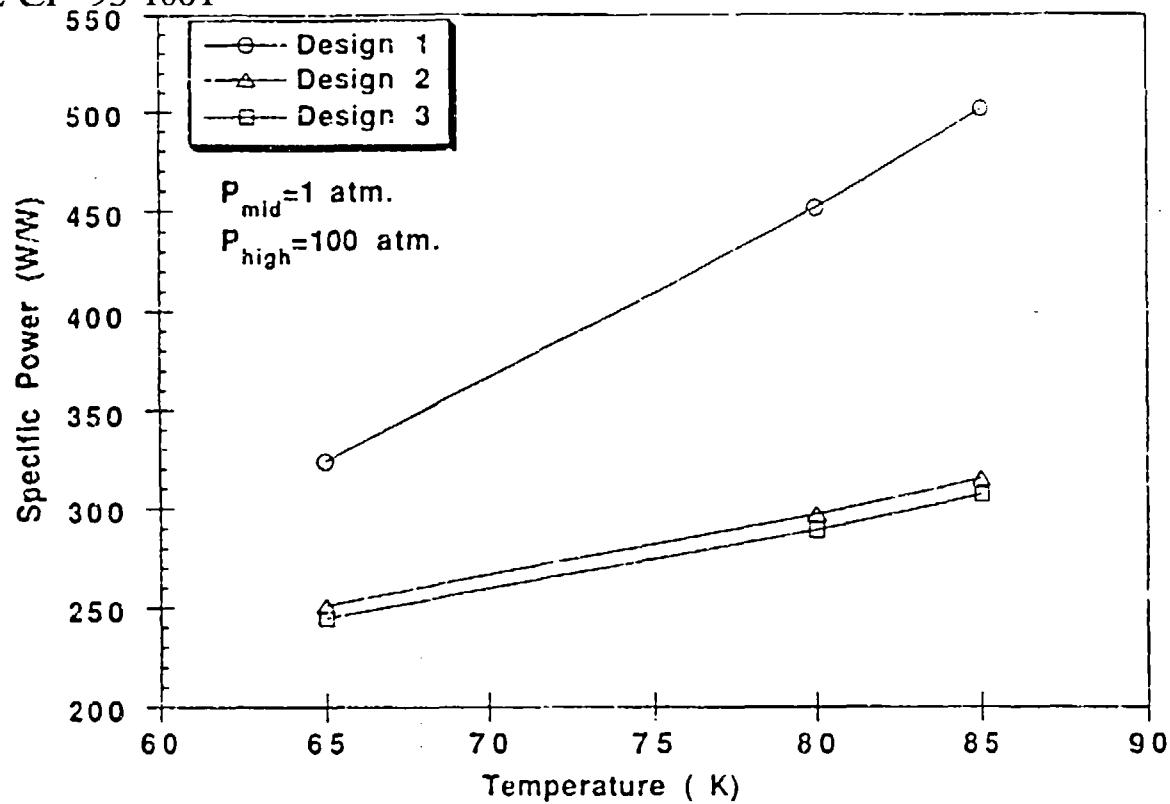


Figure 9. Dependence of Specific Power on Precooler Temperature

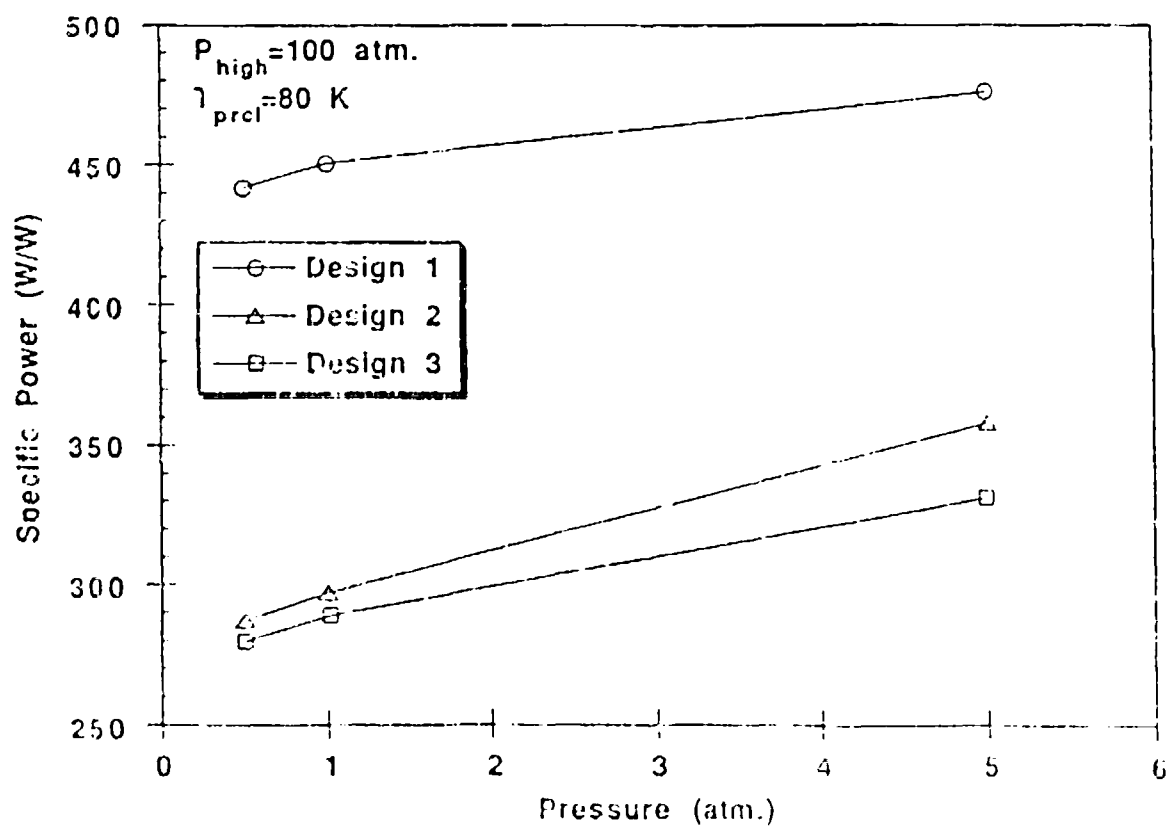


Figure 10. Dependence of Specific Power on Intermediate Pressure



higher than those of Designs 2 and 3. Within the high pressure range of 80 to 120 atmospheres specific power decreases somewhat with increasing system pressure for all three designs. However, Designs 2 and 3 have a small change compared to Design 1. Actually a minimum in these curves is to be expected, but is probably located at a pressure somewhat greater than 120 atm (7, 8).

In Figure 9, specific power is shown as a function of precooler temperature. As can be seen, in the pre-cooler temperature range of 65 to 85K, specific power increases rapidly with increasing pre-cooler temperature. Similar to the effect of system high pressure, Design 1 showed a larger change than for either Design 2 or 3.

Figure 10 shows the effect of varying mid-pressure on specific power. Although system high pressure and precooler temperature had relatively little effect on Designs 2 and 3, the mid-pressure, the pressure between the beds, is a more important variable for both of these designs. This mid-pressure sets the pressure and temperature of the envisioned vapor-liquid separator in Design 2 and the pressure and temperature of the starting liquid pool in Design 3. As can be seen in Figure 10, specific power for both Designs 2 and 3 increases relatively sharply with increasing mid-pressure compared to the corresponding trend for Design 1.

The effect of considering thermal mass of the sorption compressor containers for Designs 1 and 2 is shown in Figure 11. Over the pressure range considered, the compressor thermal mass was held constant. As can be seen, a minimum in the specific power vs. system high pressure curve is observed for both Design 1 and Design 2. This minimum is similar to our past results (7) in a single stage 20K refrigerator.

A final parameter was investigated for Design 3: Specific power as a function of vapor fraction present prior to venting. Figure 12 shows that specific power increases from 289 w/w at base case conditions (including 0 mass percent vapor present) to about 305 w/w at 12 mass percent vapor. As can be seen, the increase is nearly linear. It is expected that comparable increases would be seen for the parameter variations presented in Figures 8-10.

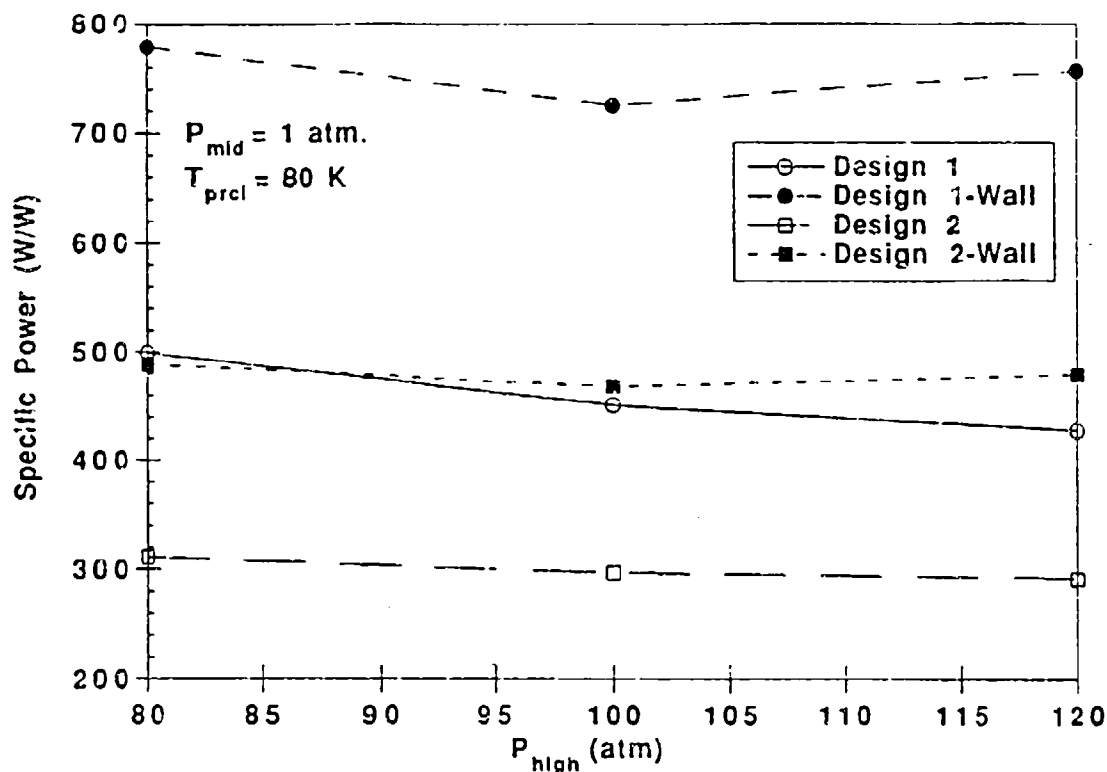


Figure 11. Compressor Thermal Mass Effect on Specific Power for 10K Designs 1 & 2

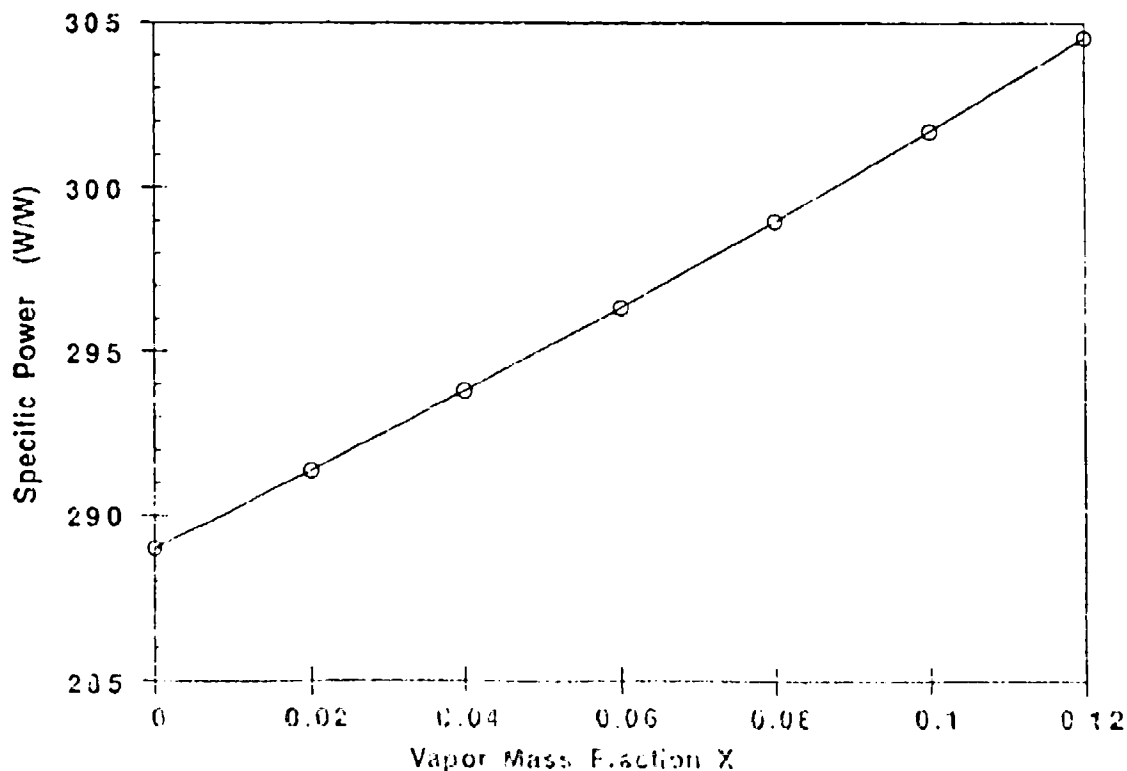


Figure 12. Dependence of Specific Power on Initial Vapor Fraction for Design 3

## CONCLUSIONS

All three designs presented are capable of producing solid-hydrogen refrigeration near 10K. Each of the designs employs a distinct process with at least one J-T expansion and each has its special hardware requirements. Specific power results are promising.

The most likely metal-hydride candidates for this application have been identified and characterized. They are  $ZrNiH_x$  for the low-pressure compressor and  $VH_x$  for the high pressure compressor. An energy balance, based on new thermo-physical properties, for the  $ZrNiH_x$  compressor closes within 1.5%.

The sorption variables investigated were: pressure to the J-T valve, pressure between the two compressors, and precooler temperature. Over the range of variables investigated, Design 2 (two J-T expansions) and Design 3 (J-T expansion plus liquid venting) showed significantly lower specific powers than Design 1 (one J-T expansion) because not all of the hydrogen flow is required to enter the  $ZrNiH_x$  compressor. Designs 2 and 3 are fundamentally different processes, but the resulting specific power for each is nearly the same.

## ACKNOWLEDGEMENTS

We wish to thank Ellen Liu for her assistance. We also thank Dan Friend for making available information on hydrogen properties and Eric Cotts for providing us his measured heat capacities of  $ZrNiH_x$  prior to publication.

# REFERENCES

1. H. H. van Mal and A. Mijneer, Proc. ICEC 4 (Guildford, UK, IPC Press, 1972), pp. 122-125.
2. J. A. Jones and P. M. Golben, Cryogenics 25, 212 (1985).
3. K. Karperos, Proc. 4th Intern. Cryocooler Conf., Easton, MD, (1986) pp. 1-16.
4. T. Kumano, B. Tada, Y. Tsuchida, Y. Kuraoka, T. Ishige, and H. Baba, Z. Physik. Chem. N. F. 164, 1509 (1989).
5. J. A. Jones, U. S. Patent No. 4,641,499 (10 Feb. 1987).
6. S. Bard, et. al., Proc. this conference.
7. R. C. Bowman, Jr., B. D. Freeman, and J. R. Phillips, Cryogenics 32, 127 (1992).
8. R. C. Bowman Jr., B. D. Freeman, and J. R. Phillips, in Advances In Cryogenic Engineering, Vol. 37B, edited by R. W. Fast (Plenum, New York, 1992) p. 973.
9. Z. Gaura, G. Kimmel, Y. Gefen, and M. M. Mintz, J. Appl. Phys. 57, 4548 (1985).
10. M. L. Post and J. J. Murray, J. Less-Common Met. 134, 15 (1987).
11. K. Nakamura and T. Hoshi, J. Vac. Sci. Technol. A 3, 34 (1985).
12. G. D. Sandrock, U. S. Patent No. 4,668,424 (26 May 1987).
13. W. Luo, A Craft, T. Kuji, H. S. Chung, and T. B. Flanagan, J. Less-Common Met. 162, 251 (1990).
14. E. J. Cotts, et al., unpublished data (1992).
15. W. Luo, J. D. Clewley, and T. B. Flanagan, J. Chem. Phys. 93, 6710 (1990).
16. P. C. Souers, Hydrogen Properties for Fusion Energy, (U. of California Press, Berkeley, CA, 1986).
17. J. M. Smith, and H. C. Van Ness, Introduction to Chemical Engineering Thermodynamics, 4 ed., McGraw-Hill, (1987) New York, p. 214.

EXPERIMENTAL VERIFICATION OF JOULE-THOMSON  
CRYOCOOLER COOLDOWN PERIOD SIMILARITY RATIOS

B-Z. MAYTAL  
Rafael, P.O. Box 2250 (38)  
Haifa 31021, Israel.

ABSTRACT

Cooldown periods similarity ratios were established for a Joule-Thomson (J-T) cryocooler over the space of coolants, pressures and ambient temperatures. It might serve for scaling the cooldown periods by one experiment at given conditions. Those similarity ratios were derived assuming: (a) proportionality with cooldown temperature range  $(\Delta T)_H$ , and with high pressure stream Reynolds number and (c) cooling down power significantly exceeds heat load. A 5.2 millimeter diameter J-T cryocooler operating in a highly evacuated dewar was tested. Pressure range up to 70 MPa was well covered at 295K and 340K ambient by nitrogen and argon. Quite satisfactory match of measured and predicted ratios relating cooldown periods was observed.

NOMENCLATURE

K	Thermal conductivity ( $\text{J m}^{-1} \text{K}^{-1}$ )
$\dot{m}$	Mass flowrate ( $\text{g s}^{-1}$ )
P	Pressure (Pa)
T	Temperature (K)
$(\Delta T)_H$	Isenthalpic integral J-T effect (K)
$T_{CL}$	Nozzle inlet temperature at liquefaction start (K)
t	Time (s)
$\mu$	Dynamic viscosity (Pa.s)
$\tau$	Cooldown period (s)
$\tau(\text{REF})$	Reference cooldown period (s)
$\Pi$	Similarity ratio, $\tau/\tau(\text{REF})$

INTRODUCTION

Constant nozzle area J-T cryocoolers are mainly used for fast cooldown applications<sup>(1)</sup>. However, even a flow regulated cryocooler does operate with a fixed (open) nozzle till liquefaction is reached. Little<sup>(2)</sup> has derived similarity relations for the J-T cryocoolers in the domain of their dimensions and flowrates. Longsworth<sup>(3)</sup> provided the experimental verifications. Maytal<sup>(4)</sup> developed cooldown period similarity ratios for a constant nozzle J-T cryocooler in the domain of operation pressures, ambient temperatures and coolants. Thermodynamic aspects of coolants oriented to J-T cryocooler's operation was treated on references (5) and (6). Those relations are supposed to scale up a cooldown period experimentally reached at a given vector of (P, T, coolant) for prediction of the cooldown period at other operating conditions such as higher ambient temperature and another coolant or different pressure. This work intends to present some systematic experimental verifications to the similarity ratios<sup>(4)</sup> previously derived.

COOLDOWN RATIOS SIMILARITY MODEL

Integration of a partial differential equation longitude and time dependent would be needed for complete prediction of the cooldown transient. It might be avoided if adapting the following assumptions concerning the cooldown periods of a given cryocooler:

- (a) proportionality with cooldown range,  $T - T_{C0}$ , namely, nozzle's inlet cooling range till first liquefaction occurs at its outlet.
- (b) inverse proportionality with the initial integral isenthalpic J-T effect,  $(\Delta T)_H$ .
- (c) inverse proportionality with the initial high pressure stream Reynolds number.

- (d) cooling down power significantly exceeds heat leaks.
- (e) heat exchanger's efficiency is weakly affected by varying operation conditions.

All these result in<sup>(4)</sup>

$$\tau \propto \frac{T - T_{CD}}{\left[ \left( \frac{\dot{m}}{\mu} \right)^{0.8} \cdot K \cdot (\Delta T)_{II} \right]_{t=0}} \quad (1)$$

Cooldown period for each coolant is defined as elapsed time from pressurization till  $T_{CD}$  is reached at nozzle's inlet.

#### THE EXPERIMENT

A central issue in the experiment design is the good fulfillment of assumptions (d) and (e) of the cooldown periods similarity ratios model. J-T cryocooler of 5.2 millimeters diameter was used. Its 40 millimeters finned tube heat exchanger is adequately long for keeping efficiency quite constant at various operation conditions, thus satisfying assumption (e). Assembled in a well evacuated glass dewar of 0.2W heat leak, the total heat load did not exceed a figure of 0.3W at steady stage operation. However, during cooldown process it is estimated to be half of the figure. Flowrate was high enough to provide cooling power of several watts. This combination of evacuated dewar with high cooling capacity was directed to satisfy assumption (d). Temperature time dependence was measured through a thin metal cover involving a time lag lower than 0.1 s.

Pressurizing up to 70 OMpa was covered by about 13 measurements for each coolant, argon and nitrogen at room temperatures of 295K. This set of operations was repeated at ambient of 340K.

EXPERIMENTAL RESULTS

Measured cooldown periods are presented through their similarity ratios  $\Pi$  to be compared with the model.

$$\Pi = \frac{\tau}{\tau(\text{REF})} \quad (2)$$

For each set of results  $\tau(\text{REF})$  though chosen arbitrarily, does not affect generality. Figure 1 compares pressure dependence of measured similarity ratios for operation by argon and nitrogen, both with the common reference

$$\tau(\text{REF}) = \tau(30 \text{ MPa}, 300\text{K}, \text{nitrogen}) \quad (3)$$

put another way

$$\Pi(30 \text{ MPa}, 300\text{K}, \text{nitrogen}) = 1 \quad (4)$$

Quite acceptable agreement with the proposed similarity model is observed. Above the 40 MPa pressure, argon cools down faster than nitrogen at least by a factor of 4.

Ambient temperature dependence of measured cooldown periods similarity ratios for nitrogen is shown in Figure 2. The same above  $\tau(\text{REF})$  (equation 3) is adapted. Some isotherms are plotted to demonstrate the resolution extent and agreement with model. The relevant isotherms of 295K and 340K are bolted.



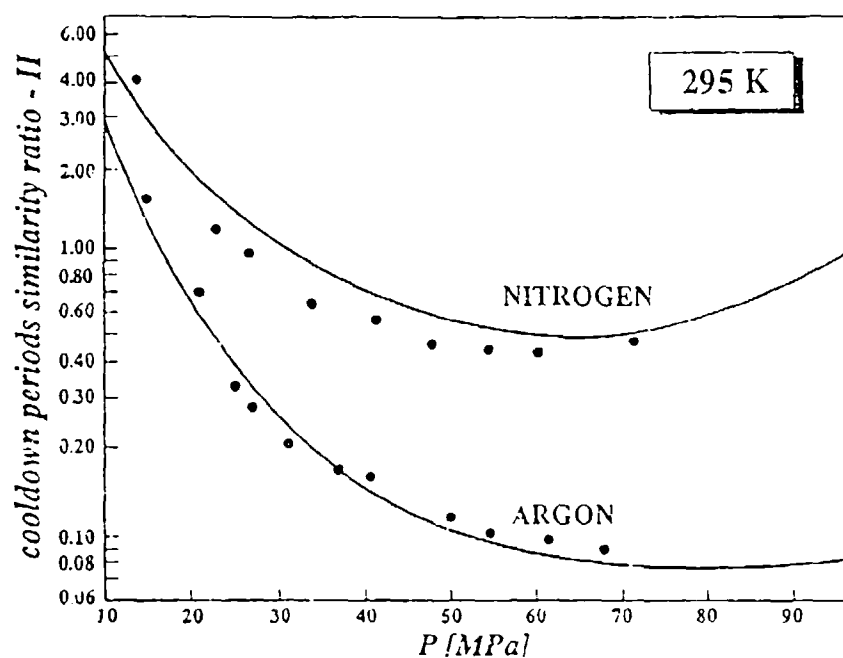


Fig. 1: Cooldown periods similarity ratios for nitrogen and argon. Dots and curves represent experiments and model correspondingly.

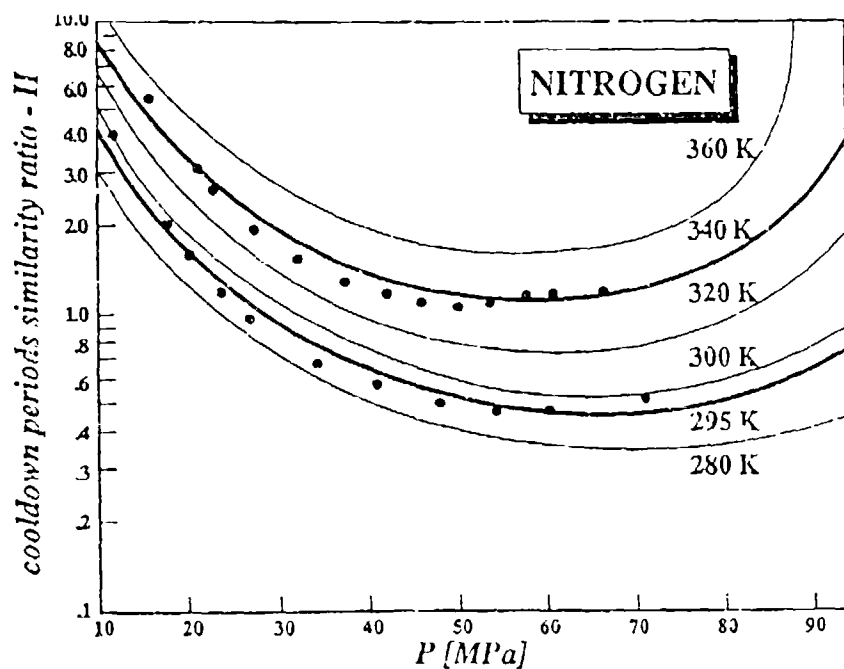


Fig. 2: Cooldown periods similarity ratios for nitrogen at different ambient temperatures. Dots represent measurements at 295K and 340K. Curves represent theoretical model.

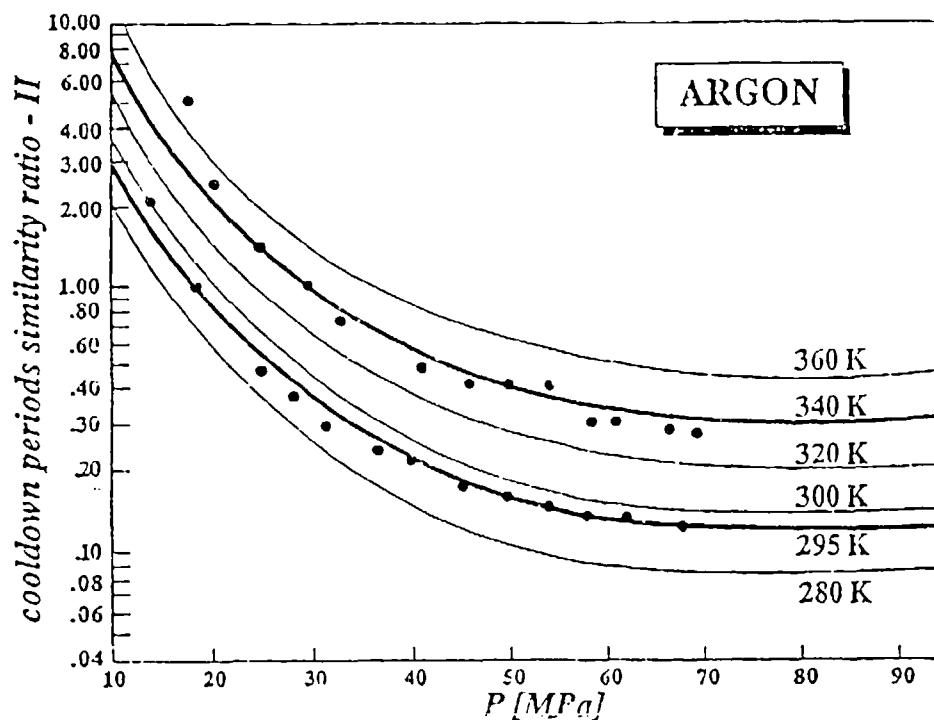


Fig. 3: Cooldown periods similarity ratios for argon at different ambient temperatures. Dots represent measurements at 295K and 340K. Curves represent theoretical model.

In a similar way, Figure 3 checks temperature dependence for argon. Once again, modeling resolution is fair enough to distinguish quite accurately between the bolted 295K and 340K isotherms. Those argon measurements are presented through

$$\tau(\text{REF}) = \tau (30 \text{ MPa}, 300\text{K}, \text{argon}) \quad (5)$$

A roughly presenting factor for scaling the 295K cooldown periods to those of 340K for both argon and nitrogen might be a figure of 2.5.

# SUMMARY

The experiments verify quite well the model for prediction of cooldown periods similarity ratios, being examined for two coolants, two ambient temperatures and a wide range of pressures. The theory originated prediction of cooldown periods decrease for argon up to about 90 MPa is reflected in experimental results. Similarly, for nitrogen its increase when exceeding 55 MPa is reflected as well.

Next recommended experiment candidate might be a non-evacuated encapsulation with higher heat leak and a short heat exchanger.

# REFERENCES

1. Aubon, C.R., Joule Thomson Cooling - An Overview, Proceedings of the Int. Soc. for Optical Eng., Vol. 915, p.32, June 7-8, Londong, UK (1988).
2. Little, W.A., Scaling of Miniature Cryocoolers to Microminiature Size, in Application of Closed Cycle Cryocoolers to Small Superconductivity Devices, NBS (NIST) SP-508 (April 1978), p.75.
3. Longsworth, R.C., Advances in Joule-Thomson Cryocoolers, Adv. Cryog. Eng. (1990), Vol.35, p.1315.
4. Maytal, B-Z., Cooldown Periods Similarity for a Fast Joule-Thomson Cryocooler, Cryogenics, Vol.32, No.7, p.653, (1992).
5. Maytal, B-Z. and Van Sciver, S.W., Characterization of Coolants for Joule-Thomson Cryocoolers, Proc. 6th Int. Cryocoolers Conf., Plymouth, MA, USA, Vol.1, p.245 (Oct. 24-26, 1990).
6. Maytal, B-Z., Principles in Applying Joule-Thomson Cryocoolers for Infrared Detectors, Proc. 24th Israeli Conf. Mech. Eng., paper 1.1.2, (May 18-19, 1992).

**BI-MATERIAL CONTROLLED  
DEMAND FLOW JOULE-THOMSON COOLERS**

GLENN E. BONNEY  
APD CRYOGENICS INC  
ALLENTOWN, PA 18103

INTRODUCTION

Joule-Thomson (JT) coolers have been designed to meet the needs of a wide variety of cryogenic refrigeration applications. They have been utilized mostly for their attributes as low cost, miniature, portable, reliable and fast cooldown open-cycle refrigerators.<sup>1</sup> They have been manufactured in a variety of forms with single or multiple stages of refrigeration and capable of operating with various refrigerants.<sup>2</sup> They are also made available with and without self-contained flow control mechanisms. Fixed orifice JT coolers that do not contain a mechanism to vary the refrigerant flow during operation produce refrigeration at a high rate when the supply pressure is high. They are good for fast cooldown applications but are inefficient for steady-state operation. Demand flow JT coolers that do contain a flow control mechanism adjust the refrigeration rate according to the heat load over a wide range of supply pressures and ambient temperatures in order to conserve refrigerant. Dual-orifice JT coolers are a combination of fixed orifice and demand flow types for use in special applications.<sup>3</sup>

Various refrigerant flow control mechanisms of the type adaptable for use with JT coolers include bi-metallic mechanisms,<sup>4</sup> gas-charged bellows mechanisms,<sup>5,6,7</sup> and bi-material mechanisms.<sup>8</sup> These flow control mechanisms are typically adjusted to respond in correlation with the temperature of the refrigerant at or near the cold end of the JT cooler or with the temperature gradient in the heat exchanger. These flow control mechanisms can usually be adjusted to provide a small excess of refrigeration, if desired, to assure a continual presence of liquid refrigerant at the cold end.

The heat that is transferred from the flow control mechanism to the colder refrigerant and heat exchanger during cooldown causes the flow control mechanism to either expand or contract. This temperature-induced movement is employed to operate a valve to reduce or throttle the flow of refrigerant as the temperature surrounding the flow control mechanism approaches a desired cold end operating temperature. After achieving the desired operating temperature, the same temperature sensitive movement is employed to regulate the flow of refrigerant in order to stabilize the cold end operating temperature under conditions of varying refrigerant supply pressure, ambient temperature, and heat load.

To date, demand flow JT coolers have predominantly used gas-charged metallic bellows mechanisms. In pursuit of a simpler, smaller, less expensive and more reliable device, the bi-material demand flow control mechanism has been developed.

### MECHANICAL DESIGN COMPARISON

Gas-charged bellows demand flow control mechanisms are typically an assembly of a cylindrical bellows that is sealed at both ends and pressurized with a gas. One end of the assembly is fixed at some location relative to the JT cooler heat exchanger. The free end of the assembly is connected to a variable flow valve. The gas pressure in the bellows increases or decreases as the bellows is heated or cooled, which causes the bellows to expand or contract relative to the fixed end and to open or restrict the flow valve. The bellows temperature may be reduced to the point where the charge gas liquefies, depending on the refrigerant and operating conditions. The bellows is typically made of metal to contain the charge gas, and it is typically fabricated by an electroplated or electroformed method. The characteristics of the bellows are similar to a coil spring, such that its length, diameter, wall thickness, number of active convolutions and elastic modulus determine its spring rate. The charge gas and initial pressure are chosen for the desired operating temperature, and for the desired pressure and length bellows response ( $dP/dL$  and  $dL/dT$ ). Typical response values for the miniature bellows used by APD Cryogenics are  $dP/dL = 5-20 \text{ GPa/m @ } 300 \text{ K}$  and  $dL/dT = 2-2.5 \text{ } \mu\text{m/K @ } 100 \text{ K}$  with a net available valve actuation force of 1-4 N. The flow valve is sized for the desired flow range and can be of various designs (e.g. a moveable needle point over a fixed circular orifice). The valve is typically adjustable for setting the initial flow rate. Typical miniature JT coolers have orifices or nozzles with diameters of 50-350  $\mu\text{m}$  and flow rates of 1-10 std L/min (with  $\text{N}_2$  @ 21 C and 6.9 MPa  $\Delta P$ , referred to as Co as an APD Cryogenics standard). All these variables plus the assembly's coefficient of thermal expansion, its natural frequency as a spring-mass system, and its location relative to the heat exchanger's temperature gradient determine the response, sensitivity and hysteresis of this type of flow control mechanism. Gas-charged bellows are complex to design and manufacture, requiring lengthy empirical development, and therefore are a very long lead item when considering new product development or custom adaptations.

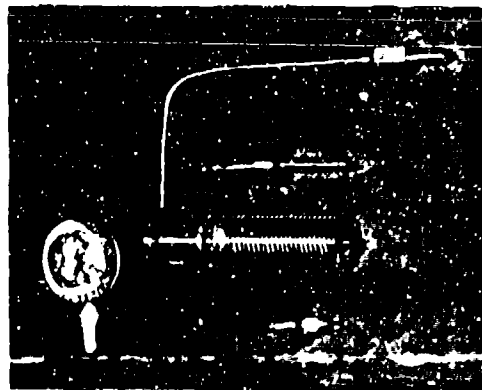
Bi-material demand flow control mechanisms are typically an assembly of a simply machined cylindrical rod.<sup>8</sup> Similar to the gas-charged bellows, one end of the rod is fixed at some location relative to the JT cooler's heat exchanger while the free end is connected to a variable flow valve. As the rod (i.e., the actuator) is heated or cooled, it either expands or contracts relative to the fixed end, and the flow valve is either opened or restricted. The material for the rod is chosen primarily for its thermal expansion characteristics relative to the thermal expansion characteristics between the intended anchor point with the heat exchanger and the variable flow valve. Any combination of materials can be used to provide the differential thermal expansion for a given temperature change. Since many plastics have higher coefficients of thermal expansion relative to metallics or ceramics, the best available combinations exist with them. Typical miniature bi-material mechanisms have a differential expansion of  $> 50 \text{ } \mu\text{m/(m} \cdot \text{K)}$  over the temperature range of 80-300 K. Choosing material combinations that provides the maximum

relative  $dL/dT$  will then minimize the actuator's length. Presently, a typical high  $dL/dT$  value would be  $1-1.5 \mu\text{m/K}$  @ 100 K. Although the low temperature sensitivity of the bi-material mechanism is less than that of the gas-charged bellows, the 300-80 K  $dL/dT$  response is similar. Additionally, the bi-material actuator has an essentially infinite spring rate compared to the gas-charged bellows, and it can provide a valve actuation force several times greater than the gas-charged bellows. The adequate response and the lack of a gas charging fitting have allowed bi-material mechanisms to be made smaller than gas-charged bellows mechanisms. Because of the obvious simplicity of this design, having few variables, bi-material mechanisms are more quickly adapted to new products or custom applications.

Demand flow control mechanisms can be installed in JT coolers having various heat exchangers, such as the more prevalent finned tube heat exchanger<sup>9</sup> or a matrix tube heat exchanger.<sup>10</sup> APD Cryogenics has manufactured miniature demand flow JT coolers in sizes down to  $\varnothing 5 \text{ mm} \times 23 \text{ mm}$  long. Presently with bi-material control mechanisms, the lower limit on demand flow cooler size is estimated to be less than  $\varnothing 3 \text{ mm} \times 15 \text{ mm}$  long depending on the application. However, it must be remembered that shorter heat exchangers are also less efficient because of higher end-to-end heat conduction losses. Figure 1 displays the geometric comparison of gas-charged bellows and bi-material flow control mechanisms for a typical finned tube heat exchanger demand flow JT cooler. The photo inset displays the same with a  $\varnothing 9.52 \text{ mm} \times 37.5 \text{ mm}$  long JT cooler designed for a typical infra-red detector cooling application.

### CRYOGENIC PERFORMANCE COMPARISON

The cooldown performance of a demand flow JT cooler is determined by the heat exchanger efficiency, pressure drop, supply pressure, ambient temperature, orifice size, by the thermal load of itself and the load to be cooled, and by the throttle response of the flow control mechanism. A JT cooler operating with nitrogen typically contributes ~ 50 % of the heat exchanger (i.e. the colder half) to the total thermal load. For the smallest demand flow coolers, the flow control mechanism typically doubles the contributed amount of thermal load. The throttle response of the flow control mechanism will effect the rate at which the flow is reduced in proportion to the load being cooled. The heat transfer from the flow control mechanism, both longitudinal and radial, and the thermal diffusivity are important factors in controlling the throttle response. For instance, a metallic bellows would respond faster than a plastic bi-material actuator. As the flow is throttled, the pressure drop across the exhaust side of the heat exchanger is reduced which reduces the saturation temperature of the liquid refrigerant at the cold end. The flow is continually throttled until the net refrigeration capacity is in some proportion with the steady-state heat load. The primary concern with any flow control mechanism is its balance between throttle sensitivity, or the ability to delay throttle, and stability after throttling. After throttling, the remaining transient cooldown of the load is governed by the rates of diffusion of heat flowing into the cold end from various parts of the load's assembly. Hence, a demand flow JT cooler can establish a stable liquid refrigerant temperature, but the load may not reach steady-state temperature until several seconds later.



1006

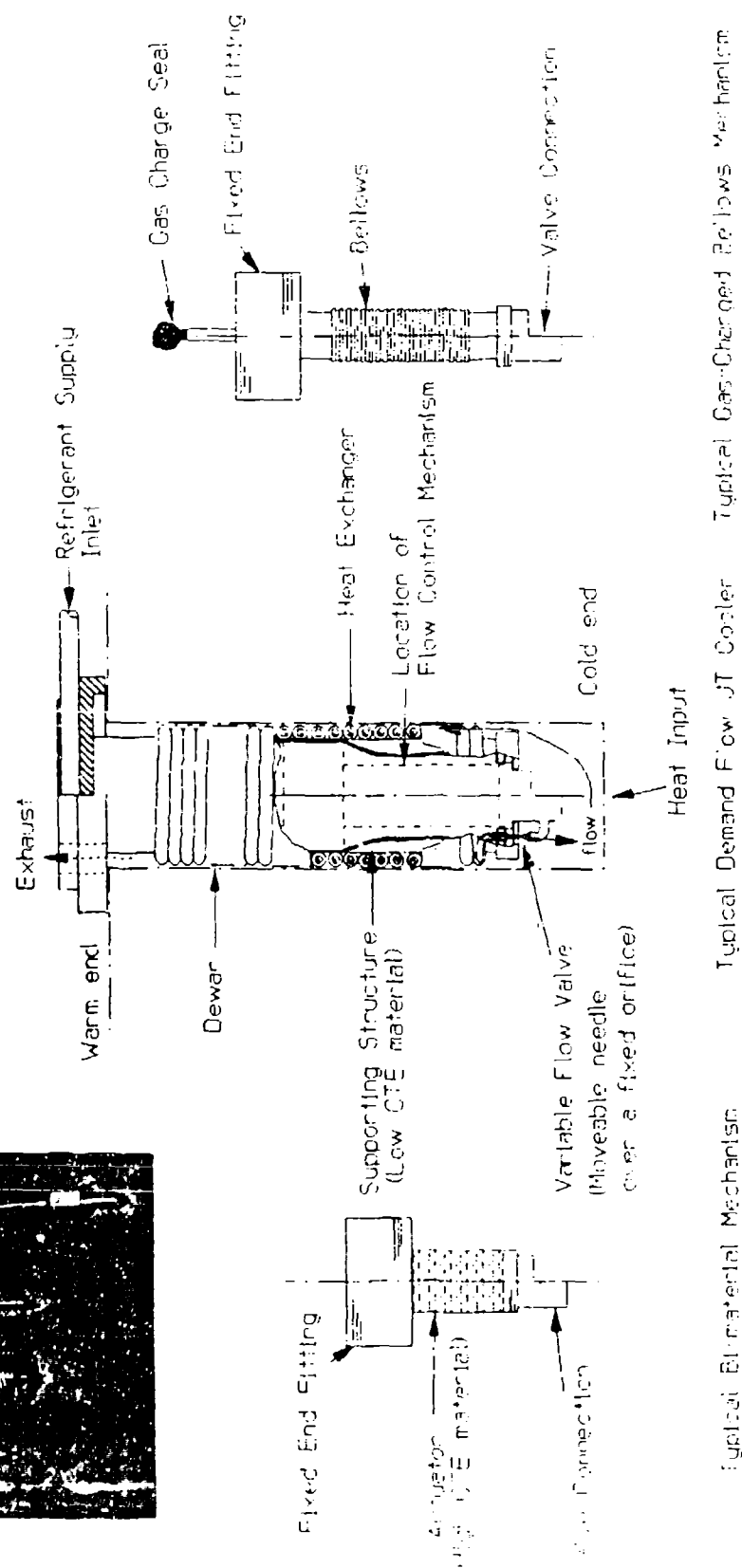


FIGURE 1: Geometric Comparison of Gas-Charged Bellows and Bi-Material Flow Control Mechanisms for a Typical Demand Flow JT Cooler  
(Photo Inset shows the same with a Javelin program JT cooler)

Bi-material controlled demand flow JT coolers have been made to provide identical cooldown performances compared to gas-charged metallic bellows controlled coolers at ambient temperatures from -40 C to 71 C. Performance with various refrigerants was also similar. If demand flow JT coolers are initially set to provide a minimum after-throttle flow rate with a given refrigerant, then they will usually provide a higher after-throttle flow rate when operated with a warmer boiling point refrigerant (and vice versa, a lower flow with a colder boiling point refrigerant). This effect can be worse with a gas-charged bellows mechanism, depending on the intended refrigerants and the chosen bellows charge gas.

After cooldown, the steady-state gas consumption and temperature stability of a demand flow JT cooler are determined by the heat exchanger efficiency, pressure drop, the internal heat loss due to conduction from the warm end, by the conduction, convection, and radiant heat losses entering the device being cooled, and by the response of the flow control mechanism to changes in refrigerant supply pressure and cold end temperature. The major performance differences between bi-material and gas-charged bellows flow control mechanisms have been observed during steady-state operation.

Gas-charged bellows controlled demand flow JT coolers have a flow control hysteresis that is inversely proportional with the refrigerant supply pressure. This is partly due to a non-linear  $dp/dT$  bellows response after the charge gas begins to liquify inside the bellows. It is partly due to the bellows spring rate that allows deflections and oscillations from refrigerant supply pressure and flow forces acting on the flow valve which is connected to the free end of the bellows assembly. It is also due to an imbalanced  $dp/dL$  response resulting from variations in the exhaust pressure via variations in the flow rate or local ambient pressure. As a result, these coolers typically exhibit some flow instability, increasing with decreasing supply pressure. The flow instability directly affects the cold end temperature stability and wastes refrigerant. These coolers can also exhibit a cyclic control behavior, basically on-off flow control. This is adjustable primarily by the initial flow setting of the variable flow valve. On-off flow control extends the steady-state operating time from a given quantity of refrigerant at the expense of temperature stability, and it increases the susceptibility of the flow valve to clogging from contaminants in the refrigerant during the "off" period. On-off flow control typically produces cold end temperature cycles of 1-10 K @ 0.05-0.5 Hz. To obtain a more proportional flow control, the many variables previously discussed must be balanced. Proportional flow control thus improves temperature stability and reduces the susceptibility to clogging by providing a higher average flow rate at the expense of more refrigerant consumption.<sup>11</sup>

Bi-material controlled demand flow JT coolers typically exhibit better proportional flow control stability, and thus better cold end temperature stability, than gas-charged bellows controlled coolers. Temperature stability has been achieved within 0.5 K with < 0.1 K peak-to-peak variations @ 1 Hz -1 kHz for extended periods. The more stable flow control also reduces refrigerant consumption, thus extending the steady-state operating time from a given quantity of refrigerant, without compromising temperature stability or increasing the susceptibility to clogging from contaminants in the refrigerant. The improved flow stability is attributed to the bi-material mechanism's  $dl/dT$  response, and its higher stiffness and net valve actuation force. This



makes it less sensitive to temperature variations at the cold end, flow aberrations at the valve, or supply and exhaust pressure variations. The noticeably reduced susceptibility to clogging for bi-material controlled coolers is also attributed to the flow stability. However, when these coolers clog with excessive contamination they typically warm up to a higher temperature before recovering than do gas-charged bellows controlled coolers.

Figure 2 displays some of the best performance seen with both bi-material and gas-charged bellows controlled demand flow JT coolers. It plots the temperature stability of the center of a silicon disk epoxy bonded to an alumina substrate that is brazed to the cold end of a titanium alloy dewar bore. The coolers were both  $\varnothing$  9.52 mm x 37.5 mm long; PC3 is a bi-material controlled unit, and BFC6 is a gas-charged bellows controlled unit. The tests were conducted at 21 C with nitrogen in a blowdown mode from a fixed 0.1 L volume initially pressurized to 40 MPa. The total cooldown load,  $Q_{(\text{dewar} + \text{cooler})}$  was  $\cong 300$  J, and the total steady-state heat loss,  $Q'_{(\text{dewar} + \text{cooler})}$  was  $\cong 0.29$  W. The upper two traces compare the entire test run of each cooler. The lower two traces display the first 100-300 s of the same tests at a higher resolution. Data was collected at a higher sample rate for the first 200 s and at a reduced sample rate thereafter because of limited computer memory. The characteristics of the higher sample rate data should be envisioned as being superimposed over the lower sample rate data for the entire test. Note the differences in the throttle response during the cooldown phase, and the stability near the end of each test. Also, note the generally decreasing temperature as the test proceeds after cooldown. As the nitrogen supply pressure decreases from the fixed 0.1 L volume, the refrigeration capacity decreases, reducing the liquid fraction in the JT process. The flow control mechanism then senses a slight warming in the heat exchanger and responds by increasing the flow rate. Therefore, the decreasing temperature is not due to a decreasing flow and exhaust pressure, it is due to an increasing coefficient of heat transfer in the liquid nitrogen.<sup>11</sup>

## RELIABILITY COMPARISON

Overall reliability with these types of mechanisms and JT coolers is typically related to maintaining manufacturing tolerances and assembly techniques at the highest possible quality level. The sensitivity of these devices to damage and contamination is naturally increased by their miniature size.

The obvious reliability concern with gas-charged metallic bellows demand flow control mechanisms is leakage of the charge gas. A total assembly leak rate of  $\sim 1$  std pL/s of helium is necessary for a multi-year life. This problem can be well controlled by the use of porosity-free metallic bellows, proper sealing techniques, and appropriate solder and braze alloys. Long-term failures due to possible fatigue, creep, or micro-crack propagation have been studied during cyclic thermal fatigue tests. Several batches of different gas-charged bellows assemblies were cycled 10000 times per batch. Each cycle consisted of 20 s in liquid nitrogen, 40 s warm-up, 20 s in 90 C distilled water, and 40 s cooldown. A special machine was constructed for these tests, entitled the Bellows Aging Tester, which is now a standard manufacturing test at APD Cryogenics. The results showed the following failure rate for variously assembled gas-charged bellows: 0 failures

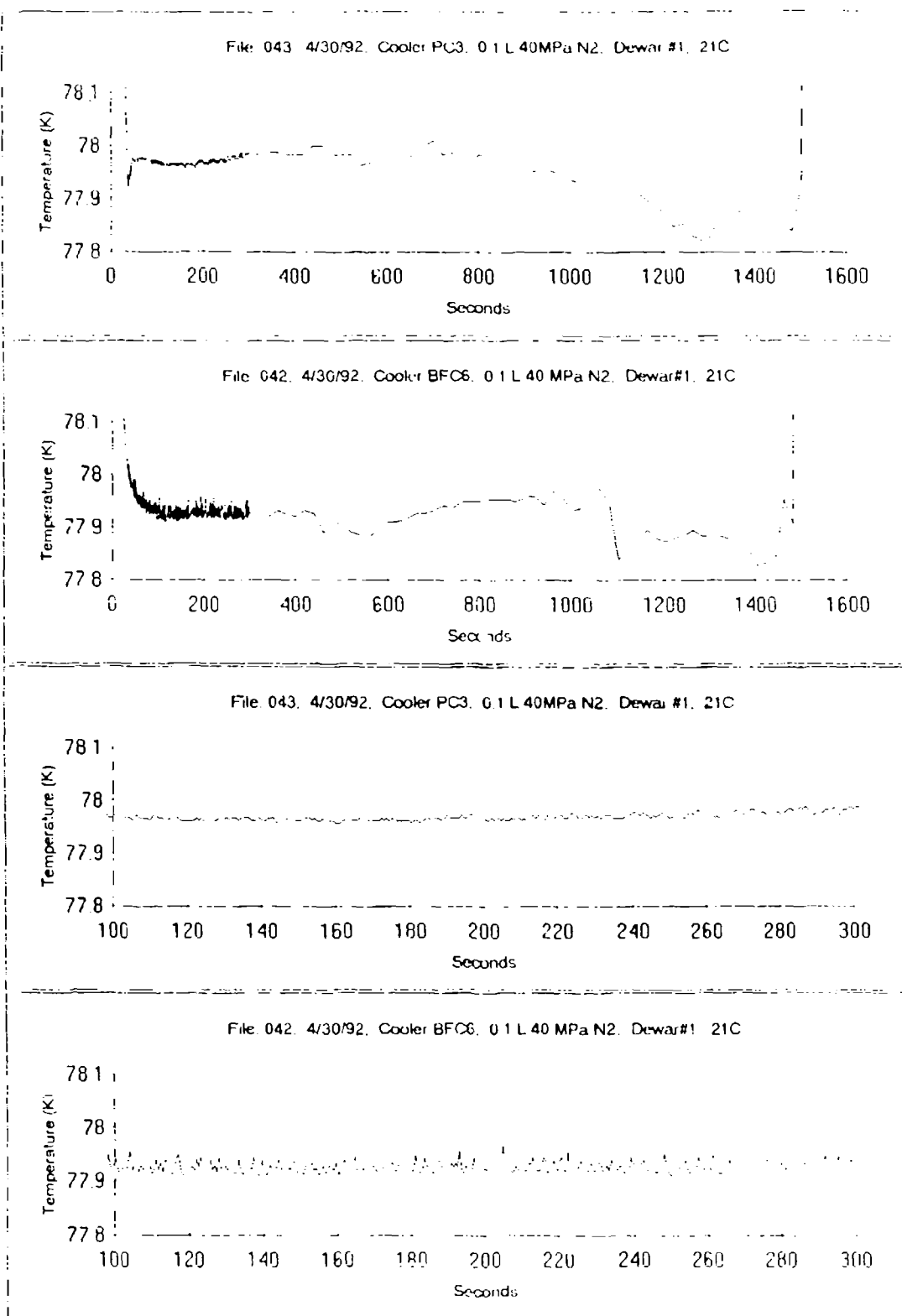


FIGURE 2 Performance Comparison of Bi-material (PC3) and Gas-Charged Bellows (BFC6) Controlled Demand Flow JT Coolers in Blowdown Mode

@ 0-600 cycles, < 5 % @ 0.6-1.7 k cycles, ~ 5 % additional @ 1.7-6.7 k cycles, and < 15 % additional @ 6.7-10 k cycles (i.e. < 25 % total failures over 10 k cycles). Failures due to gas loss were typically at joints and attributed to fatigue failure of the bond. The other major failure was the bellows itself becoming distorted (tilted, curved, or twisted). Distortion was attributed to fabrication stresses in the bellows being relieved.

Bi-material demand flow control mechanisms have essentially no mechanical failure modes, provided the assembly employs proper fastening techniques. No mechanical failures were revealed with a batch of assemblies during a 10 k cycle thermal fatigue test (4 min @ 77 K, 1 min warm-up, 4 min @ 70 C, 1 min cooldown). Other reliability concerns with bi-material mechanisms are primarily associated with the properties of the materials chosen. For instance, the use of certain plastics raises concern for possible failures due to exposure to excessively high temperature or humidity. Tests have been conducted on bi-material mechanisms that utilize thermoplastic polymers with low melting temperatures and low moisture absorption rates. Over the extreme temperature range of -51 C to 71 C per Mil-Std-810 there were no failures nor changes in operating performance after either short-term or long-term exposure. Exposure to higher temperatures of 80-110 C also did not cause mechanical failure, but did cause the operating performance to become inconsistent. In all cases the average flow rate after throttling increased. Therefore, the present temperature limit for these bi-material control mechanisms has been set @ 80 C. Exposure to humidity extremes of 0-100 % relative humidity did not cause any mechanical failures, but did cause inconsistent operation. Specifically, dry assemblies (vacuum baked for several weeks @ < 3 kPa and 70 C) were exposed to 100 % relative humidity for 5-19 days. This caused only a 2-4 % change in throttle response. Again, in all cases the average flow rate after throttling increased. To keep this issue in perspective, one must remember that > 2 ppm<sub>v</sub> of water vapor is enough to cause a typical miniature demand flow JT cooler to malfunction.<sup>11</sup> Therefore, exposure to humidity is not desirable for any JT cooler.

## SUMMARY

Bi-material flow control mechanisms have been developed to a level that offers an alternative to the more prevalent gas-charged bellows mechanisms for demand flow JT cooler applications. The bi-material mechanism reduces the complexities of product development and manufacturing for diverse customer applications. It allows for the design of smaller demand flow JT coolers. It has been shown to provide improved flow and temperature stability for better refrigerant utilization, and it improves the cooler's mechanical reliability.

## REFERENCES

1. Longworth, "Advances in Small Joule-Thomson Coolers", Advances in Cryogenic Engineering, Vol. 35, Plenum Press, NY, 1990

REFERENCES continued

2. Longworth, "Heat Exchangers for Joule-Thomson Cryocoolers", to be presented at the 1st International Conference on Aerospace Heat Exchanger Technology in 1993
3. Longworth and Chalmers, U.S. Patent 4,237,699 (1980)
4. Jepsen et al, U.S. Patent 3,320,755 (1967)
5. Buller, "A Miniature Self-Regulating Rapid-Cooling Joule-Thomson Cryostat", Advances in Cryogenic Engineering, Vol. 16, Plenum Press, NY, 1970.
6. Campbell, U.S. Patent 3,590,597 (1971).
7. Longworth, U.S. Patent 3,728,868 (1973)
8. Longworth, U.S. Patent 4,152,903 (1979)
9. Geist and Lashmet, "Miniature Joule-Thomson Refrigeration Systems", Advances in Cryogenic Engineering, Vol. 5, Plenum Press, NY, 1960.
10. Longworth and Steyert, U.S. Patent 4,781,033 (1988).
11. Bonney and Longworth, "Considerations in Using Joule-Thomson Coolers", International Cryocooler Conference, 1990.

CONTAMINATION CONTROL IN CLOSED CYCLE JOULE-THOMSON  
CRYOCOOLERS AND A NEW J-T VALVE

James Lester and Steve Nieczkoski  
Ball Aerospace Systems Group  
Electro-Optics/Cryogenics Division  
1600 Commerce Street  
Boulder, Colorado 80301

INTRODUCTION

Cryocoolers are sensitive to the effects of contamination. This is the result of low temperatures which cause contaminants to freeze and block flow passages. Also, particulate contamination can block flow passages or cause mechanical damage. Long life Cryocoolers must be designed to both minimize the sources of contamination and to tolerate some contamination. The correct design approach depends on the nature of the cryocooler. The closed cycle J-T cooler we are developing uses a combination of contamination mitigation features. These features include design and fabrication to minimize contamination sources, a built-in gas purifier, and design features that provide tolerance for small amounts of contamination that cannot be eliminated.

This paper discusses the contamination control effort (which is a major part) of a long life J-T cryocooler development at Ball Aerospace Systems Division. First, the nature of contamination and its effects are explained. Next, the design of the J-T cryocooler is described with particular emphasis on the contamination control aspects of this design. A new design for a contaminant tolerant J-T valve is explained. Finally, our significant test results are described.

Most importantly we have shown that long term (multi-year) operation of a J-T cryocooler can be achieved with proper attention to contamination control. This has been shown to be

true even when the cooler uses an oil lubricated compressor and is intended for space flight application.

### CONTAMINANTS AND THEIR EFFECTS ON J-T CRYOCOOLERS

Contaminants fall into three classes: particulates, liquids and gaseous contaminants in the working gas. Particles can come from mechanical wear or shedding of parts. Also, particles can be left in the cooler after manufacturing. In our J-T cooler, the liquid contaminant is the lubricating oil used in the compressor. Gaseous contaminants come from outgassing of parts and materials or virtual leaks from partly trapped volumes in the cooler. The initial charge of nitrogen gas can be contaminated. Gaseous contaminants can even enter the cooler through external seals by partial pressure differences.

Particulate Contamination. Some particles are left in the cooler during fabrication even if very strict controls are imposed. The hardest ones to control are those that are weakly attached to parts. These can work loose later as a result of environmental factors such as temperature changes or vibration. Very small particles are generated at some of the bearing surfaces. There are two major effects: Particles can collect in small flow passages and change or stop the flow. Also, particles could be abrasive and cause additional wear and this would result in more particles. The additional wear itself could lead to a decrease in performance or mechanical failure.

Liquid Contamination. Our cooler uses oil to lubricate the compressor. The liquid oil is a contaminant because, if allowed to reach the cold head, it can freeze there and stop the flow. The liquid oil will be in the form of large floating droplets, slugs, fine mist or films on the surrounding surfaces. The large droplets and slugs can be moved by pressure or gas flow or by gravity. Combinations of these forces can occur in various situations in one-g or zero g causing significant oil movement. Fine mist can be transported by flow or by the action of Brownian Motion in the working gas. An oil film can creep along tube walls of tubes if unimpeded by gravity.

Gaseous Contaminants. There are several sources of gaseous contamination. The most suspected source was the lubricating oil. But, since we are using a very low vapor pressure oil, the oil itself turns out to be a negligible source. The oil, however, is a large reservoir for dissolved gases which can slowly outgas into the working gas and be carried to the cold head.

Other sources of outgassing are the solid materials of construction. Non metallics such as epoxies are particularly gassy. Metal surfaces are much better but a smooth surface finish is better than a rough one. Where parts fit tightly, air can be trapped during fabrication. This is the category of virtual leaks. Faying surfaces and screw threads are bad offenders. Air bubbles could be trapped in epoxies. Some contaminating gases are present in the initial charge of working gas. If non-metallic seals such as elastomeric o-rings are used, these can be sources of contamination by two mechanisms, their outgassing and their transparency to the atmosphere by diffusion caused by partial pressure differences. If the interior of the cooler is very dry, the water in the atmosphere will be at a pressure of several Torr and will flow through the o-rings at a rate which can seriously contaminate the cooler.

The primary effect of gaseous contamination is to freeze in the cold head and block flow passages. A secondary effect could be to promote chemical reactions with the cooler materials which could lead to a variety of problems.

### THE DESIGN OF A LONG LIFE, CLOSED CYCLE, J-T CRYOCOOLER

The closed cycle J-T cryocooler is discussed in another paper in these proceedings titled "Progress Report on the Development of the Ball J-T Cryocooler" by R. Scarlotti and R. Levenduski. The paper gives details on the design and the development progress of the machine with emphasis on cooling performance, modeling, fabrication and test results. Here we will concentrate our discussion on the contamination control effort. Figure 1 is the block diagram of the cooler. The cooler consists of three main sections: the compressor and gas purifier, the cold head and the electronics.

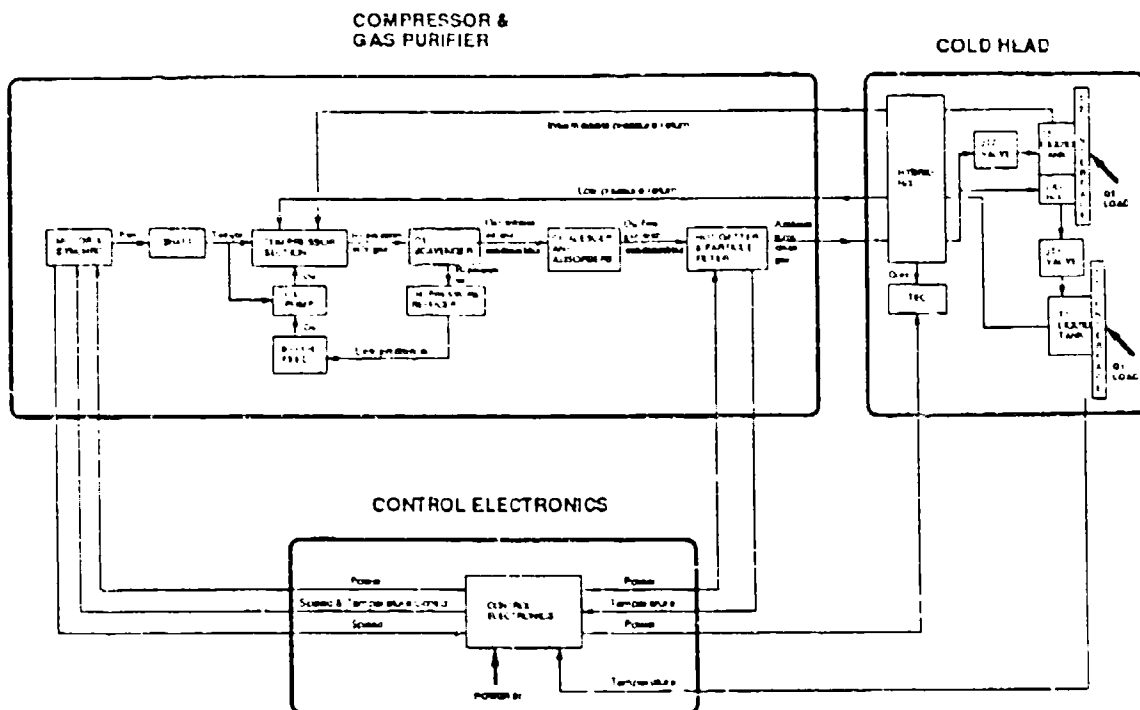


Figure 1. EDM block diagram.

The nitrogen working gas is compressed in a four stage positive displacement compressor. The slightly oily compressed nitrogen at 1000 PSIA passes through a gas purifier, where the oil and other contaminants are removed, and then to the cold head where expansion and cooling takes place. The low pressure effluent gas returns to the compressor for recompression.

The Contamination Control Technique. The contamination control technique used in our J-T cooler consists of three main parts. First, we design the cooler to minimize contaminants, then we make the cooler tolerant of contamination, and finally we incorporate a gas purifier to remove residual contaminants.



Minimizing the Initial Contamination Load. Minimizing outgassing starts with careful material selection. As much as possible we use metallic materials which can be surface finished to better than 10 micro-inches. This ensures that the real surface area which can outgas is minimized. We chose materials that can be cleaned by solvent and ultrasonic methods and subsequently vacuum baked to at least 150 C. Stainless steel (316L Vacuum Arc re-melt) is a favored material. Quantities of non-metallic materials are minimized because these are usually the worst outgassers. For nonmetallic parts, polyimides are favored because they can be baked at temperatures well above the 150 C goal. Epoxies are needed in small quantities and these are chosen from a list of materials that has been thoroughly investigated for its outgassing properties. When we use o-rings, they are made of Viton elastomer because this material can also be vacuum baked. Glass sealed hermetic electrical connectors are acceptable. The oil we use has a vapor pressure of less than  $1\text{E-}10$  Torr at 300 K. This means that the oil vapor arising from the oil is only a tiny fraction of the total outgassing load on the cooler and is not a design driver.

The mechanical design of the cooler includes many features that minimize contamination. Faying surfaces and screw threads are relieved. That is, gas venting holes or slots are located at each potential trap to allow the trapped air to be removed during the final vacuum bake process. The epoxy encapsulated drive motor windings are canned in a metal sleeve that prevents escape of outgassing contaminants into the working fluid.

Parts are designed so that clean assembly processes can be used. For example, we use welding instead of brazing to eliminate the residual flux that would be present after brazing operations. All parts are thoroughly cleaned prior to assembly to specified levels that allow strategically placed filters to be used without fear of filter overloading. Filters are placed where they are needed to protect critical components.

To protect against atmospheric in-leakage through elastomeric seals, the number and size of these seals are minimized and eliminated wherever possible.

The lubricating oil we use is carefully processed prior to installation in the cooler. This oil has a very low vapor pressure so very little oil vapor is present in the cooler. At the same time, though, the oil is a reservoir for dissolved atmospheric gases including (importantly) water. These dissolved gases are potentially the largest single source of contamination. We have built a processor to remove most of these gases from the oil before the oil is loaded into the cooler.

The processor is a hot vacuum degassing apparatus. A 1000 liter per second turbo-vacuum pump is connected to a glass bell jar. Inside the bell jar there is a thermally-conducting surface which is heated to 100 C. Unprocessed oil is dripped onto this hot surface while being continuously evacuated to a pressure of less than  $1 \times 10^{-6}$  Torr. The process continues until the apparent vapor pressure of the oil, with trace amounts of residual gaseous contaminants, approaches that of the base oil.

The processed oil is transferred under vacuum to a clean holding tank until it is needed in the compressor. Before the oil is transferred to the compressor, the compressor is thoroughly vacuum baked to remove most of the gaseous contaminants. The oil is transferred to the compressor from the holding tank under vacuum to prevent it from re-absorbing atmospheric contaminants.

A New Contamination Resistant J-T Valve. The purpose of a J-T valve is to restrict the gas flow and cause a large pressure decrease. This pressure decrease produces the desired cooling effect. J-T valves are small openings in the flow passage and are subject to being plugged by contaminants. Gaseous contaminants in the nitrogen can freeze and solid particles can plug these valves. To achieve high reliability and long life, a new design was developed.

Two problems must be solved: Plugging by frozen contaminants and plugging by solid particles. The contaminants must be prevented from reaching the valves and the valves must be tolerant of some contamination.

A J-T valve could be a localized restriction such as a single orifice, it could be a series of orifices, or a long, thin tube (capillary). A single orifice has the smallest opening of these types and; therefore, it can be plugged by smaller particles or a smaller amount of ice than the other types. We are using capillary J-T valves for the following reasons: A capillary restricts flow as a result of its length as well as its diameter. The greater the length, the larger its diameter can be to produce a given flow resistance. Capillaries of convenient length (a few inches) can be several times larger in diameter than a single orifice. Typical capillary diameters are 50 to 150 microns in our cooler. In comparison to an orifice, an equivalent resistance capillary can tolerate much more contamination before the flow is significantly decreased.

Virtually all of the gaseous contaminants which could freeze in the J-T valves are removed by the gas purifier. Still, there is a possibility that residual contaminants could cause problems in a cooler operating continuously for years. We have installed small heaters on the valves to evaporate (defrost) these contaminants should they accumulate. This procedure has been completely successful in clearing the frozen contaminants in the past. Since we have incorporated the gas purifier and used capillary valves, defrosting has not been needed. The heaters are retained as a reliability feature to increase the safety margin.

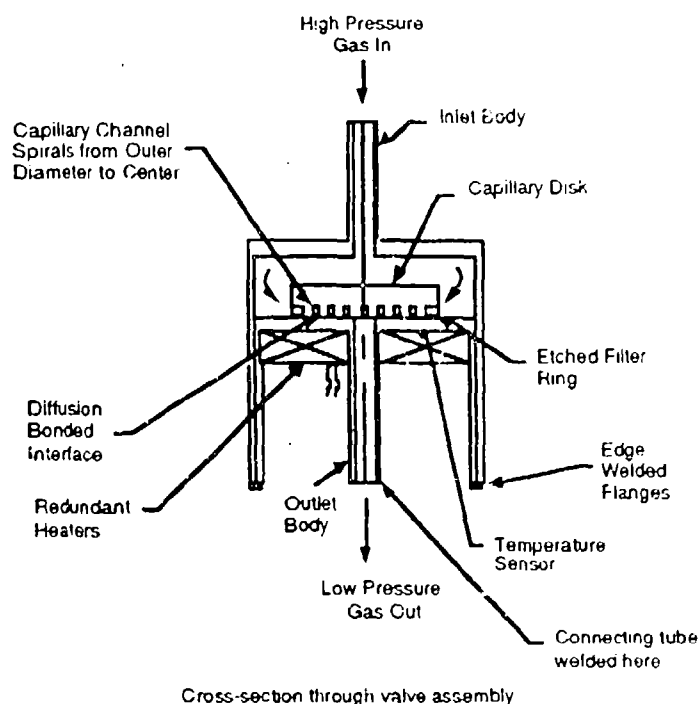


Figure 2. J-T valve design concept.

assembled in a highly controlled, clean environment. Once fabricated and tested, this assembly can be installed in the cold head in a less restricted clean environment. In effect, we have designed a protected device analogous to a packaged microcircuit. Figure 2 shows the design concept. The valve consists of three, 316L stainless steel parts. The defrost heaters and temperature sensors are attached after assembly of these parts. The capillary is machined as a spiral channel on a flat disk (the valve seat). Dimensions for the channel in a typical valve are two to six thousandths of an inch (50 to 150 microns) wide by 3 to 6 inches long. The valve seat and mating outlet body are lapped to a finish of better than 4 micro-inches and are very flat. This design provides good surfaces for the gold compression bonding assembly process. A ring on the outside of the outlet body is machined away by about 15 microns to create an annular gap between this ring and the mating valve seat. This gap is the final filter protecting the channel from particles. Cleaning and assembly procedures limit this the actual quantity of particles to a safe, low level which will not plug the filter. The outlet body has a central outlet tube. The inlet body piece is welded to the outlet body piece forming an assembly which can be welded to tubes in the cold head.

The greatest challenge was finding a way to protect a J-T valve from particles. A fine filter must always be installed upstream of the valve. A difficulty with this approach, though, is that no large particles can be left in the space between the filter and the valve. We are concerned with particles larger than one fourth of the capillary diameter, about 15 microns. This leads to the requirement for a thoroughly cleanable and inspectable design. We have adopted the philosophy that the final filter and valve must be

The Gas Purifier. The gas purifier performs three functions:

- It separates and returns most of the oil in the high pressure gas stream leaving the compressor.
- It removes contaminants in the high pressure gas stream so no freeze-up or blockage by particulates will occur in the cold head.
- It prevents contaminant back streaming in the low pressure gas streams.

The basic requirement is to ensure that 7 year life plus storage is achieved. Figure 3 shows the gas purifier. The purifier consists of several internal components which will be described.

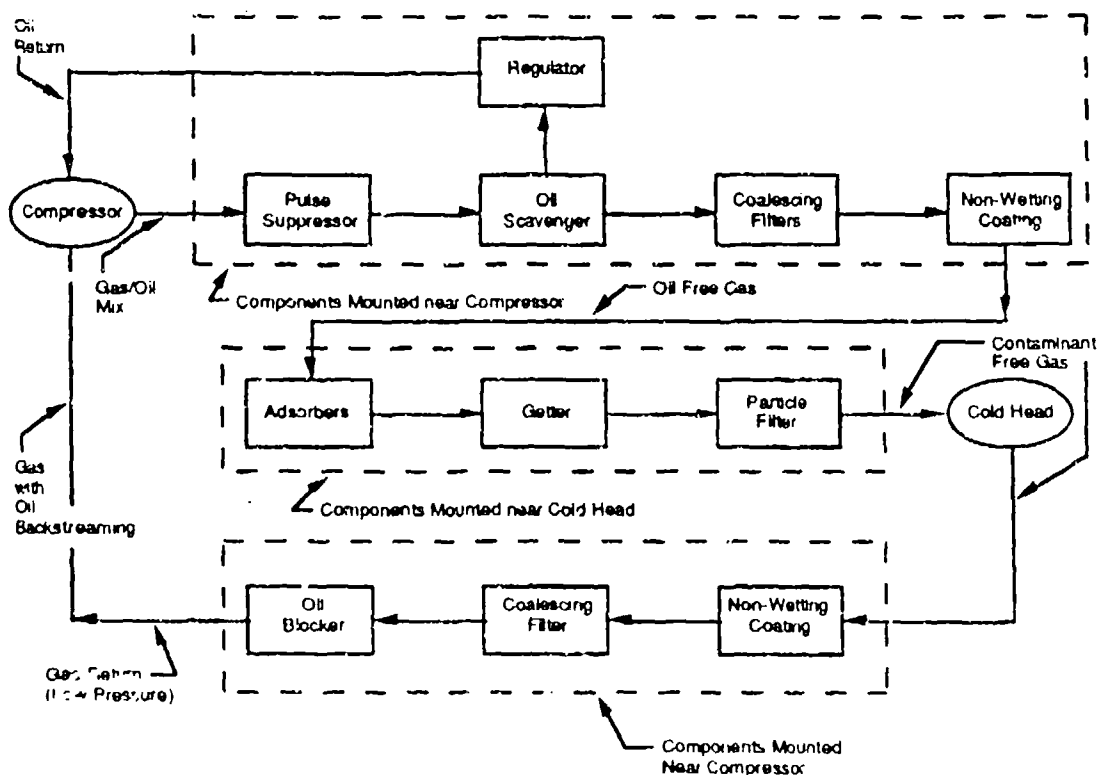


Figure 3. Gas purifier.

## Component Functions, Requirements and Design

The pulse suppresser reduces the ripple in the pressure of the compressed gas which arises from the periodic compression process. It prevents periodic gas breakthrough at the oil scavenger separation screen. It works by viscous friction losses to dampen the pressure wave. A slender, tubular configuration is necessary to prevent pooling of oil in zero-g.

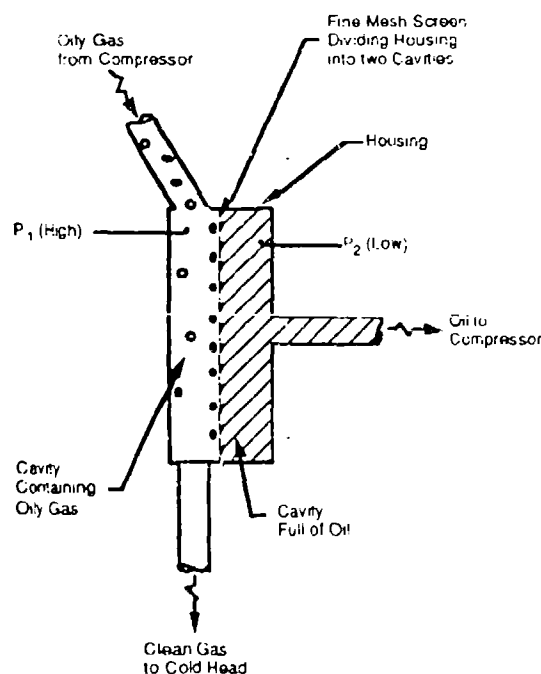


Figure 4. Oil scavenger concept.

The oil scavenger removes most of the oil from the compressed gas stream and returns that oil to the compressor crankcase. It maintains an adequate supply of oil for compressor lubrication and prevents too much oil from flowing to the downstream gas purifier components. Figure 4 shows the concept of the scavenger. A fine mesh screen divides the housing into two cavities. There is an inlet for oily gas, an outlet for oil, and an outlet for clean gas. Removal of oil is based on surface tension and momentum principles. The screen is very fine. When it is wetted with oil, it takes over 1.6 PSI for gas to break through the oil

membrane. More oil arriving on the upstream side of the membrane, however, coalesces and flows through the membrane as long as  $P_1$  is higher than  $P_2$ . A pressure regulator controls this pressure difference. As long as the pressure difference is less than the breakthrough pressure or "bubble point" of the screen, only oil will pass through. The geometry of the scavenger is arranged so the oily gas impinges on the screen. This arrangement improves the efficiency of oil collection and reduces the required area of the screen. The bubble point is independent of screen area so the screen can be as large as needed to pass the required oil flow at a pressure difference well below the bubble point. The out-flowing gas is nearly oil free. Tests of the device show that it removes more than 99.997 percent of

the oil from the gas stream. The pressure regulator maintains a small pressure difference across the screen in the scavenger. Also, this regulator reduces the pressure of the oil and feeds it back to the compressor crankcase. The regulator must maintain a pressure differential of  $0.8 \pm 0.2$  PSI across the screen to ensure oil removal from the gas. At the same time it must prevent gas from breaking through the membrane of oil on the screen and flowing back to the compressor through the oil path. Since the pressure is 1000 PSIA in the oily gas stream, two stages of regulation are needed to provide the small pressure differential in the scavenger.

There are two oil coalescing filters in the cooler. They collect and permanently store the small amount of oil that escapes the scavenger. These filters collect approximately 150 grams of oil over the life of the cooler and reduce the downstream carry-over to less than  $1\text{E-}14$  grams per second. They are configured to work in one-g and in zero-g. The filters can be thought of as porous blotters through which all the gas must flow. The first filter captures most of the oil and the second filter captures virtually all of the remaining oil. Coalescing filters are also installed in the return lines from the cold head. Their function is to collect any oil mist that might be generated by the action of the compressor from migrating back to the cold head. This could occur just after cooler shutdown.

The elements in the coalescing filters slowly become wet as they accumulate oil. Over a very long time the oil could creep along the surfaces of the coalescing filter housing and downstream toward the adsorbers. Eventually the adsorbers could become contaminated with oil and be less effective for removing trace gaseous contaminants. The non-wetting coating stops this creeping action in all three tubes connecting the compressor to the cold head. Tubes on the cold head sides of the coalescers are internally coated for a short distance with a material which is not wetted by the oil. Therefore, a film of oil cannot cross this barrier by creeping along the wall. The technique is standard practice to protect sensitive equipment in space instruments from contamination by lubricants.

The adsorbers remove some of the gaseous contaminants from the nitrogen before the nitrogen reaches the getter. About 100 grams of activated charcoal and mole sieve are used.

A hot reactive getter performs the final clean-up of the gas before it enters the cold head. The getter material is an alloy of Iron, Zirconium and Vanadium kept at 350 C by an externally controlled heater. The getter is a commercial device used to purify gases for microcircuit manufacture where the purity requirements are more severe than for our cooler. The output level of gaseous contaminants is lower than one part per billion. A 5 micron filter is built into the getter housing to prevent particles from traveling to the cold head.

When the compressor is oriented with the inlet of the first stage pointing down in one-g, there is a tendency for a small amount of oil to drip into the return line from the cold head when the cooler is not running. This action could eventually lead to contamination of the cold head. The oil blocker prevents this from happening. The return line from the cold head is bent into a trap configuration that dictates that the oil must always go up to go to the cold head regardless of orientation. If any oil tries to accumulate in the line, it is continuously purged back to the compressor by the gas flow.

### DEVELOPMENT RESULTS

The features described above have been incorporated into several models of the cooler and operated without any failure of the contamination control system. In addition, a special long term test was performed just to evaluate the contamination control approach.



The Gas Purification Demonstration. We based the gas purification techniques on component manufacturer's data and on separate analysis and component testing done at Ball. This testing showed that contamination could be reduced sufficiently to permit very long term (greater than seven years) operation without maintenance. We had not, however, proven long term operation on a closed cycle, oil lubricated J-T cooler. The objective of the gas purification demonstration was to do such a test.

The gas purification demonstration system was a complete closed loop cryocooler with instrumentation.

Test Instrumentation. We detected the presence or absence of flow blockage in the cold head by gas flow meters. We calibrated these flow meters to  $\pm 5\%$  of the flow through the cold head. Pressure transducers were installed to check the health of the system. Pressure and temperature sensors were also installed since this information is needed to interpret the flow meter readings.

Results. The test was run continuously for over 3300 hours. We saw no detectable change in gas flow downstream of the J-T valves throughout this period, indicating no detectable blockage or loss of cooling performance. This means that the purifier worked as required. We can extrapolate the system's acceptability for multi-year missions by observing that the J-T valve heaters would be required to operate very infrequently, or not at all.

## CONCLUSION

The contamination control approach used on the Ball J-T cryocooler has been shown to be valid for multi-year operation. A flight worthy model is currently under design and three units will be extensively tested over the next several years.

PHASE EQUILIBRIA IN CRYOGENIC MIXTURES

Lawrence B. Robinson  
Department of Chemical Engineering  
University of California, Los Angeles  
Los Angeles, CA 90024-1592  
and  
BEI Electronics Company  
Sylmar, California 91342

INTRODUCTION

An important aspect of the design of cryocoolers is the understanding of the thermodynamics of fluid-solid equilibria (involving mixtures) at low temperatures. Helpful analyses of the relevant phenomena have been provided by Maytal, Van Sciver and McMahon, by J. T. Jones, by W. Little, as well as authors of textbooks, e.g. S. Sandler and S. Walas.

One problem is that a large refrigeration effect is desired, which requires a cryogen having a high boiling temperature. At the same time, a low boiling fluid is required to achieve the needed low operating temperature at atmospheric pressure of the cryocooler. Another problem is that solids may be formed in fluids having otherwise desirable properties; hence the piping of the fluid would be brought to a halt. Hence a magic gas is required, consisting of a proper mixture of high and low boiling cryogens, having the requisite solubility properties. Hence one obtains (a) a high refrigeration effect, (b) a low operating temperature, and (c) no solids. It is evident that the subject of the thermodynamics of mixtures is very important in the above context.

Only a few remarks will be made at this time regarding the background for the analysis relating to the main aspects of the problem. It is clear that some combination of theoretical and experimental work is required in order to achieve some workable solution. The theoretical analyses rest very heavily upon macroscopic concepts and computer programs. Previously discussed thermal equations of state (e.g., van der Waals, compressibility, BWR, Peng-Robinson) and caloric equations (e.g., heat capacity information) play significant roles. The computer codes

to be used represent the culmination of the work of many individuals, groups, and organizations. The two interactive programs to be used in the analysis have the names DDMIX and JTMIX. The first named code, DDMIX (prepared at NIST, formerly NBS) deals largely with the relationships among various thermodynamic properties. The second code JTMIX (prepared at JPL) deals with the manner in which the separate properties of the members of a mixture relate to the overall refrigeration effect provided by the mixture.

The main problem to be dealt with in connection with cryocoolers has many different aspects. Nevertheless, the problem can be (relatively) simply stated, viz.: Relate (a) the mixture of cryogens, (b) the initial (pre-cool) temperature and initial pressure, (c) the exit temperature at atmospheric pressure, (d) mass flow rate, and (e) the refrigeration effect. Some of the above are interrelated. The specific problem must be clearly stated, however. Perhaps the major problems with which one has to deal are (a), (b), and (c).

In this article the sole problem which will be discussed is the role of phase equilibria in the selection of a refrigerant. In preparing a refrigerant for our purposes, the following points (among others) should be noted. The refrigerant must have properties that can produce a low temperature, a large refrigeration effect, no solids to block the flow of the fluid, and low (or no) toxicity. It is evident that a mixture of cryogens is required in that conflicting properties of materials are needed (e.g., low temperature and no resulting solids).

Based on the large effort which has already been made in this regard, we consider a system that is a mixture of hydrocarbons to be used as the operating fluid refrigerant. However, many candidates which have otherwise suitable properties, freeze in the operating temperature range. In this temperature range, nitrogen is a liquid, serving as a possible solvent for the solidified hydrocarbons. Neon remains in the vapor phase throughout the operating temperature range, and probably will not provide much help with solubility problems. Therefore, a mixture of nitrogen, methane, ethane and propane has been chosen for analysis as the operating refrigerant. A method of selecting an "optimal" mixture will now be described briefly.

The first step in the process is the determination of the maximum solubility (saturation mol fraction) of the various cryogens (separately) in binary mixtures with liquid nitrogen. This gives the ratio of hydrocarbon to nitrogen (solute to solvent ratio) in the binary solution. It is generally accepted that the addition of other solutes to a saturated binary solution, does not alter significantly the solute to solvent ratio. Having obtained these three ratios separately, we then use them for the determination of the maximum of each of the three hydrocarbons in the four component mixture.

The algorithm to be presented consists of the following steps.

- (I) The maximum solubility of methane in nitrogen (i.e. mol fraction ratio) is followed by a determination of the maximum solubility of ethane in nitrogen and then by the same parameter for propane in nitrogen. These ratios provide a starting point for determining a blend of the four constituents in the desired temperature range, so that no solids will form. The second part of the algorithm consists of one of two procedures, both of which will be discussed in some detail.
- (II) One procedure is to use the above ratios to calculate the mol fraction of methane when the other components are specified. All of the mol fractions might not add up to 100%. Repeat the same type of calculation with ethane and then with propane. Repeat the iterations until consistency is obtained.
- (III) An alternate procedure is to solve the four relevant nonlinear equations, simultaneously. The procedure, like many types of approximations, is also an iterative one. Here the technique discussed by N. V. Kopchenova and I. A. Maron (Computational Mathematics) is implemented.

## OVERVIEW

### I. General

There are four temperature ranges of interest which relate to the system consisting of nitrogen, methane, ethane, and propane. The ranges are: (I)  $90 < T < 325$ , (II)  $77 < T < 90$ , (III)  $63 < T < 77$ , and (IV), below 63. All of the temperatures are in degrees Kelvin and the region boundaries are approximate.

In region I, the hydrocarbons are liquid and nitrogen is the vapor phase. There is no problem with respect to flow but the full effect of nitrogen has not yet been obtained. Region II is especially bad as far as the flow of the cryogen is concerned. The hydrocarbons are in the solid state and nitrogen is still a vapor. Nitrogen offers very little effect as far as solubility is concerned and it seems almost a certainty that blockage to flow will occur in this range. In temperature region III nitrogen has become liquified and the solid hydrocarbons are soluble in nitrogen in varying degrees.

It is desirable to have the low temperature of the cryocooler in the range III. The low temperature aids the refrigeration effect and also provides the opportunity for the dissolving of the solid hydrocarbons in liquid nitrogen. Passing from range II to III could re-establish the flow, which will probably choke when we have only solids and vapor. Region IV is to be avoided since all components can solidify.

## II. Single Nonlinear Equations

First we shall determine the maximum solubility (as a function of temperature) in liquid nitrogen of each solid hydrocarbon. These studies will provide some guidance as to the desirable ratios of the constituents in the mixture. For example, if we determine the maximum solubility of methane in nitrogen (at a given temperature) we would not exceed this ratio in the operating mixture. The same goes for each of the other constituents.

The procedure is as follows. Nitrogen will be designated as component 1, with methane, ethane, and propane designated 2, 3 and 4 respectively. The maximum solubility, or saturation mole fractions of the hydrocarbons are designated  $x_2$ ,  $x_3$  and  $x_4$  (in the binary solutions) with  $x_1$  being the nitrogen mol fraction.

The maximum saturation mol fractions  $x_2$ ,  $x_3$  and  $x_4$ , each in a binary solution with nitrogen as the other component, are determined by a procedure to be detailed later. The ratios  $x_2/x_1$ ,  $x_3/x_1$  and  $x_4/x_1$  are determined in turn. Recall that these ratios are determined for binary solutions. In a multicomponent system, the ratio of methane to nitrogen would be no larger than the  $x_2/x_1$  already determined for the binary system. It is highly unlikely that the addition of other solutes

will increase the solubility of methane. The same goes for ethane and propane.

The operating solution is prepared according to the following scheme. Since  $x_2/x_1$ ,  $x_3/x_1$  and  $x_4/x_1$  are known, we have (for the multicomponent system)

$$\frac{x_2}{x_1} + \frac{x_3}{x_1} + \frac{x_4}{x_1} = K, \quad (1)$$

where the value of  $K$  is also determined. It follows that

$$x_2 + x_3 + x_4 = Kx_1 \quad (2)$$

Because,

$$x_1 + x_2 + x_3 + x_4 = 1 \quad (3)$$

we can combine the last two equations, and get

$$x_1 = 1/(1 + K). \quad (4)$$

Hence the composition of the desired solution is determined, since the pertinent ratios are known.

It is evident that this procedure will not produce an exact solution to our problem, but we do have some reliable guidelines so that the method for selecting the composition can be refined. We shall now demonstrate the use of the method.

In the last approach to the solution to the problem, we begin by obtaining the saturation mole fraction (maximum solubility) of each methane, ethane, and propane in a binary solution with liquid nitrogen. The set of equations to be used in obtaining the saturation mole fraction,  $x_2$ , is given immediately below. The symbol  $\delta_2$  is the solubility parameter for component 2 and  $\delta_m$  is the average or mean solubility parameter for all of the components. More will be said about  $\delta_m$  shortly. A few remarks will now be made regarding the calculation procedures.

*If we have a mixture of several components, for example components A, B, and C and we desire the maximum solubility of component D in this blend. We can represent the constituent mol fractions as  $x_A$ ,  $x_B$ ,  $x_C$ , and  $x_D$ , respectively or we can relate each of the mol fractions of*

*the original components to the mol fraction of D. The first representation gives us four nonlinear equations in four unknowns to be solved simultaneously. The second representation gives four separate nonlinear equations, each in only one unknown; the solutions of these separate equations are then interrelated. We shall consider the latter and better known representation first.*

We proceed in the following manner for the case in which all mole fractions are to be related to the one whose solubility is sought. Consider a blend of the following composition: (20% A, 50% B, and 30% C). When D is added to the mixture, the mol fractions of A, B, and C can be represented as follows:

$$x_A + x_B + x_C + x_D = 1$$

$$x_B/x_A = 0.5/0.2, \quad x_C/x_A = 0.3/0.2, \quad x_B/x_C = 0.5/0.3$$

Thus

$$x_A(1+2.5+1.5) + x_D = 1$$

or

$$x_A = 0.20(1-x_D)$$

Also

$$x_B \left( \frac{0.2}{5} + 1 + \frac{0.3}{5} \right) + x_D = 1$$

or

$$x_B = 0.50(1-x_D)$$

And

$$x_C(0.67 + 0.67 + 1) + x_D = 1$$

$$x_C = 0.30(1-x_D)$$

This is the manner in which all of the components are related to the one whose solubility is sought, i.e., D.

$$x_2 = \exp \left\{ - \left[ \frac{\Delta H_f}{R} \left( \frac{1}{T} - \frac{1}{T_m} \right) + \frac{V_2}{RT} (\delta_2 - \delta_m)^2 \right] \right\} \quad (5)$$

or

$$x_2 = \exp \left[ - \frac{\Delta H_f}{R} \left( \frac{1}{T} - \frac{1}{T_m} \right) - \frac{V_2}{RT} (\delta_2 - \delta_m)^2 \right] \quad (6)$$

or

$$x_2 \exp \left[ \frac{V_2}{RT} (\delta_2 - \delta_m)^2 \right] = \exp \left[ - \frac{\Delta H_f}{RT} + \frac{\Delta H_f}{RT_m} \right] \quad (7)$$

Equation (6), or any of its equivalents can be solved simply by the technique shown in Fig. 1. Of course, a computer solution is easily implemented.

We can rewrite Eq. (7) as

$$\ln x_2 + \left[ \frac{V_2}{RT} (\delta_2 - \delta_m)^2 \right] = \frac{\Delta H_f}{RT_m} - \frac{\Delta H_f}{RT} \quad (8)$$

or

$$\ln x_2 + \frac{V_2}{RT} (\delta_2 - \delta_m)^2 = Q_m - Q \quad (9)$$

where

$$\delta_m = \frac{\sum_i x_i V_i \delta_i}{\sum_i V_i \delta_i} \quad (10)$$

We can solve Eq. (5) for  $T$  and get a direct relationship between temperature and maximum solubility of the component represented by  $x_2$ .



$$T = E/F, \quad (11)$$

where

$$E = \frac{\Delta H_f}{R} + \frac{V_2}{R}(\delta_2 - \delta_m)^2 \quad (12)$$

and

$$F = \frac{\Delta H_f}{RT_m} - \ln x_2. \quad (13)$$

Some comments are required to clarify the meaning of the symbol  $\delta_m$  in Eq. (10). In order to determine the saturation mol fraction of methane in the mixture of nitrogen, ethane and propane we proceed as follows. Conceptually, we prepare a mixture of these three solvents with the previously assigned ratios. From Table II, the solvent blend contains 0.37 nitrogen, 0.075 ethane and 0.075 propane. As one begins to add methane to the solvent blend the mol fractions are written as below.

$$x_1 = 0.712(1 - x_2) \quad \text{nitrogen} \quad (14)$$

$$x_3 = 0.144(1 - x_2) \quad \text{ethane} \quad (15)$$

$$x_4 = 0.144(1 - x_2) \quad \text{propane} \quad (16)$$

where  $x_2$  is the mol fraction of methane. The numbers are the fractions of the specific component in the original solvent blend. Note that for all values of  $x_2$ ,

$$x_1 + x_2 + x_3 + x_4 = 1. \quad (17)$$

Equations (14), (15) and (16) allow us to write  $\delta_m$  in terms of the one variable  $x_2$ . Finally, Eq. (8) has only the one variable  $x_2$  in it. The form which  $\delta_m$  takes is

$$\delta_m = \frac{A + Bx_2}{C + Dx_2}. \quad (18)$$

Equation (10) gives the averaged value of the solubility parameters  $\delta$ ; the equation is valid for

a binary solution or one with more than two components. Special forms for the solubility parameter  $\delta_m$  are given in Eqs. (14) through (18). All of the mole fractions are given in terms of the constituent whose solubility is desired, in this case it is  $x_2$  by definition.

The results are summarized in the two graphs. The first graph shows  $x_2$  (vertical axis) vs.  $T$  (horizontal axis). The numerical values are estimates from the Tables. The second graph shows  $T$ , the temperature at which a maximum solubility  $x_2$  is obtained vs.  $x_2$  on the horizontal axis. The results are obtained from a direct solution of Eq. (13). In both cases, the results are confined to region III, already discussed in the beginning. Calculated values of the solubilities are shown in Table II. Equations (5) through (13) are used in the calculations. Theoretically we should be able to vary  $x_2$  between 77 K and 67 K with a mixture shown in the Table. In suggesting a mixture for actual use, we increased the amount of nitrogen, and decreased the amounts of the other constituents accordingly.

### III. Simultaneous Nonlinear Equations

The other procedure involves a technique for the solution of a set of simultaneous nonlinear equations. The equations, obtained from Eqs. (2) and (6). They are

$$F_1 = x_1 + \sum_{i=2}^N x_i - x_1(1 + K) \quad (19)$$

$$F_2 = x_2 - \exp u_2(x_1, \dots, x_N) \quad (20)$$

$$F_j = x_j - \exp u_j(x_1, \dots, x_N) \quad j \neq 1 \quad (21)$$

$$\frac{\partial F_j}{\partial x_k} = \delta_{jk} - \exp u_j(x_1, \dots, x_N) \frac{\partial u_j}{\partial x_k} \quad (22)$$

$$j = 2, 3, \dots; k = 1, 2, 3, \dots$$

The kronecker delta is  $\delta_{jk} = \begin{cases} 0 & \text{if } j \neq k \\ 1 & \text{if } j = k \end{cases}$

$$u_j = -\frac{\Delta H_j}{R} \left( \frac{1}{T} - \frac{1}{T_j} \right) - \frac{V_j}{RT} (\delta_j - \delta_m)^2 \quad (23)$$

$$\frac{\partial u_j}{\partial x_k} = \frac{2V_j(\delta_j - \delta_m)}{RT} \frac{\partial \delta_m}{\partial x_k} \quad (24)$$

By a method of cyclic permutation, viz.,  $1 \rightarrow 2 \rightarrow 3 \rightarrow 4 \rightarrow 1$ , we can utilize the following set of equations,

$$\frac{\partial \delta_m}{\partial x_i} = \frac{V_i[x_{i+1}V_{i+1}(\delta_i - \delta_{i+1}) + x_{i+2}V_{i+2}(\delta_i - \delta_{i+2}) + x_{i+3}V_{i+3}(\delta_i - \delta_{i+3})]}{(\sum_j x_j V_j)^2} \quad (25)$$

A solution of the set of nonlinear equations can be obtained by a method known as Newton's method. We begin with the equations to be solved, written symbolically as

$$\left. \begin{aligned} F_1(x_1, x_2, \dots, x_N) &= 0 \\ F_2(x_1, x_2, \dots, x_N) &= 0 \\ F_N(x_1, x_2, \dots, x_N) &= 0 \end{aligned} \right\} \quad (26)$$

$$\mathbf{x} = \begin{bmatrix} x_1 \\ x_2 \\ \dots \\ x_N \end{bmatrix} \quad (27)$$

$$\mathbf{F} = \begin{bmatrix} F_1 \\ F_2 \\ \dots \\ F_N \end{bmatrix} \quad (28)$$

Equation (26) can be written more simply

$$\mathbf{F}(\mathbf{x}) = 0 \quad (29)$$

Also

The inverse of  $\mathbf{W}(\mathbf{x})$ , which is written as  $\mathbf{W}^{-1}(\mathbf{x})$ , is used in obtaining approximate solutions to

$$W(x) = \begin{bmatrix} \frac{\partial F_1}{\partial x_1} & \frac{\partial F_1}{\partial x_2} & \dots & \frac{\partial F_1}{\partial x_N} \\ \frac{\partial F_2}{\partial x_1} & \frac{\partial F_2}{\partial x_2} & \dots & \frac{\partial F_2}{\partial x_N} \\ \dots & \dots & \dots & \dots \\ \frac{\partial F_N}{\partial x_1} & \frac{\partial F_N}{\partial x_2} & \dots & \frac{\partial F_N}{\partial x_N} \end{bmatrix} \equiv \left( \frac{\partial f_i}{\partial x_j} \right) \quad (30)$$

Eq. (26). The set of solutions is written as

$$x^{(p+1)} = x^{(p)} - W^{-1}(x^{(p)})F(x^{(p)}) \quad (31)$$

$$p = 0, 1, 2, 3, \dots$$

Step 1. Find the  $x^{(p)}$  vector, i.e. find  $x_1, x_2, x_3, \dots$  for the 0th approximation. Put these values into the matrix  $W$  and get  $W(x^{(p)})$ . Now find the inverse matrix, i.e.  $W^{-1}(x^{(p)})$ . Now this inverse matrix is multiplied by the vector  $F(x^{(p)})$  and we get (by definition for  $\epsilon^{(p)}$ )

$$-\epsilon^{(p)} = W^{-1}(x^{(p)})F(x^{(p)}) \quad (32)$$

Hence we obtain

$$x^{(p+1)} = x^{(p)} + \epsilon^{(p)}, \quad (33)$$

or

$$x^{(p+1)} = x^{(p)} - W^{-1}(x^{(p)})F(x^{(p)}) \quad (34)$$

Step 2. The new  $x^{(p)}$  are used in Eq. (30) in order to calculate the new matrix  $W$ . The inverse matrix  $W^{-1}$  is now re-calculated from which the  $x^{(p+2)}$  are calculated.

Step 3. The process is repeated until previously assigned convergence criteria are met.

Examples now follow.

The preceding analysis provides an exploratory technique for the evaluation of phase equilibria. Two systems were examined, the first one was a blend of nitrogen, methane and propane; the second one was a four component system which included ethane. One difficulty in the application of the technique results from the frequent occurrence of sums and differences of numbers having values nearly the same. Also it has not been established how reliable the technique is when two or more of the mol fractions have the same (or close to the same) value.

For the system with only three components, the analysis was successful. Analysis based on the graphs and Eq. (11) suggested that the saturation mol fractions are 0.275, 0.613 and 0.112 for nitrogen, methane and propane, respectively. Three iterations involving Eq. (...) yielded 0.282, 0.703 and 0.089. The initial set of values was arbitrarily taken to be 0.282, 0.630 and 0.088. The analysis involving four components was unsuccessful; it is to be noted that our "actual" values for ethane and propane are identical.

#### SUMMARY

The topic of phase equilibria involving multicomponent systems has been discussed with emphasis on cryogenic materials. Our conclusions are that Eq. (11) provides the most simple, direct and reliable basis for predictions. Equations (5) through (10), actually the content of Eq. (11) in a more complicated form provide the next most reliable basis of analysis. However, the nonlinear analysis, as provided by Eqs. (19) through (34) are probably closer to the physical representation in that they are simultaneous equations. More development along these lines will quite likely yield important results.

Table I. Parameters Used in the Calculations

		V (cm) <sup>3</sup>	$\delta$ (joule/cm <sup>3</sup> ) <sup>1/2</sup>	T <sub>m</sub> (K)	$\Delta H_f$ (joule/mol)
I					
x <sub>1</sub> = 0.37	N <sub>2</sub>	38.1	10.84		
x <sub>3</sub> = 0.075	C <sub>2</sub>		12.38		
x <sub>4</sub> = 0.075	C <sub>3</sub>	84	13.09		
x <sub>2</sub> → C <sub>1</sub>		52	11.62	90.7	941
II					
x <sub>1</sub> = 0.37	N <sub>2</sub>	38.1	10.84		
x <sub>3</sub> = 0.48	C <sub>1</sub>	52	11.62		
x <sub>4</sub> = 0.075	C <sub>3</sub>	84	13.09		
x <sub>2</sub> → C <sub>2</sub>		68	12.38	89.9	2859
III					
x <sub>1</sub> = 0.37	N <sub>2</sub>	38.1	10.84		
x <sub>3</sub> = 0.48	C <sub>1</sub>	52	11.62		
x <sub>4</sub> = 0.075	C <sub>2</sub>	68	12.38		
x <sub>2</sub> → C <sub>3</sub>		84	13.09	85.5	3524

Table II. Some Saturation Mol Fractions

T = 68 K		
Binary Solutions		
x-methane		0.65
x-nitrogen		0.35
x-ethane		0.25
x-nitrogen		0.75
x-propane		0.25
x-nitrogen		0.75
	Calculated*	Suggested**
x-nitrogen	0.28	0.37
x-methane	0.53	0.48
x-ethane	0.0945	0.075
x-propane	0.0945	0.075

\*See Equations (5)-(13)

\*\*Values are suggested so as to allow for margin of error.

Stanley M. Walas, Phase Equilibria in Chemical Engineering, Butterworth Publishers, Stoneham, MS, 1985, pp. 397-404.

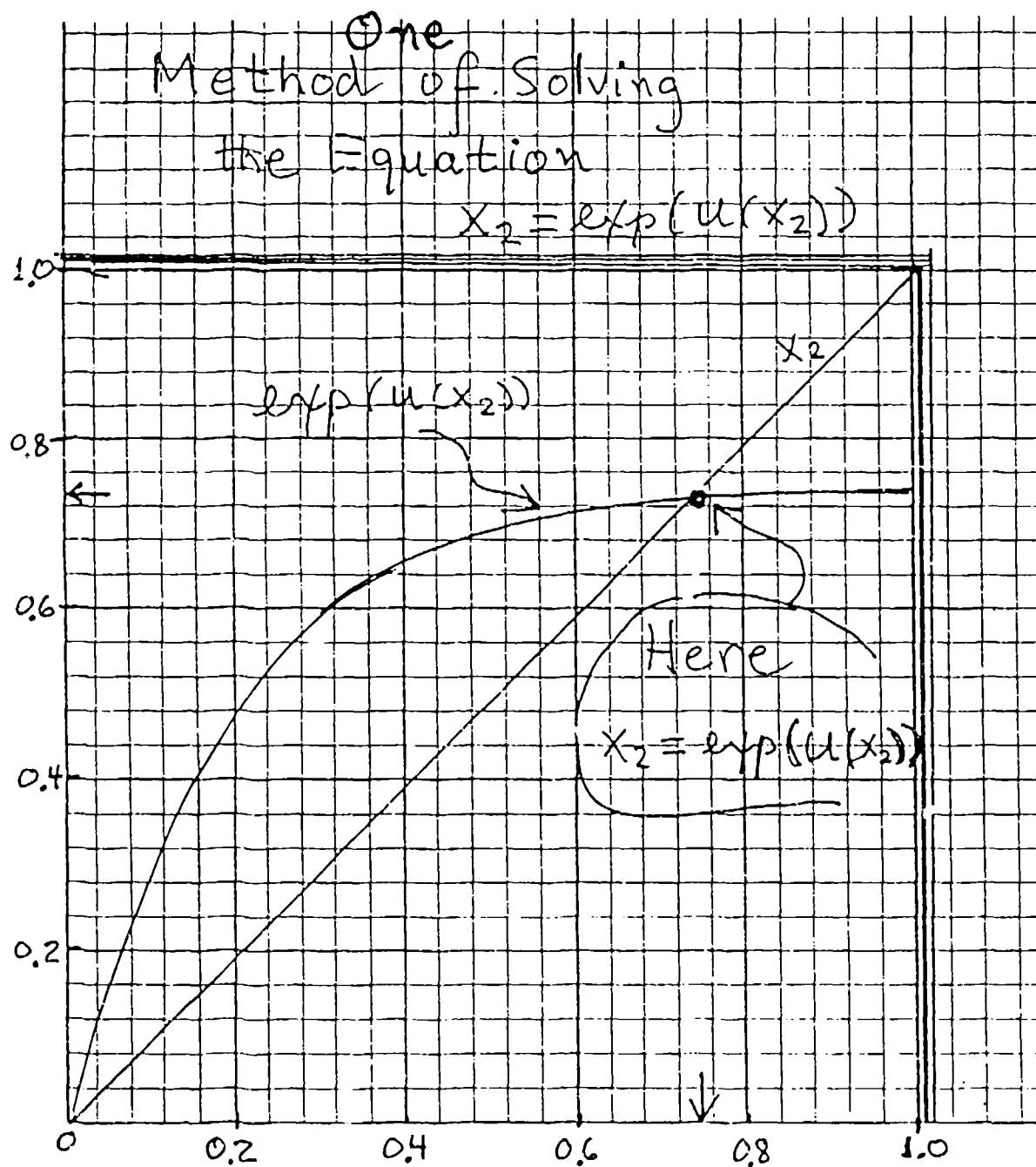
Stanley I. Sandler, Chemical and Engineering Thermodynamics, Second Edition, John Wiley & Sons, New York, 1989, pp. 460-468.

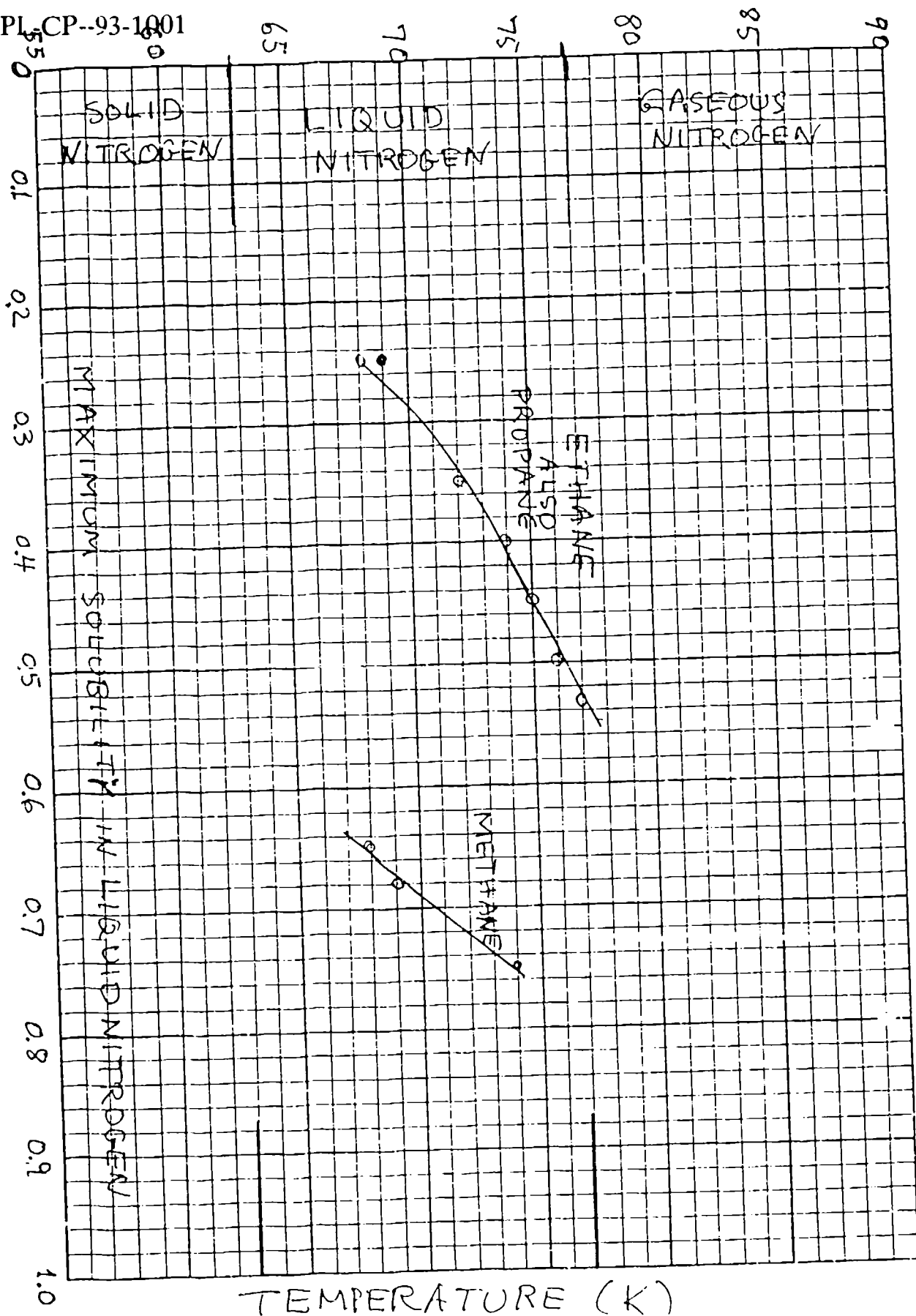
Michael R. J. Dack, Editor, Solutions and Solubilities, Part II, John Wiley & Sons, New York, 1976, pp. 48-53 (Charles A. Eckert).

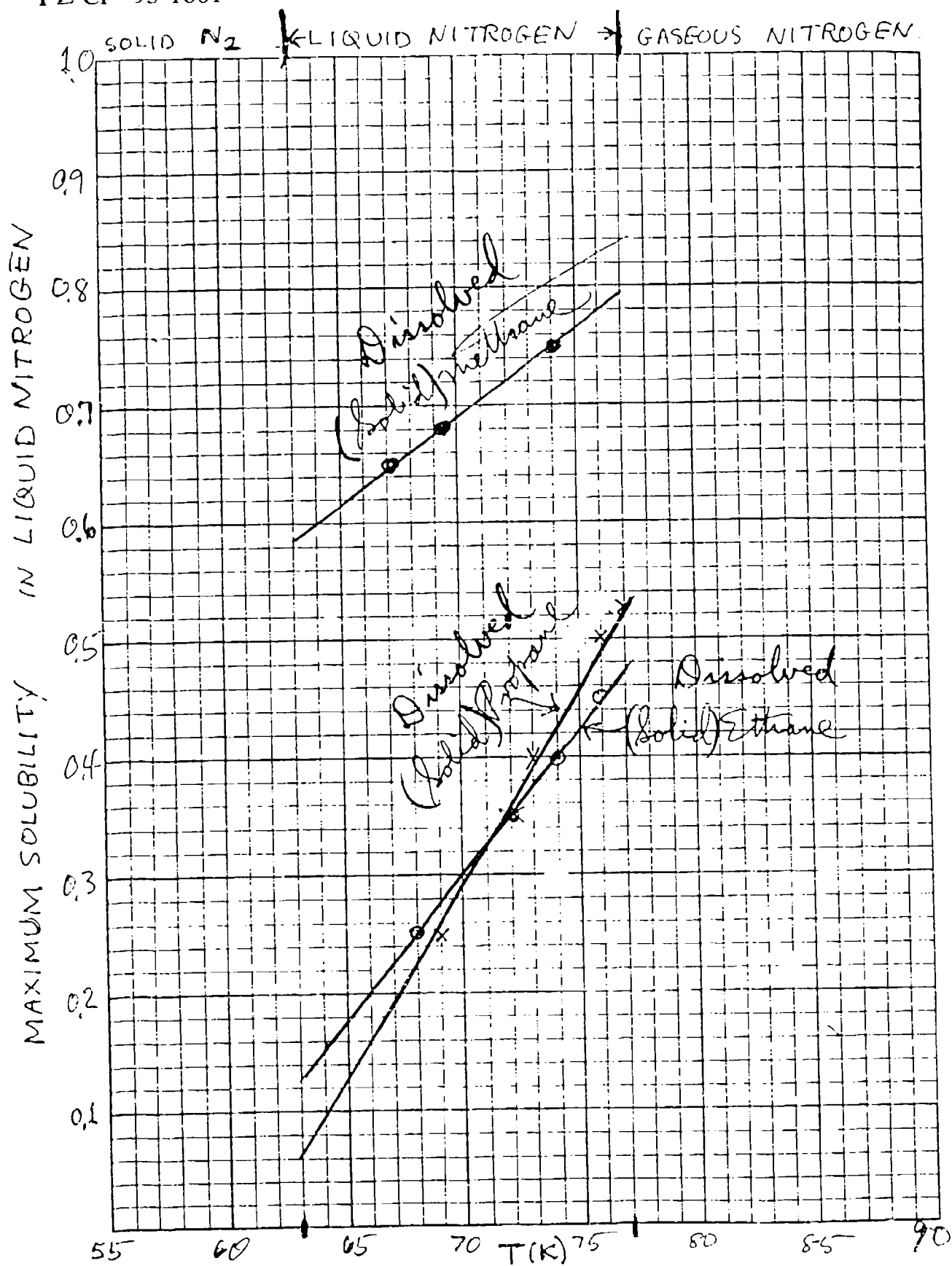
Truman S. Stornik and Stanley I. Sandler, Editors, Phase Equilibria and Fluid Properties in the Chemical Industry, American Chemical Society, Washington, D.C., 1977, pp. 189-194 (Stanley B. Adler et al.).

B. G. Kyle, Chemical and Process Thermodynamics, Prentice-Hall, Englewood Cliffs, NJ, 1992, pp. 304-317.









INCORPORATING A MECHANICAL REFRIGERATOR WITH A REFREEZABLE  
CRYOGEN IN SPACE APPLICATIONS

Brian G. Williams<sup>1</sup> and J. Clair Batty<sup>2</sup>

Utah State University

Logan, UT 84322-4130

ABSTRACT

This paper examines the concept of incorporating a small mechanical cooler along with a relatively small quantity of solid cryogen into the cooling system of spacecraft borne instruments which operate with a duty cycle less than 100%. The relatively high operational heat loads would be absorbed by the latent heat of fusion of the cryogen as it melts. The refrigerator could be turned off during the instrument operational period to eliminate vibrations and turned on as necessary to refreeze the cryogen during the instrument's quiescent period. Because the refrigerator need not be sized to meet the peak heating loads during instrument operation, it can be downsized and have lower mass and input power requirements. The paper also examines the concept of using one or more mechanical coolers to enhance the long-term storage of cryogens in space. A computer code, written at USU simulating the freezing and melting of the cryogen, is used in the evaluation of these two concepts. The paper concludes that the integrated cooler system eliminates vibration concerns during instrument operation and allows the sensor heat loads to exceed the cooling capacity of the refrigerator. Also, there is a significant mass and lifetime advantage in using the refreezable cryostat as compared to a standard expendable solid cryogen (sublimation to space).

---

<sup>1</sup> Graduate student, Department of Mechanical and Aerospace Engineering.

<sup>2</sup> Professor, Department of Mechanical and Aerospace Engineering.

INTRODUCTION

An increasing number of spacecraft borne instruments require cryogenic cooling to reach mission objectives. Some applications of these instruments are earth observation; gamma ray, X-ray, and infrared astronomy; military space surveillance; and interplanetary missions. One reason these instruments require cooling to cryogenic temperatures is that the detectors are more sensitive at lower temperatures. Also, it is desired that the thermal-radiation noise from the instrument itself not interfere with the incoming electro-magnetic radiation from the target. Two common types of cryogenic coolers are mechanical refrigerators and stored cryogens.

There are several problems associated with using these two types of coolers. Refrigerators generally require relatively large amounts of input power in order to produce large cooling capacities at cryogenic temperatures. Also, during operation, some refrigerators produce a level of vibration which can seriously interfere with the operating performance of an instrument. The lifetime of mechanical refrigerators is limited based upon the wear or fatigue of their mechanical components.

The lifetime of a stored cryogen cooler is limited based upon the amount of cryogen stored. After the cryogen has been totally vaporized (liquid cryogens) or sublimated (solid cryogens), the instrument becomes useless because the cooler can no longer maintain the instrument within its desired temperature range. It has been shown by Schick<sup>(1)</sup> that the amount of cryogen stored is limited due to the restrictions imposed by parasitic heat loads for large dewar sizes.

A possible resolution to reduce the vibration and lifetime problems associated with mechanical and stored cryogen coolers is the concept of the refreezable solid-cryogen cooler. This paper

presents the functional concept of the cooler, and its possible utilization to scenario applications.

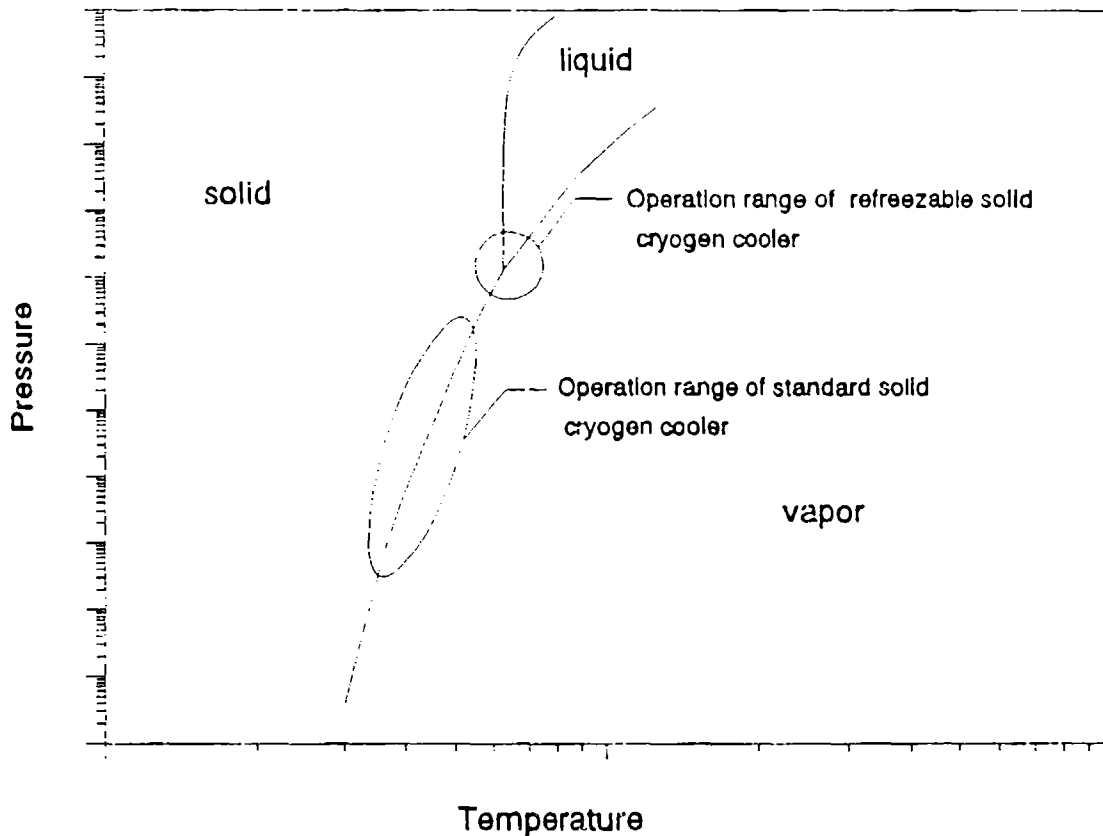


**Figure 1.** Temperature-pressure diagram of the operating range for the refreezable solid-cryogen cooler versus that of a sublimating solid cryogen.

#### CONCEPT

The basic concept of the cooler is to operate around the triple-point of a cryogen (see Figure 1). The instrument and parasitic heat loads would be absorbed by the cooler system by melting the cryogen from solid to liquid. As the cryogen is melting across the triple-point, the temperature and pressure must remain constant. Therefore, there is no need to vent excess vapor to space in order to maintain the cryogen within its desired temperature range. This implies a closed cryogen system. This is an important feature of the concept because the mass of the

cryogen remains constant inside of the dewar. Thus, mission life is independent of the mass of cryogen.

The amount of heat which can be absorbed by the cooler system during one operational cycle will depend upon the mass of cryogen stored and the cryogen's heat of fusion. The heat of fusion may be taken as the difference between the heat of sublimation and the heat of vaporization at the triple-point of the cryogen. By specifying the mass of solid cryogen needed, the instrument operation time can be defined. Conversely, by specifying the operational time of the instrument, the mass of cryogen required is defined.

After the cryogen has melted, the instrument will be shut off and a refrigerator will be turned on. The refrigerator's job is to refreeze the cryogen back across the triple-point. As soon as all of the cryogen has been refrozen, the refrigerator will be turned off and the instrument will then be available for another cycle of operation. The amount of time required to refreeze the cryogen is a very important factor in deciding the feasibility of using this cooler concept because the time to refreeze directly effects the instrument's non-operational time period. The refreeze time of the cryogen is dependent upon the amount of cryogen which must be refrozen and the cooling capacity of the refrigerator.

The cryogen section is composed of a cryogenic dewar which is thermally linked to the cold-finger of the refrigerator. The dewar will contain some form of a metal-foam heat exchanger (such as aluminum or copper) in which the liquid cryogen can be poured into before it is frozen. The metal foam serves the purpose of keeping the cryogen's temperature as uniform as possible. It also allows the solid cryogen to keep in contact with the heat exchanger so that the cryogen will not shrink away once it starts melting. Possible additions to the dewar design could include connecting the external shell to a passive radiator in order to

reduce the temperature of the outside surface, minimal heat-leak optimization of structural supports, and an optimization to determine the number of radiation shields.

It is assumed that the inactive refrigerator could be thermally unlinked from the cryogen while the instrument is in operation. For example, a gas-gap heat switch could be used. With this heat switch, a small amount of a given gas is injected into a gap completing the thermal link during refrigerator operation. To disconnect the link during instrument operation, the gap is opened to space and the gas is evacuated.

**Table 1**  
Preliminary Refrigerators for the Conceptual Design.

ID	Cooler Name	Type
1	British Aerospace <sup>[3,4,5]</sup>	Stirling
2	Centre d'Estudes Nucléaires, France <sup>[6]</sup>	Vuilleumier
3	Creare <sup>[7,8]</sup>	Brayton
4	CTI Cryogenics CM-1 <sup>[9]</sup>	Stirling
5	CTI Cryogenics CM-3 <sup>[9]</sup>	Stirling
6	Cryogenic Laboratory, Beijing, China <sup>[10]</sup>	Pulse-Tube
7	Hughes Hi Cap <sup>[11]</sup>	Vuilleumier
8	Hughes 77 Ms-1A <sup>[9]</sup>	Stirling
9	JPL CH <sub>4</sub> + PCO <sup>[12]</sup>	Sorption
10	JPL C/Xe + C/Kr + PCO <sup>[13]</sup>	Sorption
11	Lockheed/Lucas CCS 1000 <sup>[14]</sup>	Stirling
12	Lockheed/Lucas CCS 500 <sup>[14]</sup>	Stirling
13	Magnavox MX 7043 <sup>[15,16]</sup>	Stirling
14	Magnavox Magnetic Bearing <sup>[17,18]</sup>	Stirling
15	Mitsubishi/Electrotechnical Laboratory <sup>[19]</sup>	Vuilleumier
16	Philips Rhombic-Drive <sup>[20]</sup>	Stirling
17	Ricor K506B, Israel <sup>[21]</sup>	Stirling
18	USSR/SIAME Optimized <sup>[22]</sup>	Stirling

From a technology review of available refrigerators by Williams<sup>[2]</sup>, 18 preliminary refrigerators were chosen. These 18 refrigerators, their corresponding ID number, and their type are listed in Table 1. The reason these refrigerators are chosen is because of the availability of data on their refrigeration



capacity, input power required, and mass. All candidate refrigerators also have an operating temperature around 70 K.

By a comparison of the specific power, operating lifetime, specific mass, and amount of data available, the British Aerospace refrigerator is chosen for use with the cooler analysis. This refrigerator can supply 0.8 W of cooling at 80 K with a power consumption of 35 W and has a mass of 8.4 kg<sup>(3)</sup>. This results in a specific power of 43.75 W/W and a specific mass of 10.5 kg/W. The designed operating lifetime is three to five years<sup>(4)</sup>. Figure 2 shows a schematic diagram of the integrated mechanical cooler/stored cryogen system.

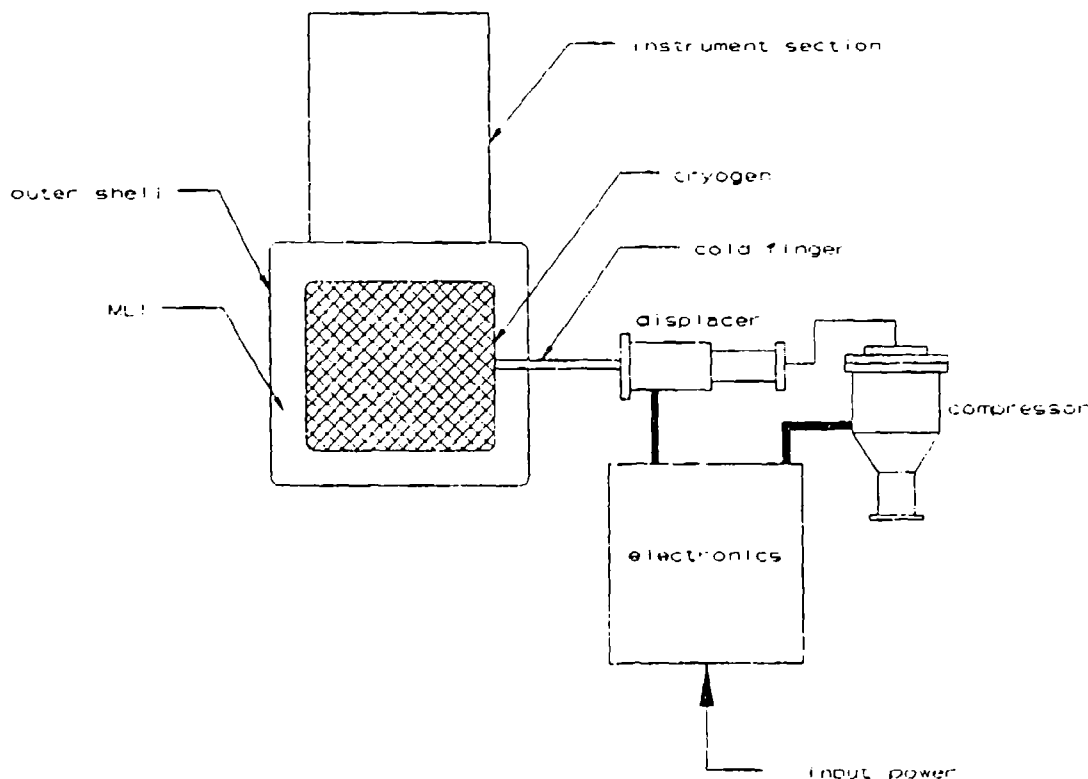


Figure 2. Schematic diagram of the mechanical cooler/cryogen system with relative sizing of refrigerator components.

For the cooler analysis, nitrogen was selected as the stored cryogen because a large number of space application refrigerators

currently available are designed to operate between 60 to 80 K. The triple-point temperature of nitrogen (63.152 K) falls within this range.

Computer code developed at Utah State University was used in the evaluation of the cooler concept. This code simulates the macroscopic freezing and melting processes of the cooler. An in depth description of the mathematical model and computer code was presented by Williams<sup>[2]</sup> and will not be discussed in this paper.

#### COOLING OF A SPACECRAFT BORNE INSTRUMENT

The instrument cooling mission chosen was the earth-limb viewing of an ICBM target. The target heat load and duration of look are similar to those expected with the SPIRIT III instrument on the SDIO MSX satellite<sup>[2]</sup>. Table 2 lists the baseline parameters for the mission scenario.

**Table 2**  
Baseline Parameters for Cooling of Instrument

Target Heat Load . . . . .	7.8 W
Parasitic Heat Load . . . . .	100 mW
Duration of Instrument Operation . .	23 minutes
Initial Ullage in Tank . . . . .	10%
Mass of Cryogen . . . . .	0.56 kg
Starting Temperature . . . . .	65 K
Minimum Temperature . . . . .	63.0 K
Maximum Temperature . . . . .	63.3 K
Refrigerator . . . . .	British Aerospace

The amount of cryogen required (m) was estimated from the equation

$$m = \frac{q_{\text{tot}} \Delta t_{\text{op}}}{h_{\text{sf}}} \quad (1)$$

where:

$q_{\text{tot}}$  = total heat load on cryogen in Watts

$\Delta t_{\text{op}}$  = operational time of instrument (duration of look) in seconds

$h_{\text{if}}$  = latent heat of fusion in J/kg.

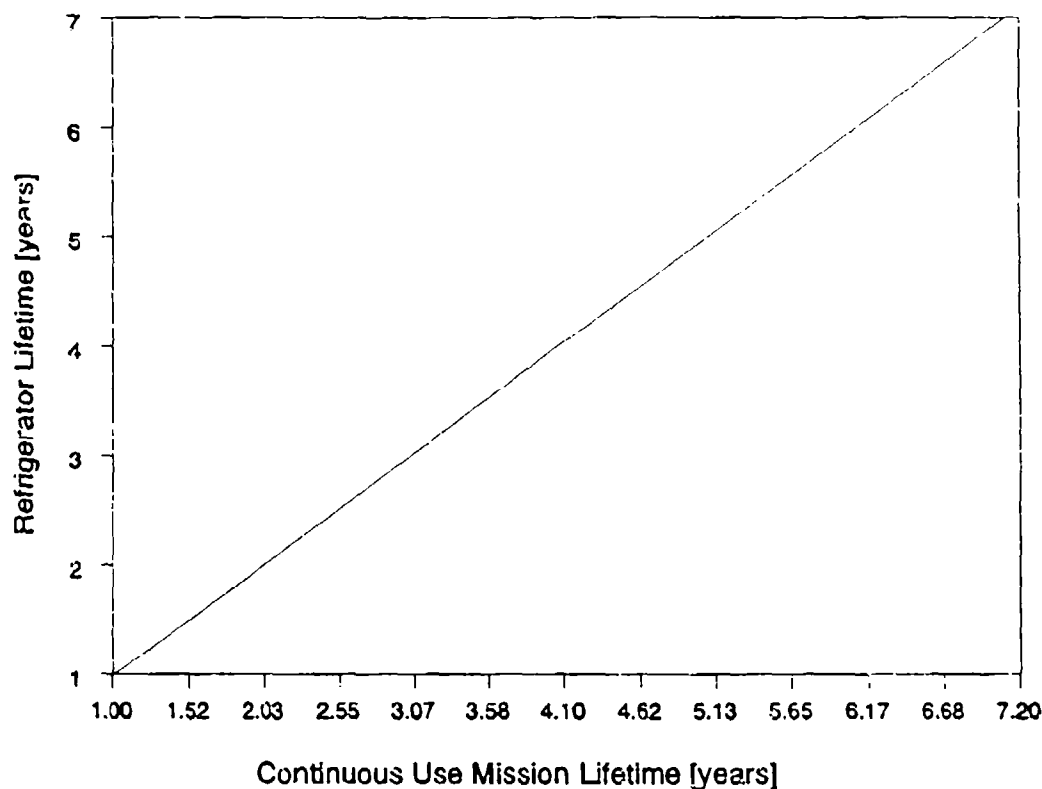


Figure 3. Continuous use mission lifetime versus refrigerator lifetime for the instrument cooling mission.

Figure 3 shows the relationship between continuous use mission lifetime and refrigerator lifetime. The continuous use mission lifetime refers to the total mission lifetime if the system is continuously cycled. This corresponds to the lifetime at the maximum duty cycle. The maximum duty cycle occurs when there is no idle time between refreeze of the cryogen and sensor operation. The maximum duty cycle with the British Aerospace refrigerator is approximately 1.5%, which corresponds to a time

of 25.7 hours to refreeze the given mass of cryogen. From this graph, the new cooler concept increases the mission lifetime by approximately 1.05 times as compared to just using a refrigerator alone.

One possible way to increase the mission lifetime would be to operate the instrument and cooler system at a lower duty cycle. For instance, if it is desired to use the instrument only once per week, then the refrigerator would have ample time to refreeze the cryogen. Also, if the refrigerator operates intermittently at longer interval periods, then the refrigerator lifetime would not have as large an impact on the total mission lifetime.

Another possibility would be to have more than one instrument/cooler system operating on board the spacecraft at the same time. For example, if there are four instrument/cooler systems on board, then the possibility could be four times greater that there would be an instrument ready for unexpected operation. Also, four instrument/cooler systems could increase the reliability of the overall system; if one failed, there would be three others to continue the mission.

Figure 4 shows the total available instrument operational time versus the continuous use mission lifetime. The total instrument operational time available refers to the amount of time that the instrument could be operated for the maximum duty cycle. From this graph, for every year of mission lifetime, there are 0.015 years available to operate the instrument. This is equivalent to about 22 minutes per day.

Figure 5 shows the relationship between mass of an equivalent lifetime sublimating solid cooler and the continuous use mission lifetime. The mass of an equivalent lifetime sublimating solid cooler refers to the amount of cryogen mass required if the cooler were to operate by sublimation. This value is calculated by using equation (1) and substituting the heat of sublimation at

the triple-point temperature in place of the latent heat of fusion. When the instrument is off,  $q_{tot}$  equals the parasitic heat load only and  $\Delta t_{op}$  is the time required to refreeze the cryogen. When the instrument is on,  $q_{tot}$  is the target heat load plus the parasitic heat load and  $\Delta t_{op}$  is the duration of the instrument's look. From this graph, a five-year mission would require a cryogen mass of 140 kg for a sublimating cooler.

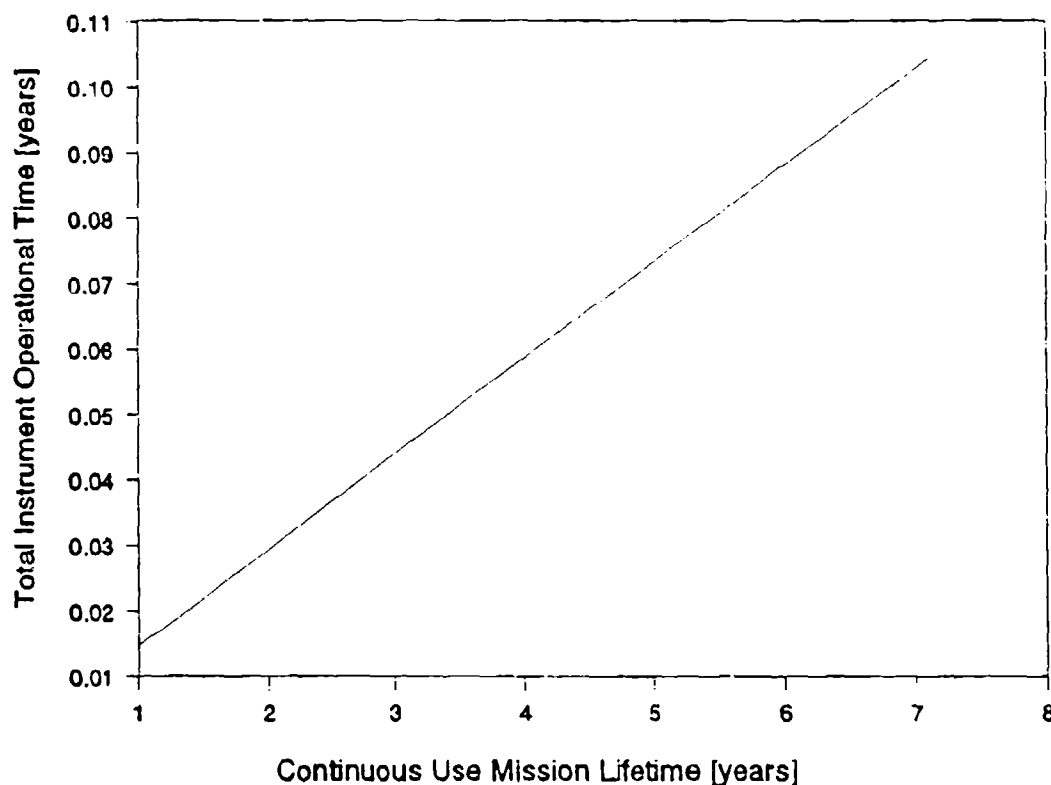


**Figure 4.** Continuous use mission lifetime versus available instrument operation time.

It should be noted that the calculations for Figure 5 did not include a varying parasitic heat load. A more realistic approach would be as the mass of cryogen increases, the tank size also increases, and consequently, the parasitic heat load increases. Therefore, an increased cryogen mass for a sublimating cooler

would result in a smaller increase in mission lifetime as compared to that shown in Figure 5.

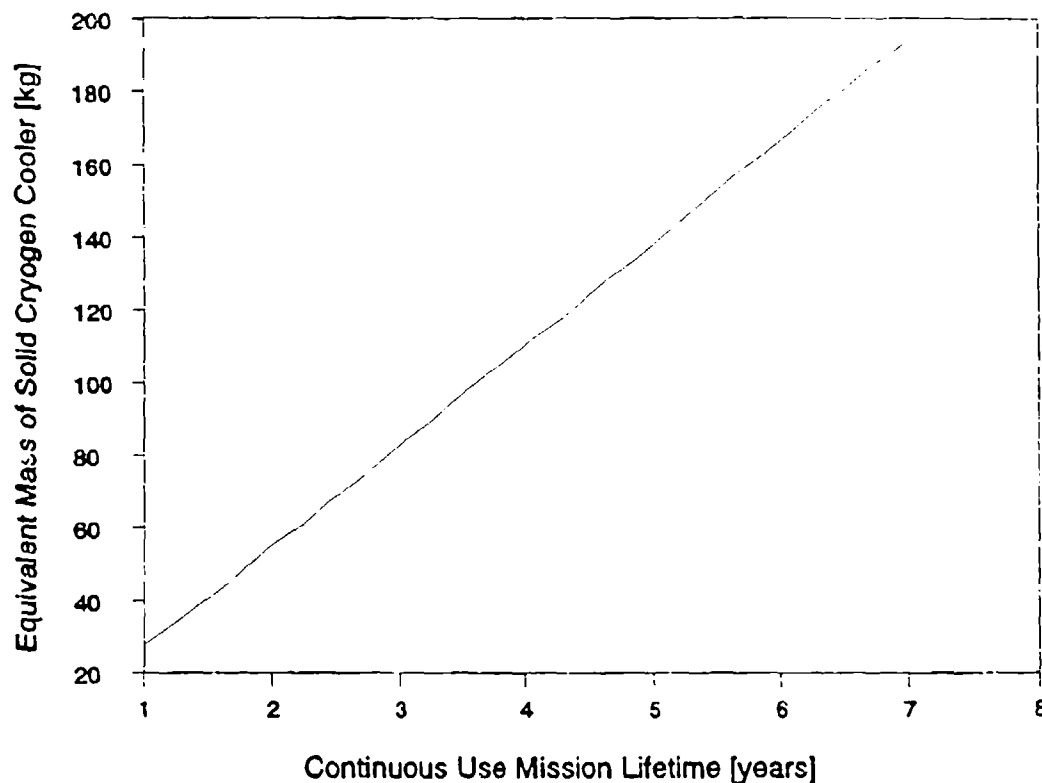


**Figure 5.** Continuous use mission lifetime versus mass of equivalent lifetime sublimating solid cooler for the instrument cooling mission.

Figure 6 shows the lifetime of an equivalent mass sublimating solid cryogen cooler versus the mass of the mechanical cooler/cryogen system. The mass of the British Aerospace cooler and the baseline amount of cryogen is 8.96 kg. From this graph, it is equivalent to a sublimating cooler lifetime of about 0.0085 years or about 3.1 days. It can also be implied from this graph that there is a significant increase in total mission lifetime, with equivalent masses, by using a mechanical cooler/cryogen system as compared with a sublimating solid cooler.

It should be noted that during the operation of the instrument, there would be no vibrations from the refrigerator. During the refreezing of the cryogen when the refrigerator is in operation, the instrument would be turned off. An advantage of this would be that a less expensive refrigerator, having a vibrational environment which exceeds that required by the sensor, could be used.

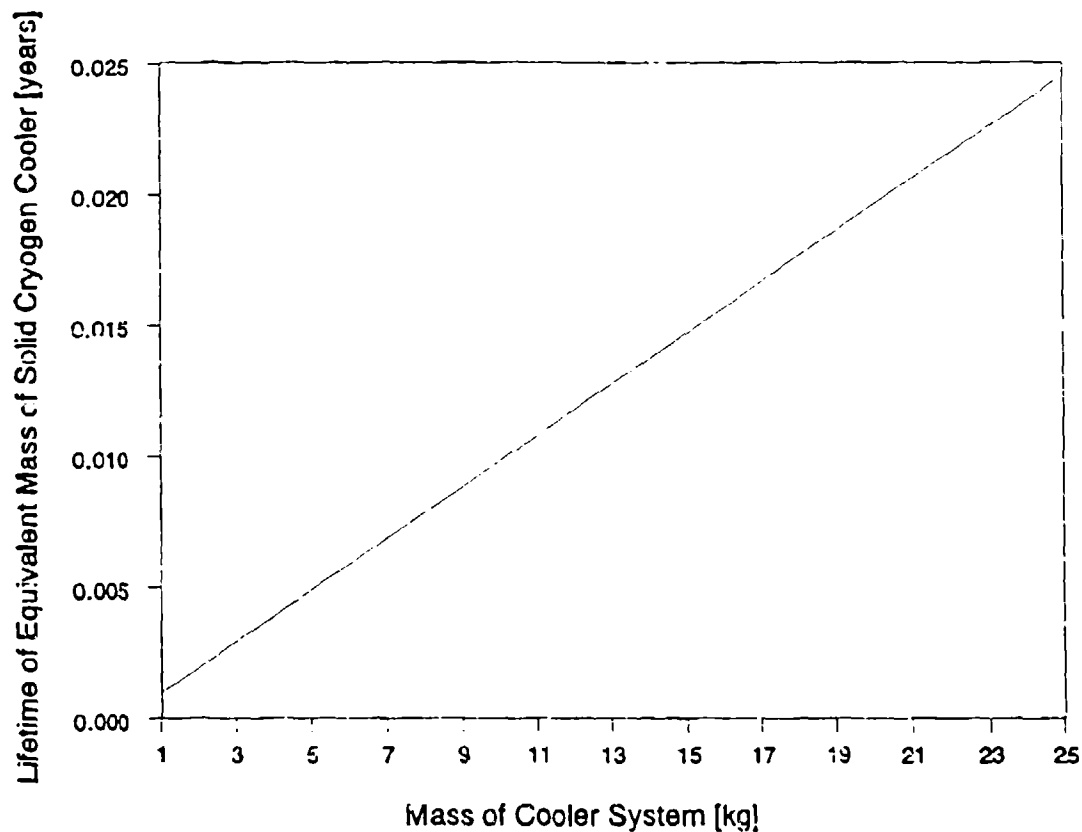


**Figure 6.** Mass of cooler system versus lifetime of a sublimating cooler for the instrument cooling mission.

Another advantage of the integrated refrigerator/cryogen system is that the system can accommodate sensor heat loads much greater than the cooling capacity of the refrigerator. The sensor heat load for this mission scenario is 7.8 W, yet the British Aerospace cooler can supply only 0.8 W of cooling at 80 K. At the triple-point temperature of nitrogen, the cooling capacity of

the refrigerator is even less. The integrated system could also handle unexpected high sensor loads for a period of time dependent upon the mass of cryogen contained.

#### LONG TERM STORAGE OF A CRYOGEN

It is also possible to utilize the refreezable cooler concept with one or more mechanical coolers for the long duration storage of a cryogen in space. An example of this kind of mission would be storing a small amount of propellant required for maneuvering with thrusters at the destination of an interplanetary mission. Another example would be a small amount of stored solid nitrogen and a refrigerator which are both used to cool a 63 K shield for a large hydrogen storage tank. The refrigerator would cool the shield and the solid nitrogen would absorb any spikes in the parasitic heat loads by melting. Once the parasitic heat loads had returned to a nominal value, the nitrogen would be refrozen with the refrigerator.

With these types of mission scenarios, the cryogenic propellant could require cooling for years. Also, with these scenarios, there are no instrument target heat loads for the storage period, therefore, the only heat loads are in the form of parasitic heat leaks.

To demonstrate using the refreezable cooler, a generic interplanetary mission was evaluated. This mission has no set destination, but instead focuses on how long of a mission lifetime is possible. Since different trajectories require different amounts of time, the resulting mission lifetime could be applicable to a variety of intrasolar destinations. It is assumed that the rocket used would incorporate an integrated nuclear power/propulsion system. With this rocket system, a nuclear reactor, such as the Idaho National Engineering Laboratory's (INEL) Small Ex-core Heat Pipe Thermionic Reactor (SEHPTR)<sup>[24]</sup>, would supply electrical power to on-board systems as



well as thermal power for a nuclear thermal rocket. Table 3 lists the baseline parameters of the scenario which are used in the computer code.

Table 3  
Baseline Parameters for Long Duration Storage

Target Heat Load . . . . .	0 W
Parasitic Heat Load . . . . .	100 mW
Duration of Instrument Operation . .	0 minutes
Initial Ullage in Tank . . . . .	10%
Mass of Cryogen . . . . .	5 kg
Starting Temperature . . . . .	65 K
Minimum Temperature . . . . .	63.0 K
Maximum Temperature . . . . .	63.3 K
Refrigerator . . . . .	British Aerospace

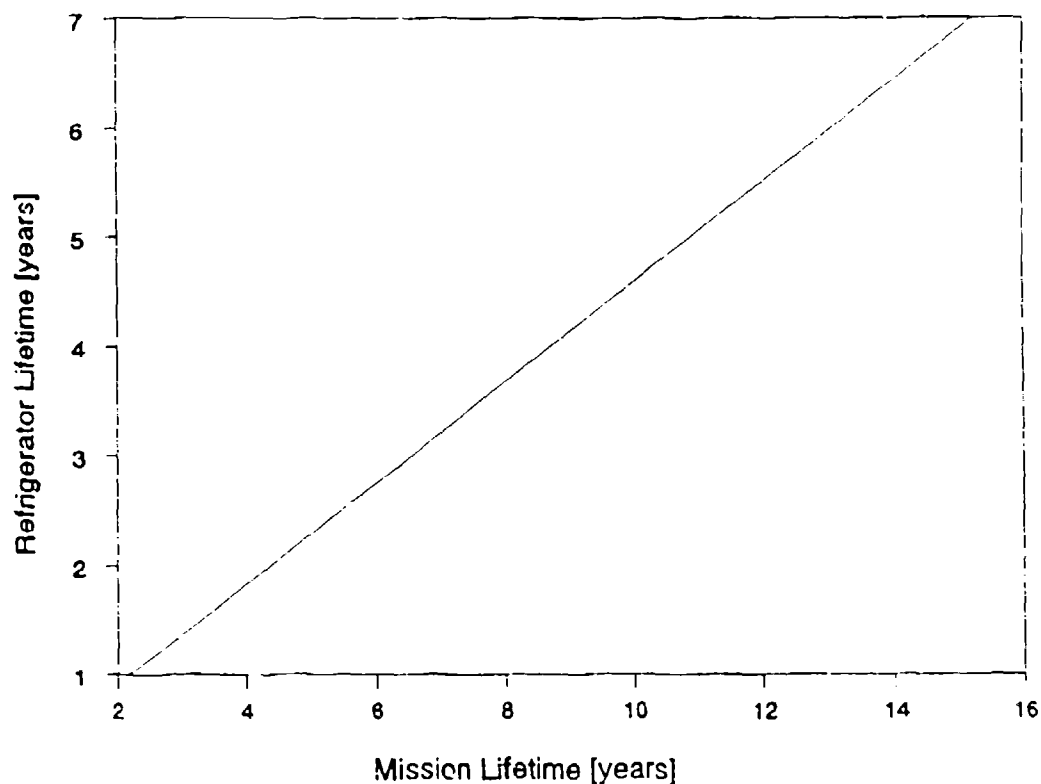


Figure 7. Total mission lifetime versus refrigerator lifetime for the long duration storage of a cryogen.

Figure 7 shows the relationship between the total mission lifetime and the lifetime of the British Aerospace cooler. Here, the mission lifetime refers to the duration of time that the refrigerator could maintain the cryogen with the given parasitic heat load. For a three-year refrigerator lifetime, the overall mission lifetime is approximately 6.5 years.

If ten refrigerators are used and if their usage is rotated so that each refrigerator is used once every ten cycles, then the three-year lifetime for each refrigerator could be extrapolated out to a total lifetime of 30 years. A reliability of 100% for all ten refrigerators is assumed. This results in a total storage mission lifetime of 65 years. A potential problem with this idea would be the thermal unlinking of the refrigerators not in use.

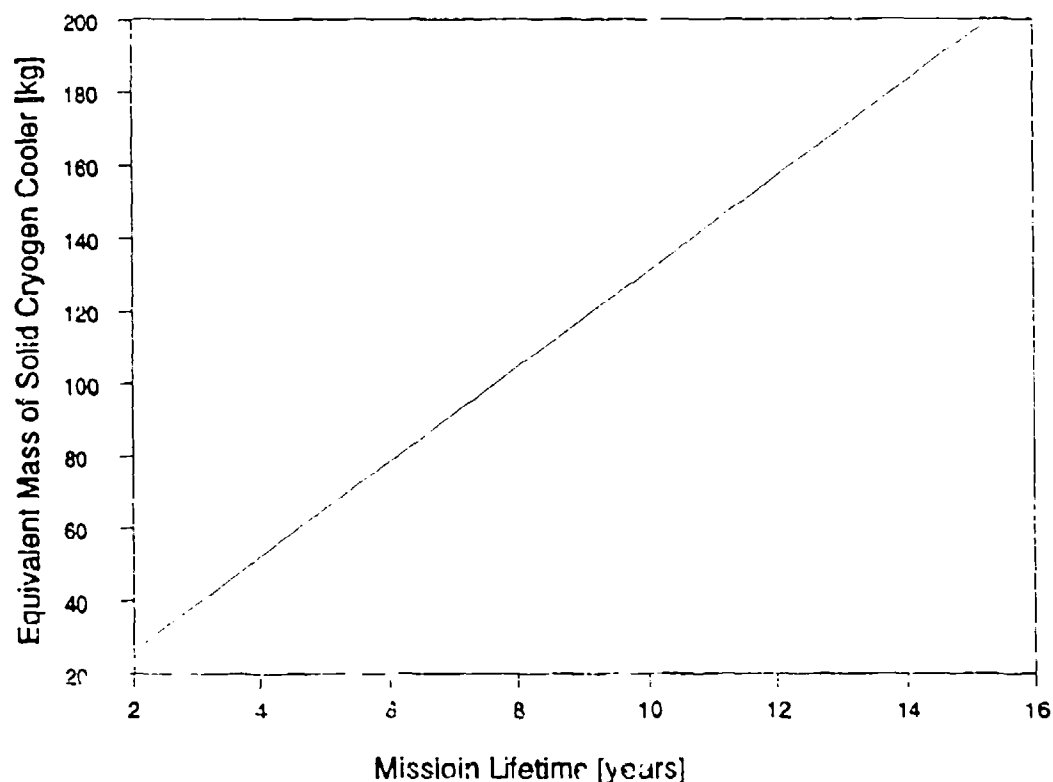


Figure 8. Total mission lifetime versus mass of an equivalent lifetime sublimating solid cooler for the long duration storage of a cryogen.

Figure 8 graph the relationship between total mission lifetime and mass of an equivalent lifetime sublimating solid cryogen cooler. For a 6.5 year total mission lifetime, a sublimating cooler would require approximately 85 kg of cryogen. Again, it is assumed that the parasitic heat loads would be constant with increasing cryogen mass. The mass of the mechanical cooler/cryogen system is 13.4 kg with this mission scenario.

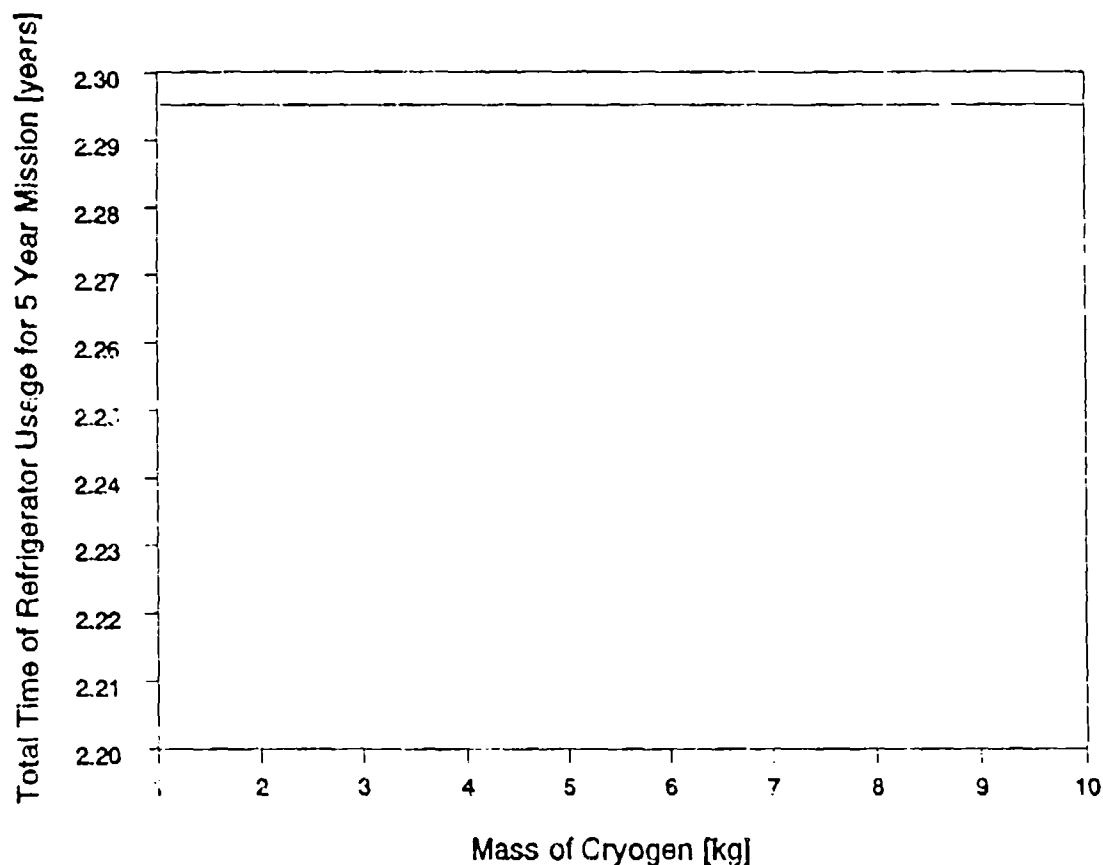


Figure 9. Mass of stored cryogen versus total refrigerator usage time for a five-year storage mission.

Figure 9 shows a graph of the mass of stored cryogen versus total refrigerator usage time for a five-year mission. For this five-year mission, the British Aerospace cooler requires 2.295 years of operation. It can be assumed from this graph that if the parasitic heat load is constant for all cryogen masses, then

varying the amount of stored cryogen has no effect on the total refrigerator usage time.

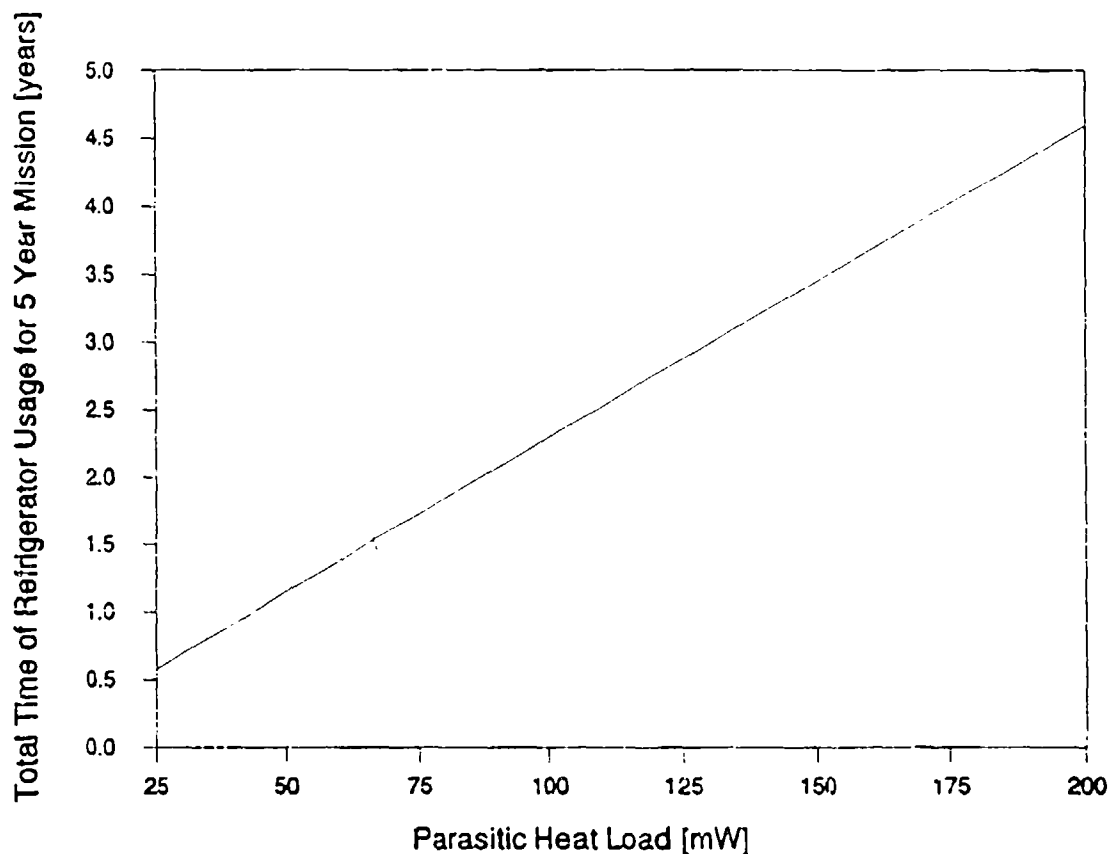


Figure 10. Varying parasitic heat load versus total refrigerator usage time for the long duration storage of a cryogen.

The effect of varying parasitic heat loads on the total refrigerator usage time is shown in Figure 10. From this graph it was evident that as the parasitic heat load increases, the total refrigerator usage time also increases. An in-flight variation to the parasitic heat load could be due to an increase in the solar flux incident on the storage tank. For example, if the spacecraft traveled closer to the sun or if there is unusual increased solar activity.

SUMMARY

By incorporating a refreezable cryogen with a mechanical refrigerator, it should be possible to eliminate the vibrations to a sensor during operation, while possibly utilizing a higher vibration refrigerator during refreezing. This could potentially allow a less expensive refrigerator to be used.

The integrated system could handle a sensor heat load greater than the cooling capacity of the refrigerator. The maximum duration of sensor operation was directly dependent upon the mass of cryogen contained in the system. The instrument idle period was dependent upon the cooling capacity of the refrigerator, which dictated the time required to refreeze the cryogen.

An increase in the overall mission lifetime as compared with only using a refrigerator or a sublimating solid system was shown. For equivalent masses, the integrated mechanical cooler/cryogen system had dramatically increased mission lifetime as compared with a sublimating solid cryogen cooler. It was also evident that the refrigerator lifetime has a major effect on the overall mission lifetime of the mechanical cooler/cryogen system.

A disadvantage of the integrated system is that the instrument operation temperature and cryogen storage temperature must be at the triple-point of the cryogen. Also, a majority of space application refrigerators are designed to operate around 70 K, therefore, for lower temperature missions, cryogen combinations other than nitrogen and 63 K refrigerators must be developed.

Another disadvantage is that the integrated cooler relies upon the latent heat of fusion to absorb heat loads, which is much less than the heat of sublimation. The refreezable cooler also relies on a large number of on/off cycles and it is unknown at this time whether or not the investigated refrigerators could reliably handle a large number of cycles.

Finally, there is a period of time in which the refrigerator would be refreezing the cryogen. During this period, the instrument would be unavailable for use. By selecting a refrigerator with the appropriate cooling capacity, the quiescent period of the instrument could be adjusted to meet mission requirements.

#### REFERENCES

- 1 Schick, Scott H. 1990. Extended life, earth-orbiting cryogenic dewars. Master's thesis, Utah State University.
- 2 Williams, Brian G. 1991. Extended life refreezable solid cryogenic cooler. Master's thesis, Utah State University.
- 3 Werrett, S. T., G. D. Peskett, G. Davey, T. W. Bradshaw, and J. Delderfield. 1985. Development of a small Stirling cycle cryocooler for spaceflight applications. In Advances in Cryogenic Engineering 31, ed. R. W. Fast, 791-9. New York and London: Plenum Press.
- 4 Bradshaw, T. W., J. Delderfield, S. T. Werrett, and G. Davey. 1985. Performance of the Oxford miniature Stirling cycle refrigerator. In Advances in Cryogenic Engineering 31, ed. R. W. Fast, 801-9. New York and London: Plenum Press.
- 5 British Aerospace Public Limited Company. n.d. Mechanical cryogenic coolers for space applications. Company brochure.
- 6 Ravex, A., G. Claudet, and P. Rolland. 1990. A Vuilleumier refrigerator for lone-life spaceborne applications. Cryogenics 30 (September supplement): 277-81.
- 7 Creare single stage reverse Brayton. n.d./n.p. Photocopy of overhead.
- 8 Single stage turbo cooler. n.d./n.p. Photocopy of overhead.
- 9 Donabedian, Martin. 1989. Cooling systems. The Infrared Handbook, ed. William L. Wolfe and George J. Zissis, Chapter 15. Ann Arbor, Michigan: The Infrared Information Analysis (IRIA) Center.
- 10 Wang, Junjie, Wenxiu Zhu, Pingsheng Zhang, and Yaun Zhou. 1990. A compact co-axial pulse tube refrigerator for practical application. Cryogenics 30 (September supplement): 267-71.

- 11 Sherman, Allen. 1982. History, status, and future applications of spaceborne cryogenic systems. In Advances in Cryogenic Engineering 27, ed. R. W. Fast, 1007-29. New York and London: Plenum Press.
- 12 Jones, Jack A. 1987. Sorption cryogenic refrigeration--status and future. In Advances in Cryogenic Engineering 33, ed. R. W. Fast, 869-78. New York and London: Plenum Press.
- 13 Jones, J. A., S. Bard, H. R. Schember, and J. Rodriguez. 1990. Sorption cooler technology development at JPL. Cryogenics 30 (March): 239-45.
- 14 Lucas Aerospace Limited and Lockheed Missiles & Space Company, Inc. 1990. Mechanical cryogenic cooling systems for space applications. Company brochure.
- 15 Magnavox Government and Industrial Electronics Company. 1988. Ultra-reliable split mini-cooler MX 7043 series. Application notes.
- 16 Magnavox Government and Industrial Electronics Company. n.d. Linear resonant split Stirling cooler MX 7043. Company brochure.
- 17 Stolfi, F., M. Goldowsky, J. Ricciardelli, and P. Shapiro. 1982. A magnetically suspended linearly driven cryogenic refrigerator. In Refrigeration for cryogenic sensors: Proceedings of the second biennial conference on refrigeration for cryogenic sensors and electronic systems, NASA Goddard Space Flight Center, Greenbelt, Maryland, 7-8 December 1982, ed. Max Gasser, 263-303.
- 18 Keung, C., P. J. Patt, M. Starr, and R. McFarlane. 1990. Performance of a prototype, 5 year lifetime, Stirling cycle refrigerator for space applications. Presented at the 6th International Cryocooler Conference, October 25-26, Plymouth, Massachusetts. Photocopied.
- 19 Yoshimura, Hideto and Masakuni Kawada. 1987. Small Vuilleumier cooler. In Advances in Cryogenic Engineering 33, ed. R. W. Fast, 837-44. New York and London: Plenum Press.
- 20 Lindale, E, and D. Lehrfeld. 1982. Life test performance of a Philips rhombic-drive refrigerator with bellows seals. In Refrigeration for cryogenic sensors: Proceedings of the second biennial conference on refrigeration for cryogenic sensors and electronic systems, NASA Goddard Space Flight Center, Greenbelt, Maryland, 7-8 December 1982, ed. Max Gasser, 197-213.
- 21 Kollmorgen Corporation. 1990. Ricor micro IDCA cryocooler model K506B. Company brochure.

- 22 Gresin, A. K., Y. O. Prousman, A. V. Smirnov, and L. A. Babi. 1990. Analitical and experimental study of the small Stirling cryocoolers. Cryogenics 30 (September supplement): 241-6.
- 23 Space Dynamics Laboratory. 1990. SPIRIT III CDR, Volume II, 30 January to 2 February. Logan, Utah: Space Dynamics Laboratory/Utah State University.
- 24 Snyder, A. M., Watts, K. D., and Sulmeisters, T., "Satellite Laser Communications Nuclear Power Integration Study", EGG-CEN-9936, September 1991, Idaho National Engineering Laboratory, EG&G Idaho, Idaho Falls, Idaho.



## Applications and Packaging of Semiconductor Devices for use at Cryogenic Temperatures

Kevin P. Hyde, Joseph R. McCoy, and Charles S. Naiman  
Infrared Components Corporation  
311 Turner Street  
Utica, New York 13501

### Introduction and Applications

The benefits of operating semiconductor devices at low temperatures are well known(1). The payoffs of lower noise, higher speed, and increased dynamic range have fostered the use of cryogenics for electronic devices and systems. Many electronic and optoelectronic systems can benefit from the cryogenic operation of key components. Listed below are possible applications where cryogenically cooled devices have been shown to improve the component performance. Alternatively such cooling allows repartitioning of a system to improve overall performance, by enabling closer coupling of various components or subsystems.

- *Computer systems* from supercomputers to general-purpose computers can benefit from the increased speed offered by the cryogenic operation of key subsystems.

- *Imaging systems* can benefit from increased speed by co-locating a cryo-cooled comparator, signal processor or data processor at the imaging array. This could apply to general *imaging with CCD's*, and specifically to *HDTV*. Image capture or processing speed in general could also benefit from cryogenically cooled processing of data, with major applications in *medical imaging* and *non-destructive testing*. An important variant of this is the area of high performance *computer vision*.

- Higher *data processing* speed can be obtained through cryogenic operation of digital subsystems, particularly highly integrated ones. Application areas include *computer workstations*, *high speed modems*, and *sensor fusion*.

- *Diode lasers and diode laser arrays* could benefit from higher *efficiency*, narrower *linewidth*, and better *thermal stability*. Heat removal from the laser material will yield less *frequency chirp* during pulsed operation. Modulation *frequency* and system *speed* could be improved. Another aspect is the use of controlled variable-temperature cryocoolers for *wavelength tuning* of lasers.

- *Sensitivity of radar receivers* is improved by the reduction of electronic noise. Radar transmitters could possibly be made more efficient, and heat generation problems ameliorated by cryocooling.

- Improved signal to noise from the *front-end pre-amplifier* of *satellite receivers*.

- Cryocooling might also be applied to *frequency-agile systems* to increase the rapidity of *frequency shifting* and to reduce *settling time* (post-tuning drift).

### Cryogenic Packaging Technology

ICC's technology base was developed at General Electric in the 1980's when system size and weight constraints placed low heat load requirements on the cryogenic package for infrared detection. The available technology at that time, the so-called "First Generation Common Module" (commonly referred to as "Common Mod"), fell short of the heat load requirement and GE was forced to develop new technology. The technology base developed at GE and others has been collectively called an "Integrated Detector Assembly" or IDA. A cross sectional view of a typical IDA is shown in Figure 1.

This technology incorporates the expander of the cryogenic subsystem into the all metal dewar, making it integral with the high vacuum vessel. The device to be cooled is attached directly to the cold tip of the cryogenic expander. This technology has been previously reported<sup>(2)</sup>. The direct attachment method of the IDA eliminates the major source of heat loss in the system, namely, the thermal interface between the cold tip of the expander and the device to be cooled. By eliminating this heat load, the cooling requirements of the cryogenic subsystem are reduced allowing for a smaller, lighter, less expensive, and lower capacity cooler. Furthermore, despite its direct

integration with the cold tip, a defective device can be easily demounted from the cold tip and replaced.

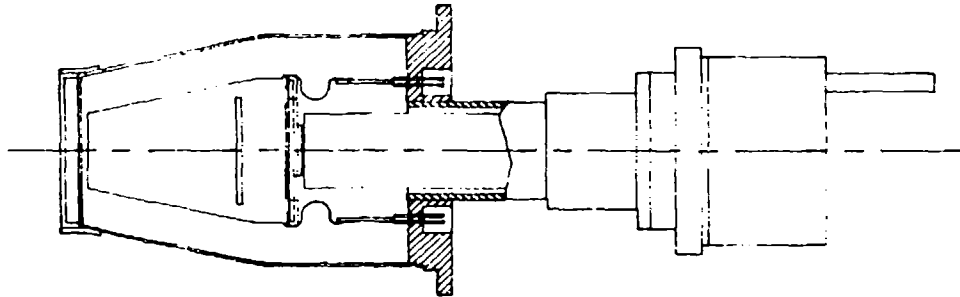


Figure 1. Cross Sectional view of a typical IDA

The goal of this study is to identify the specific problem areas associated with a given application. Then to propose solutions based on previous experience, and/or recommend further development.

The typical problems encountered in the design of an IDA for infrared detectors are *microphonics*, *induced stress* in the cooled materials from expansion differences, *vacuum life*, *optical registration*, suitable *electrical interconnects*, and *line of sight jitter* due to excessive expander deflection. Finding solutions to these problems are sometimes system dependent, but in general, the solutions proposed and demonstrated by ICC apply to all systems.

Ideally, the cryogenic package design and technology should be easily adapted to any type of *cryogenic cooler*. This is especially important to the equipment manufacturer who has multiple applications and/or requirements and wants minimal expense to adapt a particular cooler to the end product. The designs offered by ICC have been adapted to multiple cooler types as shown in Figure 2 and 3 where similar dewar designs are interfaced to different coolers. We discuss some of these issues

This same technology developed for infrared detectors applies equally to other technologies such as superconducting multi-chip modules (MCMs), cryogenic CMOS for supercomputers, and RF detection systems where lower noise and higher frequency systems are desirable. The issues common to these technologies include the electrical interconnects between the cryogenically operated device and the environment external to the dewar, material selection for both mechanical and electrical properties, and method of cryogenic cooling.

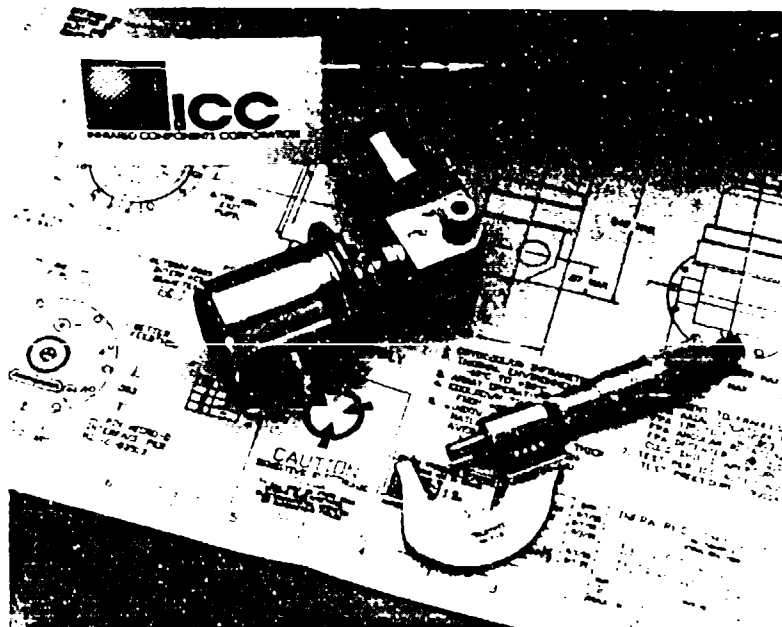


Figure 2. Microcooler based IDA

### **Electrical Interconnect Issues**

The electronic components operating at cryogenic temperatures must eventually be electrically connected to an external environment which generally is at a much higher temperature. The ideal interconnection would have zero electrical and infinite thermal impedance. Unfortunately, in accordance with the Weidemann-Franz law<sup>(3)</sup>, materials which have low electrical impedance also have low thermal impedance. This law applies to pure metals and alloys at temperatures above 10 Kelvin. It is therefore imperative for these systems to limit the number of dewar penetrations

For *low frequency* (<100 MHz) systems, there is a trade between electrical impedance which could limit the speed of the data, and thermal impedance which adds to the heat loss through conduction. For *infrared detectors*, where speed is generally limited by the external 12-14 bit A/D converter and not the RC time constant of the signal lead, this trade has resulted in electrical impedances on the order of a few ohms and thermal losses on the order of 1-2 milliwatts per trace for a temperature difference of 260 Kelvin. For high speed data systems, the low electrical impedance is obtained at the expense of increased heat load.

For diode laser applications, the pulsed and continuous current characteristics, used to drive the devices, can have a profound effect on heating. These need to be analyzed and measured case by case.

For the higher frequency *microwave/RF systems*, the requirements are different. Here we must account for performance parameters such as characteristic impedance, dissipation factor and losses, shielding and spurious signals and thermal coefficients. Interconnection technologies like *stripline*, *waveguides* and *co-axial* lines must be further investigated for performance over the cryogenic to ambient temperature transition. RF systems must successfully address the specific requirements of each of these design domains. Each domain has specific primary performance parameters which dictate that certain material and physical or geometric criteria be met in order to achieve meaningful, if not optimum operation.

For *stripline* interconnects, care must be taken in the selection of compatible materials. Electrical parameters like dielectric constants and dimensional stability vs temperature which could affect the characteristic impedance must be carefully selected to be compatible with the mechanical, cryogenic, and high vacuum dewar requirements. For example, it is unlikely that the dielectric material polyimide, which has low outgassing, superb mechanical flexibility down to 4 K, and CTE on the order of 6 ppm/K would be chosen for RF circuits. This is because of the relatively high dielectric constant (~3.7) demands nearly twice the substrate or carrier thickness to compensate for the lower dielectric constant (~2) of the more desirable teflon materials. However, many of the preferred teflon-based RF materials either lack the flexibility or the low CTE of polyimide.

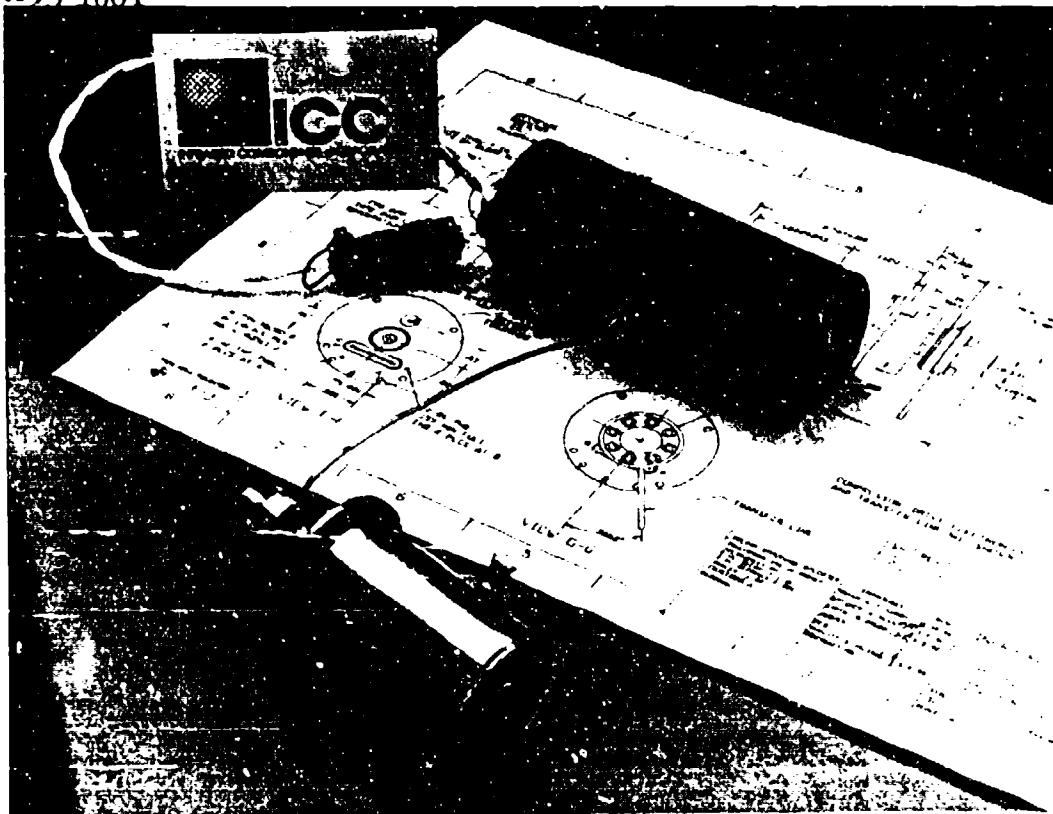


Figure 3. Split Stirling based IDA

With *co-axial* lines, there is a trade between insertion losses and thermal losses which drives the cable material and diameter selection. Typical semi rigid, all stainless steel *co-axial* cables have the lowest heat loss and the highest attenuation (relative to  $0.0034\sqrt{f(\text{GHz})}$ )<sup>(4)</sup>. Other cables such as silver plated, copper clad stainless steel or silver plated beryllium copper have lower relative attenuation losses at the expense of higher thermal losses. Additionally thermal losses increase and attenuation losses decrease with increasing inner, outer, and dielectric diameter. It should be noted that at microwave frequencies, a conductor could be fabricated with a lower conductivity core with a plating of a high conductivity material, and a thickness on the order of the skin depth.

Very few material suppliers, RF and superconducting device designers, and cryogenic packaging engineers share a broad common knowledge base. Thus, building an informed understanding of design goals, acceptable compromises, and performance expectations is both more difficult and more important than in more conventional single technology design/development. Specific challenges which need to be addressed in combined *cryogenic/RF* systems are:

- *RF-rated dielectrics* subjected to cryogenic temperatures may exhibit substantial changes of electrical parameters and system performance.
- *Conductor alloys* preferred for low cryogenic heat load may impact characteristic impedance and losses at RF frequencies.
- *Coefficient of Thermal Expansion* (CTE) mismatch of selected materials.
- Thicker dielectrics required for RF will reduce packaging *form factor* options.

What should be clear from the foregoing discussion is not that suitable materials are unavailable, but cryogenic operation of these materials requires further characterization and testing such that the selection of a suitable material can be done both carefully and creatively.

#### **Mechanical and Thermal Packaging Issues**

Extensive research into the characteristics of the materials used in the dewar, both steady state and cyclic, have been carried out by ICC. Issues such as the *Coefficient of Thermal Expansion* for the cooled materials, the joining (welding or brazing) of dissimilar materials used for the vacuum vessel, and outgassing, drive the selection of materials compatible with a high vacuum environment.

Differences in material CTE lead to *induced stresses* upon cooling. Figure 4 shows a comparison of the CTEs for various materials used in the IDA field. To further complicate the issue, the *cool down rate* can also lead to induced stresses even in well matched coefficients under equilibrium conditions if the two materials are cooled at different rates. Detrimental effects such as the generation of piezoelectric charges, modulation of charge, and in the extreme case, device failure due to stresses exceeding the elastic limit can occur. To eliminate or reduce these effects to acceptable levels requires matching of the material expansion properties and quasi-isothermal cooling.

The *joining* of dissimilar materials is another issue which requires proper material selection, and this ties in with vacuum life. If the joint is to be a hard vacuum seal, then porosity and intergranular structure of the resulting joint must be addressed. Often, the hermetic sealing technology typically applied to military electronic devices is not adequate. This is indicated by the leak specification which is several orders of magnitude above the requirements of the hard vacuum seal ( $<1\text{E-}13$  SCCM He) needed for long life dewars.

*Outgassing* properties of all materials exposed to the high vacuum environment must be known and controlled if long vacuum life is to be obtained. Material outgassing causes virtual leaks in the high vacuum environment and increases the heat load on the cryogenic cooler. In some components, such as the metal piece parts, pre-processing of the material prior to assembly can reduce the outgassing. Typically, this is done by a vacuum and stabilization bake, at the maximum permissible temperature without changing the selected material properties. The vacuum life in such systems is then limited by the outgassing of the components which have relatively low bake temperature limits. These components are generally the electronic devices, cryogenic expander, and the epoxies and organics. The emphasis is therefore placed on the characterization and selection of these components.

Another critical packaging issue is the design of the platform to support the device being packaged. The issue here, aside from the CTE problem discussed earlier, is low mass and corresponding low thermal mass. The low mass is desirable from a dynamic standpoint as the natural frequency of the system increases as  $1/\sqrt{M}$ . This is important on highly stable platforms where line of sight jitter under random vibration must be held to low levels. Higher thermal mass increases the cool down time, or dictates the use of a higher capacity cooler. The platforms designed by ICC meet these requirements and are CTE matched with the help of an established data base that has been accumulated over a decade.



# Coefficient of Thermal Expansion Comparison

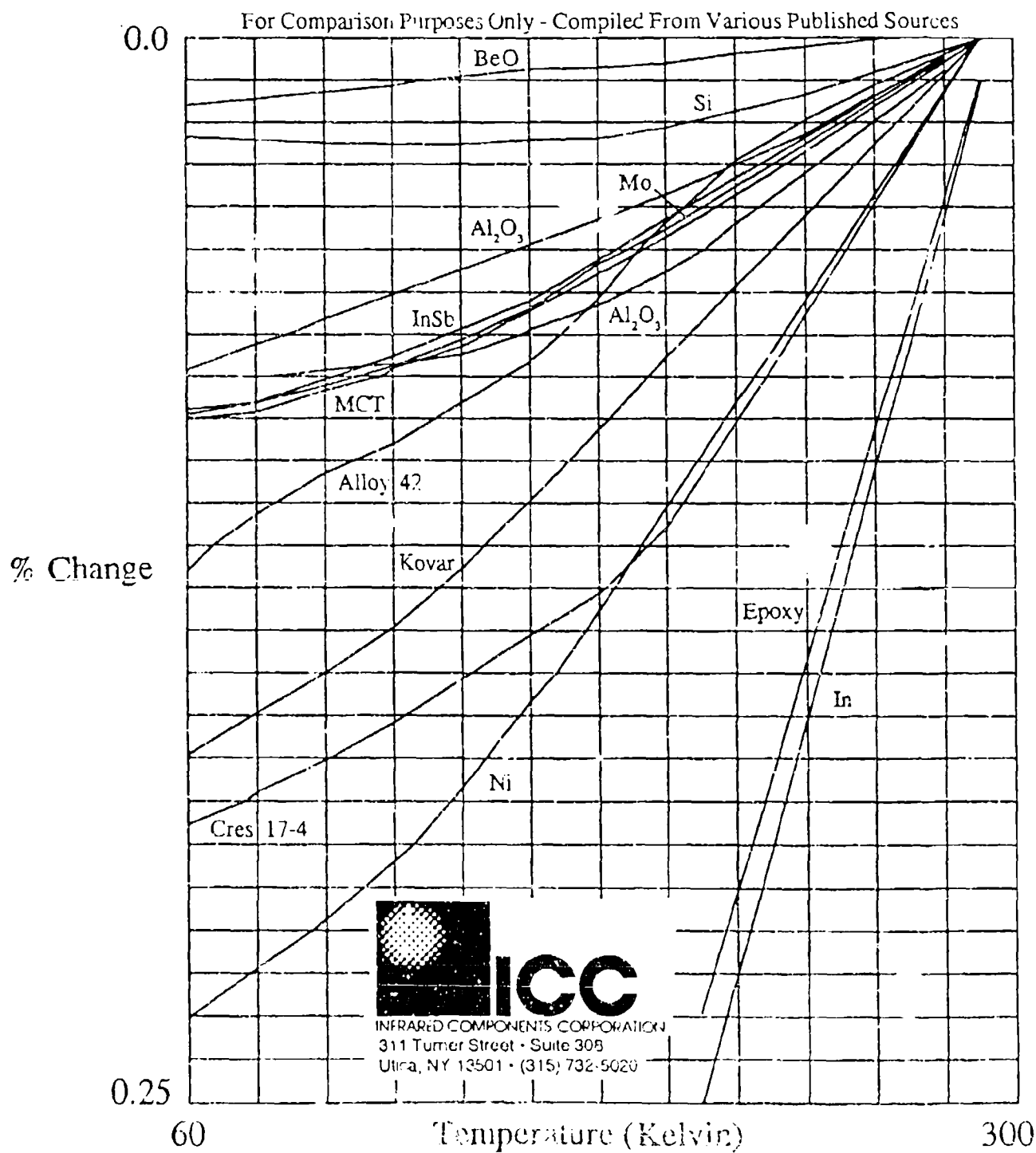


Figure 4 Comparison of coefficients of thermal expansion for several common materials used in IDA designs

To reduce the heat load on the device, a *cold shield* is used. On infrared FPAs they are used to block the radiation from outside the field of view. The cold shield typically is attached to the FPA or platform so that it operates at temperatures slightly above the FPA temperature. To be effective, the cold shield must have a high emissivity coating on the interior and a high reflectivity coating on the exterior. The high emissivity coating on the interior assures that stray radiation (radiation outside the field of view) is absorbed by the cold shield rather than reflected onto the image plane. The high reflectivity coating on the exterior reduces the heat loading by reflecting the energy away. This also applies to non-optical devices where complete cold shielding is desired.

The issues associated with the cold shield are low weight and proper selection of coatings. Low weight is important for two reasons: 1) the *dynamic behavior* of the system. Increased cold shield mass lowers the natural frequency, thus increasing the magnitude of the dynamic deflection; and 2) the increased *cool down time* associated with the increased thermal mass. The coating design involves not only selection of high emissivity and high reflectivity coating materials, but the ability of the coating to adhere to the base material. Coatings which may flake off could potentially render the device useless. ICC has developed a proprietary low mass cold shield with a non organic, non-particulating coating that has a measured emissivity of greater than 90%.

### Cryogenic Coolers

The selection of the cryogenic cooler is a direct flow down from the system requirements. Issues such as *cool down time*, *mission duration*, *steady state temperature*, *heat load*, and *operating environment* drive the selection of the cooler. The format for cooler selection is similar to the design guidelines established during the Common Mod Program; Joule-Thomson (J-T) for fast cool down, Stirling cycle for continuous operation, and thermo-electric (TE) coolers for applications above 150 Kelvin. Recent trends toward continuously operating, closed cycle J-Ts may allow for some added versatility in distributed aperture and multi-chip cooling applications.

Independent of cooler type, if low cost, easily adaptable packages are to become a reality, the cooler suppliers must work towards a *common interface*. To some extent,

the military has been working towards this goal on the Army's Standard Advanced Detector Assembly (SADA) Program. Although cooler manufacturers have been tailoring their products to meet this interface, the end product is costly. For commercial applications, a suitable, *designed-to-cost* interface must be established. ICC has been working with several cooler manufacturers to set this standard. The interface established by ICC has been successfully implemented on both commercial and military products.

Proper selection and design of the cryogenic expander can reduce *microphonics* to a negligible level. It is our experience that microphonics stems from two sources. The first source is the noise induced from the mechanical impact of the regenerator on the cold tip. This type of noise generally manifests itself as periodic light/dark patterns in the video output at the cooler operation frequency. Solutions for this include short stroking the regenerator, so that impact does not occur and incorporation of a "shock absorber" into the expander design. Both methods have been successfully implemented by ICC.




































The second source of microphonics is a modulation of the field of view due to the motion of the focal plane array relative to the optic caused by vibration of the expander. The obvious solution for this problem is to stiffen the expander, however, increasing the wall thickness increases the heat path adding to the heat load. ICC has developed and demonstrated a 5x decrease in expander deflection with a proprietary stiffening technique which has minimal impact on the heat load.

*Diode laser arrays* can produce many tens and even hundreds of watts/cm<sup>2</sup> in a "laser Diode Bar". Most are operated near room temperature. All benefit from lower temperature and even cryogenic operation, where they are wavelength compatible. Near and at room temperature, liquid microchannel coolers are being developed to remove thousands of watts/cm<sup>2</sup> of heat. Cryocoolers for these applications will require cooling capacities in the 100's of watts and kilowatt level. Their cooling interface will also require extensive design, to also maintain the proper laser output characteristics.

**Summary**

Infrared detector assemblies have been under development since the early 1980's and are now in production at ICC. The technologies developed for packaging of these infrared detector assemblies are being applied to other technologies such as superconductivity, high sensitivity microwave/RF systems, etc. The potential issues with these systems, shown in Table 1, are similar to the problems encountered in infrared FPA systems where solutions have been implemented. For these advanced applications, especially in the areas of signal interconnection technology and material characterization, additional research and development is necessary.

# Applications versus Typical Problems

Problem / Application	Microphonics	Temperature Uniformity	Optical Registration	Signal Interconnects	Coldshield	Mechanical Stress	LOS Jitter
IR and Visible FPAs							
Diode Lasers & Arrays							
MOS Device Structures							
MMICs							
Superconducting Microwave Devices							

## Legend

 Solution In Hand  
 Potential Problem  
 Not Applicable

Table 1. Typical Problems Associated with Various Technologies

*References*

1. For an excellent overview, including multiple references, see R.K. Kirschman, *Cold Electronics: An Overview*, Cryogenics, Volume 25, March 1985
2. D. Amuso, T. Clynne, and J. McCoy, *Integrated Detector Assemblies in Production*, 1991 IRIS Conference on the Producibility of Infrared Focal Plane Array Assemblies.
3. H. M. Rosenberg, *The Behavior of Materials at Low Temperatures*, Advanced Cryogenics, ed. C. C. Bailey, New York, Plenum Press, 1971.
4. S. Weinreb, *Cryogenic Performance of Microwave Terminations, Attenuators, Adsorbers, and Coaxial Cable*, National Radio Astronomy Observatory, Electronics Division Internal Report No. 223.

# A METHOD TO ESTIMATE THE PULSE TUBE REFRIGERATOR PERFORMANCES

MARC DAVID, JEAN-CLAUDE MARECHAL AND YVAN SIMON  
DEPART. MENT DE PHYSIQUE DE L'ECOLE NORMALE SUPERIEURE  
24 RUE LHOMOND, 75005 PARIS, FRANCE

## ABSTRACT

The main purpose of this paper is to give :

- i) a practical method to calculate the theoretical gross refrigeration power  $\langle \dot{q}_c \rangle$  of an ideal Orifice or Double Inlet Pulse Tube Refrigerator (O.P.T.R. or D.I.P.T.R.),
- ii) an experimental method to measure the actual value of  $\langle \dot{q}_c \rangle$  and independently the regenerator losses  $\langle \dot{q}_c' \rangle$ .

An analytical model of the ideal O.P.T. has been developed recently <sup>1</sup>. In this paper, it is shown that this model is also suitable to describe the D.I.P.T. principle. The performances of the ideal O.P.T.R. or D.I.P.T.R. are easily deduced by only measuring the gas pressure as function of time in the tube and in the reservoir.

This ideal refrigeration power can be then compared to experimental results. As the amount of heat evacuated to the hot end averaged over a cycle,  $\langle \dot{q}_a \rangle$ , is equal to the gross refrigeration power  $\langle -\dot{q}_c \rangle$  (Ref. 1), the idea is to measure  $\langle \dot{q}_a \rangle = \langle -\dot{q}_c \rangle$  at the hot end by a double-weighing method.

## INTRODUCTION

Because of its mechanical simplicity and inherent reliability, the O.P.T.R. has great potential for long-life space applications.

An analytical model of the ideal O.P.T. has already been successfully developed for any pressure form in the tube <sup>1</sup>. An "ideal O.P.T." is defined with the usual following assumptions, as justified in the previous paper <sup>1</sup>: ideal gas, uniform pressure along the pulse tube, one-dimensional laminar flow, adiabatic transformations and perfect heat exchangers.

Two important results are derived. Firstly, the available power at the cold end  $\langle -\dot{q}_c \rangle$ , averaged over a cycle, and the rate of heat flow  $\langle \dot{q}_a \rangle$ , rejected to the hot end (Fig. 1), are found to be equal :

$$\langle -\dot{q}_c \rangle = \langle \dot{q}_a \rangle = \langle \dot{q} \rangle, \quad (1)$$

in agreement with the enthalpy flow analysis by Radebaugh<sup>2</sup>. In experiments, we only have access to the net refrigeration power  $\langle \dot{q}_c + \dot{q}_c' \rangle$ , where  $\dot{q}_c'$  represents the regenerator losses. Therefore, an estimation of the gross refrigeration power  $\langle \dot{q} \rangle$  will be made more conveniently at the hot end, providing that the temperature homogeneity of the hot part be ascertained (i.e. the hot heat exchanger, the orifice and the reservoir). Secondly,  $\langle \dot{q} \rangle$  can be easily calculated only from the measurement of the gas pressure wave form (in the tube  $P(t)$  and in the reservoir  $P_r(t)$ ):

$$\langle \dot{q} \rangle = (5/2\tau) \cdot T_a \int_{t_1}^{t_1 + \tau/2} \dot{m}_a(t) \left( (P(t)/P(t'))^{2/5} - 1 \right) dt \quad (2)$$

or

$$\langle \dot{q} \rangle = 3/2 V_r / \tau \int_{t_1}^{t_1 + \tau/2} \dot{p}_r(t) \left( (P(t)/P(t'))^{2/5} - 1 \right) dt \quad (3)$$

where  $V_r$  represents the reservoir volume,  $\tau$  the pulse period and  $p_r = P_r - \bar{P}$  where  $\bar{P}$  is the average pressure and  $\dot{p}_r(t) = dP_r/dt$ .  $t_1$ ,  $t'$  and  $m_a$  are defined below.

In any case, the pressure oscillation  $p_r(t)$  is observed to be quasi-sinusoidal for any pressure form in the tube. This is due to the fact that the orifice-reservoir system acts as a low-pass RC filter which essentially restores the first harmonic. Thus, if  $p_r = -a$  is minimum at  $t = t_1$  (Fig. 2), it is reasonably well approximated as:

$$p_r(t) = -a \cos \omega(t - t_1) \quad (4)$$

Recording small pressure variations may reveal difficult. However, with the sinusoidal approximation Eq. (4), only the peak-to-peak  $2a$  amplitude of  $p_r$  is required. The gas mass  $m_a$ , downstream the hot exchanger, is equal to the mass  $m_r$  in the reservoir if the void volume between the hot exchanger and the reservoir is neglected. During the half period  $[t_1, t_1 + \tau/2]$ ,  $\dot{p}_r > 0$  and  $m_a$  increases so that the gas is flowing out of the hot end. Consider the history of the element of gas that leaves the tube at some time between  $t_1$  and  $t_1 + \tau/2$ . It has entered the tube ( $x = L$ ) at a time  $t'$  (Fig. 2) when the tube pressure was  $P' = P(t') < P(t)$ . The relationship between  $t$  and  $t'$  is obtained on merely writing that  $m_a = m_r(t) = m_r(t')$ .

Or equivalently:

$$P_r(t) = P_r(t') \quad (5)$$

Eq. (4) yields  $t'$  versus  $t$  as illustrated in Fig. 2. According to the approximate expression (Eq. (3)) for  $p_r$ ,  $\tau \sim 2t_1 - \tau$ . In travelling back and forth along the tube, the element of gas has experienced an isentropic process. Consequently, its temperature has



changed from  $T_a$  at  $t'$  to  $T_L = T(L,t)$  in accordance with the isentropic law of an ideal monoatomic gas,  $T = \text{const } P^{2/5}$  :

$$T_L(t) = T_a (P/P')^{2/5} > T_a \quad (6)$$

The demonstration of the Eq. (3) can be found in Ref. 1. It is interesting to note that, in the same manner, the temperature and the velocity of any element of gas entering the tube at  $x = 0$  can be calculated at any time during its travel in the tube. Thus, this analytical model clearly exhibits that an element of gas entering the tube at  $t'$  will leave the tube at  $t$  with a temperature  $T(t) < T(t')$  and consequently will extract some heat from the cold end.

This paper has three objects :

- i) To describe a method to measure accurately the available power of an experimental O.P.T.R. and to compare it with the ideal O.P.T.R. as defined above (Eq. (3)).
- ii) To extend the analytical model of the O.P.T.R. (Ref. 1) to the D.I.P.T.R.
- iii) To describe a simple method to estimate the performances of an experimental D.I.P.T.R. and to compare it with the ideal theoretical system.

### EXPERIMENTAL MEASUREMENTS OF O.P.T.R. PERFORMANCES

An experimental apparatus has been designed as shown Fig. 3. By just recording  $P(t)$  and  $P_r(t)$  with two piezoelectrical sensors, we get all the necessary data for calculating  $\langle \dot{q} \rangle_{\text{the}}$ .  $\langle \dot{q} \rangle_{\text{exp}}$  can be measured by a double-weighing method. An auxiliary heater was inserted in the hot heat exchanger. We observe (over a few K) the first rising of the temperature  $T_a$ ,  $(dT/dt)_{1,t=0}$ , that resulted from a short interruption of the cooling water flow. Then, in the same working conditions as previously (cold temperature, pressure in the tube and reservoir temperature  $T_a$ ), a known power  $\langle \dot{q}_J \rangle$  is injected in the hot exchanger through the heater and simultaneously the cooling water flow is stopped, providing a second data  $(dT/dt)_{2,t=0}$ . Thus  $\langle \dot{q} \rangle_{\text{exp}}$  can be easily calculated :

$$\langle \dot{q} \rangle_{\text{exp}} = \langle \dot{q}_J \rangle \left( \frac{(dT/dt)_2}{(dT/dt)_1} - 1 \right) \quad (7)$$

### GROSS REFRIGERATION POWER OF THE D.I.P.T.R.

A lower temperature limit, and correlatively a most important available power at a given temperature, can be achieved by addition of a second orifice, as shown Fig. 4. These better performances, obtained with a so called D.I.P.T.R., have never been theoretically predicted.

From the point of view of our analytical model, the only difference between the two types of Pulse Tube Refrigerators is the  $\langle \dot{m}_a \rangle$  calculation. In other words, in both cases, the assumptions are the same, and Eq. (1) and Eq. (2) hold. Nevertheless, for the D.I.P.T.R.,  $\langle \dot{m}_a \rangle$  cannot be only expressed as function of the reservoir pressure variations. Here :

$$\dot{m}_a = \dot{m}_o - \dot{m}_{DI} \quad (8)$$

$\dot{m}_o$  and  $\dot{m}_{DI}$  are respectively the mass flow rates through the first and the second orifice ; the positive direction of the flow is shown in Fig. 4.

Assuming that the gas flow through the orifice and in the reservoir is adiabatic, a relation follows between the variation of  $m_r$  and the variations of  $P_r$  of the reservoir pressure :

$$\dot{m}_r = 3/5 (V_r / r T_a) \dot{P}_r = C \dot{P}_r \quad (9)$$

Here  $V_r$  is the reservoir volume,  $r$  the ideal gas constant and  $C$  is defined as the reservoir capacity in an electric analog (current/mass flow, voltage/pressure). Then we assume that the mass flow through the orifice obeys a linear law in the form :

$$P - P_r = R_o \dot{m}_r \quad (10)$$

which defines the resistance  $R_o$  of the orifice. As the linear behavior implied by Eq.(9) may be questionable at large dynamic pressures, the  $R_o$  constancy must be first checked by comparing  $\dot{m}_r$  values obtained with both Eq. (9) and Eq. (10). Thus, if both valves of the D.I.P.T.R. are the same, the previous calibration of  $R_o$  may be used to characterize the resistance  $R_{DI}$  of the auxiliary orifice, so that :

$$\dot{m}_a = (P(t) - P_r(t))/R_o - (P_{comp}(t) - P(t))/R_{DI} \quad (11)$$

where  $P_{comp}(t)$  is the input compressor pressure.

Therefore, Eq. (3) for a D.I.P.T. becomes :

$$\begin{aligned} \langle \dot{q} \rangle = & (5/2r) r T_a \int_{t_1}^{t_1 + t/2} ( (P(t)/P(t'))^{2/5} - 1 ) \\ & * ( (P(t) - P_r(t))/R_o - (P_{comp}(t) - P(t))/R_{DI} ) dt \end{aligned} \quad (12)$$

$t_1$  is now defined as the time between 0 and  $t/2$  such as :

$$\dot{m}_a(t_1) = 0 \quad (13)$$

and  $\dot{m}_a > 0$  for  $t > t_1$ .

The relationship between  $t$  and  $t'$  has the same physical meaning as for an O.P.T.R. But, as  $\dot{m}_a$  cannot be measured directly,  $t'$  must be numerically deduced from  $t$  by the following integral equation :

$$\int_{t_1}^t \dot{m}_a(t) dt = - \int_{t_1 - T/2}^{t'} \dot{m}_a(t) dt \quad (14)$$

$\langle \dot{q} \rangle_{\text{exp}}$  is then compared to the theoretical value of the ideal D.I.P.T.R. by using the same double-weighing method as described above.

In the two Pulse Tube Refrigerators, the regenerator losses  $\langle \dot{q}_c' \rangle$  can be deduced from measurements of the gross refrigeration power  $\langle \dot{q} \rangle$  and from the effective available power at the cold part  $\langle \dot{q}_c + \dot{q}_c' \rangle$ . With our experimental apparatus, errors in measuring  $\langle \dot{q} \rangle_{\text{exp}}$  are lower than 1 %. Both the theoretical gross refrigeration power of the O.P.T.R. and of the D.I.P.T.R. are known with a 5 % precision. Some experimental results are reported in Ref. 1.

## REFERENCES

- 1 M. David, J-C. Maréchal, Y. Simon and C. Guilpin, "Theory of the ideal Orifice Pulse Tube Refrigerator", CRYOGENICS, to be published.
- 2 R. Radebaugh , "Pulse Tube Refrigeration - A New Type of Cryocooler", Proceedings of the 18th International Conference on Low Temperature Physic (Kyoto, Japan 1987), Journal Appl. Phys., Vol. 26 p 2076, (1987).

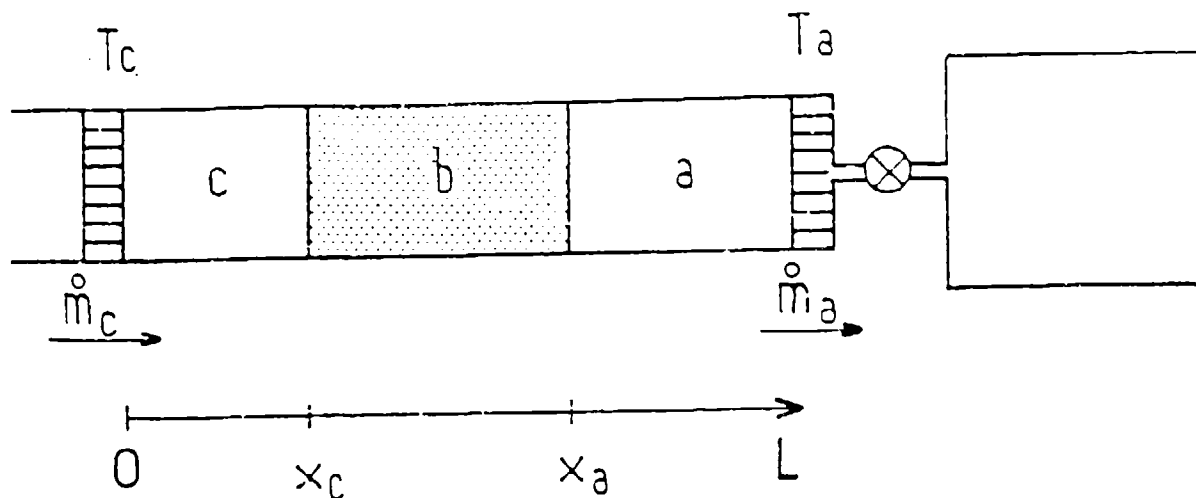


Figure 1 : Schematic of the Orifice Pulse Tube. The gaz (b) referred never leaves the tube

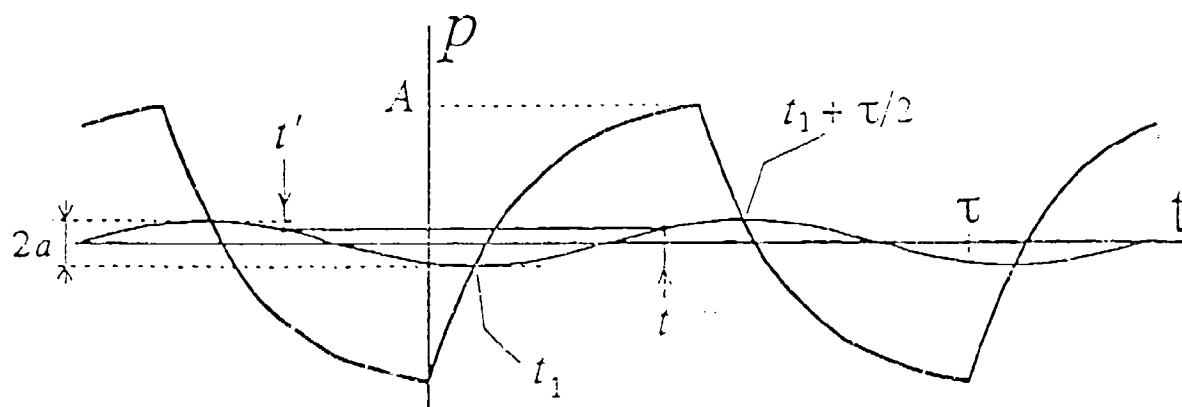


Figure 2 : The gaz pressure in the tube (alternate exponential) and the pressure in the reservoir as function of time when a valved compressor is used

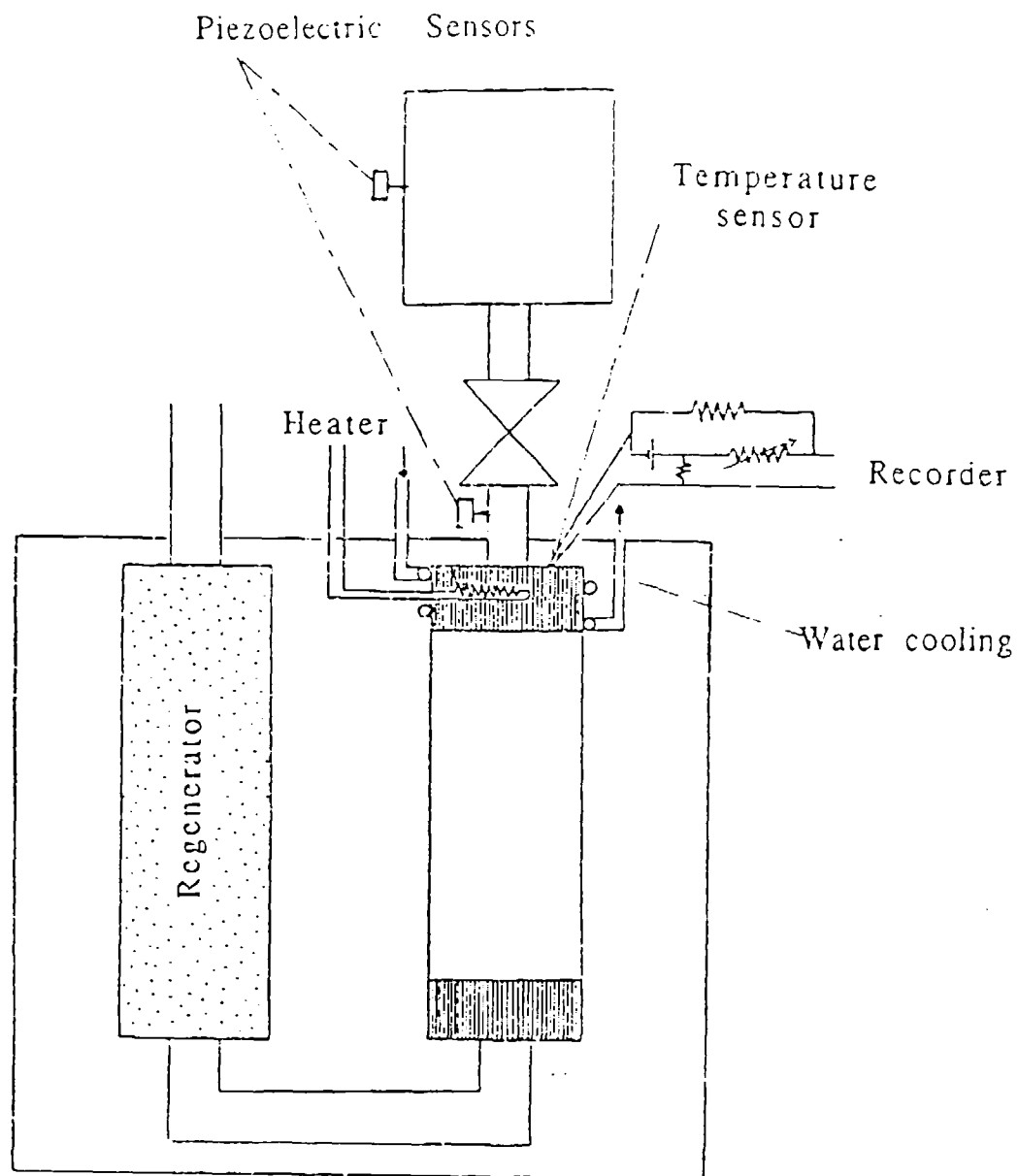


Figure 3 : Experimental apparatus for the gross refrigeration power measurement

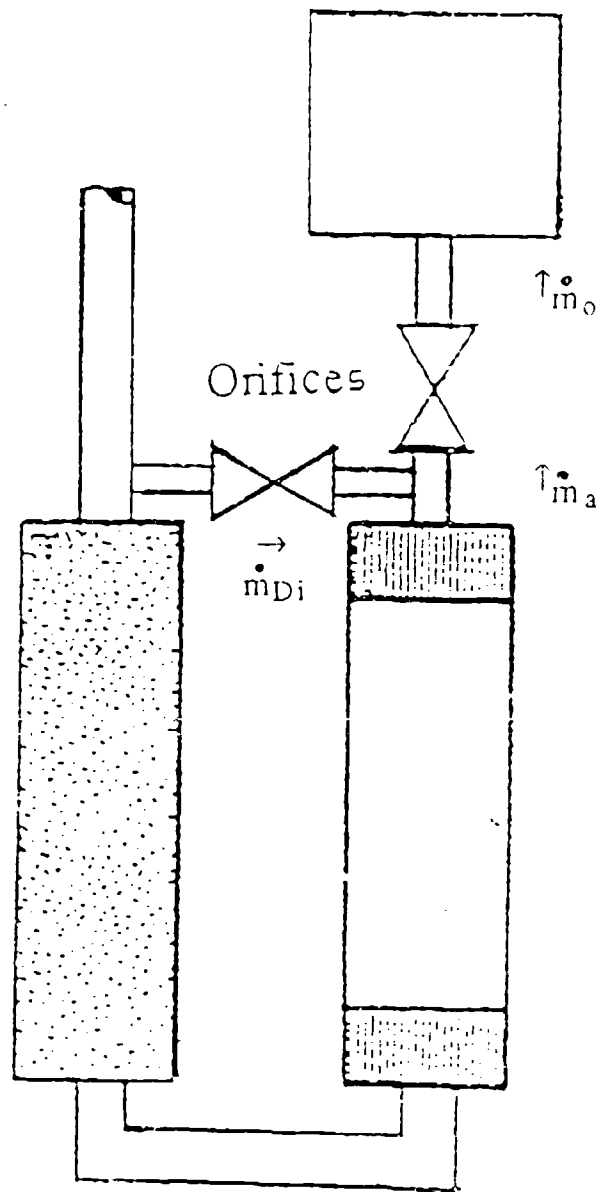


Figure 4 : Schematic of Double Inlet Pulse Tube Refrigerator

## **CRYOCOOLER TIP MOTION SUPPRESSION USING ACTIVE CONTROL OF PIEZOELECTRIC ACTUATORS**

R. J. Glaser, R. G. Ross, Jr. and D. L. Johnson

Jet Propulsion Laboratory  
California Institute of Technology  
Pasadena, California 91109

### **ABSTRACT**

Under Strategic Defense Initiative Office (SDIO) sponsorship the Jet Propulsion Laboratory is developing a flight experiment to demonstrate advanced control technologies for quieting cryocooler tip vibration in three axes. The experiment is scheduled to fly as a small 15-watt payload on the Space Technology Research Vehicle (STRV-1b), a small English satellite scheduled for launch on the Ariane-4 in late 1993. To meet stringent power, weight, and space constraints, the experiment makes use of a tiny 1/5-watt 80K Texas Instruments tactical Stirling cooler. Two different vibration-cancellation actuator techniques are being demonstrated: 1) an applique ceramic piezoelectric actuator set that is bonded to the coldfinger and stretches the coldfinger to cancel tip motion, and 2) a commercial low voltage piezoelectric translator set that similarly cancels tip motion by moving the entire cryocooler in three axes. Motion of the coldfinger tip is measured in all three axes to 10 nanometer accuracy using eddy-current transducers. Two types of control systems are also being demonstrated: 1) an adaptive feed-forward digital control system that continually updates the harmonic content of the steady-state command signal to each actuator to cancel the tip vibration, and 2) an analog control system that uses a bandpass filter to track the drive signal and suppress it. Either control system can be used with either actuator system.

### **INTRODUCTION**

If uncompensated, the moving parts and pressure pulses within the compressor and displacer of a Stirling-cycle cryocooler can create considerable mechanical vibration that can adversely affect the performance of a precision space-science instrument. This vibration can consist of either the transmission of vibration forces from the cryocooler into the instrument via the cooler supports, or vibratory motion of the tip of the cryocooler coldfinger relative to the instrument optical bench; this latter category--cold tip motion--is particularly important for applications where the detector is directly mounted to the cooler cold tip.

Considerable progress has been made in recent years using momentum compensated, back-to-back coolers together with active vibration control systems to minimize the level of transmitted vibration force [1,2,3]. However, much less emphasis has been placed on the challenge of cold tip vibratory motion suppression.

There are two fundamental manifestations of cold-tip vibratory motion: 1) motion of the coldfinger cold-tip relative to the base of the cold-finger, and 2) motion of the overall cryocooler including the coldfinger. The largest component of the cold-tip relative motion is caused by mechanical distortion of the cold finger caused by the large sinusoidal pressure variation (typically around 300 psi peak-to-peak) that is output from the cryocooler compressor. This cyclic pressure loading, which is fundamental to the Stirling-cooler operation, results in the cold finger undergoing cyclic elongation along its longitudinal axis, and can lead to lateral bending of the cold finger if the wall thickness of the cold-finger is not uniform around its circumference. The lateral motion is also amplified by the natural cantilever-bending-mode resonances of the coldfinger.

As shown in Fig. 1, the resulting motion of the coldfinger tip is often on the order of one to two microns in the longitudinal (Z) axis, and is somewhat less in the lateral (X,Y) directions [4]. Notice the high level of fifth harmonic in the lateral vibration in Fig. 1; this is caused by the first lateral bending frequency of the coldfinger being close to the fifth harmonic of the 60-Hz drive signal. Thus, the high frequency lateral response is considerably amplified by the lateral modal response of the coldfinger.

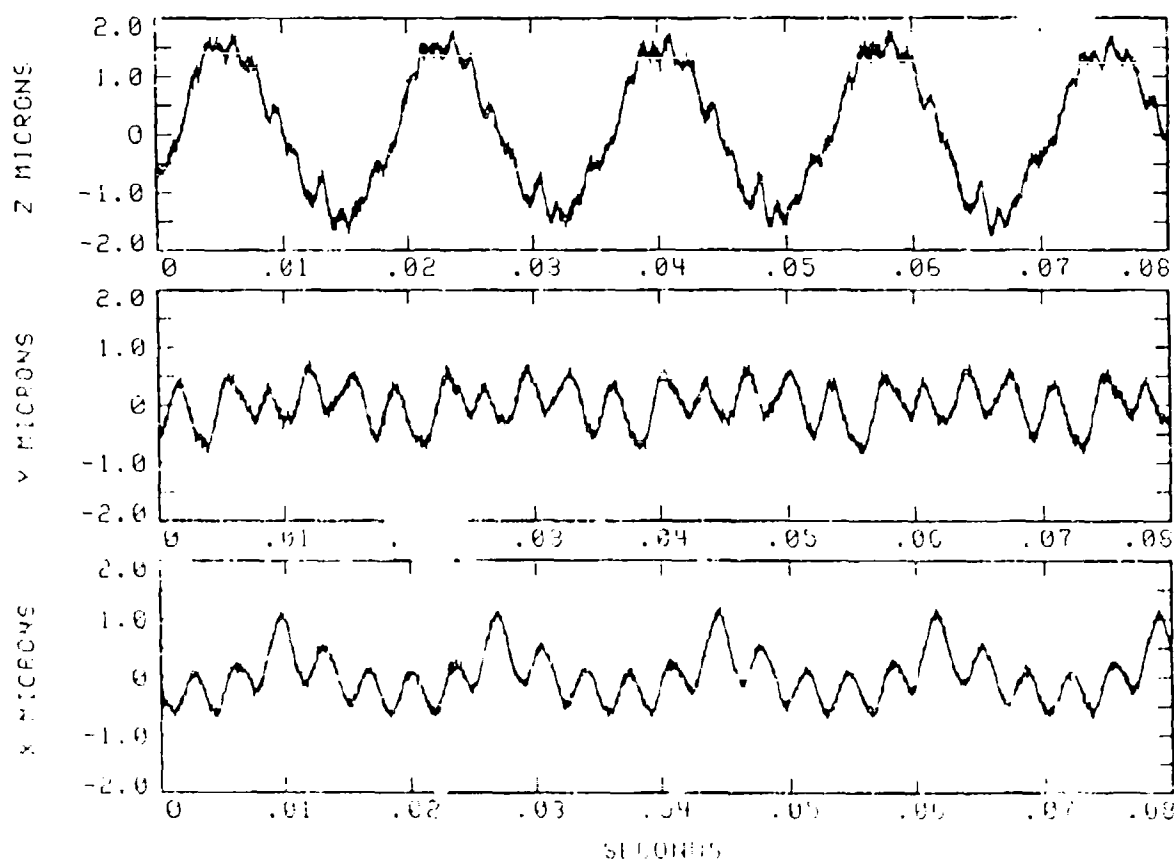


Fig. 1 Typical measured cold finger tip motion



FLIGHT EXPERIMENT OBJECTIVES

The primary objective of the JPL STRV cryocooler vibration suppression experiment is to demonstrate the applicability of piezoelectric motion suppression technology to the problem of cryocooler cold-tip motion suppression. In addition to gathering engineering data on the performance of the unique control-system features, the experiment will also provide a flight-heritage ensuring that the technology has successfully dealt with the important spacecraft interface issues including launch survivability, tolerance to operating temperatures, EMI compatibility, and radiation hardness: in short, successfully building a flight experiment demonstrates that the technology is mature enough to fly. It is expected that the availability of successful flight data will speed the adoption of these technologies by future applications, as unexpected problems will already have been uncovered. Since a variety of techniques are being demonstrated, comparisons can be made between the techniques, and informed choices can be made for future projects.

In addition to the primary objectives for the experiment, there are also two secondary objectives: one is to measure the vibration of the satellite resulting from the operation of the cryocooler; the second is to provide a cryogenically cooled environment for a two-pixel IR-detector experiment mounted to the coldfinger tip. The IR experiment involves measuring the detector dark current as a function of the integrated radiation exposure as the satellite passes through the Van Allen belts. With the limited power of the STRV-1b satellite, the longest duration of continuous cooling is likely to be a period of a few days when the satellite is in continuous sunlight.

SPACE TECHNOLOGY RESEARCH VEHICLE (STRV-1B)

The STRV-1b is a small 50-kg British Royal Aerospace Establishment (RAE) satellite [5] being designed to fly on a French Ariane-4, and will be placed into a geostationary transfer orbit that involves passing through the Van Allen belts twice per 10.5-hour orbit. As a result, the satellite will receive approximately 100 krad/yr radiation exposure at the outside of its structure, and will have a design life of one year.

The satellite is about the size of a PC computer (480×480×400 mm), is spin stabilized at 5 rpm, and uses a nutation damper and a magnetorquer to maintain spin stabilization. Power, which is extremely limited, is provided by solar cells on the surface of the satellite. Temperature control is entirely passive, with the internal payloads designed to operate between -50°C and 50°C.

Communications are provided by the RAE from Farnborough with a capability of 125 bits/sec uplink and 1000 bits/sec downlink. Data storage is limited to 50 kbytes of data and 30 kbytes of commands.

The mechanical part of the cooler experiment is allocated 1.75 kg of mass. In addition to the cooler, the total JPL STRV experiment includes an electronics box containing three radiation exposure experiments and the cooler electronics. This electronics box is allocated 4.75 kg of

mass and  $400 \times 150 \times 75$  mm of space. The radiation exposure experiments are a chip sized radiation monitor, an advanced IR detector, and a neural net chip. The STRV also contains a European radiation-environment monitor, a solar cell technology experiment, laser reflectors, and several technology items incorporated into the basic satellite design.

In one respect the STRV-1b satellite provides an ideal testbed for a hardware demonstration because the demanding constraints of its environment should encompass most future applications of vibration suppression technology. There is very little power, space, weight, or data storage. In addition, the thermal and radiation environments are very severe.

### CRYOCOOLER EXPERIMENT MECHANICAL DESIGN

Figure 2 illustrates the hardware elements of the experiment. These include:

- Texas Instruments 1/5-watt 80K tactical Stirling cooler
- Physik P-842.10 low voltage piezo translators
- $120^\circ$  tubular segments of Vernitron PZT5H applique ceramic bonded to the coldfinger
- Kaman SMU 9200-15N eddy current displacement transducers
- Lake Shore Cryotronics PT-111 platinum thermometers
- Kistler 8692B5M1 triaxial accelerometer
- Assorted structural elements including thermal mounting plate, motor-mount truss, titanium flexures, housing, housing bottom, and non-flight lid

The Texas Instruments 1/5-watt 80K tactical Stirling cooler is a back-to-back, dual-piston, linear-drive compressor with integral displacer mounted orthogonal to the compressor piston axis; this balanced, dual-piston cooler achieves a low vibration level below 5 N.

The cooler weighs 380 grams without electronics and is about 100 mm long by 40 mm in diameter. The coldfinger is about 70 mm long and 6.35 mm in diameter. In the experiment, the cooler will be operated with a cold-tip temperature of 95 K; this will require between 3.75 and 5.75 watts of input power, depending on the heatsink temperature between  $-32^\circ\text{C}$  and  $50^\circ\text{C}$ . The cooler is not designed to operate at heatsink temperatures below  $-32^\circ\text{C}$ .

### Piezoelectric Actuator Design

Two different vibration cancellation actuator techniques are being demonstrated in the experiment: 1) an applique ceramic piezoelectric actuator set that is bonded to the coldfinger and stretches the coldfinger to cancel tip motion, and 2) a commercial low voltage piezoelectric translator set that similarly cancels tip motion by moving the entire cryocooler in three axes.

In the first actuator technique a set of three ceramic appliques is used to stretch the coldfinger itself to cancel the cold tip lateral motions as well as the longitudinal motion. The process for

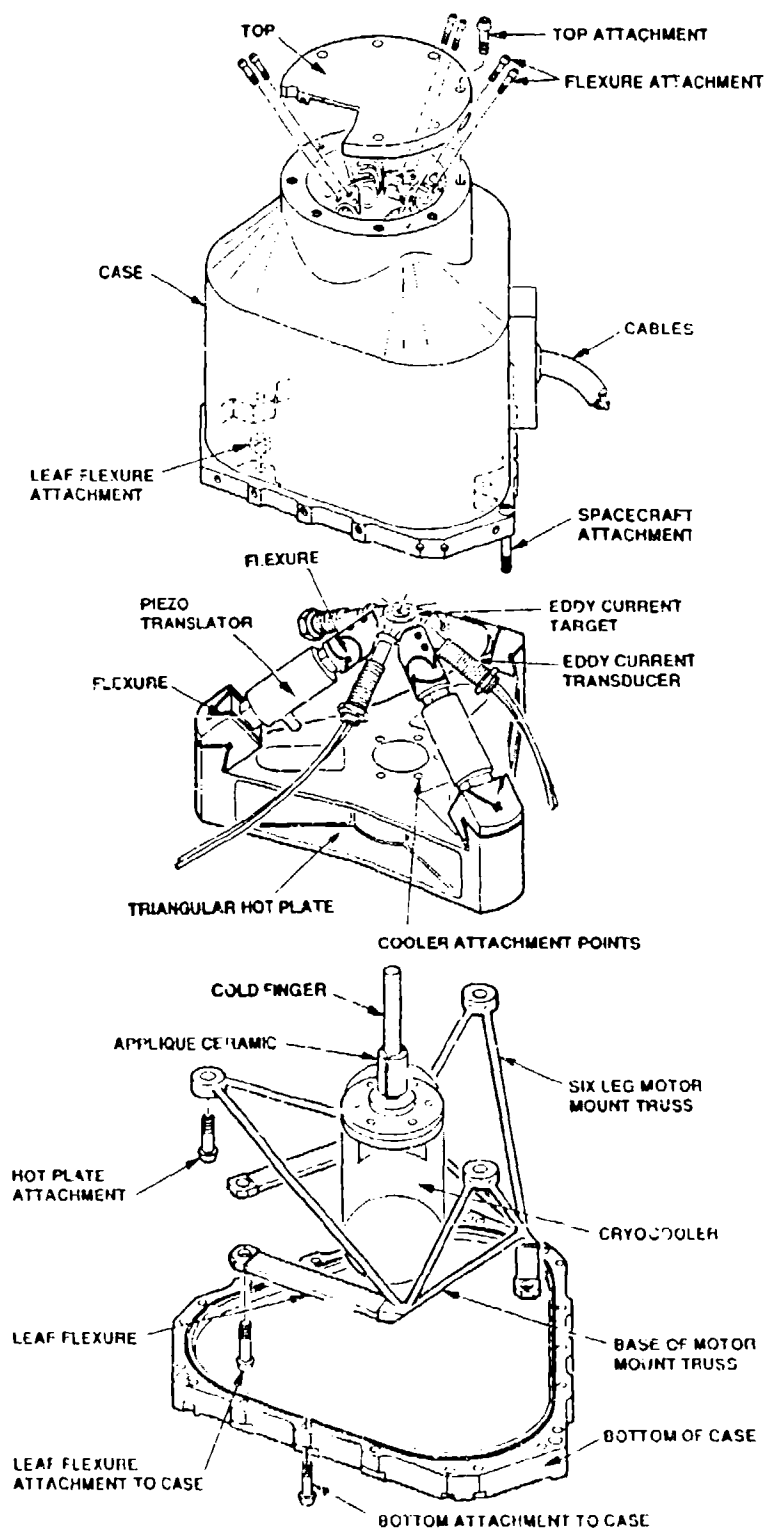


Fig. 2. Mechanical components of cryocooler vibration suppression experiment.

fabricating and using the applique ceramics was developed as part of the flight experiment.

The ceramic length (25.4 mm), thickness (1 mm), voltage (500 volts), and material (Vernitron's PZT5H) were selected to optimize the applique performance. The ceramic tube is cut into three parts using a diamond saw, and is bonded to the coldfinger using Hysol 9396. The bond line thickness is 0.0254 mm and is maintained with glass fiber threads uniformly wrapped around the coldfinger. During the bonding process, the specimen is clamped along its entire length between two precision-machined circular clamps. The clamp is designed to leave just enough room for the ceramic and bond-line without causing deformation. The coldfinger is also pressurized to 68 atm and raised to 93°C throughout the 1-hour bonding process. Conducting the bonding operation while pressurized and heated preloads the ceramic in compression upon cooling; this helps ensure that the ceramic will not be placed in tension during normal operation.

In the second piezoelectric actuation technique, three Physik P-842.10 low voltage piezo translators are used to move the entire cooler to cancel the tip motion. These piezos are designed to move 18  $\mu\text{m}$  at 120 volts, but are being operated at 32 volts to provide 4.8  $\mu\text{m}$  of motion. The actuators have been preloaded to 450 N to prevent the translators from experiencing tension during launch. The capacitance of these actuators is 1.8  $\mu\text{F}$ , and the power consumption is expected to be about 0.1 watts per actuator.

#### Eddy-Current Motion Sensing

To provide the necessary cold-tip motion feedback to the control system, motion of the coldfinger tip is measured in all three axes to 10 nanometer accuracy using eddy-current transducers. The Kaman SMU 9200-15N eddy-current transducers are a non-contacting method of precisely measuring the distance between an aluminum target attached to the coldfinger tip and the cryocooler experiment structural housing. The units have the additional advantage that their signal processing electronics are very small (about 5 cm by 5 cm of board space) and consume very little power (about 0.1 watts/channel). Although some penalty in sensitivity was accrued, the distance between the eddy-current transducer and the target was opened up to 0.5 mm to maintain sufficient clearance for launch. More clearance would be needed if the support structure was not as stiff as it is. The cooler supports (including the piezo translators) are designed to maintain the first-mode resonance above 400 Hz.

In another aspect of the transducer selection and operation, there was initially concern that the eddy-current electronics would suffer degradation due to the severe radiation environment. Subsequent testing revealed significant shifts in the DC measurement over the radiation range expected in flight. However, the AC gain of the device was not sensitive to radiation. As a result of these tests, and to increase tolerance to differential thermal expansion motion, the eddy-current transducers were AC coupled for this application.

#### Thermal and Vibration Instrumentation

To measure the temperature of the coldfinger and the heatsink, Lake Shore Cryotronics PT-111 platinum thermometers were selected based on their good radiation resistance [6]. Custom

electronics were developed to operate the thermometers in pulse mode so that current will only be applied to the thermometers when measurements are being made.

Finally, a Kistler 8692B5M1 triaxial accelerometer was selected to measure the very small acceleration levels associated with the cooler vibration. The expected vibration force--of the order of 5 N--will move the 50 kg spacecraft approximately 0.01 g at the cooler drive frequency of 60 Hz. The accelerometer was selected based on its good sensitivity and low power consumption. Again, custom electronics were developed to operate the accelerometers in the STRV environment.

### VIBRATION SUPPRESSION ELECTRONICS

Two types of control systems are being demonstrated in the STRV vibration suppression experiment: 1) an adaptive feed-forward digital control system that continually updates the harmonic content of the steady-state command signal to each actuator to cancel the tip vibration, and 2) an analog control system that uses a bandpass filter to track the motion signal and suppress it. Either control system can be used with either of the above two piezoelectric actuator systems. A block diagram of the overall experiment electronics is presented in Fig. 3.

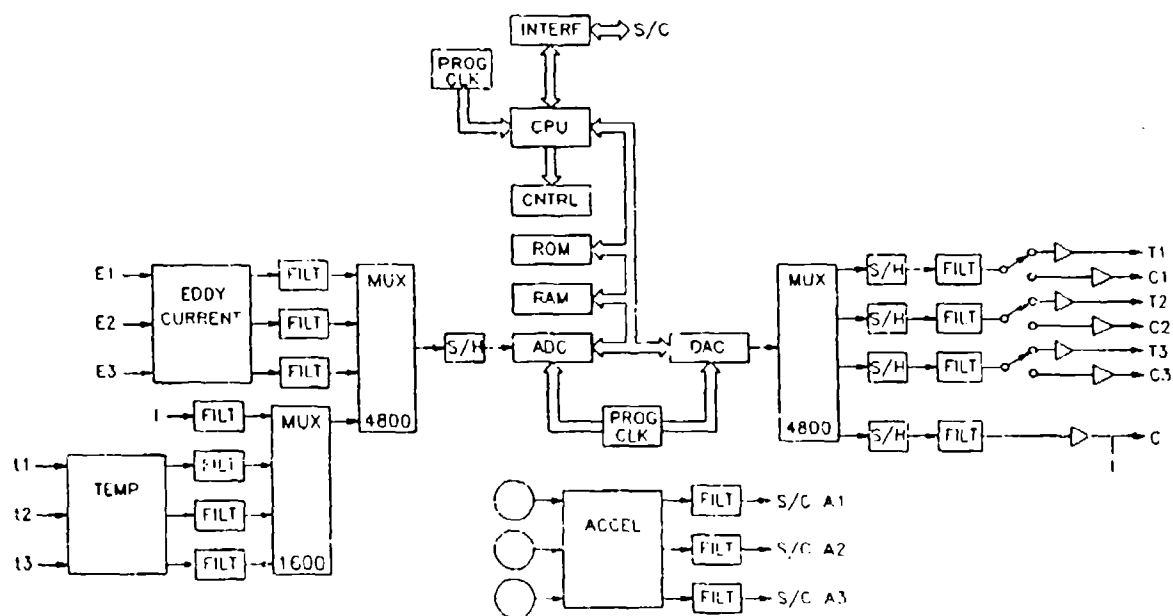


Fig 3. Block diagram of the vibration-suppression experiment electronics.

Digital Adaptive Feed-forward Control

The three-axis, digital adaptive feed-forward control system is based on the control of four signal generators: one 80-point digital waveform generator outputs a sinusoid to the cooler at the fundamental 60-Hz cooler drive frequency; the other three 80-point waveform generators output harmonic waveforms of the drive frequency to the piezo actuators and are adjusted to exactly cancel the cold-tip motion. The central processor unit (CPU) is used to setup the waveforms initially, and to update the waveforms to reflect gradual changes in the cooler transfer functions over time (approx. 1/3 second per update).

At the start of cryocooler operation, the waveform buffers are loaded with arbitrary sinusoidal command signals, and the change in the cold-tip displacement signals is measured. This provides the transfer function between the cooler drive electronics and the resulting cryocooler cold-tip motion. The resulting system of equations is then solved for the command signals that will cancel the vibration. From this point on, the system continuously updates the transfer functions and the command signals to cancel the tip motion. Corrections are always made one channel at a time. This allows the effect of the change on the three eddy-current transducers to be isolated.

Once underway, the CPU is not directly involved in operating the waveform generators. The waveform generator front-end continuously outputs the waveforms from the circular buffers. This is done using direct memory access (DMA) from the CPU to avoid bus contention between the four channel waveform generator and the CPU. Internally the memory is double buffered. One buffer is accessed by the DMA while the other buffer is accessed by the CPU. Switching between buffers is commanded by the CPU and occurs on the next frame boundary.

To drive the cooler and actuators, a programmable clock cycles through the data, converting the digital waveforms to volts with a 12-bit digital-to-analog convertor (DAC). The DAC output is demultiplexed and held with a sample-and-hold. The four sample-and-hold signals are filtered and amplified to drive the cooler and the vibration-suppression actuators. This electronics is illustrated on the right side of Figure 3.

To obtain the motion feedback signal, three eddy-current transducers are multiplexed and held for the ADC by a sample-and-hold. Again, access to the bus is managed using DMA to avoid bus contention. Also, the input data is double buffered in the same manner as the output data. Both the input and output buffers switch together, with one command, to keep the data synchronized.

The software extracts drive-harmonic amplitudes from the eddy-current signals using a curve-fitting procedure based on Equation 1. This deceptively normal-looking set of definitions hides the basic difference between a harmonic analysis and a general Fourier analysis. Normally there is no period,  $\lambda$ , for the signal to repeat, and the length of acquired data is arbitrary. In a harmonic analysis, the length of data acquired,  $n_b T$ , is one period,  $\lambda$ .  $T$  is the time between samples and  $n_b$  is the number of points in the buffer. In the STRV case,  $n_b = 80$  (10 points on 8 harmonics),  $\lambda \approx 1/60$  seconds,  $T \approx 1/4800$  seconds ( $60 \text{ Hz} \times 10 \text{ points} \times 8 \text{ harmonics}$ )<sup>1</sup>.

$$\text{signal}(t) = \sum_{m=1}^8 S_m \sin\left(\frac{2\pi m}{n_b T} t\right) + C_m \cos\left(\frac{2\pi m}{n_b T} t\right)$$

$$S_m = \frac{2}{n_b} \sum_{i=1}^{n_b} \sin\left(\frac{2\pi m}{n_b} i\right) \text{signal}(iT) \quad m = 1, 2, \dots, 8 \quad (1)$$

$$C_m = \frac{2}{n_b} \sum_{i=1}^{n_b} \cos\left(\frac{2\pi m}{n_b} i\right) \text{signal}(iT) \quad m = 1, 2, \dots, 8$$

Once the harmonic drive amplitudes have been determined using Equation 1, the change in the eddy-current signal ( $D_i$ ) from the previous time is calculated, and the ratio of the change in eddy-current signal to the change in command signal ( $C_i$ ) is calculated. This is done using Equation 2.

$$\frac{\partial D_k}{\partial C_j} = \frac{\Delta D_k}{\Delta C_j} = \frac{(C_n(k) + i S_n(k)) - (C_o(k) + i S_o(k))}{C_c(j) + i S_c(j)} = \quad (2)$$

$$\frac{[(C_n(k) - C_o(k)) C_c(j) + (S_n(k) - S_o(k)) S_c(j)] + i [(S_n(k) - S_o(k)) C_c(j) - (C_n(k) - C_o(k)) S_c(j)]}{C_c(j)^2 + S_c(j)^2}$$

In Equation 2, the subscript n means now, o means old, and c means command. The partial derivatives derived in the above process are next entered into Equation 3:

$$\begin{Bmatrix} \Delta D_1 \\ \Delta D_2 \\ \Delta D_3 \end{Bmatrix} = \begin{bmatrix} \frac{\partial D_1}{\partial C_1} & \frac{\partial D_1}{\partial C_2} & \frac{\partial D_1}{\partial C_3} \\ \frac{\partial D_2}{\partial C_1} & \frac{\partial D_2}{\partial C_2} & \frac{\partial D_2}{\partial C_3} \\ \frac{\partial D_3}{\partial C_1} & \frac{\partial D_3}{\partial C_2} & \frac{\partial D_3}{\partial C_3} \end{bmatrix} \begin{Bmatrix} \Delta C_1 \\ \Delta C_2 \\ \Delta C_3 \end{Bmatrix} \quad (3)$$

By inverting the matrix, Equation 3 is solved for the change in command signal needed to cancel the measured eddy-current displacements. Only one command is solved for at a time, using Cramer's rule. If more than one command is updated, it is not possible to identify which part of the change is caused by which command.

### Analog Control

To assess the relative advantages of digital and analog vibration control systems, the STRV experiment also includes an analog cold-tip motion control system based upon feeding back the eddy-current signals to adjust the command voltages to cancel the cold-tip displacements.

The feedback-system parameters are derived empirically, based upon measured properties of the complete cooler system. This is done by commanding a voltage on each command line, and measuring the resulting eddy-current displacements. This provides the parameters for a system of equations, similar to Equation 3 above, that can be inverted to provide the resulting coefficients for the analog circuit.

Unfortunately the equations for the ceramic appliques are not the same as for the piezo translators. For this reason, the control system must switch between the two systems of equations, depending on the actuators being used.

In order for the analog system to remain stable, the frequency content of the closed-loop circuit must be limited. The first structural flexibility of the system is expected to be the lateral bending of the coldfinger around 300 Hz. The next highest mode is a 420-Hz bounce mode where the cryocooler bounces on the translators. Around these frequencies the phase of the eddy current displacement will change significantly from the rigid-body response characteristic that predominates near the 60-Hz cooler drive frequency. As a result, the control system must be carefully designed to avoid instabilities at these frequencies.

Initial attempts to use a simple cutoff filter to achieve the necessary stability margin were unsuccessful. As a result, the final system design uses a system of tracking filters tuned to the drive frequency. These are implemented with switched-capacitor filters driven from the digital programmable clock.

### Cryocooler Drive Electronics

During operation, the electrical drive of the cryocooler compressor is also controlled by the digital controller electronics; this guarantees frequency and phase locking between the two systems. The cryocooler drive control includes closed-loop control of the cold-tip temperature, and closed-loop control of the cooler drive frequency to obtain maximum drive motor efficiency. This maximum motor efficiency is achieved if the cryocooler is operated at its mechanical resonant frequency, which also corresponds to the point where the cooler drive current and voltage are in phase (unity power factor).

Based upon cold-tip and heat-sink temperature measurements, the temperature controller works on a simple dead-band principle whereby two temperature limits (e.g., 94.75 K to 95.25 K) are established. When the coldfinger temperature is above the high limit, 95.25 K, the cooler drive voltage is increased slightly to drive the temperature down; when the coldfinger temperature is below the lower limit, 94.75 K, the cooler drive voltage is decreased slightly, allowing the temperature to increase. Precise control is not needed in this application.



In addition to the temperature measurements, the current going to the cryocooler is measured to establish the phase angle between the current and the voltage. Equation 1 is used to curve fit the current to calculate the phase angle. When the phase angles are the same, the drive frequency is on resonance. During operation, the current and voltage at digital frequencies on either side of the nominal 60-Hz frequency are used to update the drive frequency and bring the cooler back into resonance. The drive frequency is changed by the programmable clock in the flow diagram in Figure 3.

The frequency controller takes advantage of the rapid change in phase angle compared to the change in temperature. Frequency tables provide a starting point, and give changes to be applied for heatsink variations.

### SUMMARY

STRV-1b offers an interesting opportunity to test state-of-the-art piezoelectric adaptive control technologies in orbit. The many challenges associated with STRV, e.g., a maximum of 20 watts of power, poor thermal control, very little available weight, and a high radiation environment, have led to a number of innovative developments that should be useful for future applications.

Two types of control-system drive actuators have been developed and are being contrasted: an applique ceramic applied directly to the coldfinger, and piezo translators supporting the entire cooler. New, non-contacting, low-wattage, low-profile eddy-current transducers are being used to measure the cryocooler cold-tip displacement amplitudes.

Two types of control systems are also being contrasted: a fully adaptive digital control system that controls both the cryocooler and the vibration suppression, and an analog controller that uses a tracking filter to suppress the fundamental drive frequency. Either control system can operate either type of actuator. This redundancy provides some protection against total loss of the experiment due to single-point failures; however, several single-point failures do exist in the experiment (e.g., loss of the CPU).

The digital control concept developed here is applicable to a wide variety of vibration suppression hardware. Force cancellation, or dual drive coils, could easily be accommodated within the same control system.

### ACKNOWLEDGEMENT

The work described in this paper was carried out by the Jet Propulsion Laboratory, California Institute of Technology, and was sponsored by the Strategic Defense Initiative Organization/Air Force Phillips Laboratory through an agreement with the National Aeronautics and Space Administration.

REFERENCES

1. Johnson, B.G., et al., "Demonstration of Active Vibration Control on a Stirling-cycle Cryocooler Testbed", Proceedings of the American Control Conference, Chicago IL, June 24-26, 1992.
2. Johnson, B.G., et al., "Demonstration of Active Vibration Reduction on a Stirling-cycle Cryocooler Testbed", 7th International Cryocooler Conference, Santa Fe, NM, November 17-19, 1992.
3. Aubrun, J-N., et al., "A High Performance Force Cancellation Control System for Linear Drive Split Cycle Stirling Cryocoolers", Adv. Cryo. Engin., Vol. 37B (1991).
4. Ross, R.G., Jr., Johnson, D.L. and Kotsubo, V., "Vibration Characterization and Control of Miniature Stirling-cycle Cryocoolers for Space Application," Adv. Cryo. Engin., Vol. 37B (1991), pp 1019-1027.
5. Kyden, K. A., "The Space Technology Research Vehicle (STRV-1," Proc. Roy. Aero. Soc. Conf. on Small Satellites, Culham Laboratory, UK, January 24, 1991.
6. Courts, Scott, "Neutron and Gamma Radiation Effects on Temperature Sensors," presented at the 7th International Temperature Symposium, Toronto, Canada, April 28-May 1, 1992.

## HIGH TEMPERATURE SUPERCONDUCTING SPACE EXPERIMENT CRYOGENIC SYSTEM OVERVIEW

Thomas Kawecki  
Systems Analysis Branch  
Spacecraft Engineering Department  
Naval Center for Space Technology  
U.S. Naval Research Laboratory  
Washington, DC 20375

### ABSTRACT

The High Temperature Superconductivity Space Experiment (HTSSE) program was initiated by the U.S. Naval Research Laboratory (NRL) in 1988 to promote and develop the potentially significant benefits of utilizing High Temperature Superconducting (HTS) materials in satellite electronic components. Long life, high reliability cryogenic cooling in the 60 to 80K range is essential for the successful utilization of HTS electronics in operational space applications. The new generations of clearance seal Stirling cycle mechanical refrigerators offer the potential for continuous, >5 year operation at >0.95 reliabilities, but there has been little space flight experience. In addition to testing HTS device performance in the space environment an important HTSSE objective is to develop the engineering experience to integrate, launch, and operate long life spacecraft cryogenic systems. The HTSSE cryogenic subsystem consists of 15 microwave HTS experiments cooled by a production British Aerospace (BAe) 80K cryocooler. Extensive on-board instrumentation monitors cryocooler performance and assists in problem diagnosis from the ground. HTSSE has been integrated and tested on a host DOD spacecraft and awaits a 1993 launch. This paper describes the thermal design, instrumentation, and integration experience of utilizing a BAe cryocooler in a HTS space application.

### INTRODUCTION: THE HTSSE PROGRAM

Each new evolutionary step in electronic technology has led to commensurate increases in spacecraft capabilities. This is evident by comparing the history of spacecraft system capabilities with the development of the transistor, IC, and VLSI. In late 1987, just after the discovery of HTS materials with a  $T_c$  above 90K, and in-house NRL survey of ongoing HTS R&D was conducted. The result of the study indicated that the potential benefits of HTS materials for enhancing satellite electronic components was potentially significant. In 1988, NRL formulated the HTSSE program in three successively more sophisticated phases: HTSSE-I, HTSSE-II, and HTSSE-III to promote the development of HTS technology into space applications. The HTSSE plan is to demonstrate HTS viability and survivability on HTSSE-I to be launched in 1993, demonstrate advanced

HTS devices on HTSSE-II in a 1996 launch, and eventually demonstrate operability of a fully functional HTS system in a 2000 launch of HTSSE-III. The HTSSE program goal was to provide a focus and a forum for the HTS R&D community to make practical hardware for space applications and to develop and demonstrate the critical cryogenic subsystems required to support HTS technology. The approach was to provide the HTS community access to space and leverage off of existing HTS programs such as those funded by DARPA, SDIO, NASA, and corporate R&D efforts. HTSSE does not fund research in HTS device development but does fund adapting and repackaging HTS devices for the HTSSE payload.

HTSSE-I, the subject of this paper, contains 15 HTS experiments from government, industry, and academia. These HTS experiments will demonstrate passive microwave circuit devices including: thin-film ring and linear resonators, coated-bulk cavity resonator band-pass filter, branchline coupler, and a miniaturized patch antenna. Most of these devices have one to two orders of magnitude increase in quality factor (Q), or reduction in size as compared to normal metal circuitry. HTSSE-I is a secondary experiment on a DOD spacecraft and runs on the BOL power margin of the spacecraft. The host spacecraft orbit will subject HTSSE-I hardware to a fairly high radiation dose of  $10^6$  to  $10^8$  rads(Si) in the planned 6 month life of the experiment. The six dosimeters on board HTSSE will allow correlation of device degradation with high energy particle dose, if observed. Both the electronic and mechanical systems of HTSSE-I were conceived, designed, fabricated, and tested at NRL in a short time to meet the host spacecraft schedule. Concurrent engineering and development of the HTS experiments and HTSSE-I flight experiment was necessary to meet the schedule. Preliminary design review, to the delivery of flight hardware was a 14 month period. HTSSE-I has been integrated on host spacecraft and tested successfully and is awaiting a mid 1993 launch.

There are three subsystems to HTSSE-I the cryogenic experiment subsystem, the microwave measurement subsystem, and the digital control electronic subsystem. The microwave measurement subsystem functions as a scalar network analyzer which measures insertion loss of the HTS devices. The digital control electronics subsystem performs command, control, signal processing and data collection for all HTSSE-I subsystems. Cryocooling is provided by a British Aerospace (BAe) 80K cooler, one of the first production lot of 6 cryocoolers that BAe has built. An important part of the HTSSE program is to develop and demonstrate the cryogenic subsystems necessary for HTS space applications. For this reason the cryogenic package and cryocooler have been extensively instrumented to provide health status and diagnostic capabilities while on orbit. This paper

presents the thermal environment and performance of HTSSE-I, thermal and structural design specifics of the BAe cryocooler interface, and information on the cryogenic subsystem diagnostic instrumentation included on HTSSE-I.

### HTSSE-I CONFIGURATION & ENVIRONMENT

The 15 HTS experiments and 4 conventional RF metal reference devices on HTSSE-I are packaged in the 9 inch diameter by 9 inch tall cryogenic cold bus. The cold bus is structurally secured in an aluminum frame by six glass-fiber epoxy composite straps. The HTS experiments and metal reference devices are radially located on the circumference of the cold bus for easy access and even unattenuated exposure to the high energy particles of the orbit environment. Figure 1, an early CAD drawing of the HTSSE-I experiment deck, illustrates the location of the cold bus, it's structure and the BAe 80K cryocooler.

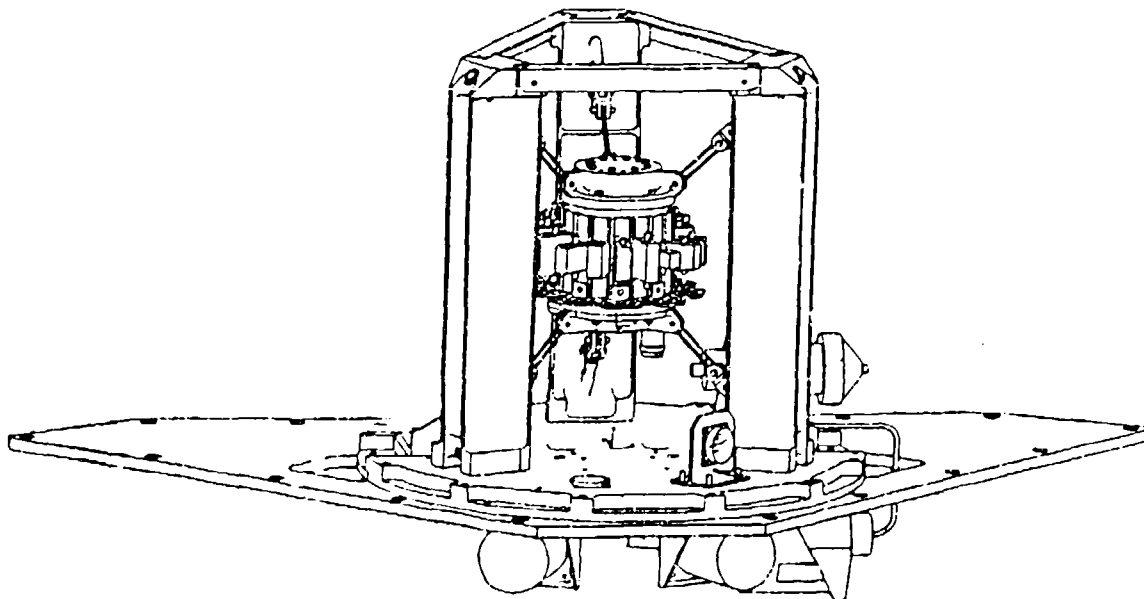


Figure 1. HTSSE-I Experiment Deck Without Thermal Blankets

The cold bus tension support structure is attached to a trapezoidal shaped honey comb deck that sits flush with the exterior skin of the spacecraft. The BAe cryocooler displacer is positioned just above deck with the cold finger protruding just underneath the cold bus. The flexible copper strap that conductively links the cold finger to the cold bus is not shown in this CAD drawing but is described in detail in the following section. The Helium

gas transfer tube of the BAE displacer can be seen leading to the compressor which is located under the deck. There are two 100 mil thick cylindrical aluminum radiation shields for the displacer and compressor which are not shown in this figure for clarity. Also not shown for clarity is a 40 layer MLI blanket on the cold bus to minimize thermal radiation parasitics and the silver Teflon surfaced radiators on the three sides and top of the tension strap frame to minimize the temperature of the outer MLI layer. The Lockheed Research Laboratory designed and fabricated a high performance 40 layer MLI radiation blanket. Heat is rejected from the cryocooler into the honeycomb deck and then radiated to space. Figure 2 shows the HTSSE-I experiment and electronics decks on the aft end of a spacecraft.

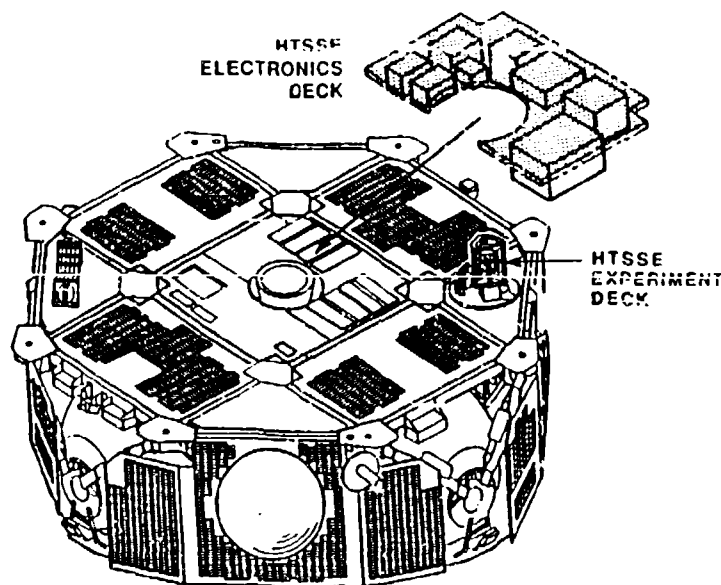


Figure 2. HTSSE-I Position on a Spacecraft Aft End

The spacecraft spins about its cylindrical center line. The sun angle varies between a  $45^\circ$  angle from the spin axis on the aft end to a  $45^\circ$  angle with the spin axis on the forward side of the spacecraft over a 120 day period. The hot condition occurs when the sun is  $45^\circ$  on the aft end at the end of life, the cold condition occurs at the beginning of life with the sun on the forward side. There are three principle thermal loads on the cryogenic cold bus; thermal radiation parasitics, conductive parasitics through the six tension support straps, and conductive parasitics through the coax I/O cables that interface with the HTS devices in the cryogenic cold package. There are two 0.021 diameter coax RF cables to provide input and output for each device making a total of 38 cryogenic I/O coax cables. Table 1 presents the significant thermal parameters of the hot and cold conditions of HTSSE-I.

<u>Parameter</u>	<u>Cold Case Condition</u>	<u>Hot Case Condition</u>
Cryogenic Parasitic Load		
MLI Radiation	131mW	205mW
Structure Conduction	59mW	72mW
<u>LO Conduction</u>	<u>60mW</u>	<u>79mW</u>
Total	250mW	356mW
Outer MLI Avg. Temp.	187K	227K
BAe Cryocooler Temp.	263K	293K
Cold Bus Temp.	77.0K	77.0K
Cryocooler Cold Tip Temp.	76.2K	75.9K
Displacer Stroke, p-p	2.9mm	2.9mm
Compressor Stroke, p-p	5.10mm	6.15mm

Table 1. Predicted On-Orbit HTSSE-I Hot and Cold Conditions

#### BAe CRYOCOOLER CRYOGENIC PAYLOAD INTERFACE

The BAe 80K cryocooler has been designed with the intent of meeting the long life and high reliability requirements of space applications. To accomplish this goal the Oxford University design has eliminated the wear mechanism of contacting dynamic seals in the compressor and displacer by using close gap clearance seals. Great design and assembly effort is exercised by the cryocooler manufacturer to maintain alignment of the regenerator piston within the cold finger bore of the displacer to avoid contacting. The cold finger inside diameter is the bore of the clearance seal. The cold finger is also designed to minimize the conductive parasitic heat flow from the warm displacer body to the cryogenic end in order to maximize cooling capacity. For this reason the cold finger has a thin wall and is vulnerable to deflection from transverse forces. A flexible conductive strap is employed at the cold finger/payload interface to minimize transverse forces. Flexibility is needed to allow for the mismatch that occurs from tolerance build up and thermal contraction, and to minimize force transfer during the dynamic launch environment. Conflicting requirements are inherent in thermal link design, flexibility is not compatible with the high thermal conductivity required to maximize the cryocooler cold tip temperature and thus cooling capacity. From the HTSSE-I perspective the thermal link interface is the highest risk aspect of integrating a clearance seal cryocooler in a space application. This section presents the configuration and performance of the HTSSE-I thermal link interface. HTSSE-I thermal link was not fully optimized due to the short development schedule but

does seem to offer a good compromise between flexibility and conductivity. HTSSE-I utilized a bundled copper wire approach for a thermal link design as shown in Figure 3.



Figure 3. Cryocooler / Cryogenic Payload Flexible Thermal Link

Flexibility and heat conduction are provided in this thermal link design by four fine wire bundles as shown. The copper end blocks interface with a the cryocooler cold finger and a beryllium stem that penetrates the cryogenic bus MLI as shown in Figure 4. To assemble

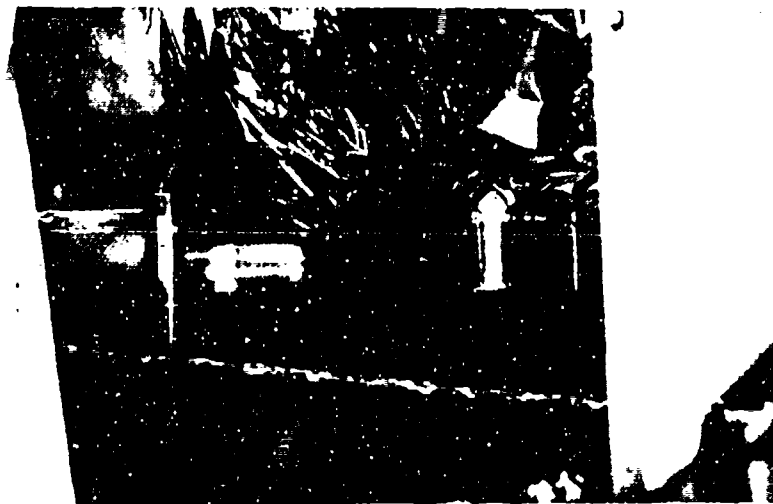


Fig. 4. Cryocooler Cold Finger & Beryllium Stem Interface



the thermal link, the copper block with the large bore in the background of Figure 3 is fit over the the outside diameter of the beryllium stem shown on the right in Figure 4 and pinned in place. With the thermal link assembly in place on the beryllium stem, the cryocooler/bracket assembly is slid forward along the cold finger axis until the cold finger end is adjacent to the bore of the copper block face shown in the foreground of Figure 3. The thermal link bore to cold finger alignment was checked and some bending of the thermal link was required to eliminate mismatch due to tolerance buildup. Once alignment was established to minimize residual transverse forces, the cryocooler was pushed into the bore of the copper block it's full thickness. Epoxy is used to bond the cold finger to the thermal link. In operation, cool down causes the copper thermal link to shrink onto the beryllium stem causing high surface pressures to provide a low thermal resistance interface. The Cu/Be shrink fit design and hardware was provided by the Lockheed Research Laboratory.

Each of the four wire bundles in the thermal link consists of 900 wires of 0.005 inch diameter oxygen free copper. The unassembled length of each bundle is 1.40 inches. The ends of each bundle are silver epoxied and clamped to squeeze out excess epoxy. The cured bundle ends are silver epoxy bonded in 0.25 deep by 0.190 inch diameter holes in the solid copper end blocks. The termination holes are oriented at a 30 degree angle from the long axis to provide a natural bend to reduce the axial stiffness. Figure 5 presents the average spring rate of this thermal link design as function of maximum deflection in the axial and transverse directions. The thermal conductance of this thermal link is 380mW per °K.

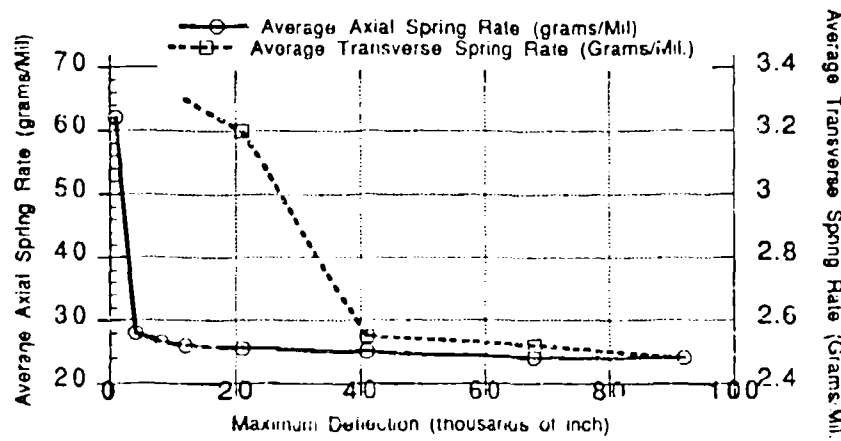


Figure 5. HTSSE -I Thermal Link  
Spring Rate Vs. Deflection

## HTSSE-I FLIGHT CRYOCOL SYSTEM DIAGNOSTIC INSTRUMENTATION

An important element of the HTSSE program is to develop and demonstrate the cryogenic subsystems required to utilize HTS devices in space applications. There have been few mechanical cryocoolers flown for durations longer than 6 months. Cryocoolers having the potential for 5 year life with high reliability have only just begun operating in orbit within the past year. The two Stirling cycle clearance seal cryocoolers currently operating are of different designs from Oxford University and Rutherford Appleton Laboratory. The launch of HTSSE-I in midyear 1993 is likely to be the first production clearance cryocooler on orbit. For these reasons HTSSE-I has been extensively instrumented to monitor cryocooler and cryogenic payload health while on orbit. Table 2. presents a list of the cryogenic subsystem instrumentation included on HTSSE-I. Fast simultaneous

<u>Item Monitored</u>	<u>Sensor Comments</u>
Displacer Motor Current*	HTSSE-I Electronics
Displacer Motor Voltage*	"
Compressor Motor Current*	"
Compressor Motor Voltage*	"
Displacer Axial Accelerometer*	Endevco #7290-10
Displacer Transverse Accelerometer*	"
Compressor Axial Accelerometer*	"
Compressor Transverse Accelerometer*	"
* 2 Channel Fast Sample Wave Form Plot Capability, 1600 sample/sec. rate for 62 msec window on each channel	
Temperature Sensors, Cryogenic $\pm 0.1K$	Lakeshore Platinum Resistance Thermometers
Outer MLI Blanket Temp.	
Cryogenic Bus Temp.	
Thermal Link Cold Finger End Temp.	
Thermal Link Cryogenic Bus End Temp.	
Temperature Sensors, Ambient $\pm 2.0K$	14 Total
Thermal Heat Flow Meter	Calibrated Thermal Resistance of Thermal Link

Table 2. HTSSE-I Cryogenic  
Subsystem Instrumentation

sampling of any two channels of the first eight items in Table 2 is possible on HTSSE-I. Accelerometer and cryocooler voltage and current wave form data will be useful for

monitoring cryocooler health. Temperature sensors will provide data to accurately predict the cryogenic cooling load, and the heat flow meter will provide cryocooler cooling capacity. A fast sample data baseline will be established after initial cool down in orbit. The hot and cold conditions are 120 days apart in orbit, thus it will be difficult to obtain subsequent cryocooler health data under similar environmental conditions as the initial baseline data. Large changes in cryocooler performance should be detectable. The data from the sensors listed above will be down linked to an NRL ground station and will be available for operations monitoring from a central NRL computer via modem.

### SUMMARY

The HTSSE program was developed at NRL to promote the use of HTS electronics in space applications. A critical aspect of this program is the development and demonstration of the cryogenic technologies and subsystems to support electronic devices in a 77K environment in space. HTSSE-I utilizes a BAe 80K cryocooler for cryocooling. Cryocooler vibration and motor voltage and current wave forms can be monitored from the ground after a 1993 launch. Great attention is required in cryocooler integration to avoid residual transverse loads on the cold finger that can cause clearance seal contacting and premature cryocooler failure.

### ACKNOWLEDGEMENTS

Sponsorship and funding for HTSSE are provided by the U.S. Navy's Space and Naval Warfare Systems Command (SPAWAR). Several other U.S. government agencies provided funding for development of some HTS devices used in HTSSE such as DARPA, SDIO, NASA, and the Office of Naval Research (ONR). Several industry groups provided HTS devices developed with their own IR&D funds. Great appreciation is expressed for the dedication and effort of the many managers, engineers, scientists, technicians and administrative personnel who contributed to HTSSE-I. Special thanks are given to the many highly motivated employees and contractors of the Naval Center for Space Technology for their can-do commitment that made this project possible in a short time frame. Thanks to Nick Davinic for reviewing this paper.

**10 K SORPTION CRYOCOOLER  
FLIGHT EXPERIMENT (BETSCE)**

Steven Bard, Parker Cowgill, Jose Rodriguez, Larry Wade, and J. J. Wu  
Jet Propulsion Laboratory (JPL)  
California Institute of Technology  
4800 Oak Grove Drive  
Pasadena, CA 91109

Capt. Michael Gehrlein  
Air Force SMC/CNST  
Los Angeles AFB, CA 90009-2960

Werner Von Der Ohe  
The Aerospace Corporation  
El Segundo, CA 90245-4691

**ABSTRACT**

This paper presents an overview of the objectives and design of the Brilliant Eyes Ten-Kelvin Sorption Cryocooler Experiment (BETSCE) planned for launch on the Space Shuttle in 1994. The BETSCE objectives are to: (1) demonstrate 10 K sorption cooler technology in a microgravity space environment, (2) advance the enabling technologies and integration techniques by developing an automated, space flightworthy instrument, and (3) characterize spaceflight performance and develop the needed flight database to aid the future cooler development effort. Key technologies and elements to be characterized include hydride sorbent beds, phase change materials, heat sinks, heat exchangers and other refrigeration loop components, the cold head assembly containing a wicked solid/ liquid cryogen reservoir, cycle process controls, and cycle repeatability. This spaceflight experiment is designed to mitigate the risks of utilizing sorption cooler technology for spacecraft sensor cooling applications that require periodic quick-cooldown, negligible vibration, low power consumption, and long-life (5 to 10 years).

**INTRODUCTION**

Sorption cooler technology provides an ideal method to produce intermittent operation of cryogenic infrared sensors for future astronomy, earth-observation and surveillance satellite systems. Sorption cooling provides low-vibration, long-life, and repeated quick cooldown capability, and the intermittent operation results in low average power consumption. A potential application for this technology is the Brilliant Eyes - E surveillance satellite system, since one of the BE system concepts includes a very long-wavelength infrared (VLWIR) detector focal plane that needs to be periodically operated at near 10 K.

The periodic 10 K sorption cooler concept for BE was originally conceived by Johnson and Jones [1,2]. The concept has been investigated analytically, and the proof-of-principle of a 10 K stage has been experimentally demonstrated in laboratory experiments [3]. Alternately heating and cooling beds of metal hydride powders circulates hydrogen in a closed cycle and periodically cools the detector cold head assembly to 10 K on command. Figure 1 describes the basic cycle concept.

A comprehensive technology development program is underway to advance the maturity level and mitigate the risks of utilizing this novel technology for spaceflight systems such as BE [4]. The various elements of this development program [5] include component-level characterization and reliability physics investigations, engineering model and protoflight development by industry, and a near-term spaceflight technology demonstration experiment (BETSCE). BETSCE is an element of the Shuttle Pallet Satellite (SPAS III) mission that is mounted on the Shuttle side wall. Specific BETSCE objectives are to:

- Demonstrate 10 K sorption cooler technology in a microgravity space environment,
- Advance the enabling technologies and develop integration techniques by developing an automated, space flightworthy instrument, and
- Characterize spaceflight performance and develop the needed flight database to aid the future cooler development effort.

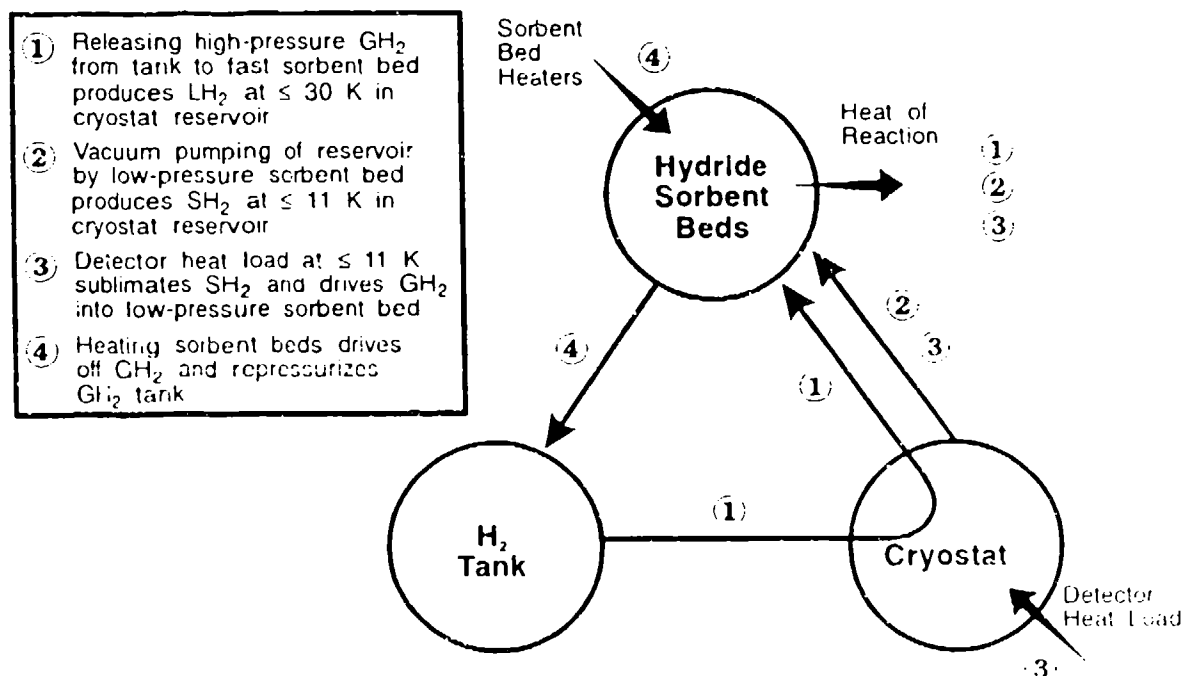


Figure 1. Periodic 10 K sorption cryocooler basic cycle.

Key technologies and elements to be characterized include hydride sorbent beds, phase change materials, heat sinks, heat exchangers and other refrigeration loop components, the cold head assembly containing a wicked solid/ liquid cryogen reservoir, cycle process controls, and cycle repeatability.

## FUNCTIONAL REQUIREMENTS

To meet the objective of demonstrating the 10 K sorption cooler process in space, the BETSCE flight instrument requirements are reasonably representative of typical 10 K cooler goals for the BE VLWIR system. Some of the BE goals may be relaxed for the BETSCE flight instrument to accommodate constraints imposed by the SPAS III Shuttle flight, such as unfavorable thermal environment, safety, limited development schedule, and heat rejection limitations. Although these constraints may cause the BETSCE flight instrument weight, power, and volume to be greater than for a GPALS BE cooler, BETSCE will still effectively demonstrate the critical technologies. Also, to demonstrate the 10 K sorption cooler process in space, the BETSCE flight instrument does not need to contain ancillary equipment, such as an IR detector and optics; only the hydrogen refrigeration cycle system and supporting systems need to be flown.

The basic functional requirements selected for the BETSCE instrument are a scaled version of representative BE 10 K cooling goals:

- A. Cooldown in  $\leq 2$  minutes from 60-70 K to:
  - (1) A cold stage detector interface temperature of  $\leq 11$  K.
  - (2) An intermediate stage temperature of  $\leq 30$  K.
- B. Sustain an I<sup>2</sup>R simulated detector heat load of  $\geq 100$  mW at  $\leq 11$  K for 10 minutes.
- C. Recycle the system to operate again in  $\leq 24$  hours.
- D. Demonstrate  $\geq 3$  full repeatable cycles.
- E. Record data required to characterize spaceflight/ microgravity performance of the BETSCE instrument.

Table I summarizes the key technologies and phenomena that BETSCE is designed to characterize, and the associated instrumentation sensors.

## EXPERIMENT DESIGN

Physically, the BETSCE flight equipment comprises a Sorbent Bed Assembly, Tank and Valve Assembly, Cryostat Assembly, Control Electronics Assembly, Structure, and Cabling/Installation hardware. Figure 2 depicts the BETSCE instrument mounted on a Get Away Special (GAS) adapter beam on the Shuttle payload bay sidewall. BETSCE draws power from the Shuttle 28 VDC power bus, downlinks data and uplinks commands, stores data on BETSCE's dedicated mass storage device, receives the Shuttle Mission Elapsed Time(MET) feed at the data interface

Table I. Key BETSCE Measurements

Phenomenon to be Measured	Sensors
Achievement of system functional requirements	<ul style="list-style-type: none"> <li>- Temperatures at simulated detector interface</li> <li>- Voltage and current to cold head heater</li> <li>- SBA and tank pressures and temperatures</li> <li>- Time</li> </ul>
Sorbent bed heat transfer	<ul style="list-style-type: none"> <li>- SBA temperatures &amp; pressures</li> <li>- Time</li> </ul>
Sorbent bed fast sorption capability/ desorption/ recycling	<ul style="list-style-type: none"> <li>- SBA/ CA temperatures, &amp; SBA/ TVA pressures</li> <li>- Time</li> </ul>
Sorbent migration/ compaction	<ul style="list-style-type: none"> <li>- SBA temperatures &amp; pressures</li> <li>- Pre and post-flight inspection &amp; X-ray, valve leak-check</li> <li>- Time</li> </ul>
Heat switch heat transfer	<ul style="list-style-type: none"> <li>- SBA temps., pressures, heater volts &amp; amps</li> <li>- Time</li> </ul>
Phase change material freeze/ thaw/ heat transfer	<ul style="list-style-type: none"> <li>- SBA temperatures</li> <li>- Time</li> </ul>
Cryostat reservoir liquid/ solid cryogen retention and phase separation	<ul style="list-style-type: none"> <li>- CA temperatures &amp; pressures</li> <li>- Time</li> </ul>
J-T loop thermodynamics & heat transfer	<ul style="list-style-type: none"> <li>- CA and TVA temperatures &amp; pressures</li> <li>- Time</li> </ul>
Thermal storage device and mechanical cryocooler interface performance	<ul style="list-style-type: none"> <li>- CA and TVA temperatures &amp; pressures</li> </ul>
Cycle process controls and repeatability	<ul style="list-style-type: none"> <li>- SBA, TVA, CA, CEA temperatures, pressures, volts &amp; amps for heaters</li> </ul>
Thermal radiator heat rejection	<ul style="list-style-type: none"> <li>- CA, SBA, CEA temperatures</li> </ul>

Notes: SBA = Sorbent Bed Assembly; TVA = Tank & Valve Assembly; CA = Cryostat Assembly; CEA = Control Electronics Assembly

connector, accepts crew inputs via the Standard Payload Switch Panel, and rejects heat to space with radiative coolers. connector, accepts crew inputs via the Standard Payload Switch Panel, and rejects heat to space with radiative coolers.

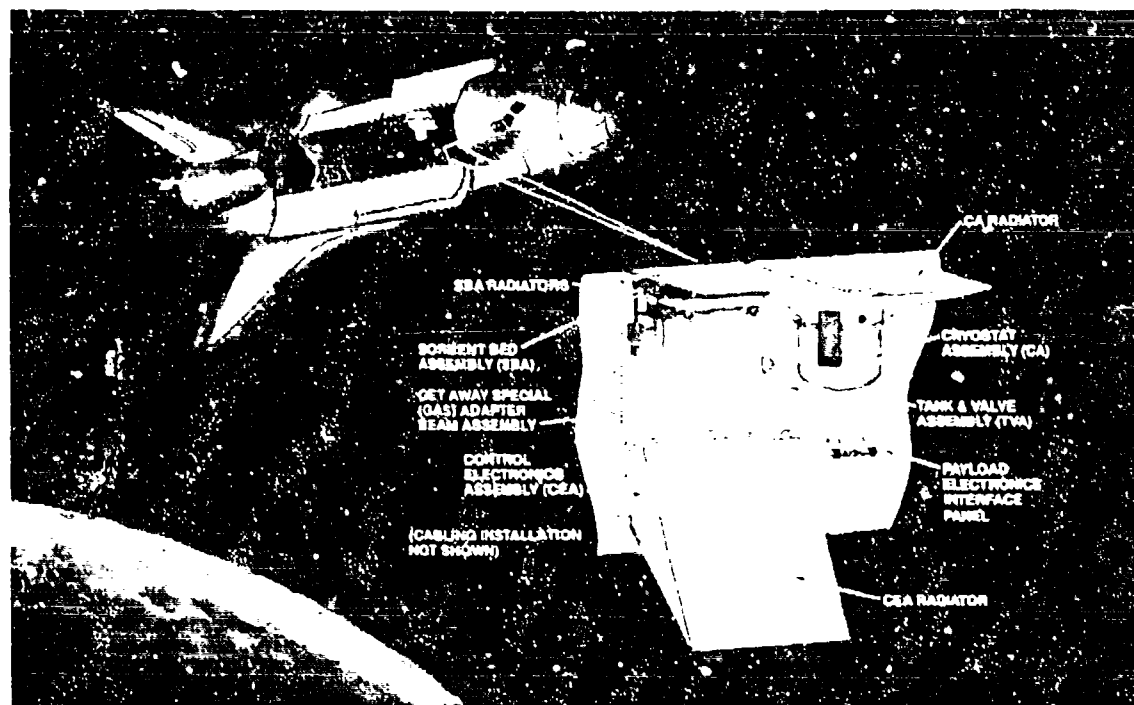


Figure 2. BETSCE instrument mounted on a Get-Away Special (GAS) adapter beam.

The BETSCE cycle exploits the properties of certain metallic hydride powders that desorb hydrogen to high pressures when heated and adsorb hydrogen to high vacuums when cooled. By alternately heating and cooling beds of these hydride powders, BETSCE circulates hydrogen gas through a closed system. The process produces 0.31 g of solid hydrogen in about 2 minutes, enough to cool a simulated infrared sensor for 10 minutes at  $\leq 11$  K. See Figure 3.

Figure 3 shows the BETSCE fluid schematic. Figure 4 shows the basic operating sequence. At launch, the total fill of hydrogen in the BETSCE system is less than 34 g, about 57% of which is in hydride form. When the experiment is powered-up, the high pressure sorbent bed is heated to desorb, pressurize, and transfer its  $H_2$  to the  $H_2$  storage tank. After hydrogen desorption is completed, the high pressure bed is cooled. The low pressure and fast absorption sorbent beds are next heated in turn, transferring their  $H_2$  gas to the high pressure sorbent bed. The high pressure sorbent bed is then heated again to pressurize the  $H_2$  storage tank to its operating pressure.

Also during BETSCE startup, mechanical cryocoolers pre-chill the cryostat thermal storage device to 60-70 K. With startup conditioning sequences completed, BETSCE is ready to enter its operating cycle. Cooldown is initiated by releasing pressurized  $H_2$  gas from the storage tank to the fast absorption sorbent bed via the cryostat, whose pre-chilled thermal storage device, heat exchangers, and Joule-Thomson valve produce liquid  $H_2$  at 26-28 K in the main heat exchanger. Next, solid  $H_2$  at  $\leq 11$  K is produced by vacuum sublimation.



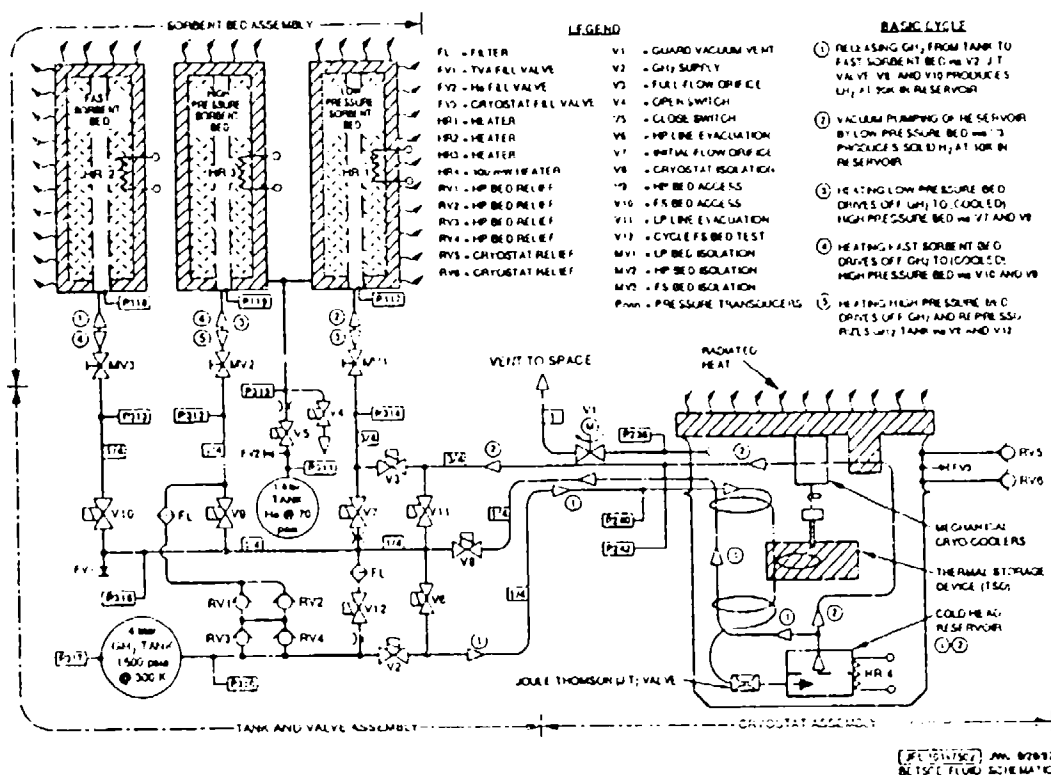


Figure 3. BETSCE fluid schematic.

about  $2.6 \times 10^{-4}$  MPa (2 torr) with the low pressure sorbent bed. Under simulated infrared sensor heat load and continued vacuum pumping the solid H<sub>2</sub> sublimates and is adsorbed by the low pressure sorbent bed. Then to recharge the system, hydrogen is returned to the tank by sequentially heating the three sorbent beds as before. The cycle repeats about every 12 to 14 hours. In each cycle, pre-planned variations of event timing are introduced to fully map operating characteristics and microgravity effects.

Table II summarizes some key experiment design and performance parameters.

### SUBSYSTEM HARDWARE DESIGN

The BETSCE Sorbent Bed Assembly comprises radiator panels, a fast absorption sorbent bed, a high pressure sorbent bed, and a low pressure sorbent bed. Design implementation of the three beds is tailored to meet performance requirements. See Figure 5. The high pressure bed pumps hydrogen to moderate pressures ( $\leq 10.3$  MPa, 1495 psia, when the tank temperature is 300 K) when heated. The fast absorption sorbent bed adsorbs large quantities of hydrogen rapidly [6]. The fast absorption and high pressure bed sorbent material is lanthanum-nickel-tin (LaNi<sub>4</sub>Sn<sub>0.2</sub>) hydride. The low pressure bed sorbent bed, designed to absorb hydrogen at moderate vacuum levels, contains zirconium-nickel (ZrNi) hydride.

## NOTES:

1. GENERIC CYCLE SKETCH  
DOES NOT DEPICT PLANNED  
CYCLE VARIATIONS

2. NOTATIONS INDICATE  
DIFFERENT VALVE CONFIGURATIONS

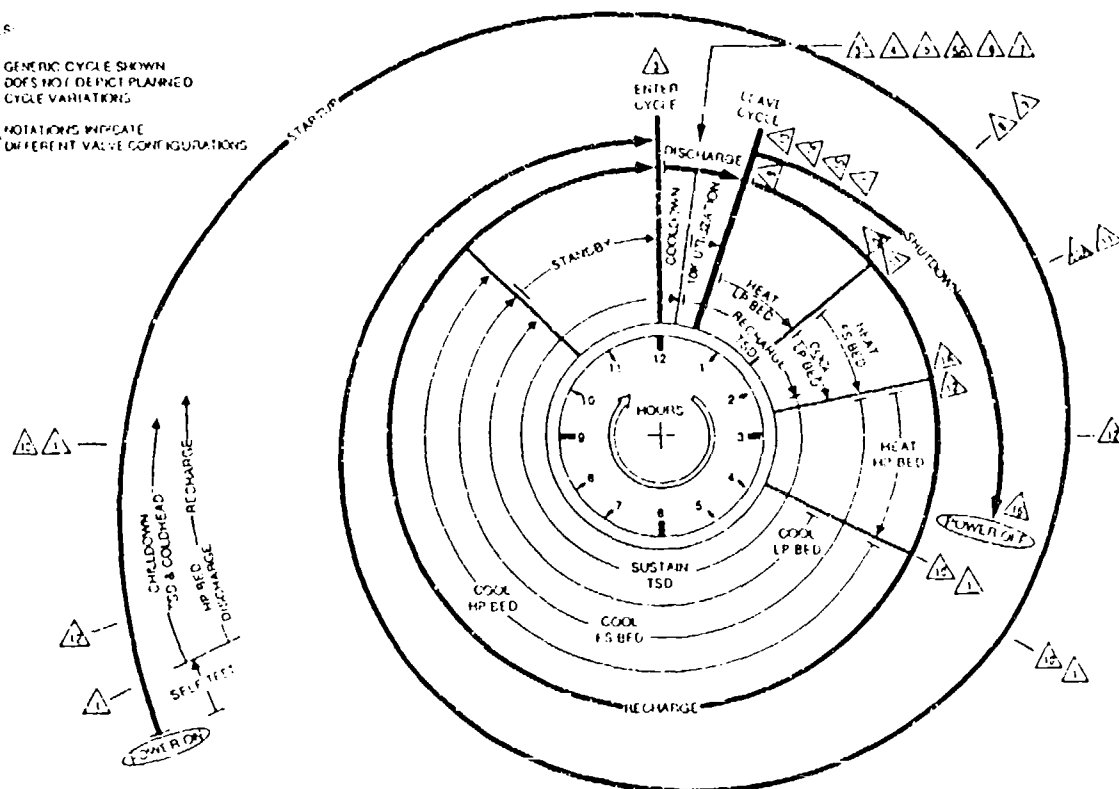


Figure 4. BETSCE operating sequence.

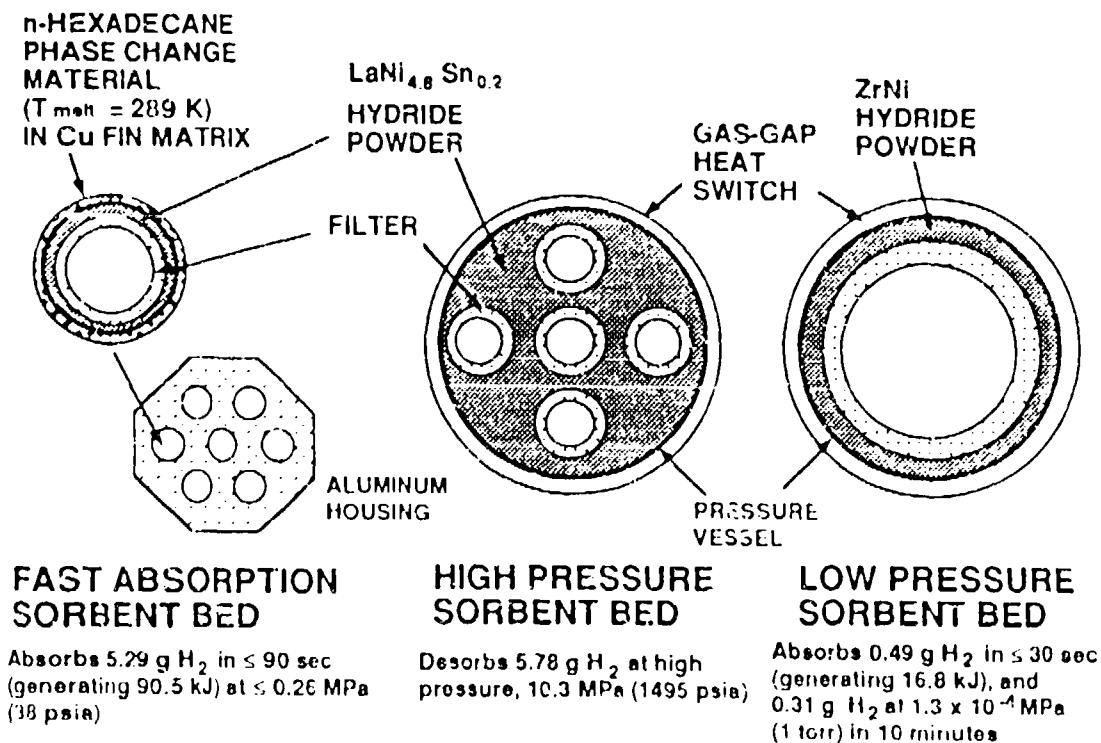


Figure 5. BETSCE Sorbent Bed Assembly.

Table II. Nominal Design and Performance Parameters

<b>Cooldown from 60 K to 27 K:</b>	
Time	≤ 90 seconds
Initial storage tank pressure (1358 psia at 0°C)	9.36 MPa
Final storage tank pressure (1030 psia at 0°C)	7.10 MPa
H <sub>2</sub> gas depleted from storage tank	6.09 g
LH <sub>2</sub> produced in cold head reservoir	0.50 g
H <sub>2</sub> gas absorbed by Fast Absorption Sorbent Bed	5.29 g
Energy dissipated by Fast Absorption Sorbent Bed	90.5 KJ
<b>Cooldown from 27 K to ≤ 11 K:</b>	
Time	≤ 30 seconds
SH <sub>2</sub> produced in cold head reservoir	0.31 g
H <sub>2</sub> gas absorbed by Low-Pressure Sorbent Bed	0.49 g
Energy dissipated by Low-Pressure Sorbent Bed	16.8 KJ
<b>Steady-state operation at ≤ 11 K:</b>	
Time	10 minutes
Cold head heat Load:	
I <sup>2</sup> R simulated detector heat load (100 mW)	250 mW
Conductive & radiative parasitics (≤ 150 mW)	
Sublimated H <sub>2</sub> gas absorbed by Low-Pressure Sorbent Bed	0.31 g
Energy dissipated in Low-Pressure Sorbent Bed	10.6 KJ
<b>Recycle Parameters:</b>	
Heater power to each sorbent bed	180 W
Total heating time for 3 beds	3.9 hours
Total energy to desorb beds/ recharge storage tank	2.6 MJ
Total time-averaged desorption power over 24 hours	29.3 W

Besides hydride sorbent material, each sorbent bed contains heater elements, a heat sink/radiator, and either a gas-gap heat switch or a thermal capacitor. The hydride powders are enclosed in cylindrical pressure containers. Multiple cartridge-type heaters are brazed to the outside of the pressure containers. Surrounding the high pressure and low pressure beds' hydride containers are 3.8 mm (0.150-inch) wide vacuum spaces that function as gas-gap heat switches. These gaps may be filled with helium gas at a pressure of about  $1.3 \times 10^{-1}$  MPa (10 torr) on command, to provide conductive paths between the hydrides and heat sinks/ radiators. When the beds are subsequently heated to recharge the system, the gaps are evacuated to the vacuum of space to provide thermal isolation. The low pressure sorbent bed is heated to about 600 K to desorb the hydrogen at about 0.21 MPa (30 psia) to transfer it to the high pressure bed. Then the high pressure bed is heated to 540 K to desorb the hydrogen at about 10.3 MPa (1495 psia when the tank temperature is 300 K) to recharge the storage tank.

The fast absorption sorbent bed consists of seven separate hydride containers located within an aluminum housing. Surrounding each hydride container is an aluminum chamber filled with n-hexadecane, a paraffin phase change material (PCM) that acts as a thermal capacitor, in a copper heat transfer enhancement matrix containing 15.7 fins per centimeter. As 5.29 g of hydrogen are absorbed by the fast absorption sorbent bed in about 80 seconds, the 90.5 KJ given off by the exothermic hydride reaction melts the PCM. Thus, the hydride temperature remains fairly isothermal at about 20 K above the PCM phase transition temperature of 289 K, allowing the hydrogen absorption pressure to remain at about 0.26 MPa (38 psia) in the fast absorption sorbent bed, which corresponds to about 0.39 MPa (57 psia) in the cryostat assembly cold head reservoir. To recharge the system, the fast absorption sorbent bed is then heated to about 360 K to desorb the hydrogen at about 0.41 MPa (60 psia), transferring the hydrogen to the high pressure sorbent bed. Then, as the radiator cools the n-hexadecane PCM to below 289 K it again solidifies.

The BETSCE Cryostat Assembly comprises the thermal storage device (TSD), mechanical cryocoolers, cryogen reservoir, heat exchangers, Joule-Thomson valve, outer shell, and associated piping. See Figures 2 and 3. The TSD is a 2.0-kg aluminum block cold sink. It is supported inside an evacuated cryostat outer shell that is vented to space by motorized valve V1 whenever BETSCE is operating. Heat is removed from the TSD by mechanical cryocoolers. When chilled to 60-65 K, the TSD is available to support the hydrogen cycle. In the initial stage of the cooldown cycle, hydrogen gas circulated past the TSD raises the TSD temperature by about 10 K.

The mechanical cryocoolers are split-Stirling rotary drive advanced tactical coolers manufactured by Hughes Electron Dynamics Division (Model No. 7044H). These coolers are identical to those used in the Cryogenic Heat Pipe Experiment (CRYOHP) planned for launch in 1992 aboard STS-53 [7], and the NASA Cryo System Flight Experiment planned for launch in 1994 [8]. BETSCE contains three of these mechanical cryocoolers; two are operated simultaneously, and the third provides redundancy.

The BETSCE Tank and Valve Assembly integrates 2 tanks, 11 valves, and associated pressurized piping into a single unit. This allows many of BETSCE's joints, seals, and pressure vessels to be intensively addressed and their performance verified before integration with the other flight equipment. The 11 normally-closed solenoid valves are activated by BETSCE Control Electronic Assembly drive circuits to produce the desired flows. See Figure 3.

The BETSCE Control Electronics Assembly directs the instrument through a series of pre-programmed sequences. Data on the status and performance of instrument components are acquired and stored in nonvolatile solid-state flash memory. Performance data are also downlinked to ground personnel so that experiment progress can be assessed. BETSCE can accept uplinked commands to modify sequences or configurations based on observed performance. All commands from the ground involve software, parameter adjustments, or valve configurations that have no safety implications. See Figure 2.

To measure and characterize the phenomena summarized in Table I, the BETSCE instrument contains an array of 96 sensors monitored by the Control Electronics Assembly. Temperatures are measured by an assortment of silicon diodes, platinum resistance thermometers (PRT's) and thermocouples. Other telemetry includes pressure sensors, and current and voltage monitors for determining electrical power consumed by heaters and mechanical cryocoolers.

The Control Electronics Assembly also provides power conditioning as needed of the  $28 \pm 4$  VDC supplied by the Shuttle. The strawman power and energy consumption profiles are shown in Figure 6.

### MISSION SCENARIO

Figure 7 summarizes the strawman mission timeline. On orbit, BETSCE is powered-on at the start of payload activities, and is capable of running continuously and operating autonomously for the full mission duration. When powered-on, BETSCE immediately does a self-check and status appraisal. In the event of power interruption, BETSCE will resume operation at the sequence where it left off.

Initially, the sorbent beds are sequentially heated to desorb their hydrogen and charge the storage tank. Simultaneously, BETSCE will vent the cryostat guard vacuum to space via valve V1 and turn on the 60 K mechanical cooler assembly, to begin pre-cooling the cryostat thermal storage device. These off-line conditioning sequences take about 18-24 hours. Then, BETSCE will execute an initial full cycle for evaluation, and a full check cycle incorporating any modifications that are necessary. Next, BETSCE will execute four conditioning cycles to establish repeatable cycle parameter data patterns. Data patterns are expected to approach the nominal 12-hour cycle in 3 or 4 cycles. See Figure 4. Additional cycles will be necessary if the data patterns have not stabilized by the fourth cycle.

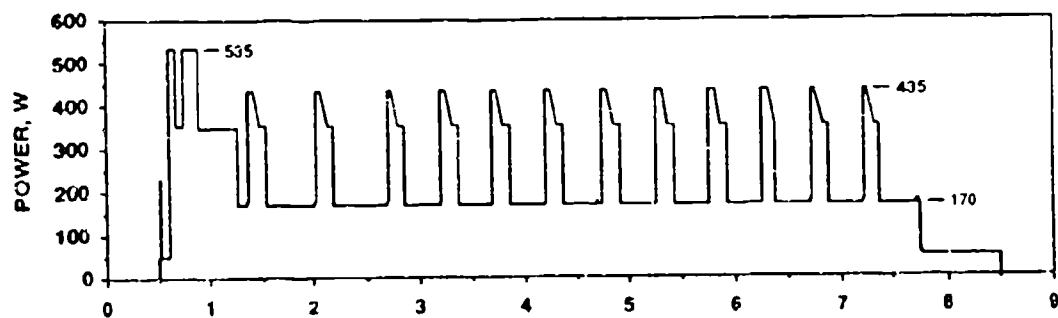
Following establishment of cycle repeatability, several utilization cycles follow, where various effects of parametric tuning are investigated. In one of these studies, it is planned to have a pressure release through calibrated orifices that bypass the cryostat to independently define sorbent bed performance. The one cycle per 12-hour period rate will be maintained. If mission duration and resources permit, additional cycles should be inserted to address any issues of opportunity that arise in the course of preplanned sequences.

Following the final sorption cycle, the mechanical coolers are shut down and the warmup of the thermal storage device and cold head is observed. While warmup is proceeding, hydrogen is returned to the sorbent beds until they are fully hydrided. Then BETSCE is configured for landing and powered-off.

### DATA ANALYSIS PLAN

The full data set will be downlinked in near-real time via the standard Shuttle communications data link, and archived. Experiment performance will be evaluated on the ground and parameter changes will be uplinked if necessary. After BETSCE is deintegrated from the Shuttle post-

## POWER PROFILE



## ENERGY CONSUMPTION

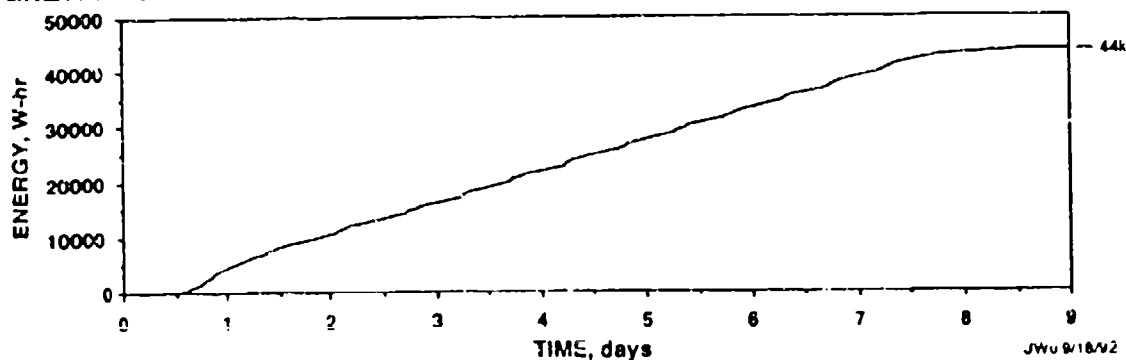


Figure 6. BETSCE strawman power and energy profiles.

FUNCTIONAL OBJECTIVE	DAY								
	1	2	3	4	5	6	7	8	9
Launch	■								
Startup	■	■							
Initial Cooldown/Recharge Cycle		■							
Modified Cooldown/Recharge Cycle			■						
Establish Nominal Cycle			■						
Establish Cycle Repeatability			■	■	■	■	■	■	■
Multiple-Cooldown Cycle					■	■	■	■	■
Sensitivity Study Test Cycles						■	■	■	■
Upper-stage (<30 K) Test Cycle							■	■	■
Hydride Bed Characterization Cycle								■	■
Re-establish Nominal Cycle								■	■
Additional Sensitivity Study Tests								■	■
Shutdown								■	■
Return									■
	Main Experiment					Extended Mission			

Figure 7. BETSCE strawman mission timeline.

flight, data will be retrieved from the on-board data storage device and again archived. After reduction and analysis, the microgravity spaceflight performance data will be compared and correlated with ground test data, and to analytical model predictions. Particular emphasis will be placed on gaining a quantitative understanding of the phenomena listed in Table I.

### SUMMARY AND CONCLUSIONS

The BETSCE offers the first opportunity to demonstrate the spaceflight performance of a sorption cryocooler. Extensive test data obtained from the 9 day mission will permit correlation of microgravity performance with ground test data and analytical model predictions. The spaceflight performance characterization database will aid in the design of future lightweight, efficient, periodic 10 K sorption coolers for Brilliant Eyes, as well as other infrared sensor cooling applications for surveillance, astronomy, planetary and earth observation satellite systems.

### ACKNOWLEDGEMENTS

The work described in this paper was carried out by the Jet Propulsion Laboratory (JPL), California Institute of Technology under contract with the National Aeronautics and Space Administration. The work was sponsored by the Brilliant Eyes program office, Strategic Defense Initiative Organization (SDIO), USAF Space and Missiles Systems Center (SMC). The authors wish to thank the entire BETSCE development team at JPL, Aerojet Electronics Systems Division, and APD Cryogenics for their technical contributions and commitment to this effort, and Dr. Donald Rapp for editing the manuscript. The support of Dr. Al Johnson in providing technical guidance and aiding the experiment requirements definition is also appreciated.

### REFERENCES

1. Johnson, A. L. and Jones, J. A., "Periodic 10 K Sorption Cooling," USA Patent No. TBD., 1992.
2. Johnson, A. L. and Jones, J. A., "Evolution of the 10 K Periodic Sorption Refrigerator Concept," 7th International Cryocoolers Conference, Santa Fe, NM, November 17-19, 1992.
3. Wu, J.-J., Bard, S., and Longworth, R., "10 K Sorption Cryocooler Proof-of-Principle Experiment," in preparation, 1993.
4. Bard, S., Fujita, T., Wade, L., Rodriguez, J., and Wu, J. J., "Development of a Periodic 10 K Sorption Cryocooler," 7th International Cryocoolers Conference, Santa Fe, NM, November 17-19, 1992.
5. London, J. R., Weissman, J. R. and McNeil, R. C., "Brilliant Eyes - A Technology Driver for Small Satellite Systems," Paper No. IAF-91-048, 42nd Congress of the International Astronautical Federation, Montreal, Canada, October 5-11, 1991.

6. Bowman, R., Freeman, B., Labor, D., Lynch, F., Marmaro, R., and Wade, L., "Evaluation of a Prototype Hydride Compressor for Periodic Sorption Cryocoolers," 7th International Cryocoolers Conference, Santa Fe, NM, November 17-19, 1992.
7. Beam, J., Brennan, P. J., and Bello, M., "Design and Performance of a Cryogenic Heat Pipe Experiment (CRYOHP)," Paper No. AIAA 92-2867, AIAA 27th Thermophysics Conference, Nashville, TN, July 6-8, 1992.
8. Russo, S., and Sugimura, R., "NASA Cryo System Flight Experiment (CSE)," 7th International Cryocoolers Conference, Santa Fe, NM, November 17-19, 1992.



GAS ATOMIZED Er<sub>3</sub>Ni POWDER FOR CRYOCOOLER APPLICATIONS

I. E. ANDERSON, M. G. OSBORNE, H. TAKEYA, AND K. A. GSCHNEIDNER, JR.  
AMES LABORATORY AND DEPARTMENT OF MATERIALS SCIENCE AND  
ENGINEERING, IOWA STATE UNIVERSITY  
AMES, IOWA 50011, USA

ABSTRACT

Although Er<sub>3</sub>Ni powder has become an important cryocooler regeneration material due to its significantly enhanced heat capacity at temperatures in the range of liquid He, an efficient method is still needed to produce commercial quantities of high quality Er<sub>3</sub>Ni powder. A high pressure gas atomization (HPGA) approach was developed to produce uniform spherical powders of high purity Er<sub>3</sub>Ni and 3 batches of about 1.3Kg each were prepared. The average yield of high quality spherical powders between 0.15 and 0.35mm was about 16% of the initial atomizer charge weight. Microstructural analysis of sectioned powder samples revealed single phase particles with some internal cracking but no evidence of an oxidized surface shell. Chemical analysis and x-ray diffraction measurements verified that single phase particles of the stoichiometric composition had been generated. Vacuum fusion measurements indicated that the powder contained 2600ppm of oxygen (by wt.). The heat capacity of a hot pressed, partially sintered Er<sub>3</sub>Ni powder sample was measured from 2K to about 80K. The results indicated a maximum heat capacity of 0.43 J/cm<sup>3</sup>K at about 7K. The heat capacity peak appears to be about 0.04 J/cm<sup>3</sup>K higher than that reported by Sahashi et al. (1) and it is also narrower. Compared to the single peak for this sample, the Sahashi et al. (1) heat capacity peak has two maxima suggesting the existence of two phases in their material. In addition, our Er<sub>3</sub>Ni powder has a larger heat capacity than Pb over the entire range of temperatures up to about 25K which should permit a lower final temperature for a cryocooler stage composed of this material.

INTRODUCTION

Er<sub>3</sub>Ni powder has become an important cryocooler regeneration material due to its significantly enhanced heat capacity at temperatures in the range of liquid He. However, the pace of development of reliable magnetic refrigeration devices which utilize rare earth intermetallic (REI)

alloys as the heat exchanger bed material has been slowed by several problems associated with the characteristics of available alloy particulate. Most of these alloys have inherently poor mechanical properties, primarily poor fracture toughness. Only limited commercial sources of suitable powder of these alloys currently exist, typically supplying powder which is non-spherical, of low purity, and sized between about 0.1 to 0.3mm.

The most typical commercial practice involves mechanical grinding or crushing of cast alloys to size which produces irregular fragmented powders that are often partially fractured (2). Premature disintegration of this substandard particulate material generally occurs after a limited period of testing in a packed bed heat exchanger. The disintegration process causes the bed to shift and lose stability, creating a loose bed that promotes further particle attrition and dusting. The abrasive dust can also severely affect the lifetime of moving parts in the refrigeration unit (2).

An improved experimental technique, spark erosion, produces a yield of  $\text{Er}_3\text{Ni}$  powders that consists of both "shatters" and spheres (3). Recent research results reported by Ludeman (4) indicate that a drop tube atomization device with a fine diameter orifice and a high melt overpressure is capable of producing extremely high yields of REI alloy spheres, albeit at a low production rate. However, because the Raleigh disintegration process requires increasingly finer melt orifice sizes for finer powders and because of their tendency to freeze-off, this device appears to have a natural lower size limit of about 0.3mm for production of REI alloy powders. Recently, one commercial source has emerged for 0.3mm spheres (1) which are produced by a "Rotating Disk Process" method but uncertainty exists about its efficiency, adaptability for smaller size spheres, and suitability for higher melting point REI alloys.

To permit widespread development of advanced cryocooler designs that utilize this high performance material, an efficient method is needed to produce uniform spherical powders of high purity  $\text{Er}_3\text{Ni}$  in commercial quantities. A modified high pressure gas atomization (HPGA) technique has been demonstrated to be effective for production of rare earth-iron-boron permanent magnet alloy powders (5), a REI alloy of similar oxidation tendency, although in a much finer particle size. Because the modified HPGA technique already produces high purity spherical powders and includes provisions for powder surface passivation of REI alloys (5), the chief development needed for adapting HPGA for this application is a "detuning" of the atomization energy level (6) to produce significantly coarser powders.

## EXPERIMENTAL PROCEDURE

The starting materials used in this study were 99.8at.% pure Er bar, which had been prepared at the Materials Preparation Center, Ames Laboratory, and 99.9at.% pure Ni shot which was purchased from INCO. The major impurities in the Er in ppma (atomic) were: H - 828, C - 97, N - 60, O - 546, F - 246, Cl - 14, and Fe - 19 (all the remaining impurities present were < 10 ppma and most < 1 ppma). The major impurities in the Ni in ppma were: H - 330, C - 580, O - 107, Cl - 1, and Mn - 2 (all the remaining impurities present were < 1 ppma). Weighted amounts of Er and Ni were arc-melted on a water cooled Cu hearth in an inert atmosphere of Ar (99.998wt.% pure) and cast in 25g buttons. A total of about 3700g of alloy was prepared and split into three similar batches for atomization processing.

The high pressure gas atomization process incorporated a melting system with a high purity (99.55%), controlled porosity (21.0% porosity) alumina crucible, a high purity (99.8%), hard-fired alumina stopper rod, and a boron nitride (93% BN) pour tube. Based on an estimated liquidus temperature of 900°C of the Er<sub>3</sub>Ni alloy composition (Er-10.47wt.%Ni), a melt pour temperature of 1100°C was selected to provide about 200°C of superheat for effective alloy homogenization and atomization. The melting and atomization chamber, as shown schematically in Figure 1, was evacuated initially to about  $6 \times 10^{-2}$  torr and, then, backfilled with ultra high purity (99.998%) Ar gas to a positive pressure (1.1atm) for the melting and atomization operations. The atomization nozzle (7) was operated at a gas pressure of 2.8MPa (400psig) with ultra high purity (99.998%) Ar gas utilizing a melt tip configuration designed to reduce the energy of disintegration process (6) to promote production of large (0.15 to 0.35mm) powder particles. In addition, an in-situ particle passivation process (5) was performed during the atomization of the powder to render the powder surfaces resistant to ambient environmental degradation.

Since initial screening of the atomizer yield resulted in both spherical powders and flattened "splat" flakes, a fluidized bed sorting technique was developed which utilized a 2.5cm diameter by 0.7m long separation tube with an upward flow of Ar. At a selected gas flow setting the splats were transported up and out of the top of the open separation tube with the spherical powder retained in the lower portion of the tube for collection after termination of the gas flow.

To characterize particle shape, loose powder was observed with SEM using a conducting adhesive mount. Microstructural analysis included optical microscopy and SEM of powder particle cross-sections in etched (2% nital) and unetched conditions to observe internal particle microstructure and

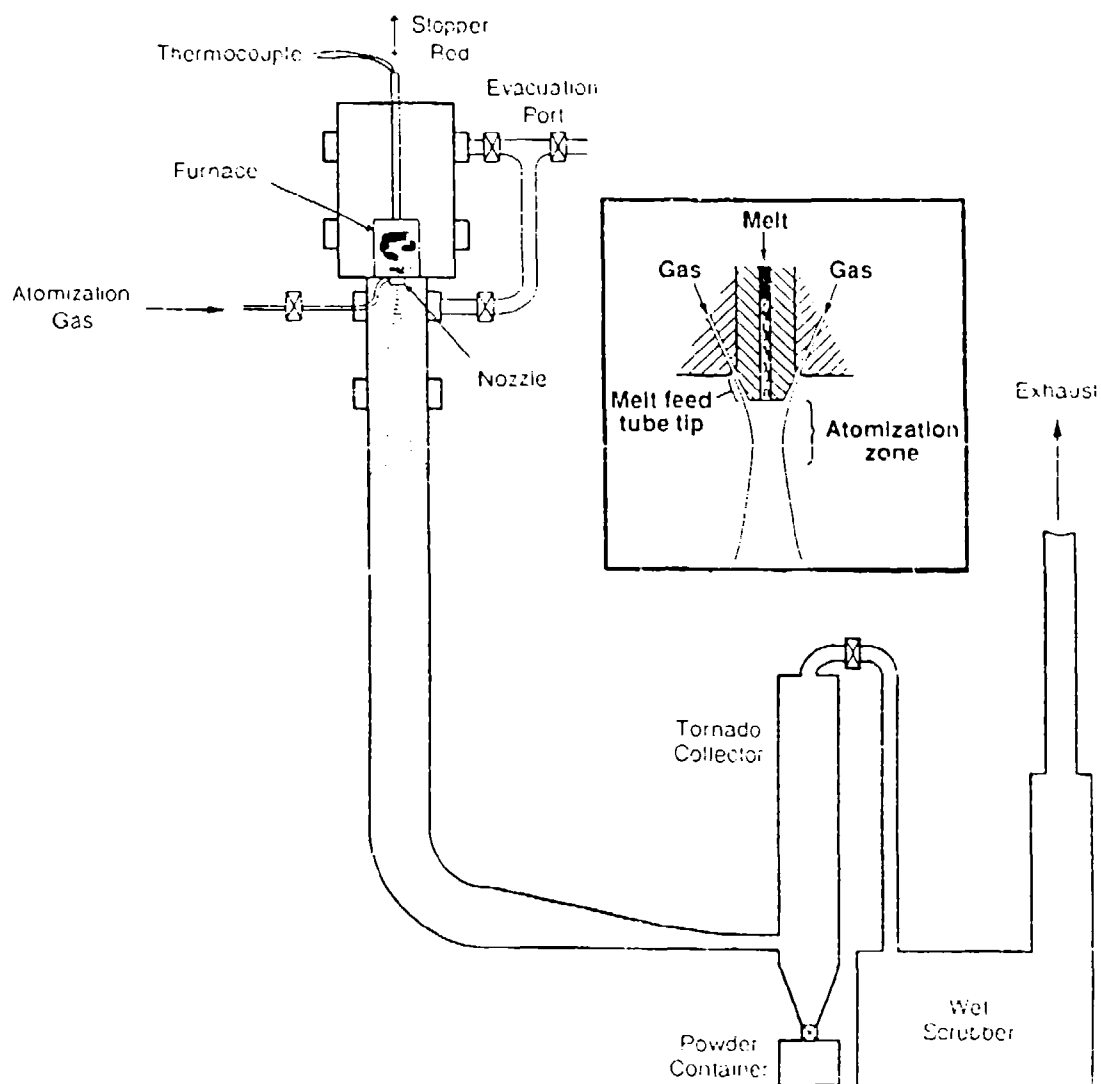


Figure 1. Schematic of high pressure gas atomization (HPGA) at the Ames Laboratory, with inset sketch of nozzle/pour tube configuration.

porosity, respectively. Metallographic sample preparation of these samples involved epoxy mounting of the loose powders and standard grinding and polishing techniques.

Because the measurement fixture of the sub-ambient calorimeter required a sample shaped like a right circular cylinder rather than loose particulate, the spherical  $\text{Er}_3\text{Ni}$  powders were partially sintered into this shape. Powder that had been screened to  $0.212 < \text{dia.} < 0.300\text{mm}$  and sorted to remove flakes was poured into a cylindrical BN die cavity, 3mm dia. by 3mm height, which was fitted with a BN plunger. The plunger was weighted with a stainless steel block of about 500g. The powder sample and die assembly was loaded into a resistance furnace chamber and vacuum ( $5 \times 10^{-6}\text{torr}$ ) sintered at 700°C for 44hr. The partially sintered sample exhibited sufficient mechanical integrity to permit removal from the BN die and handling in the calorimeter.

The low temperature (2 to 80K) heat capacity was measured using an adiabatic heat-pulse type calorimeter (8). The accuracy of the heat capacity measurements is estimated to be within 1% of the reported value below 20K, within 2-5% between 20 and 60K, and within 5-10% above 60K, with the accuracy decreasing with increasing temperature in the range above 20K. The reproducibility from one run to another, however, is much better: less than or equal to 1% below 40K, 2% between 40 and 50K, 3% between 50 and 60K, and 4 to 5% above 60K.

## RESULTS

Uniform spherical powders of  $\text{Er}_3\text{Ni}$  were produced by a high pressure gas atomization (HPGA) approach in 3 batches of about 1.3Kg each. The average yield of high quality spherical powders between 0.15 and 0.35mm was about 16% of the initial atomizer charge weight. The typical shape and surface character of the HPGA powder is given in Figure 2 which shows powders screened to  $0.106 < \text{dia.} < 0.150\text{mm}$ . Occasional small singular "nubs" are commonly attached to the spheres, but no large clusters of "satellite" particles are observed, as Figure 2 indicates. It should be noted that a fairly large fraction of the as-atomized yield (approximately 10 to 20% by weight) consisted of splat flakes and that the flakes were removed by a fluidized bed separation method described above. Observations of the  $\text{Er}_3\text{Ni}$  atomization spray suggested that the wide spray cone which resulted from the detuned atomization parameters contributed to impingement of a large number of molten droplets on the narrow spray chamber wall, probably producing the splats found in the powder yield.

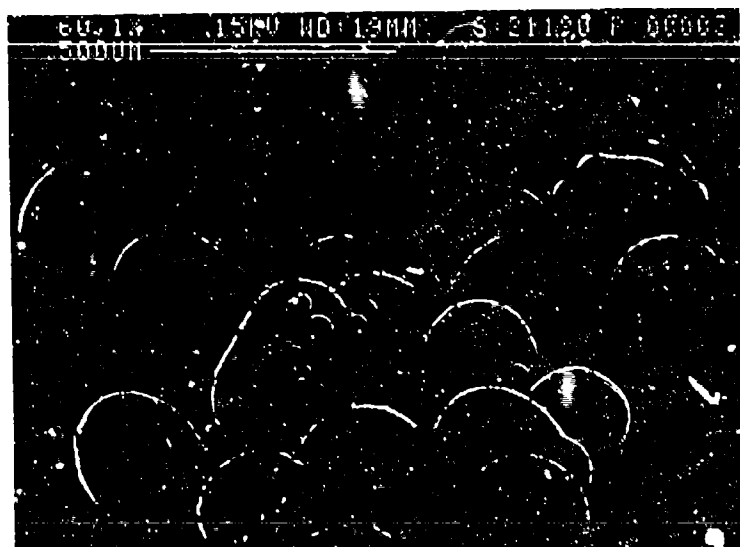


Figure 2. SEM micrograph of as-atomized  $\text{Er}_3\text{Ni}$  powder prepared by HPG-A after screening to  $0.10\phi < \text{dia.} < 0.150\text{mm}$  and removal of flake particulate.

Microstructural analysis of sectioned and etched powder samples, represented by Figure 3 which shows  $0.212 < \text{dia.} < 0.300\text{mm}$  powders, revealed single phase particles with some internal cracking and a proportion (10 to 30%) containing large internal pores. Also, Figure 3 shows that the powder surfaces do not exhibit a thick exterior shell suggesting that the in-situ passivation treatment produces a surface film thinner than the SEM resolution limit. However, evidence of the passivation treatment effectiveness is provided by our recent observations of the lack of obvious degradation, typically in the form of a light colored oxide dust, of the HPGA powder surfaces even after extended exposure (nearly 2 years) in the ambient environment.

X-ray diffraction measurements indicated that single phase powders of the  $\text{Er}_3\text{Ni}$  compound (orthorhombic, Pnma,  $\text{DO}_{19}$ ) had been generated by rapid solidification of the gas atomized particles. In spite of the complex Bragg diffraction pattern shown in Figure 4, a computer-aided comparison of the observed and calculated patterns, including both reflection positions and intensities, revealed excellent agreement. This suggests that the particles are single phase  $\text{Er}_3\text{Ni}$  within the resolution limit of the x-ray diffraction technique.

Chemical purity of the atomized powder which is another important characteristic that affects cryocooler performance was analyzed by atomic emission spectroscopy (AES), titrimetric titration, and vacuum fusion. The Er concentration of a random sample of as-atomized particulate was measured by both titration and AES, while the Ni concentration was measured only by AES. The results indicated that the nominal alloy composition, i.e., the initial composition charged into the atomizer crucible, was maintained in the resulting powder and that the final powder alloy stoichiometry was  $\text{Er}_{3.00}\text{Ni}$  within the resolution of the analysis techniques. Vacuum fusion measurements indicated that the powder contained 63ppmw of hydrogen, 67ppmw of nitrogen, and 2000ppmw of oxygen. The elevated oxygen content of the particulate is probably affected by the significant fraction of splat flakes in the random sample of the yield. Since the oxygen content is probably associated primarily with particulate surfaces, the contribution to total surface area of the splat flakes compared to the spherical powders is likely to be disproportionately large (by weight) and probably inflates the oxygen content of the total particulate yield.

The heat capacity of a hot pressed, partially sintered  $\text{Er}_3\text{Ni}$  powder sample was measured from 2 to about 80K. Figure 5 gives our  $\text{Er}_3\text{Ni}$  heat capacity results from 2 to 30K along with the Sahashi et al. (1) results for both  $\text{Er}_3\text{Ni}$  and Pb. The results of this study show a maximum heat capacity of  $0.43 \text{ J/cm}^3\text{K}$  at about 7K. The heat capacity of our  $\text{Er}_3\text{Ni}$  sample is somewhat higher than that reported by Sahashi et al. (1) from 5 to 25K, except in the 8 to 10K range just above the

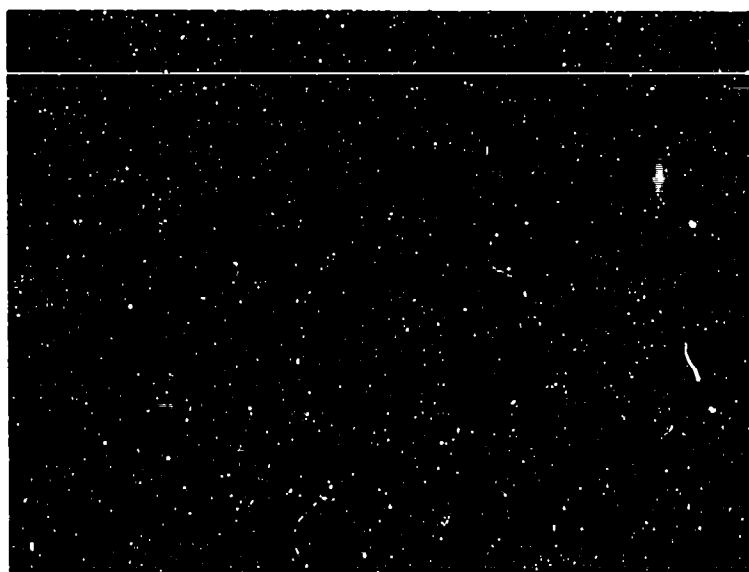


Figure 3. SEM micrograph of as-atomized Er<sub>3</sub>Ni powder prepared by HFCA after screening to  $0.212 < \text{dia.} < 0.300\text{mm}$  and removal of flake particulate. Powder was encapsulated in epoxy, metallographically sectioned, and etched (2% nital) to reveal particulate microstructure.



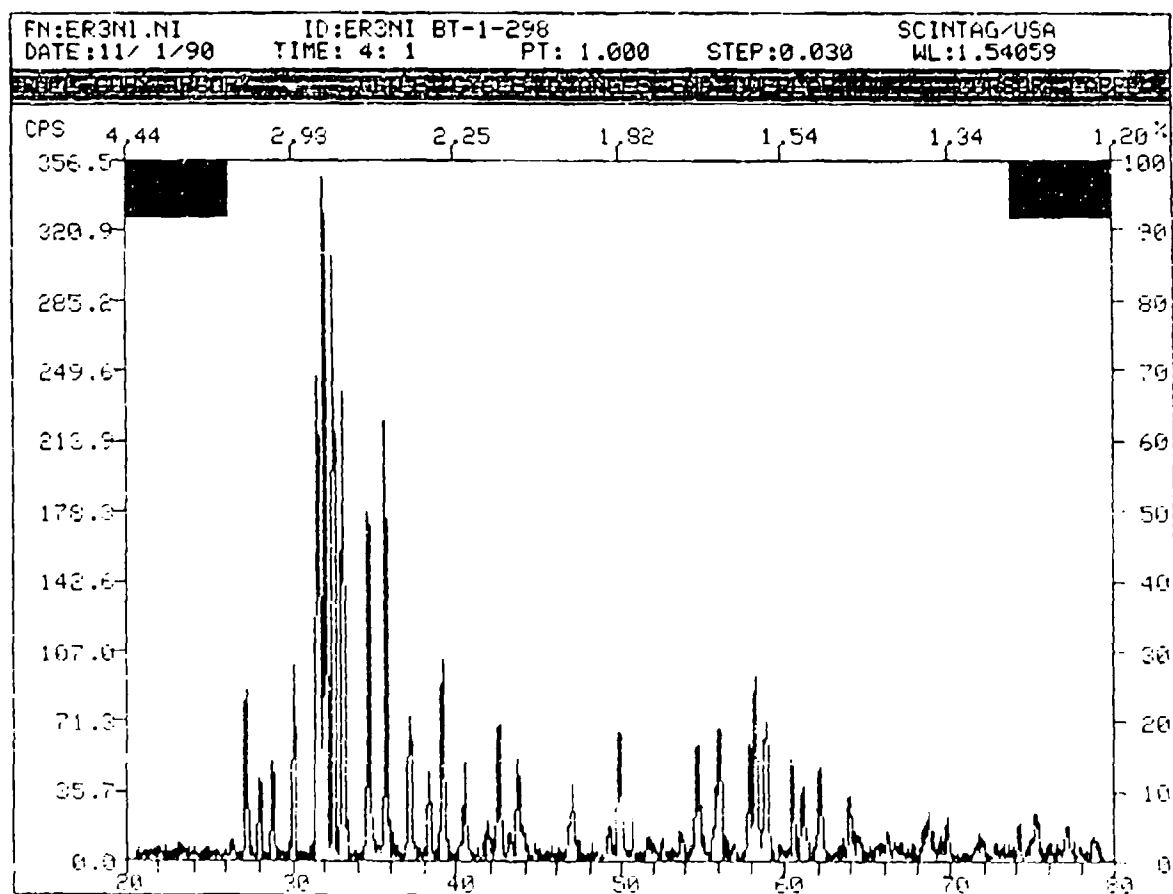


Figure 4. Results of x-ray diffraction analysis using Cu-Kalpha radiation of a random sample of as-atomized  $\text{Er}_3\text{Ni}$  powder prepared by HPGA, where the lower x-axis scale is in degrees 2 theta and the left y-axis scale is in arbitrary counts per second (CPS).

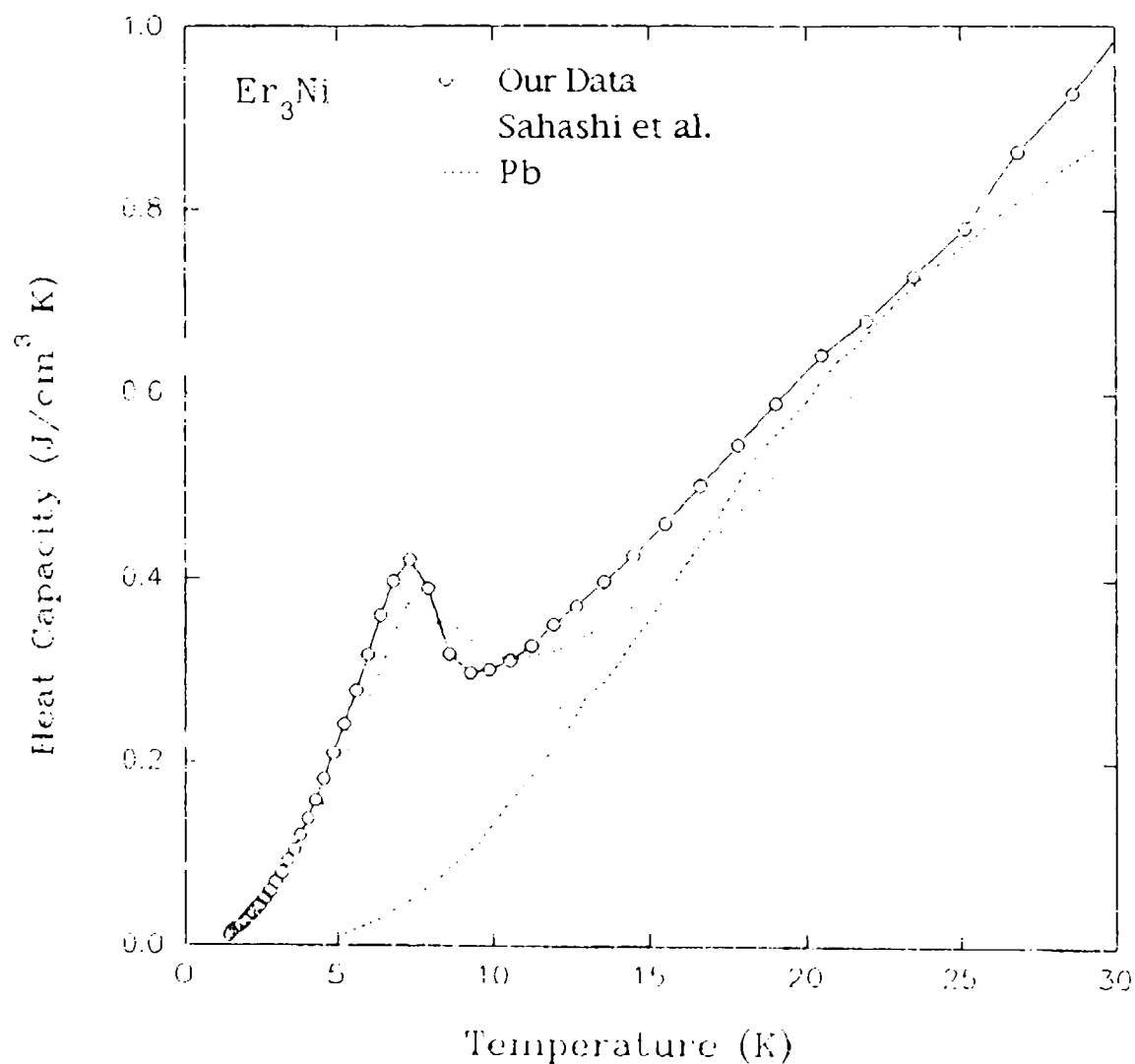


Figure 5. Low temperature portion of subambient (2 to 80K) calorimetry results for  $\text{Er}_3\text{Ni}$  alloy sample prepared from HPGA powder after screening to  $0.212 < \text{dia.} < 0.300\text{mm}$ , removal of flake particulate, and partial sintering. Also shown for comparison are the results that Sahashi et al. (1) reported for  $\text{Er}_3\text{Ni}$  and Pb.

antiferromagnetic ordering temperature. This is due to the broader heat capacity peak of the Sahashi et al. (1) sample. The heat capacity peak of our sample is about  $0.04 \text{ J/cm}^3\text{K}$  higher than that of Sahashi, et al. (1) and is also narrower.

## DISCUSSION

High pressure gas atomization (HPGA) experiments at the Ames Laboratory have yielded research quantities of  $\text{Er}_3\text{Ni}$ . These experiments resulted in 0.15 to 0.35mm spheres with an average yield of 16% of the original atomizer charge weight at a production rate of about 75g per second. Most of the remaining yield was splat flakes or finer powders. While the HPGA process yield of 16% spheres in the desired size range does not appear especially laudable, especially in light of the high cost of the alloy, our average yield is probably at least four times that of a competing gas atomization research program at NIST (2) which reported a 3% yield of both spheres and irregular particulate between 0.12 and 0.25mm.

Unfortunately, all gas atomized powders with diameters greater than about 0.075mm contain a fraction, usually about 10%, of particles with large central pores that arise from gas trapped during the atomization process. These hollow spheres are difficult to separate from the solid ones and can contribute to a reduction in total heat capacity of the packed bed. It is important to note that if the particle size requirements in new packed bed heat exchanger designs are decreased below 0.075mm, the HPGA process could produce significantly greater yields of solid spherical powders. Alternatively, a new atomization process under development at the Ames Laboratory (9) can produce internally sound spherical powders of large (0.15 to about 0.7mm) pure metals and alloys of transition metals. This centrifugal atomization into a rotating quench bath (CA/RQB) approach is currently being extended to REI alloys, including  $\text{Er}_3\text{Ni}$ , and the results of these experiments will be reported in the future.

In Figure 5, we also compare the results of our heat capacity measurements on  $\text{Er}_3\text{Ni}$  with those reported by Sahashi et al. (1) for  $\text{Er}_3\text{Ni}$  and for Pb. The sharper peak in our sample compared to that of the Sahashi et al. (1) sample indicates that our material is purer, either chemically or structurally, or both. Unfortunately, Sahashi et al. (1) do not report chemical analysis results which could be used for comparison of chemical purity. However, the double peak in the Sahashi et al. (1)  $\text{Er}_3\text{Ni}$  sample, taken by itself (in lieu of x-ray diffraction results), suggests that a second phase is present in their alloy. The presence of this second phase may also account for the fact that the heat capacity of their sample is smaller than ours over the 5 to 25K range. Furthermore, we

note that the heat capacity of our Er<sub>3</sub>Ni sample is larger than that of lead over the entire range of temperatures shown in Figure 5. This should permit a lower final temperature for a cryocooler stage composed of our material and also may allow for a shorter initial cooling time to a given temperature.

#### SUMMARY

1. High pressure gas atomization (HPGA) is a viable technique for production of research quantities of spherical, passivated Er<sub>3</sub>Ni powders for cryocooler applications.
2. Chemical, structural, and calorimetric characterization of the HPGA powders indicates that single phase powders of the stoichiometric Er<sub>3</sub>Ni compound were produced without any significant level of contamination except possibly for oxygen.
3. As a result of the high quality of the HPGA Er<sub>3</sub>Ni, the calorimetric measurements revealed that the peak heat capacity of our sample at 7K exceeded all reported measurements of this alloy and is larger than that of lead from 2K to at least 30K which should permit a lower final temperature for a cryocooler stage composed of our material and also may allow for a shorter initial cooling time to a given temperature.

#### ACKNOWLEDGMENTS

We wish to thank B. Beaudry and F. A. Schmidt for their valuable insight on the design of a compatible melting system for this alloy and R. L. Terpstra for his careful preparation of the atomization system for this difficult powder processing task. This work was funded partially by the U. S. Dept. of Energy through contract no. W-7405-Eng-82 from the Materials Science Division of Basic Energy Sciences.

#### REFERENCES

1. M. Sahashi, Y. Tokai, T. Kuriyama, H. Nakagome, R. Li, M. Ogawa, and T. Hashimoto, *Advances in Cryogenic Engineering*, **35**, Plenum Press, NY, NY, 1175(1990).
2. L. F. Aprigliano, G. Green, J. Chafe, L. O'Connor, F. Biancanello, and S. Ridder, *Advances in Cryogenic Engineering*, **37B**, R. W. Fast, ed., Plenum Press, NY, NY, 1003(1992).
3. R. A. Ackermann, *Advances in Cryogenic Engineering*, **37B**, R. W. Fast, ed., Plenum Press, NY, NY, 981(1992).

4. E. M. Ludeman and C. B. Zimm, in Proceedings of the Cryogenic Engineering Conference, held in Huntsville, AL, (June 1991).
5. I. E. Anderson, R. L. Terpstra, and B. K. Lograsso, "Environmentally Stable Reactive Alloy Powders and Method of Making Same," U. S. Patent Application pending.
6. I. E. Anderson, R. S. Figliola, and H. M. Molnar, Materials Science and Engineering, **A148**, 101(1991).
7. I. E. Anderson, H. M. Molnar, and R. S. Figliola, U.S. Patent No. 5,125,574, issued June 30, 1992.
8. K. Ikeda, K. A. Gschneidner, Jr., B. J. Beaudry, and U. Atzmony, Phys. Rev., **B25**, 4604 (1982).
9. M. G. Osborne, I. E. Anderson, K. S. Funke, and J. D. Verhoeven, in Advances in Powder Metallurgy - 1992, J. M. Capus and R. M. German, eds., MPIF-APMI, Princeton, NJ, (in press).

## MAGNETIC NANOCOMPOSITES AS MAGNETIC REFRIGERANTS

R.D. SHULL, R.D. MCMICHAEL, J.J. RITTER, L.J. SWARTZENDRUBER,  
and L.H. BENNETT

MATERIALS SCIENCE AND ENGINEERING LABORATORY  
NATIONAL INSTITUTE OF STANDARDS AND TECHNOLOGY  
GAITHERSBURG, MD 20899

### I. INTRODUCTION

It has been found that materials possessing nanometer-scale dimensions, called nanocrystalline or nanostructured materials, may possess properties or property combinations which are different from those possessed by conventional materials having larger dimensions<sup>[1]</sup>. The unique properties of these new materials are a consequence of either the large volume percent of interfaces in the material or the reduction in size to less than that of the critical length scale appropriate to the particular property. For nanocomposites<sup>[2]</sup>, wherein the material is a composite of nanometer-scale species, the properties are different from, but related to, those of the individual constituents. Consequently, the properties of this subset of the class of nanostructured materials are sensitive to the volume fraction of its components. This additional degree of freedom is useful for the atomic engineering of materials with very specific properties since volume fraction is a relatively easy variable to control. For magnetic nanocomposites, a new bulk magnetic state, called superparamagnetism, may exist. This magnetic state only exists when the magnetic particles are very small. At the last cryocooler conference, this type of magnetic material was first suggested as a new type of refrigerant for magnetic refrigerators<sup>[3,4]</sup>. Theoretical reasons for this suggestion were presented which showed that enhanced magnetocaloric effects are potentially obtainable in this type of material at higher temperatures and lower fields than in paramagnetic refrigerants. Preliminary data was also presented at that conference for a 10%Fe+silica gel magnetic nanocomposite. The magnetocaloric effects in this dilute nanocomposite, although being significantly enhanced over that of pure bulk Fe at 70 K, were still small in magnitude. Since that initial announcement, an analysis of the losses, refrigeration quality factor, and power density of magnetic refrigerators using magnetic nanocomposites<sup>[5]</sup> showed that these materials represent a real potential as magnetic refrigerants. In the following section, the theoretical basis for the enhanced magnetocaloric effects in superparamagnetic and "super-ferromagnetic" (wherein the magnetic clusters are allowed to magnetically interact)

nanocomposites will be reviewed, including improvements on the theory<sup>[6-8]</sup> made since the last cryocooler conference. A new magnetocaloric effect measurement method developed in this laboratory<sup>[9]</sup> for the fast screening of material candidates is described and data measured on several new magnetic nanocomposites is reviewed showing the predicted enhancements. Included in the last section is a description of a new type of magnetic nanocomposite: one which is single phase crystallographically, but multiple phase magnetically. This new material, Fe-doped gadolinium gallium garnet (GGIG), possesses magnetocaloric effects at 15 K and 1 T which are larger than that for the presently used low temperature magnetic refrigerant gadolinium gallium garnet (GGG)<sup>[10]</sup>. GGIG also has sufficiently large magnetocaloric effects at higher temperatures to suggest potential applications at temperatures in excess of 20 K.

## II. MAGNETOCALORIC EFFECT

The change in internal energy ( $dU$ ) of a closed system with no volume change occurring may be expressed in terms of the incremental changes in the entropy ( $dS$ ) and magnetization ( $dM$ ) as follows:

$$dU = TdS + HdM \quad (1)$$

where  $T$  and  $H$  are respectively the temperature and applied magnetic field. From this exact differential, the following Maxwell relation may be derived relating the incremental entropy change accompanying an incremental change in magnetic field to the easily measurable quantities of magnetization and temperature:

$$\left(\frac{\partial S}{\partial H}\right)_T = \left(\frac{\partial M}{\partial T}\right)_H . \quad (2)$$

Upon integrating over  $H$ , the total entropy change of the system upon the application of a magnetic field may be determined:

$$\Delta S = \int_0^H \left(\frac{\partial M}{\partial T}\right)_H dH . \quad (3)$$

The magnetocaloric effect (defined as a temperature change) is just  $\Delta S$  multiplied by the temperature and divided by the heat capacity (at constant  $H$ ). For the purposes of this paper we will focus on variations in  $\Delta S$  instead of  $\Delta T$ , keeping in mind they are closely related.

**A. For Paramagnets:**

For the case of a paramagnet, the temperature and field dependence of  $M$  is described by the Langevin function<sup>(11)</sup>:

$$M = N\mu[\coth(\alpha) - (\frac{1}{\alpha})] \quad (4)$$

$$\alpha = \frac{\mu H}{k_B T}$$

where  $\mu$  and  $N$  are respectively the size and number of non-interacting magnetic moments in the system, and  $k_B$  is the Boltzmann constant. Substituting the equation 4 relationship into equation 3 and performing the integration, one obtains the following for the entropy change upon application of the field<sup>(6)</sup>:

$$\Delta S = Nk_B[1 - \alpha \coth(\alpha) + \ln(\frac{\sinh(\alpha)}{\alpha})] . \quad (5)$$

At low fields or high temperatures (well away from saturation),  $M$  follows the Curie Law and  $\Delta S$  reduces to the following simple expression<sup>(4)</sup>:

$$\Delta S = \frac{N\mu^2 H^2}{6k_B T^2} . \quad (6)$$

Because  $\Delta S$  diverges to very large values at low temperatures, adiabatic demagnetization refrigerators in this temperature range can be made using paramagnetic salts like chromic potassium alum<sup>(12)</sup> (for  $T < 1$  K) or gadolinium gallium garnet<sup>(13,14)</sup> (for  $1 \text{ K} < T < 20 \text{ K}$ ) as the refrigerant. Note, however, from equation 6 that  $\Delta S$  decreases as  $1/T$ . Therefore, at high temperatures the magnetocaloric effect in paramagnets is small, and they cease to be useful refrigerants.

**B. For Nanocomposites with No Interaction Between Magnetic Clusters:**

Operation of a magnetic refrigerator at higher temperatures than 20 K. requires a refrigerant with a larger  $\Delta S$  value than obtainable with a paramagnet. One potential way to obtain the larger  $\Delta S$  values required for higher temperature magnetic refrigerator operation is to use magnetic nanocomposites possessing superparamagnetic behavior<sup>(4,6,9)</sup>.



Note from equation 6, that if  $\mu$  is made larger (and  $N$  is simultaneously made smaller to keep the saturation magnetization,  $N\mu$ , constant),  $\Delta S$  increases because of the squared dependence on  $\mu$  (and only linear dependence with  $N$ ). This is the same situation as grouping the  $N$  spins (each with a magnetic moment of  $\mu$ ) in the system together into "n" clusters (i.e. each cluster having  $N/n$  magnetic spins). Using equation 6, one can show that  $\Delta S$  for this situation at low values of  $\mu H/k_B T$  is described by equation 7:

$$\Delta S_{\text{nano}} = \frac{n \left(\frac{N}{n} \mu\right)^2 H^2}{6 k_B T^2} \quad (7)$$

Since "n" is much smaller than  $N$ , comparison of equations 7 and 6 (in equation 6,  $\mu = \mu_J$ ) shows that  $\Delta S_{\text{nano}}$  can be much larger than  $\Delta S$  for a paramagnet at low fields and high temperatures. This is the situation of a superparamagnetic nanocomposite where the atomic magnetic moments cluster to form fewer, but larger, independently acting magnetic moments. There is a limit to this enhancement, however. According to equation 5, at high fields or very low temperatures (when saturation is approached),  $\Delta S$  will decrease when  $\mu$  is increased further. In this regime  $M$  is no longer proportional to  $\mu^2$  (it approaches the constant value of the saturation magnetization), and the reduction in  $N$  factor upon clustering becomes more important by comparison. In fact there is a maximum in  $\Delta S$  with respect to variations in  $N\mu$ , as given in equation 5, at  $\alpha \equiv \alpha_{\text{max}} = \mu H/k_B T \approx 3.5$  [6]. This means that for the maximum magnetocaloric effect there is an optimum cluster size (i.e. an optimal value for  $\mu$ ) for any given temperature of operation and applied magnetic field. Figure 1 shows mean field theory calculations of  $\Delta S$  vs.  $T$  for a system of  $N$  spin-7/2 atoms (e.g. Gd atoms) isolated and clustered into various magnetic cluster sizes. The enhancements in  $\Delta S$  at lower fields and/or higher temperatures on clustering the spins is obvious. Note also the points of intersection of the various curves. At temperatures lower than these crossover points, the **smaller** cluster sizes are better. Superparamagnetic nanocomposites do not create new entropy; they just skew the available entropy to different field and temperature ranges not normally accessible to refrigeration systems using conventional materials.

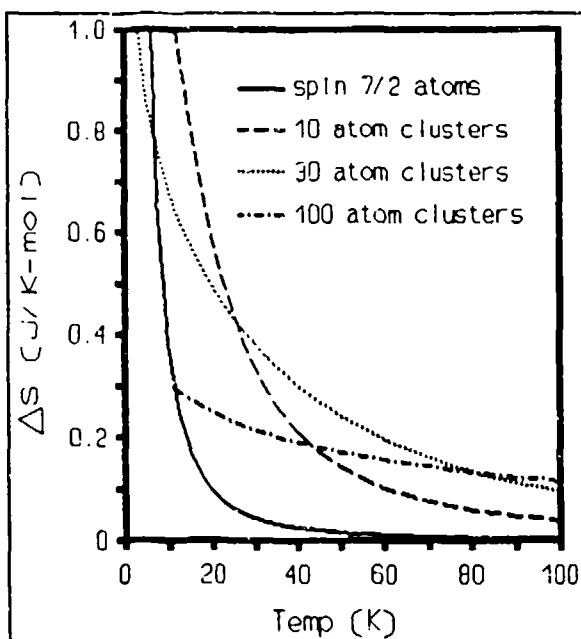


Figure 1. Calculated entropy change of a system of spin-7/2 atoms induced by the removal of a 800 kA/m field for individual spins (GGG) and for clusters of 10, 30, and 100 spins.

### C. For Ferromagnets:

In order to increase the operation temperature to very large values, ferromagnetic materials have historically been considered. In the case of a ferromagnet, examination of equation 3 indicates that the magnetocaloric effect would be small at temperatures much higher or much lower than the Curie temperature,  $T_C$ , since  $(dM/dT)_H$  is very small in those ranges. Accordingly, at  $T_C$  the magnetocaloric effect would be expected to be large. Above the Curie Point, the field and temperature dependence of the magnetization may be analyzed in the mean field approximation in a similar way as was done above for a paramagnet. The effect of the interaction between magnetic moments which occurs at temperatures below  $T_C$  is taken into account by replacing  $T$  in the above equations by  $T - T_C$  so that the parameter  $\alpha$  in equations 4 and 5 becomes

$$\alpha = \frac{\mu H}{k_B(T - T_C)} \quad (8)$$

For  $T > T_C$ , at low fields and high temperatures the entropy change on application of a magnetic field would be similar to that described in equation 6 for a paramagnet:

$$\Delta S = \frac{N\mu^2 H^2}{6k_B(T - T_C)^2} \quad (9)$$

In this case,  $\Delta S$  diverges to very large values as  $T$  approaches  $T_C$ . Consequently, near the Curie point ferromagnets are potentially useful as magnetic refrigerants. Below  $T_C$ , the magnetic spins are ordered in domains, but with an order which is incomplete at  $T_C$ . The magnetocaloric effect is proportional to the "disorder" within the domains at  $H=0$  (i.e. inversely with the spontaneous magnetization of the material below  $T_C$ ). As  $T$  decreases from  $T_C$ , the spin order within the domains increases, so  $\Delta S$  below  $T_C$  also decreases with  $T$ . Consequently,  $\Delta S$  for a ferromagnet is a sharply peaked function of  $T$  at the Curie point. Mean field theory calculations for  $\Delta S$  were performed as a function of  $T$  for a ferromagnet with a  $T_C$  near 300 K (e.g. Gd), and these are shown as the single atom curve in figure 2. Note in this figure the  $\Delta S$  systematics described above.

### D. For Nanocomposites with Interacting Clusters:

Magnetic nanocomposites may also be prepared so that the magnetic clusters interact with each other<sup>(15-16)</sup>. This situation describes the case of ferromagnetically-interacting

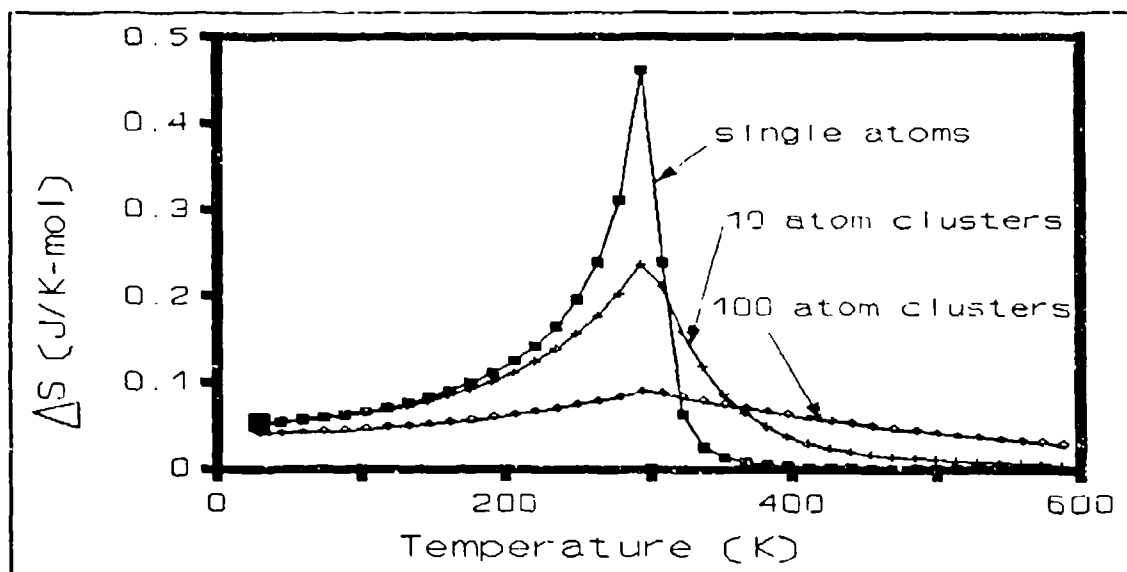


**Figure 2.** Calculated entropy change of a system of interacting spin-7/2 atoms (with  $T_I = 300$  K) induced by the removal of an 800 kA/m field for individual atomic spins (Gd) and for clusters of 10 and 100 spins.

superparamagnetic clusters. Nanocomposites of this type will possess an effective interaction temperature,  $T_I$ , analogous to the Curie temperature of a ferromagnet, which describes the interaction between clusters. Below  $T_I$  there is long range magnetic order between the clusters, and above  $T_I$  the material is superparamagnetic. Some authors have referred to this case as "super-ferromagnetic"<sup>[17]</sup>. In this case, there is also an enhancement in  $\Delta S$  above  $T_I$  (compared to that of a ferromagnet with  $T_C = T_I$ ) at low fields as  $\mu N$  (the saturation magnetization) is kept constant while  $\mu$  is increased in magnitude<sup>[4,7]</sup>. In the low field/high temperature limit  $\Delta S$  (called  $\Delta S_{\text{superferro}}$  in this case) will be similar to that expressed in equation 9:

$$\Delta S_{\text{superferro}} = \frac{n [(N/n)\mu_s]^2 H^2}{6k_B (T - T_I)^2} \quad (10)$$

where "n" is the number of interacting clusters and  $\mu_s$  is the magnetic moment of an individual elemental atomic spin. For low fields and high temperatures, the factor  $n[(N/n)\mu_s]^2$  which appears in equation 10 may be much larger than the factor  $N\mu^2$  which appears in equation 9 (where  $\mu = \mu_s$ ). The same limit to these enhancements described above for the superparamagnetic materials occurs for the ferromagnetically-interacting superparamagnets. Maximum enhancements in  $\Delta S_{\text{superferro}}$  are expected when  $\mu_c H/k_B T \approx 3.5$ , where  $\mu_c = [N/n]\mu_s$  is defined as the cluster magnetic moment. For temperatures less than or equal to  $T_I$ , i.e. when magnetic saturation is approached,  $\Delta S$  is smaller when  $\mu$  is increased by clustering the atomic moments<sup>[7]</sup>. The mean field

theory calculations are shown in figure 2. More exact Monte Carlo calculations of  $\Delta S$  for ferromagnetically-interacting superparamagnetic clusters<sup>[7]</sup> above and below  $T_c$  confirm the mean field theory calculations. In both calculations, the entropy change for a given applied field is peaked around the critical temperature ( $T_c$  for a ferromagnet and  $T_1$  for the clustered magnet). In the case of clustered magnetic moments, as in a nanocomposite, figure 2 shows that  $\Delta S$  is also spread out over a broader temperature range. For some magnetic refrigerator designs the large breadth in  $\Delta S$  is important. Also, for refrigeration cycles using an active magnetic regenerator, the slope of the  $\Delta S$  vs.  $T$  relationship below  $T_c$  is particularly important for attaining high efficiency<sup>[18-20]</sup>. Magnetic nanocomposites with interacting clusters provide a means for selecting that slope. In addition, they also provide a means for selecting  $T_1$  and for providing enhanced  $\Delta S$  values at temperatures higher than  $T_1$ <sup>[7]</sup>. All these adjustments are possible without diluting or changing the magnetic spins in the system, unlike composite ferromagnet refrigerants<sup>[21-22]</sup>. Recent calculations for an active magnetic refrigerator substantiate the potential provided by nanocomposites for obtaining refrigeration with enhanced power density and lower magnetic fields<sup>[5]</sup>. Uniaxial magnetic anisotropy can also affect the peak magnitude, peak temperature, and breadth of  $\Delta S$ . For ferromagnetic refrigerants, optimal characteristics are obtained when the magnetic field is directed normal to the easy plane of magnetization<sup>[8]</sup>. If, however, one wished to employ superparamagnetic particles in their paramagnetic regime to obtain a broad  $\Delta S$  vs  $T$  curve, then the applied field should be parallel to the favored axis of magnetization<sup>[8]</sup>.

### III. ENTROPY CALCULATION FROM MAGNETIZATION DATA

Equation 3 relates the entropy change for the application of the magnetic field,  $H$ , in terms of the measurable quantities of  $M$ ,  $T$ , and  $H$ . If one measures the magnetization as a function of field at various temperatures, then the integral in equation 3 becomes just the area enclosed between any two isotherms divided by the temperature difference between the isotherms<sup>[9]</sup>:

$$\Delta S_i = \frac{1}{\Delta T_i} \int_0^H [M(T_{i+1}, H) - M(T_i, H)] dH \quad (11)$$

$$\Delta T_i = T_{i+1} - T_i .$$

Thus the magnetocaloric effect can be measured without calorimetry. This method was tested for gadolinium gallium garnet and compared to direct calculations for spin-7/2 atoms (i.e. a system of independent Gd atoms). The agreement between the measured

data using equation 11 and the calculated values was quite good (within 10%), thereby providing confidence in this method for determining  $\Delta S$ . Since magnetization data is much faster to measure than  $\Delta T$  and heat capacity data, this non-calorimetric method is a fast way to screen prospective magnetic refrigerants. In our laboratory, it has been especially valuable for assessing the utility of various magnetic nanocomposite processing methods, including co-precipitation, solution reduction, and metal-organo complex routes, for making magnetic refrigerants.

#### IV. EXPERIMENTAL DATA

Magnetic nanocomposites are usually prepared as a physical mixture of two distinctly different crystallographic phases (e.g. Fe + alumina<sup>[23]</sup>, Ni + silica<sup>[24]</sup>, and Fe<sub>3</sub>O<sub>4</sub> + silver<sup>[25]</sup>), one of which is ferromagnetic and one phase which is not magnetic. In the last cryocooler conference, we reported on some data for a 10%Fe+silica gel nanocomposite<sup>[4]</sup> which showed that this dilute superparamagnetic material possessed a magnetocaloric effect at 70 K which, although small, far exceeded that which pure Fe would have at that temperature. In fact, the dilute nanocomposite possessed an effect which was one quarter as large as the maximum effect possessed by pure Fe at its Curie temperature. These results were consistent with the enhancements predicted above for superparamagnetic nanocomposites. Subsequent investigation of the temperature and concentration dependence of  $\Delta S$  for the Fe+silica gel nanocomposites also provided consistent results with the predictions described above, but the magnetocaloric effects were still small<sup>[9]</sup>.

Recently, in our laboratory a magnetic nanocomposite of Gd magnetic clusters<sup>[26]</sup> in a garnet structure was prepared using a metal-organo complex process. Specifically, this type of magnetic nanocomposite was created by complexing the mixed nitrates of Gd and Fe with an excess of tartaric acid in water solution. The solvent was thermally removed ( $T \approx 300^\circ\text{C}$ ) and the nanocomposite was formed by treating the resultant precursors in air at  $950^\circ\text{C}$ . This process has the advantage that large amounts of material (in excess of several cubic centimeters) may be prepared relatively easily. This magnetic nanocomposite, however, is different from the ones previously examined (and described above) in the sense that it is a single crystallographic phase rather than a mixture of structurally different phases. The overall crystal structure of the nanocomposite was confirmed by x-ray diffraction to be that of a garnet, similar to the crystal structure of gadolinium gallium garnet (GGG), and with a stoichiometry of  $\text{Gd}_3\text{Ga}_{5-x}\text{Fe}_x\text{O}_{12}$  ( $x < 5$ ). In this nanocomposite, Fe atoms have substituted for Ga atoms in the lattice of GGG ( $\text{Gd}_3\text{Ga}_5\text{O}_{12}$ ). Concurrently, the field dependence of the magnetization for the Fe-doped

garnets (for  $x < 5$ ) near 20 K lost its linearity, indicating the loss of paramagnetism. Analysis of the magnetization of the  $\text{Gd}_3\text{Ga}_{5-x}\text{Fe}_x\text{O}_{12}$  ( $x < 5$ ) materials showed the paramagnetic state of GGG had been changed by the Fe addition to that indicative of small magnetic clusters in a non-magnetic or weakly magnetic matrix (earlier referred to as superparamagnetism). The iron-doped gadolinium gallium garnet (GGIG) is, therefore, comprised of at least two magnetically different regions (or phases) even though crystallographically it is only a single phase. It is believed that the superparamagnetic state formed in the GGIG nanocomposite is a consequence of the onset of ferromagnetic interactions between those Gd atoms which are near neighbors to the Fe atoms. This Gd-Gd interaction (absent in GGG) is possibly a magnetic superexchange-type interaction

via the Fe atom, as has been observed to occur between transition metal atoms in some transition metal alloys<sup>[27]</sup>. A schematic of the structure of the gadolinium gallium iron garnet magnetic nanocomposite is shown in figure 3. In this figure the magnetic clusters are pictorially represented by the atoms enclosed in the areas bounded by the dashed lines, and inside these areas the spins of the Gd atoms are aligned. The intermediate regions contain non-interacting (non-aligned) paramagnetic Gd atoms. This picture (which does not properly reflect the crystal symmetry) was drawn only for visualizing the correspondence between atomic position and magnetic state possessed by the various Gd atoms in this novel magnetic nanocomposite. Note, that in this type of nanocomposite, there is no dilution of magnetic material required for creating superparamagnetic behavior. Consequently, there is no loss in total magnetic-spin entropy, a problem with nanocomposites like the Fe+silica gel material where non-magnetic silica must be added to break up the Fe into small regions.

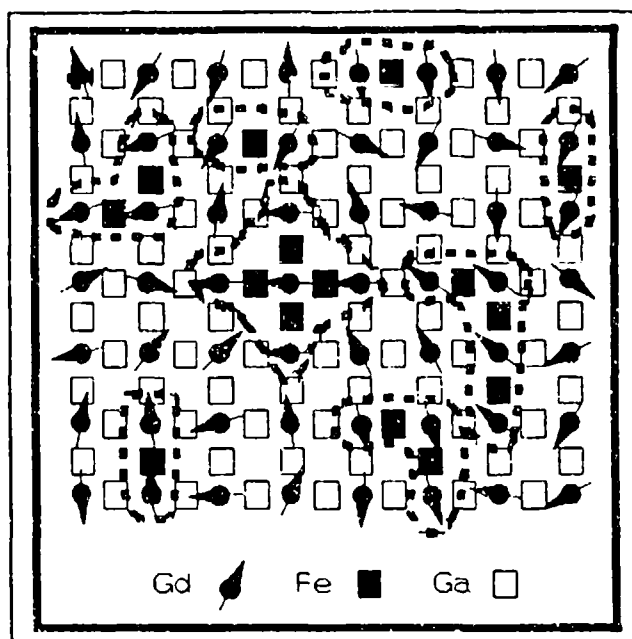


Figure 3. Schematic of the  $\text{Gd}_3\text{Ga}_{5-x}\text{Fe}_x\text{O}_{12}$  magnetic nanocomposite structure showing atomic positions, spin directions (via arrows) of the Gd atoms and the locations of magnetic clusters (dashed lines).

As an experimental test of the above predictions for enhanced magnetocaloric effects in magnetic nanocomposites, the magnetization as a function of  $H$  and  $T$  were measured for several  $\text{Gd}_3\text{Ga}_{5-x}\text{Fe}_x\text{O}_{12}$  (GGIG) samples with  $x < 5$  up to a field of 800 kA/m (1 tesla) between 4.2 K and 100 K. Calculation of the entropy change,  $\Delta S$ , for these materials upon a field change of 800 kA/m as a function of temperature was performed according

to the method described in equation 11 and compared to that measured for GGG. The results are shown in figure 4<sup>[10]</sup>. Note that as Fe is substituted for Ga in the nanocomposite,  $\Delta S$  systematically increases as more magnetic clusters are formed, in accordance with the  $\Delta S$ -enhancement predictions of equation 7. Maximum enhancements occur when half the Ga atoms are substituted by Fe. Further Fe addition was found to result in a decrease in the  $\Delta S$  enhancements over GGG. The optimal  $\Delta S$  enhancement behavior would be expected according to the predictions of equation 7, if the optimal cluster size for this field and temperature range is attained at the  $x=2.5$  composition. We argue that this proof of the earlier theoretical predictions should be used as motivation for an accelerated effort in the development of magnetic nanocomposite refrigerants. Furthermore, note from figure 4 that when half the Ga atoms are replaced by Fe atoms ( $x=2.5$ ),  $\Delta S$  was enhanced over that for GGG at all temperatures greater than 7 K. At 15 K, the GGIG nanocomposite possessed a  $\Delta S$  value at 800 kA/m (1 tesla) 3.4 times larger than that for GGG, the best present magnetic refrigerant at this temperature. At 20 K, the  $x=2.5$  GGIG possessed a  $\Delta S$  value 4.5 times larger than that of GGG. In fact, the  $\text{Gd}_3\text{Ga}_{2.5}\text{Fe}_{2.5}\text{O}_{12}$  nanocomposite possessed a  $\Delta S$  value at temperatures in excess of 70 K that was larger than that possessed by GGG at 15 K, the present maximum refrigeration temperature using GGG. This nanocomposite does not possess a remanent magnetization, and, therefore, no hysteretic losses during field cycling.

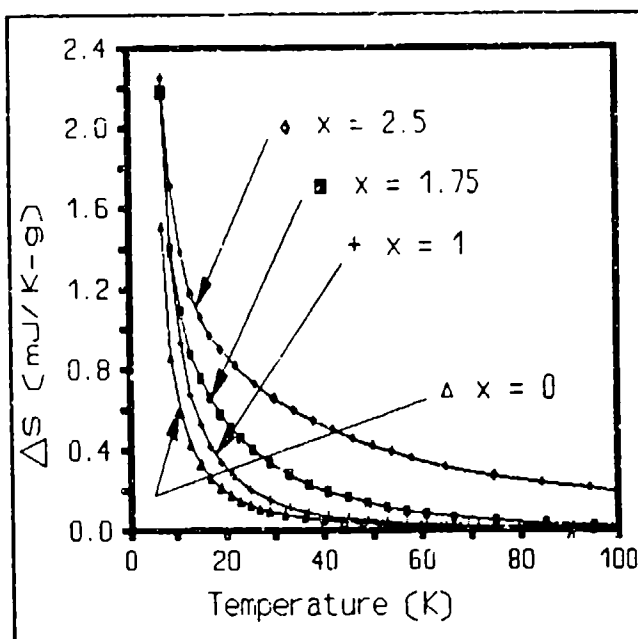


Figure 4. Measured entropy change vs T for a field change of 800 kA/m for GGG ( $x=0$ ) and the GGIG magnetic nanocomposites containing 1, 1.75, and 2.5 atomic % Fe.

## V. CONCLUSIONS

Magnetic refrigeration, which used to be restricted to  $T < 1$  K in one-shot adiabatic demagnetization refrigerators, is a viable technology at higher temperatures. Paramagnetic refrigerants are restricted to low temperature applications, while ferromagnetic refrigerants and nanocomposite refrigerants hold the promise for high

temperature refrigerators. Previous theoretical predictions for enhanced magnetocaloric effects in superparamagnetic nanocomposites have been substantiated by measurements on a new magnetic nanocomposite,  $\text{Gd}_3\text{Ga}_{5-x}\text{Fe}_x\text{O}_{12}$  ( $x < 5$ ). This nanocomposite even has potential applications as a substitute refrigerant for GGG in the  $7 \text{ K} < T < 20 \text{ K}$  temperature range, and perhaps at temperatures as high as 40 K. It has also been shown that magnetocaloric entropy changes can be calculated from the temperature and magnetic field dependence of the magnetization. This provides a fast method for screening potential magnetic refrigerants.

## VI. REFERENCES

1. "Cluster-Assembled Nanophase Materials", R.W. Siegel, *Annu. Rev. Mater. Sci.* **21** (1991) 559.
2. "Granular Metal Films", B. Abeles, *Appl. Solid State Sci.* **6** (1976) 1;  
"Nanocomposite Magnetic Materials", Shull, R. D. and Bennett, L. H., *J. Nanostructured Materials* **1**, No. 1 (1992) 83.
3. Patent Pending
4. R. D. Shull, L. J. Swartzendruber, and L. H. Bennett, *Proceedings of the Sixth International Cryocoolers Conference* (David Taylor Research Center Publ. #DTRC-91/002, Annapolis, MD, 1991), p. 231.
5. "Numerical Study of Magnetic Refrigeration Including Consideration of Magnetic Nanocomposites", C. Carpetis, *Proceedings of the 18th International Congress of Refrigeration*, Montreal (1991).
6. "Magnetocaloric Effect in Superparamagnets", R.D. McMichael, R.D. Shull, L.J. Swartzendruber, L.H. Bennett, and R.E. Watson, *J. Mag. & Magn. Mat.* **111**, No. 1-2 (1992) 29.
7. "Monte Carlo and Mean Field Calculations of the Magnetocaloric Effect of Ferromagnetically Interacting Clusters", L.H. Bennett, R. McMichael, L.J. Swartzendruber, R.D. Shull, and R.E. Watson, *J. Magnetism & Magnetic Materials* **104-107** (1992) 1094.
8. "The Magnetocaloric Effect: Role of Anisotropy", L.H. Bennett, R.D. McMichael, R.D. Shull, and L.J. Swartzendruber, to be published in the *J. Appl. Phys.* (April, 1993).
9. "Magnetocaloric Effect in Fine Magnetic Particle Systems," R.D. Shull, R.D. McMichael, L.J. Swartzendruber, and L.H. Bennett, *Magnetic Properties of Fine Particles*, edited by J.L. Dormann and D. Fiorani, Elsevier Publ., Amsterdam, (1992) p. 161.
10. "Enhanced Magnetocaloric Effect in  $\text{Gd}_3\text{Ga}_{5-x}\text{Fe}_x\text{O}_{12}$ ", R.D. McMichael, J.J. Ritter, and R.D. Shull, to be published in the *J. Appl. Phys.* (April, 1993).



11. B. D. Cullity, Introduction to Magnetic Materials (Addison-Wesley Publ. Co., Reading, MA, 1974), p. 94.
12. B. Bleaney, Proc. Roy. Soc. A204, 203 (1950).
13. T. Hashimoto, Advances in Cryogenic Engineering 32, 261 (1986).
14. T. Hashimoto, T. Yazawa, R. Li, T. Kuzuhara, K. Matsumoto, H. Nakagome, M. Takahashi, M. Sahashi, K. Inomata, A. Tomokiyo, and H. Yayama, Advances in Cryogenic Engineering 33, 733 (1988).
15. R. D. Shull, J. J. Ritter, A. J. Shapiro, L. J. Swartzendruber, and L. H. Bennett, Multicomponent Ultrafine Microstructures, MRS Symposium Proceedings 132 (North Holland Pub. Co., N.Y., 1988), p. 179.
16. R. D. Shull and J. J. Ritter, Physical Phenomena in Granular Materials, MRS Symposium Proceedings 195 (North Holland Pub. Co., N.Y., 1990), p. 435.
17. "Mössbauer Studies of Isolated and Interacting Ultrafine Magnetic Particles", S. MØrup, Magnetic Properties of Fine Particles, edited by J.L. Dormann and D. Fiorani, Elsevier Publ., Amsterdam, (1992) p. 125.
18. J. L. Smith, Y. Iwasa, and F. J. Cogswell, Advances in Cryogenic Engineering 35, 1157 (1990).
19. A. J. DeGregoria, Advances in Cryogenic Engineering 37, 867 (1992).
20. J. A. Barclay, Proceedings of the 18th International Congress of Refrigeration, Montreal (1991).
21. T. Hashimoto, M. Ogawa, A. Hayashi, M. Makino, R. Li, and K. Aoki, Advances in Cryogenic Engineering 37, 859 (1992).
22. T. Hashimoto, K. Matsumoto, T. Kurihara, T. Numazawa, A. Tomokiyo, H. Yayama, T. Goto, S. Todo, and M. Sahashi, Advances in Cryogenic Engineering 32, 279 (1986).
23. J. L. Dormann, L. Bessais, and D. Fiorani, J. Phys. C: Solid State Phys. 21, 2015 (1988).
24. J. P. Bilisoly, U.S. Patent No. 2496265 (Feb. 7, 1950).
25. R. D. Shull, U. Atzmony, A. J. Shapiro, L. J. Swartzendruber, L. H. Bennett, W. L. Green, and K. Moorjani, J. Appl. Phys. 63, 4261 (1988).
26. Patent Pending
27. A. Arrott and H. Sato, Phys. Rev. 114, 1420 (1959).

## ENTHALPY FLOW TRANSITION LOSSES IN REGENERATIVE CRYOCOOLERS

PETER KITTEL  
 Technology Development Branch  
 Space Projects Division  
 NASA, Ames Research Center  
 Moffett Field, CA 94035-1000

ABSTRACT

In regenerative cryocoolers, enthalpy flow is characterized by an oscillating temperature within the working fluid. When there are changes in enthalpy flow, the amplitude of the temperature oscillation also changes. This is an irreversible process that generates entropy. Thus, this process is a loss mechanism. Such losses occur at the transition between heat exchangers (isothermal regions) and adiabatic regions.

This paper presents a generalized method of calculating these losses. For a sinusoidal temperature variation, the fractional loss per cycle is

$$(\pi x \cos \phi)^{-1} \int_0^{2\pi} \left| \left\{ \frac{1+x \sin \theta}{\alpha x + 1} - \ln \left( \frac{1+x \sin \theta}{\alpha x + 1} \right) - 1 \right\} \sin(\theta - \phi) \right| d\theta$$

where  $x$  is the ratio of the temperature oscillation amplitude to the average temperature,  $\alpha$  is ratio of the change in the mean temperature at the transition to the temperature oscillation amplitude, and  $\phi$  is the phase angle between the mass flow and the temperature oscillation.

Approximate solutions are also developed for cases relevant to pulse tube and Stirling cryocoolers.

INTRODUCTION

Enthalpy flow analysis has become a useful tool in understanding how regenerative cryocoolers work.<sup>1</sup> Finite enthalpy flows occur in adiabatic regions of coolers and in regions with poor heat transfer between the working fluid and the surroundings. Regions with finite enthalpy flow include the pulse tube in pulse tube coolers, the expansion space in Stirling and G-M coolers that are operating too fast for isothermal expansion, and between a valveless compressor and the aftercooler

Enthalpy flow analysis has mostly been used to analyze the gross cooling power. However this technique may also be used to quantify losses within coolers. This paper discusses a loss that occurs when there is a change in enthalpy flow, in particular, when the enthalpy flow changes

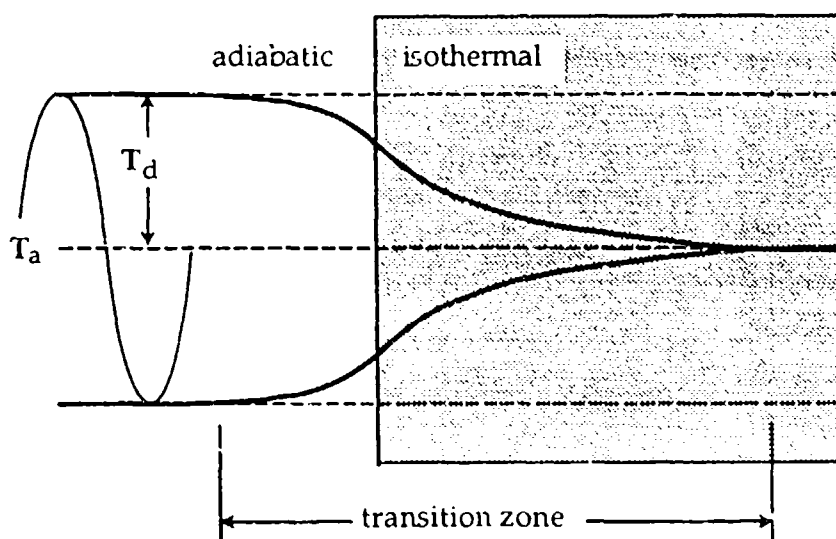


Figure 1. Representation of the change in the amplitude of the temperature oscillation at a transition from a finite enthalpy flow to isothermal flow. The amplitude changes from  $T_d$  to 0. In this example the mean temperature  $T_a$  does not change.

seen a finite value and zero. This is shown pictorially in Figure 1. Such transitions may be found at the junction of heat exchangers and adiabatic sections.

In regions with enthalpy flow the local temperature  $T$ , and mass flow,  $\dot{m}$ , of the working fluid oscillate. The enthalpy flow per cycle is given by

$$H_d = C_p \int_0^{2\pi/\omega} \dot{m} T \, dt \quad (1)$$

On entering an isothermal section, the enthalpy flow goes to zero, because the amplitude,  $T_d$ , of the temperature oscillation goes to zero. The transition occurs over a finite distance in a transition zone. In this zone gas elements undergo a temperature change from  $T$  to  $T_a$ , the mean temperature. The time it takes for this transition is small compared to the cycle time ( $2\pi/\omega$ ). This is the same as saying that the displacement of a gas element during a cycle is large compared to the length of the transition zone. Thus, we may treat the process as quasi-static. During the time it takes for an element of gas to cross the transition zone,  $\dot{m}$  and the pressure,  $P$ , do not change and  $T$  in the adiabatic section does not change. However, while crossing the transition zone, the temperature of the gas element changes. The temperature change is not caused work being done because, on the time scale of crossing the transition zone,  $P$  and  $\dot{m}$  are constant. Thus, the temperature change is caused by transferring heat to or from the surroundings. The rate heat is transferred by an incremental change in temperature,  $dt$ , of the gas element is

$$d\dot{Q} = C_p \dot{m} dt \quad (2)$$

(Positive heat flow is from the heat exchanger to the gas.) The total heat transferred by an element of gas is

$$dQ = C_p \dot{m} \left( \int_T^{T_a} d\tau \right) dt \quad (3)$$

The net heat transfer per cycle is found by integrating over one cycle:

$$Q = -C_p \int_0^{2\pi/\omega} \dot{m} (T - T_a) dt = -H_d \quad (4)$$

This is the expected result since for infinitesimal processes  $dH = dQ + V dP$  and  $dP = 0$  for this process.

However the process is not reversible. During the incremental process described above the heat flows across a temperature difference. Thus entropy is produced. The rate entropy changes is

$$d\dot{S} = C_p \left| \dot{m} \left\{ \frac{1}{T_a} - \frac{1}{\tau} \right\} d\tau \right| \quad (5)$$

where  $\tau$  is the instantaneous temperature of an element of gas within the transition zone and the absolute value sign is a reflection of the second law of thermodynamics, that  $dS \geq 0$  for all processes. The entropy change within the transition zone is found by integrating eq. (5) over the complete temperature change:

$$dS = C_p \left| \dot{m} \left( \int_{T_a}^T \left\{ \frac{1}{T_a} - \frac{1}{\tau} \right\} d\tau \right) \right| dt \quad (6)$$

In a more generalized case the mean temperature is different in the two regions. This is depicted in figure 2 where the mean temperature changes from  $T_a$  in the adiabatic region to  $(T_a + T_b)$  in the isothermal region. This situation is representative of the expander in regenerative coolers and of the flow between a compressor and its aftercooler. Equation (6) may be easily rewritten for this situation:

$$dS = C_p \left| \dot{m} \left( \int_{T_a + T_b}^T \left\{ \frac{1}{T_a + T_b} - \frac{1}{\tau} \right\} d\tau \right) \right| dt \quad (7)$$

Similarly eq. (4) may be rewritten as

$$Q = -C_p \int_0^{2\pi/\omega} \dot{m} [T - (T_a + T_b)] dt = -H_d \quad (8)$$

Equation (7) may be integrated over a cycle to yield the entropy produced per cycle:

$$\Delta S = C_p \int_0^{2\pi/\omega} \left| \dot{m} \left( \int_{T_a + T_b}^T \left\{ \frac{1}{T_a + T_b} - \frac{1}{\tau} \right\} d\tau \right) \right| dt \quad (9)$$

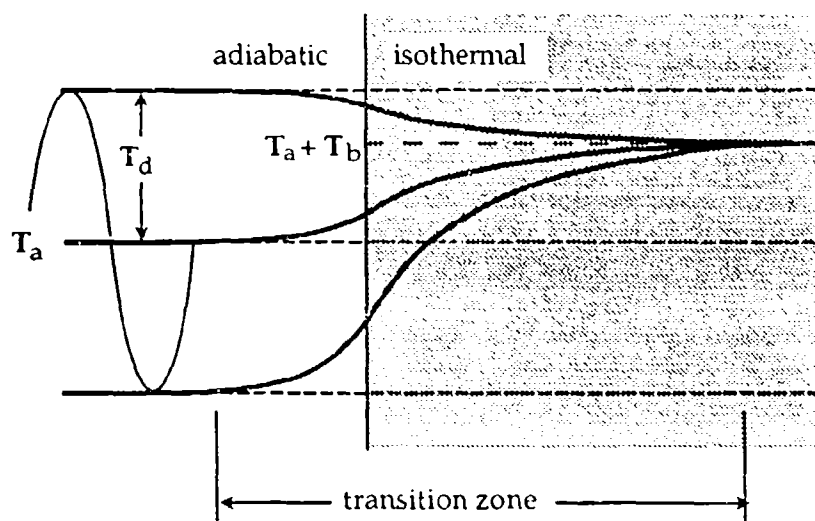


Figure 2. Representation of the change in temperature amplitude at a generalized transition from a finite enthalpy flow to isothermal flow. The amplitude changes from  $T_d$  to 0. The mean temperature changes from  $T_a$  in the adiabatic region to  $(T_a + T_b)$  in the isothermal region.

This entropy is produced by an irreversible process, the flow of heat across a temperature gradient. The enthalpy change during a process can be expressed as  $dH = T dS + V dP$ . Here, there is no pressure loss. Thus, the irreversible entropy reduces the enthalpy flow available for refrigeration. I.e., a portion of the heat transfer, eq. (8), is the result of this entropy production and is not available for cooling an external load. The lost enthalpy is  $T_a \Delta S$ . The fractional enthalpy lost per cycle is

$$\eta = T_a \Delta S / H_d \quad (10)$$

For simplicity we will assume that the temperature and mass flow are sinusoidal:

$$T = T_a + T_d \sin(\omega t) \quad (11)$$

$$\dot{m} = \dot{m}_d \sin(\omega t - \phi) \quad (12)$$

where the subscripts a and d refer to the mean and dynamic components,  $\omega$  is the frequency and  $\phi$  is the phase shift. Substituting eqs. (8), (9), (11), and (12) into eq. (10) and integrating over  $\tau$  results in:

$$\eta = (\pi x \cos \phi)^{-1} \int_0^{2\pi} \left\{ \frac{1 + x \sin \theta}{\alpha x + 1} - \ln \left( \frac{1 + x \sin \theta}{\alpha x + 1} \right) - 1 \right\} \sin(\theta - \phi) d\theta \quad (13)$$

where  $x = T_d / T_a$ ,  $\alpha = T_b / T_d$ , and  $\theta = \omega t$ . The variables  $x$ ,  $\alpha$ , and  $\phi$  are constrained to the following ranges by physical considerations:  $0 \leq x \leq 1$ ,  $-1 \leq \alpha x$ , and  $-\pi/2 < \phi < \pi/2$ .

(The loss, eq. (10), uses  $T_a$  as the reference temperature. This temperature was chosen because it is the mean temperature of the gas and it is the gas that carries the enthalpy flow. However, in cooler analysis it is more common to use the temperature of the isothermal sections,  $(T_a + T_b)$ , as the reference temperature. In this case one can define a loss:  $\eta^* = (T_a + T_b)\Delta S / H_d$  where  $\eta^* = \eta(T_a + T_b) / T_a = \eta(\alpha x + 1)$ . This paper will deal with  $\eta$  rather than  $\eta^*$ .)

### APPROXIMATE SOLUTION

The integrand of eq. (13) is shown in figure 3. This is not a simple function to integrate in closed form. Fortunately, there are ways of approximating it. It is also possible to numerically integrate eq. (13).

A lower limit,  $\eta_\ell$ , to eq. (13) can be found by making use of the relation:  $\int |I| d\theta \geq |\int I d\theta|$ . These two integrals are equal when  $I$  does not change sign over the range of integration; i.e.,  $I \geq 0$  or  $I \leq 0$  throughout the integration range. Here

$$I = \left\{ \frac{1 + x \sin \theta}{\alpha x + 1} - \ln \left( \frac{1 + x \sin \theta}{\alpha x + 1} \right) - 1 \right\} \sin(\theta - \phi) \quad (14)$$

Thus,

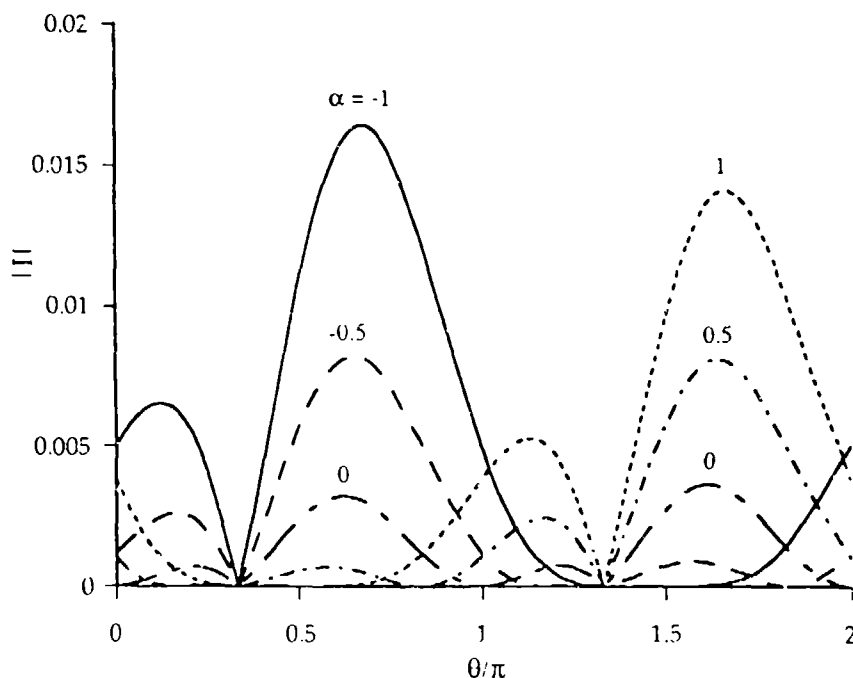


Figure 3. Plot of  $|I(x, \alpha, \theta, \phi)|$ , where  $I$  is given by eq. (14), for  $x = 0.1$ ,  $\phi = \pi/3$ , and five values of  $\alpha$  between -1 and 1.

$$\eta \geq \eta_\ell = (\pi x \cos \phi)^{-1} \left| \int_0^{2\pi} \left\{ \frac{1+x \sin \theta}{\alpha x + 1} - \ln \left( \frac{1+x \sin \theta}{\alpha x + 1} \right) - 1 \right\} \sin(\theta - \phi) d\theta \right| \quad (15)$$

An approximate form of  $\eta_\ell$  can be found by expanding the logarithmic term in eq. (15) as a power series in  $x$  and keeping the lowest order term. This results in

$$\begin{aligned} \eta_\ell &\approx \eta' = |\alpha| x (\alpha x + 1)^{-1} \\ &= |T_b| (T_a + T_b)^{-1} \end{aligned} \quad (16)$$

This approximation is the same as saying that the heat transfer process nominally involves the irreversible transport of heat from  $T_a$  to  $T_a + T_b$ ; which generates entropy:

$S = Q |T_a^{-1} - (T_a + T_b)^{-1}|$ . The same result can be reached by approximating the  $1/\tau$  term in eq.

(7) by  $1/T_a$ . However eq. (16) is derived, it is only an approximate lower limit. It does not have the  $\phi$  dependence that is explicitly contained in eq. (13). Nor does it adequately predict the behavior near  $\alpha = 0$ . Equation (7) and, therefore, eq. (13) are clearly not 0 at  $\alpha = 0$ , yet eq. (16) is.

Another approach is to find an approximate closed form solution of eq. (13) in the limit of small  $x$  and  $\alpha$ . The integral in eq. (13) can be written as  $\int |I| d\theta$ . This integral may be rewritten, since  $(\alpha x + 1) \geq 0$ , as  $\int |I| d\theta = (\alpha x + 1)^{-1} \int |J| d\theta$  where

$$J = (\alpha x + 1) I = \left\{ x \sin \theta - \alpha x - (\alpha x + 1) \ln \left( \frac{1 + x \sin \theta}{\alpha x + 1} \right) \right\} \sin(\theta - \phi) \quad (17)$$

This can be expanded in a Taylor series of  $x$ . Keeping the lowest order term results in

$$J \approx \frac{1}{2} (\alpha - \sin \theta)^2 x^2 \sin(\theta - \phi) \quad (18)$$

The function  $|J|$  may be integrated by first dividing it into segments where  $J \geq 0$  or  $J \leq 0$  and then integrating each segment separately. These regions are illustrated in figure 4. The boundaries

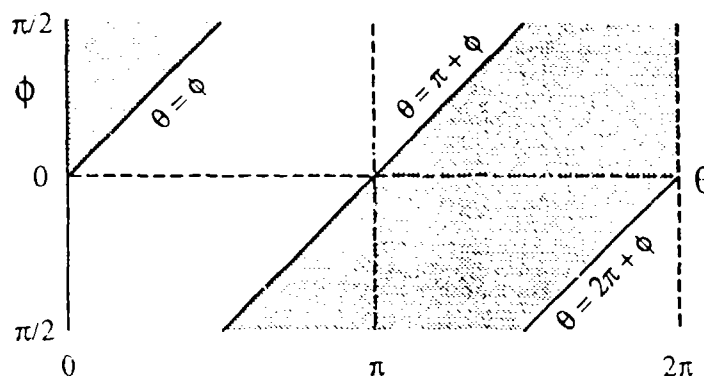


Figure 4. Regions in  $(\theta, \phi)$  space where eq. (18) is positive (unshaded) or negative (shaded).

between the  $J \geq 0$  and  $J \leq 0$  segments only depend on  $\theta$  and  $\phi$ .

Integrating  $|J(x, \alpha, \theta, \phi)|$  over  $\theta$  in this piecewise fashion yields

$$\eta \approx \eta'' = \left( \frac{1}{3} \cos(2\phi) + 2\alpha^2 + 1 \right) \frac{x}{\pi(\alpha x + 1) \cos \phi} \quad (18)$$

### COMPARISON TO NUMERICAL SOLUTION

It is possible to solve eq. (13) by numerical integration. Figure 5 shows such a solution for  $x = 0.1$ . The solution has a broad central region (where  $\alpha$  and  $\phi$  are small) in which  $\eta$  is slowly varying. At  $(\phi = 0, \alpha = 0)$   $\eta$  has a value of about  $4x/3\pi$  for a loss of about 4.2% when  $x = 0.1$ . Outside of this region,  $\eta$  increases rapidly. Figures 6, 7, and 8 show comparisons between  $\eta$  and the approximations,  $\eta'$  and  $\eta''$ . These comparisons are done around several operating conditions that are representative of conditions that might occur in coolers:  $\phi = 0$ ,  $x = 0.1$ , and  $\alpha = -1, 0$ , and  $1$ .

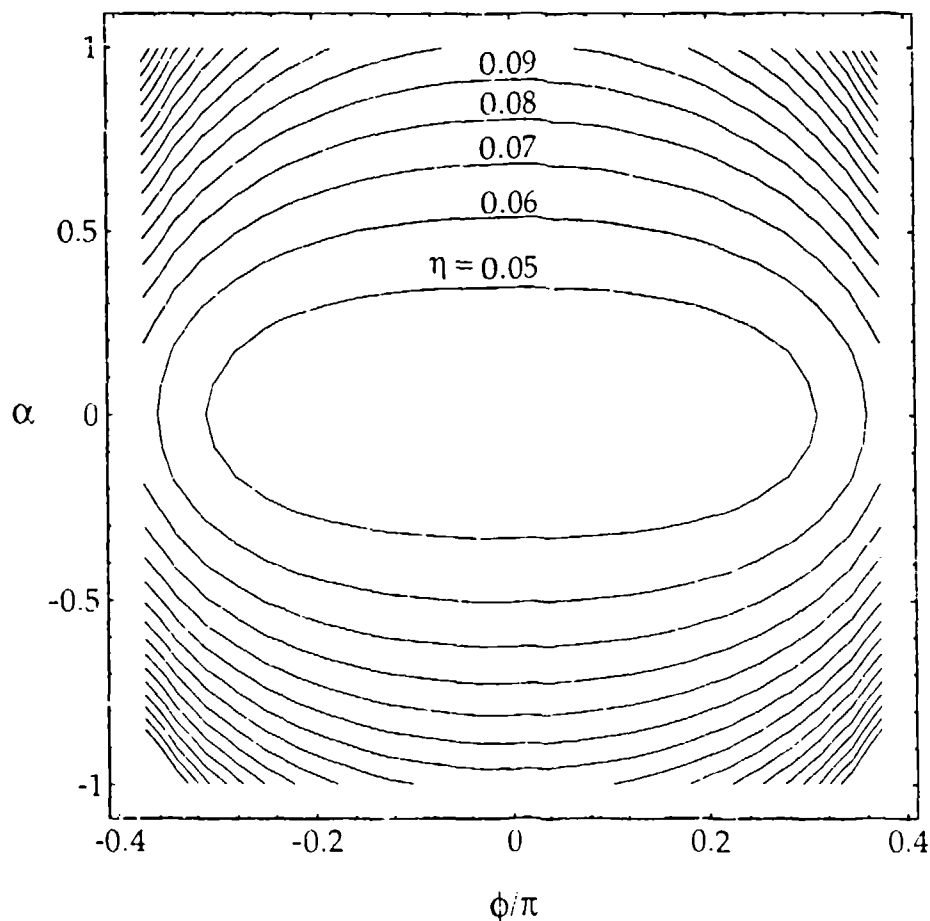


Figure 5. Contours of constant loss,  $\eta$ , in  $(\phi, \alpha)$  space for  $x = 0.1$ . The contours are 0.01 apart.



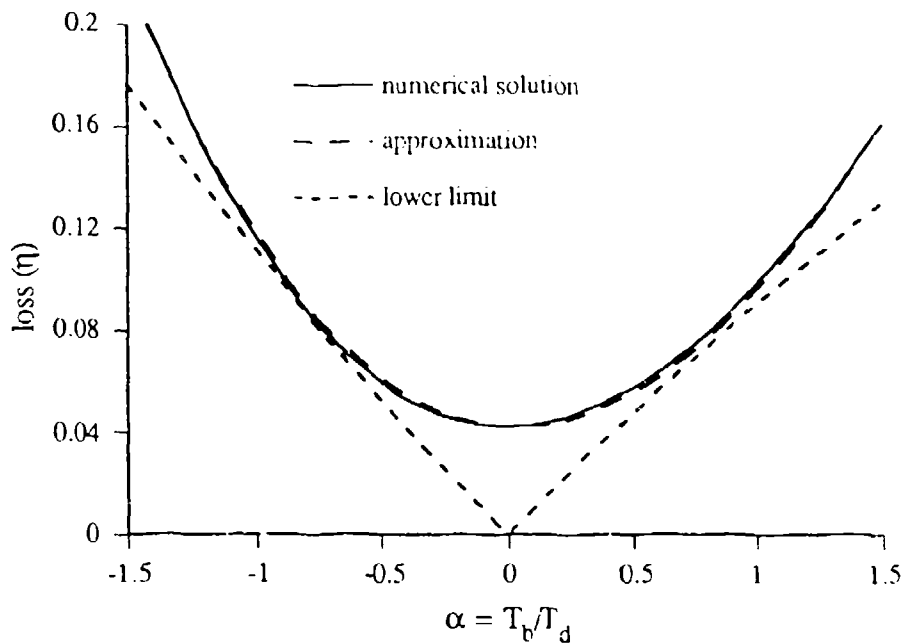


Figure 6. Comparison as a function of  $\alpha$  of the approximate lower limit,  $\eta'$ , and the approximation,  $\eta''$ , with the numerical solution of  $\eta$  for  $x = 0.1$  and  $\phi = 0$ .

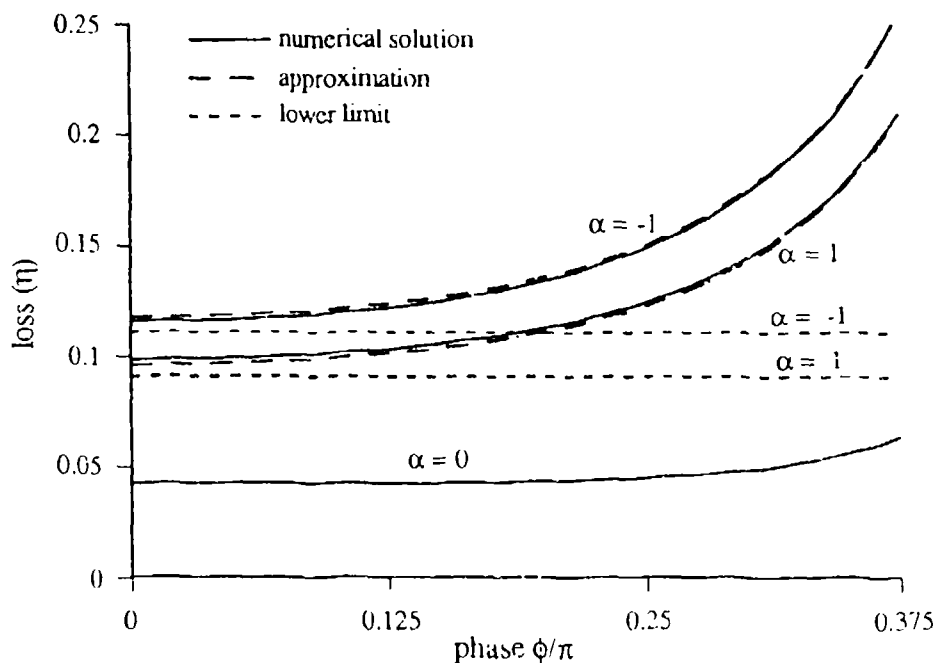


Figure 7. Comparison as a function of phase,  $\phi$ , of the approximate lower limit,  $\eta'$ , and the approximation,  $\eta''$ , with the numerical solution of  $\eta$  for  $x = 0.1$  and  $\alpha = -1, 0$ , and  $1$ . For  $\alpha = 0$ ,  $\eta$  and  $\eta''$  are indistinguishable on this scale and  $\eta' = 0$ .

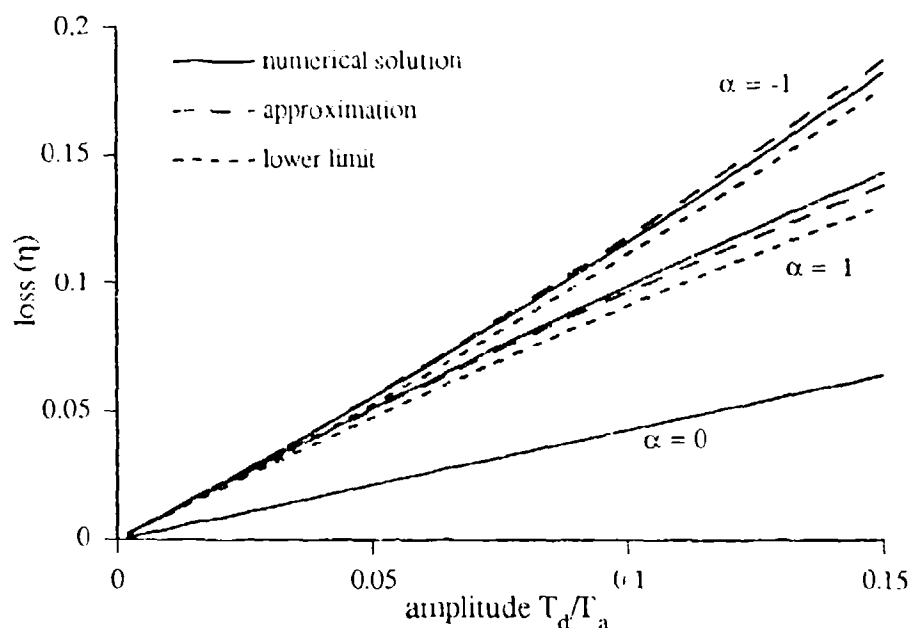


Figure 8. Comparison as a function of amplitude,  $x = T_d/T_a$ , of the approximate lower limit,  $\eta'$ , and the approximation,  $\eta''$ , with the numerical solution of  $\eta$  for  $\phi = 0$  and  $\alpha = -1, 0$ , and  $1$ . For  $\alpha = 0$ ,  $\eta$  and  $\eta''$  are indistinguishable on this scale and  $\eta' = 0$ .

The approximate lower limit,  $\eta'$ , behaves as was expected from the earlier discussion. It is not a good approximation. It does not have a phase dependence nor does it adequately predict the behavior for small  $\alpha$  or for large  $\alpha$ . It is only a good predictor for  $\phi \sim 0$  and  $0.5 \leq |\alpha| \leq 1$ . The approximation  $\eta''$  is a far better predictor. It tracks the  $\phi$  and  $x$  dependence of  $\eta$  over the range of interest. The errors are insignificant.

## DISCUSSION

Table 1 gives values of  $x$  and  $\alpha$  that might be expected for coolers. For hot heat exchangers, the exchanger temperature is near the minimum gas temperature. For cold heat exchangers, the exchanger temperature is near the peak gas temperature. The total loss may be found by combining the individual losses using:  $\eta = 1 - \prod_i (1 - \eta_i)$ . For the case given in Table 1 the overall loss would be 36%. This may be compared to the model of Wang et al.<sup>2</sup> A 3.5% loss in gross cooling power almost completely accounts for the difference between the calculated and experimental results they present. Such good agreement may be just coincidental. The losses calculated in Table 1 assume sinusoidal waveforms; the real waveforms are not. An integration of eqs. (8) and (9) using the real

Table 1: Typical values

location	$x$	$\alpha$	$\phi$	$\eta$
compressor/aftercooler	0.1	-1	0	0.12
cold heat exchanger *	0.1	1	0	0.10
hot heat exchanger *	0.1	-1	0	0.12

\* estimated from ref. 2

waveforms would give a different result. Also, the values listed in Table 1 are only rough estimates. The data presented in the table are consistent with the published data but may not adequately describe the process. Furthermore, some of the enthalpy flow losses may be already included in their model. As will be discussed below, the loss at the hot heat exchanger should not be included in the overall loss. Excluding this would reduce the total loss from 30% to 20%.

In an ideal pulse tube, all of the enthalpy flow must be irreversibly dissipated at the hot heat exchanger.<sup>3</sup> The mechanism discussed in this paper can account for part of this dissipation. (Another source of loss at the hot end is the  $V dP$  work done in the orifice.) Since this total dissipation is inherent to pulse tubes, most models probably already account for it. In any case a loss in enthalpy flow at the hot end of a pulse tube does not reduce the cooling power.

The estimate of  $\eta$  found in Table 1 was based on calculated waveforms at the ends of the pulse tube. These waveforms are probably taken from within the transition zone. Therefore Table 1 probably under estimates the loss. To improve on this, we can take a look at the temperature profile in the pulse tube. This profile has been measured for a pulse tube.<sup>1</sup> Estimated parameters based on these measurements are summarized in Table 2

There is a difficulty in using this data in the enthalpy flow loss model. The model assumes that  $T_a$  is constant in the adiabatic region. Yet, in a real pulse tube  $T_a$  has a steep gradient. This is especially true near the hot end. We would like to use temperature estimates that are neither affected by the transition zone nor by this gradient. One method is to use the minimum (or maximum) value of  $T_a$ . This choice reduces the effect of the transition zone. However, since the minimum (or maximum) occurs away from the end, the estimate is still affected by the gradient. This results in underestimating  $\eta$ . Another choice is to extrapolate  $T_a$  from the central region near the minimum (or maximum) to the ends of the pulse tube. Both of these methods are used in Table 2.

Table 2: Pulse Tube Performance Parameters ‡

position	$T_d$	$T_a$	$T_a + T_b$	$\eta$
cold end *	10 K	185 K	200 K	0.09
†	9.7 K	180 K	200 K	0.15
hot end §	30 K	360 K	300 K	0.31
†	33-35 K	400-425 K	300 K	0.75-1.11

‡ estimated from ref. 1

\* using minimum reported  $T_a$ § using maximum reported  $T_a$ †  $T_a$  estimated by extrapolating to end of pulse tube $T_d$  estimated by assuming  $T_d/T_a$  is same for both cases

The two methods give about the same result ( $\eta \sim 12\%$ ) for the cold end loss. This loss is similar to the one found in Table 1.

The hot end loss is quite different. Using the extrapolated data, the loss is  $\sim 90\%$ . Thus, this accounts for a substantial portion of the required dissipation. It also accounts for the large overshoot of the gas temperature above the hot end heat exchanger, a trait of pulse tubes. Again, this good agreement between calculated and expected loss may just be fortuitous. At the hot end of a pulse tube the mass flow is small. Only a small fraction of the mass flow through at the regenerator makes it through the orifice at the hot end. The assumption that the time to cross the transition zone is  $\ll 2\pi/\omega$  is questionable. A gas element may not even traverse the transition zone at the hot end. It may only move through part of the zone during a cycle. Thus, some of the temperature change may due to changes in  $m$  and  $P$ . Such changes are reversible and do not increase the entropy. Therefore, the loss calculated here is an upper limit for the mechanism discussed in this paper.

## SUMMARY

A method of calculating the losses caused by transitions in enthalpy flow has been developed in the convective limit. In this limit, the time an element of gas takes to cross the transition zone is  $\ll 2\pi/\omega$ . Equivalently, the displacement of a gas element during a cycle is  $\gg$  the length of the transition zone. Since, these conditions are not always met in a real cooler, the loss presented here

is an upper limit of the real loss from this mechanism. Additional losses from other mechanisms may also be present.

The losses caused by transitions in enthalpy flow are significant. Losses ~10% are typical for aftercoolers and cold heat exchangers in regenerative cryocoolers. Even greater losses can be expected at the hot end of the pulse tube where this transition loss accounts for a large part of the heat rejected. While the examples used here were for pulse tubes, other regenerative coolers have similar values of  $x$  and  $\alpha$  at their cold heat exchangers and in their compressors. Thus, they should have similar losses. For real coolers there is likely to be a significant deviation from these calculated results which comes from the real waveforms not being sinusoidal.<sup>1,2</sup>

#### REFERENCES

1. P. J. Storch and R. Radebaugh, "Development and Experimental Test of an Analytic Model of the Orifice Pulse Tube Refrigerator," *Adv. Cryo. Engin.* 33 (1988) 851.
2. C. Wang, P. Wu, and Z. Chen, "Numerical Modeling of an Orifice Pulse Tube Refrigerator," *Cryogenics*, 32 (1992) 785.
3. P. Kittel, "Ideal Orifice Pulse Tube Refrigerator Performance," *Cryogenics*, 32 (1992) 843.

presents the thermal environment and performance of HTSSE-I, thermal and structural design specifics of the BAe cryocooler interface, and information on the cryogenic subsystem diagnostic instrumentation included on HTSSE-I.

### HTSSE-I CONFIGURATION & ENVIRONMENT

The 15 HTS experiments and 4 conventional RF metal reference devices on HTSSE-I are packaged in the 9 inch diameter by 9 inch tall cryogenic cold bus. The cold bus is structurally secured in an aluminum frame by six glass-fiber epoxy composite straps. The HTS experiments and metal reference devices are radially located on the circumference of the cold bus for easy access and even unattenuated exposure to the high energy particles of the orbit environment. Figure 1, an early CAD drawing of the HTSSE-I experiment deck, illustrates the location of the cold bus, it's structure and the BAe 80K cryocooler.

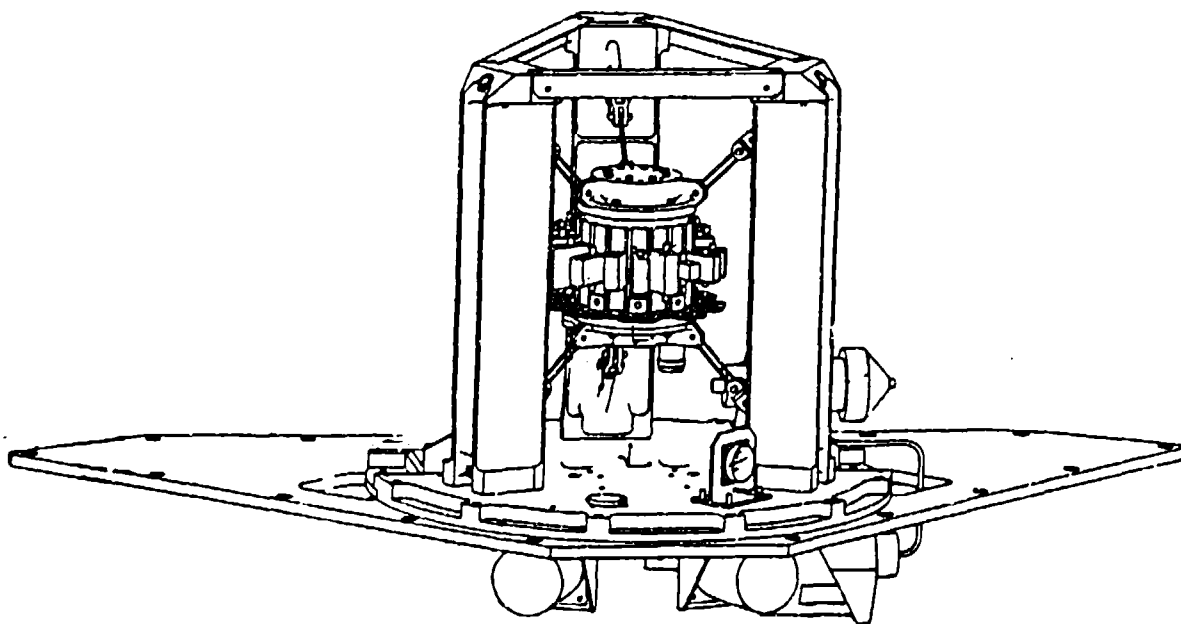


Figure 1. HTSSE-I Experiment Deck Without Thermal Blankets

The cold bus tension support structure is attached to a trapezoidal shaped honey comb deck that sits flush with the exterior skin of the spacecraft. The BAe cryocooler displacer is positioned just above deck with the cold finger protruding just underneath the cold bus. The flexible copper strap that conductively links the cold finger to the cold bus is not shown in this CAD drawing but is described in detail in the following section. The Helium

gas transfer tube of the BAe displacer can be seen leading to the compressor which is located under the deck. There are two 100 mil thick cylindrical aluminum radiation shields for the displacer and compressor which are not shown in this figure for clarity. Also not shown for clarity is a 40 layer MLI blanket on the cold bus to minimize thermal radiation parasitics and the silver Teflon surfaced radiators on the three sides and top of the tension strap frame to minimize the temperature of the outer MLI layer. The Lockheed Research Laboratory designed and fabricated a high performance 40 layer MLI radiation blanket. Heat is rejected from the cryocooler into the honeycomb deck and then radiated to space. Figure 2 shows the HTSSE-I experiment and electronics decks on the aft end of a spacecraft.

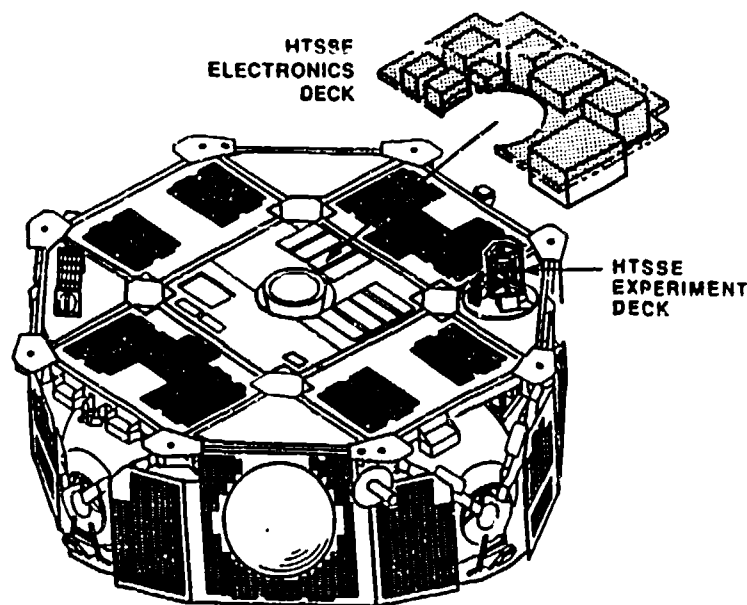


Figure 2. HTSSE-I Position on a Spacecraft Aft End

The spacecraft spins about its cylindrical center line. The sun angle varies between a  $45^\circ$  angle from the spin axis on the aft end to a  $45^\circ$  angle with the spin axis on the forward side of the spacecraft over a 120 day period. The hot condition occurs when the sun is  $45^\circ$  on the aft end at the end of life, the cold condition occurs at the beginning of life with the sun on the forward side. There are three principle thermal loads on the cryogenic cold bus; thermal radiation parasitics, conductive parasitics through the six tension support straps, and conductive parasitics through the coax I/O cables that interface with the HTS devices in the cryogenic cold package. There are two 0.021 diameter coax RF cables to provide input and output for each device making a total of 38 cryogenic I/O coax cables. Table 1 presents the significant thermal parameters of the hot and cold conditions of HTSSE-I.

<u>Parameter</u>	<u>Cold Case Condition</u>	<u>Hot Case Condition</u>
Cryogenic Parasitic Load		
MLI Radiation	131mW	205mW
Structure Conduction	59mW	72mW
<u>I/O Conduction</u>	<u>60mW</u>	<u>79mW</u>
Total	250mW	356mW
Outer MLI Avg. Temp.	187K	227K
BAe Cryocooler Temp.	263K	293K
Cold Bus Temp.	77.0K	77.0K
Cryocooler Cold Tip Temp.	76.2K	75.9K
Displacer Stroke, p-p	2.9mm	2.9mm
Compressor Stroke, p-p	5.10mm	6.15mm

Table 1. Predicted On-Orbit HTSSE-I Hot and Cold Conditions

#### BAe CRYOCOOLER CRYOGENIC PAYLOAD INTERFACE

The BAE 80K cryocooler has been designed with the intent of meeting the long life and high reliability requirements of space applications. To accomplish this goal the Oxford University design has eliminated the wear mechanism of contacting dynamic seals in the compressor and displacer by using close gap clearance seals. Great design and assembly effort is exercised by the cryocooler manufacturer to maintain alignment of the regenerator piston within the cold finger bore of the displacer to avoid contacting. The cold finger inside diameter is the bore of the clearance seal. The cold finger is also designed to minimize the conductive parasitic heat flow from the warm displacer body to the cryogenic end in order to maximize cooling capacity. For this reason the cold finger has a thin wall and is vulnerable to deflection from transverse forces. A flexible conductive strap is employed at the cold finger/payload interface to minimize transverse forces. Flexibility is needed to allow for the mismatch that occurs from tolerance build up and thermal contraction, and to minimize force transfer during the dynamic launch environment. Conflicting requirements are inherent in thermal link design, flexibility is not compatible with the high thermal conductivity required to maximize the cryocooler cold tip temperature and thus cooling capacity. From the HTSSE-I perspective the thermal link interface is the highest risk aspect of integrating a clearance seal cryocooler in a space application. This section presents the configuration and performance of the HTSSE-I thermal link interface. HTSSE-I thermal link was not fully optimized due to the short development schedule but



does seem to offer a good compromise between flexibility and conductivity. HTSSE-I utilized a bundled copper wire approach for a thermal link design as shown in Figure 3.



Figure 3. Cryocooler / Cryogenic Payload Flexible Thermal Link

Flexibility and heat conduction are provided in this thermal link design by four fine wire bundles as shown. The copper end blocks interface with a the cryocooler cold finger and a beryllium stem that penetrates the cryogenic bus MLI as shown in Figure 4. To assemble



Fig. 4. Cryocooler Cold Finger & Beryllium Stem Interface

the thermal link, the copper block with the large bore in the background of Figure 3 is fit over the the outside diameter of the beryllium stem shown on the right in Figure 4 and pinned in place. With the thermal link assembly in place on the beryllium stem, the cryocooler/bracket assembly is slid forward along the cold finger axis until the cold finger end is adjacent to the bore of the copper block face shown in the foreground of Figure 3. The thermal link bore to cold finger alignment was checked and some bending of the thermal link was required to eliminate mismatch due to tolerance buildup. Once alignment was established to minimize residual transverse forces, the cryocooler was pushed into the bore of the copper block it's full thickness. Epoxy is used to bond the cold finger to the thermal link. In operation, cool down causes the copper thermal link to shrink onto the beryllium stem causing high surface pressures to provide a low thermal resistance interface. The Cu/Be shrink fit design and hardware was provided by the Lockheed Research Laboratory.

Each of the four wire bundles in the thermal link consists of 900 wires of 0.005 inch diameter oxygen free copper. The unassembled length of each bundle is 1.40 inches. The ends of each bundle are silver epoxied and clamped to squeeze out excess epoxy. The cured bundle ends are silver epoxy bonded in 0.25 deep by 0.190 inch diameter holes in the solid copper end blocks. The termination holes are oriented at a 30 degree angle from the long axis to provide a natural bend to reduce the axial stiffness. Figure 5 presents the average spring rate of this thermal link design as function of maximum deflection in the axial and transverse directions. The thermal conductance of this thermal link is 380mW per °K.

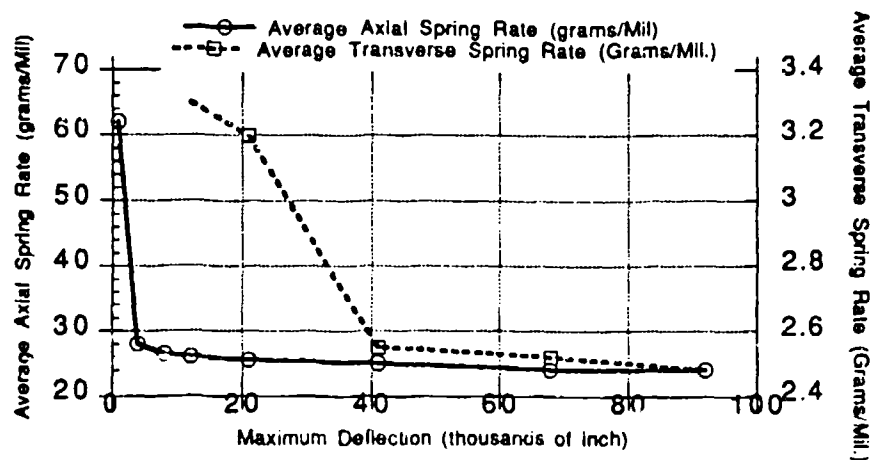


Figure 5. HTSSE -I Thermal Link  
Spring Rate Vs. Deflection

## HTSSE-I FLIGHT CRYOCOL SYSTEM DIAGNOSTIC INSTRUMENTATION

An important element of the HTSSE program is to develop and demonstrate the cryogenic subsystems required to utilize HTS devices in space applications. There have been few mechanical cryocoolers flown for durations longer than 6 months. Cryocoolers having the potential for 5 year life with high reliability have only just begun operating in orbit within the past year. The two Stirling cycle clearance seal cryocoolers currently operating are of different designs from Oxford University and Rutherford Appleton Laboratory. The launch of HTSSE-I in midyear 1993 is likely to be the first production clearance cryocooler on orbit. For these reasons HTSSE-I has been extensively instrumented to monitor cryocooler and cryogenic payload health while on orbit. Table 2. presents a list of the cryogenic subsystem instrumentation included on HTSSE-I. Fast simultaneous

<u>Item Monitored</u>	<u>Sensor Comments</u>
Displacer Motor Current*	HTSSE-I Electronics
Displacer Motor Voltage*	"
Compressor Motor Current*	"
Compressor Motor Voltage*	"
Displacer Axial Accelerometer*	Endevco #7290-10
Displacer Transverse Accelerometer*	"
Compressor Axial Accelerometer*	"
Compressor Transverse Accelerometer*	"
* 2 Channel Fast Sample Wave Form Plot Capability, 1600 sample/sec. rate for 62 msec window on each channel	
Temperature Sensors, Cryogenic $\pm 0.1K$	Lakeshore Platinum Resistance Thermometers
Outer MLI Blanket Temp.	
Cryogenic Bus Temp.	
Thermal Link Cold Finger End Temp.	
Thermal Link Cryogenic Bus End Temp.	
Temperature Sensors, Ambient $\pm 2.0K$	14 Total
Thermal Heat Flow Meter	Calibrated Thermal Resistance of Thermal Link

Table 2. HTSSE-I Cryogenic  
Subsystem Instrumentation

sampling of any two channels of the first eight items in Table 2 is possible on HTSSE-I. Accelerometer and cryocooler voltage and current wave form data will be useful for

monitoring cryocooler health. Temperature sensors will provide data to accurately predict the cryogenic cooling load, and the heat flow meter will provide cryocooler cooling capacity. A fast sample data baseline will be established after initial cool down in orbit. The hot and cold conditions are 120 days apart in orbit, thus it will be difficult to obtain subsequent cryocooler health data under similar environmental conditions as the initial baseline data. Large changes in cryocooler performance should be detectable. The data from the sensors listed above will be down linked to an NRL ground station and will be available for operations monitoring from a central NRL computer via modem.

### SUMMARY

The HTSSE program was developed at NRL to promote the use of HTS electronics in space applications. A critical aspect of this program is the development and demonstration of the cryogenic technologies and subsystems to support electronic devices in a 77K environment in space. HTSSE-I utilizes a BAe 80K cryocooler for cryocooling. Cryocooler vibration and motor voltage and current wave forms can be monitored from the ground after a 1993 launch. Great attention is required in cryocooler integration to avoid residual transverse loads on the cold finger that can cause clearance seal contacting and premature cryocooler failure.

### ACKNOWLEDGEMENTS

Sponsorship and funding for HTSSE are provided by the U.S. Navy's Space and Naval Warfare Systems Command (SPAWAR). Several other U.S. government agencies provided funding for development of some HTS devices used in HTSSE such as DARPA, SDIO, NASA, and the Office of Naval Research (ONR). Several industry groups provided HTS devices developed with their own IR&D funds. Great appreciation is expressed for the dedication and effort of the many managers, engineers, scientists, technicians and administrative personnel who contributed to HTSSE-I. Special thanks are given to the many highly motivated employees and contractors of the Naval Center for Space Technology for their can-do commitment that made this project possible in a short time frame. Thanks to Nick Davinic for reviewing this paper.

**10 K SORPTION CRYOCOOLER  
FLIGHT EXPERIMENT (BETSCE)**

Steven Bard, Parker Cowgill, Jose Rodriguez, Larry Wade, and J. J. Wu  
Jet Propulsion Laboratory (JPL)  
California Institute of Technology  
4800 Oak Grove Drive  
Pasadena, CA 91109

Capt. Michael Gehrlein  
Air Force SMC/CNST  
Los Angeles AFB, CA 90009-2960

Werner Von Der Ohe  
The Aerospace Corporation  
El Segundo, CA 90245-4691

**ABSTRACT**

This paper presents an overview of the objectives and design of the Brilliant Eyes Ten-Kelvin Sorption Cryocooler Experiment (BETSCE) planned for launch on the Space Shuttle in 1994. The BETSCE objectives are to: (1) demonstrate 10 K sorption cooler technology in a microgravity space environment, (2) advance the enabling technologies and integration techniques by developing an automated, space flightworthy instrument, and (3) characterize spaceflight performance and develop the needed flight database to aid the future cooler development effort. Key technologies and elements to be characterized include hydride sorbent beds, phase change materials, heat sinks, heat exchangers and other refrigeration loop components, the cold head assembly containing a wicked solid/ liquid cryogen reservoir, cycle process controls, and cycle repeatability. This spaceflight experiment is designed to mitigate the risks of utilizing sorption cooler technology for spacecraft sensor cooling applications that require periodic quick-cooldown, negligible vibration, low power consumption, and long-life (5 to 10 years).

**INTRODUCTION**

Sorption cooler technology provides an ideal method to produce intermittent operation of cryogenic infrared sensors for future astronomy, earth-observation and surveillance satellite systems. Sorption cooling provides low-vibration, long-life, and repeated quick cooldown capability, and the intermittent operation results in low average power consumption. A potential application for this technology is the Brilliant Eye (BE) surveillance satellite system, since one of the BE system concepts includes a very long-wavelength infrared (VLWIR) detector focal plane that needs to be periodically operated at near 10 K.

The periodic 10 K sorption cooler concept for BE was originally conceived by Johnson and Jones [1,2]. The concept has been investigated analytically, and the proof-of-principle of a 10 K stage has been experimentally demonstrated in laboratory experiments [3]. Alternately heating and cooling beds of metal hydride powders circulates hydrogen in a closed cycle and periodically cools the detector cold head assembly to 10 K on command. Figure 1 describes the basic cycle concept.

A comprehensive technology development program is underway to advance the maturity level and mitigate the risks of utilizing this novel technology for spaceflight systems such as BE [4]. The various elements of this development program [5] include component-level characterization and reliability physics investigations, engineering model and protoflight development by industry, and a near-term spaceflight technology demonstration experiment (BETSCE). BETSCE is an element of the Shuttle Pallet Satellite (SPAS III) mission that is mounted on the Shuttle side wall. Specific BETSCE objectives are to:

- Demonstrate 10 K sorption cooler technology in a microgravity space environment,
- Advance the enabling technologies and develop integration techniques by developing an automated, space flightworthy instrument, and
- Characterize spaceflight performance and develop the needed flight database to aid the future cooler development effort.

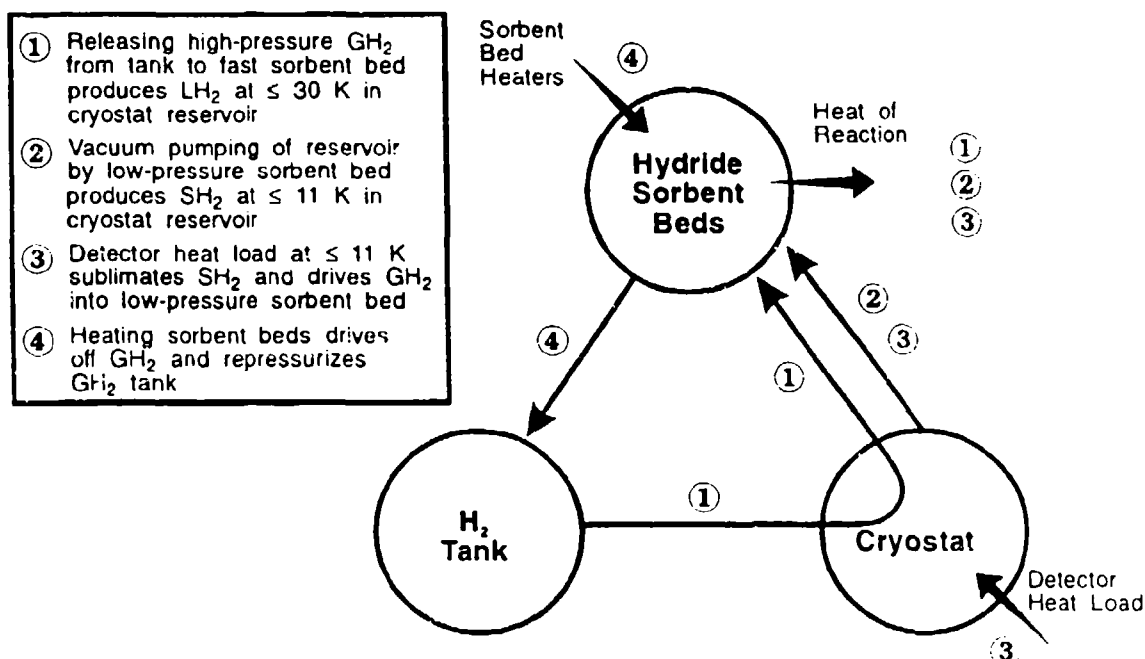


Figure 1. Periodic 10 K sorption cryocooler basic cycle.

Key technologies and elements to be characterized include hydride sorbent beds, phase change materials, heat sinks, heat exchangers and other refrigeration loop components, the cold head assembly containing a wicked solid/ liquid cryogen reservoir, cycle process controls, and cycle repeatability.

## FUNCTIONAL REQUIREMENTS

To meet the objective of demonstrating the 10 K sorption cooler process in space, the BETSCE flight instrument requirements are reasonably representative of typical 10 K cooler goals for the BE VLWIR system. Some of the BE goals may be relaxed for the BETSCE flight instrument to accommodate constraints imposed by the SPAS III Shuttle flight, such as unfavorable thermal environment, safety, limited development schedule, and heat rejection limitations. Although these constraints may cause the BETSCE flight instrument weight, power, and volume to be greater than for a GPALS BE cooler, BETSCE will still effectively demonstrate the critical technologies. Also, to demonstrate the 10 K sorption cooler process in space, the BETSCE flight instrument does not need to contain ancillary equipment such as an IR detector and optics; only the hydrogen refrigeration cycle system and supporting systems need to be flown.

The basic functional requirements selected for the BETSCE instrument are a scaled version of representative BE 10 K cooling goals:

- A. Cooldown in  $\leq 2$  minutes from 60-70 K to:
  - (1) A cold stage detector interface temperature of  $\leq 11$  K.
  - (2) An intermediate stage temperature of  $\leq 30$  K.
- B. Sustain an I<sup>2</sup>R simulated detector heat load of  $\geq 100$  mW at  $\leq 11$  K for 10 minutes.
- C. Recycle the system to operate again in  $\leq 24$  hours.
- D. Demonstrate  $\geq 3$  full repeatable cycles.
- E. Record data required to characterize spaceflight/ microgravity performance of the BETSCE instrument.

Table I summarizes the key technologies and phenomena that BETSCE is designed to characterize, and the associated instrumentation sensors.

## EXPERIMENT DESIGN

Physically, the BETSCE flight equipment comprises a Sorbent Bed Assembly, Tank and Valve Assembly, Cryostat Assembly, Control Electronics Assembly, Structure, and Cabling/Installation hardware. Figure 2 depicts the BETSCE instrument mounted on a Get Away Special (GAS) adapter beam on the Shuttle payload bay sidewall. BETSCE draws power from the Shuttle 28 VDC power bus, downlinks data and uplinks commands, stores data on BETSCE's dedicated mass storage device, receives the Shuttle Mission Elapsed Time(MET) feed at the data interface

Table I. Key BETSCE Measurements

Phenomenon to be Measured	Sensors
Achievement of system functional requirements	<ul style="list-style-type: none"> <li>- Temperatures at simulated detector interface</li> <li>- Voltage and current to cold head heater</li> <li>- SBA and tank pressures and temperatures</li> <li>- Time</li> </ul>
Sorbent bed heat transfer	<ul style="list-style-type: none"> <li>- SBA temperatures &amp; pressures</li> <li>- Time</li> </ul>
Sorbent bed fast sorption capability/ desorption/ recycling	<ul style="list-style-type: none"> <li>- SBA/ CA temperatures, &amp; SBA/ TVA pressures</li> <li>- Time</li> </ul>
Sorbent migration/ compaction	<ul style="list-style-type: none"> <li>- SBA temperatures &amp; pressures</li> <li>- Pre and post-flight inspection &amp; X-ray, valve leak-check</li> <li>- Time</li> </ul>
Heat switch heat transfer	<ul style="list-style-type: none"> <li>- SBA temps., pressures, heater volts &amp; amps</li> <li>- Time</li> </ul>
Phase change material freeze/ thaw/ heat transfer	<ul style="list-style-type: none"> <li>- SBA temperatures</li> <li>- Time</li> </ul>
Cryostat reservoir liquid/ solid cryogen retention and phase separation	<ul style="list-style-type: none"> <li>- CA temperatures &amp; pressures</li> <li>- Time</li> </ul>
J-T loop thermodynamics & heat transfer	<ul style="list-style-type: none"> <li>- CA and TVA temperatures &amp; pressures</li> <li>- Time</li> </ul>
Thermal storage device and mechanical cryocooler interface performance	<ul style="list-style-type: none"> <li>- CA and TVA temperatures &amp; pressures</li> </ul>
Cycle process controls and repeatability	<ul style="list-style-type: none"> <li>- SBA, TVA, CA, CEA temperatures, pressures, volts &amp; amps for heaters</li> </ul>
Thermal radiator heat rejection	<ul style="list-style-type: none"> <li>- CA, SBA, CEA temperatures</li> </ul>

Notes: SBA = Sorbent Bed Assembly; TVA = Tank & Valve Assembly; CA = Cryostat Assembly; CEA = Control Electronics Assembly

connector, accepts crew inputs via the Standard Payload Switch Panel, and rejects heat to space with radiative coolers. connector, accepts crew inputs via the Standard Payload Switch Panel, and rejects heat to space with radiative coolers.



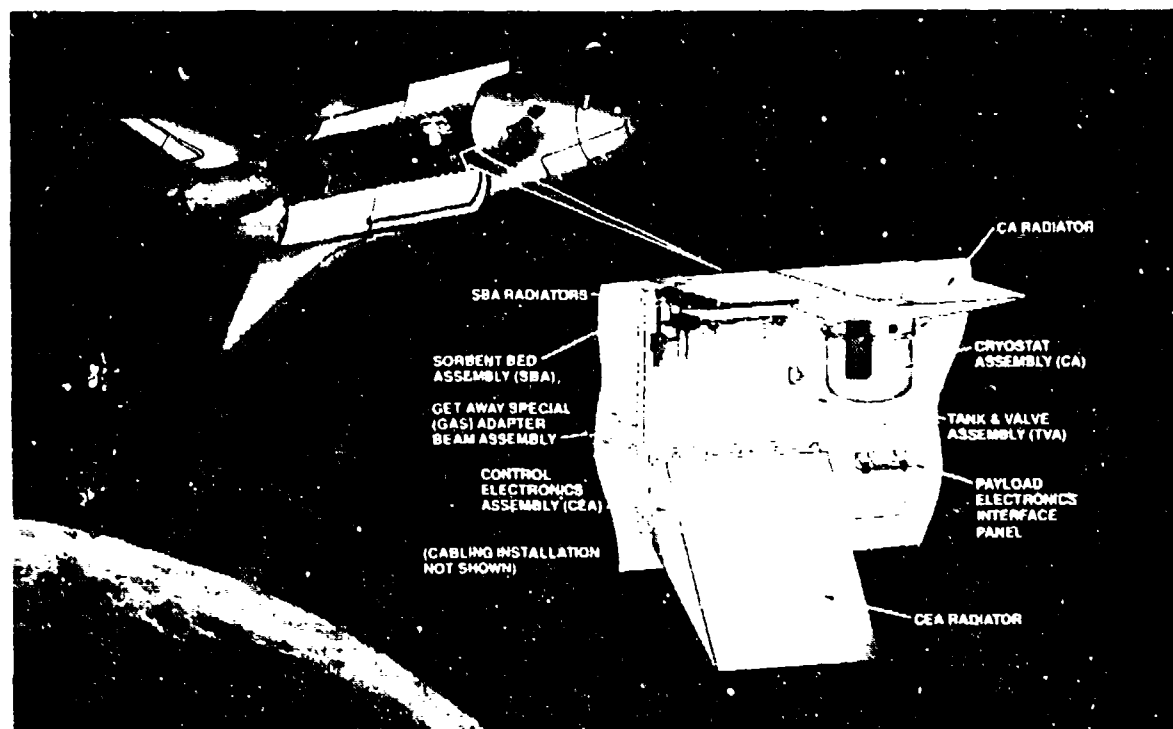
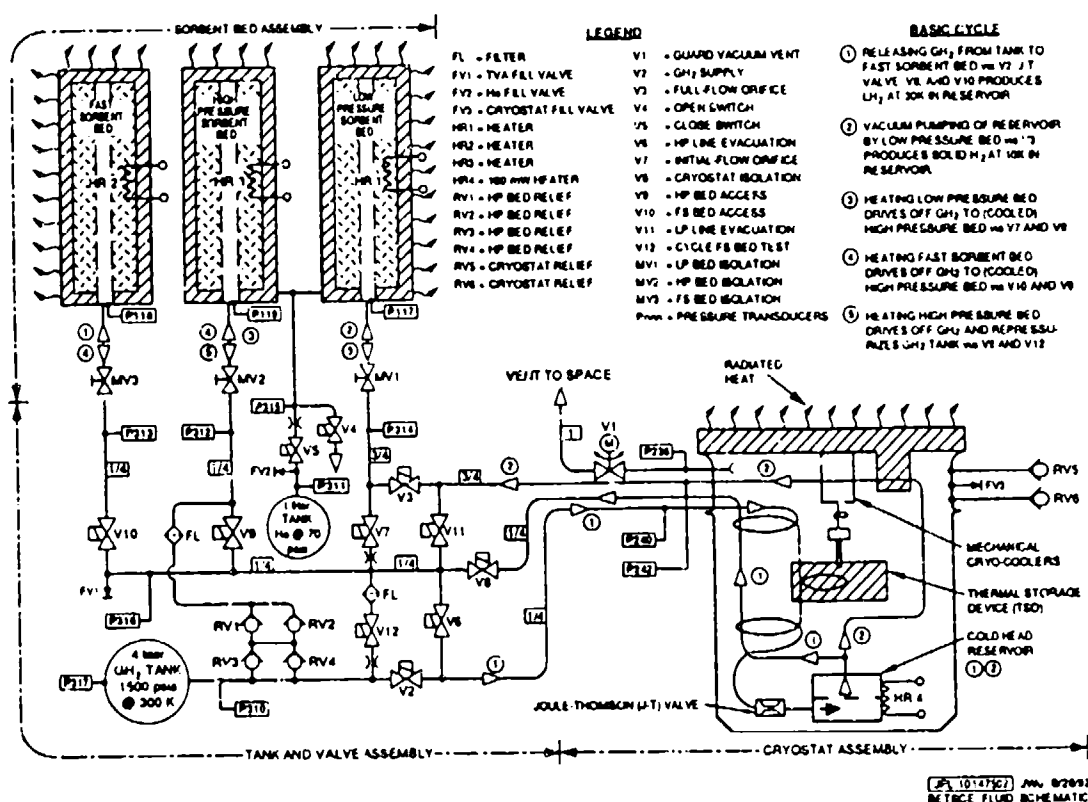


Figure 2. BETSCE instrument mounted on a Get-Away Special (GAS) adapter beam.

The BETSCE cycle exploits the properties of certain metallic hydride powders that desorb hydrogen to high pressures when heated and adsorb hydrogen to high vacuums when cooled. By alternately heating and cooling beds of these hydride powders, BETSCE circulates hydrogen gas through a closed system. The process produces 0.31 g of solid hydrogen in about 2 minutes, enough to cool a simulated infrared sensor for 10 minutes at  $\leq 11$  K. See Figure 3.

Figure 3 shows the BETSCE fluid schematic. Figure 4 shows the basic operating sequence. At launch, the total fill of hydrogen in the BETSCE system is less than 34 g, about 57% of which is in hydride form. When the experiment is powered-up, the high pressure sorbent bed is heated to desorb, pressurize, and transfer its  $H_2$  to the  $H_2$  storage tank. After hydrogen desorption is completed, the high pressure bed is cooled. The low pressure and fast absorption sorbent beds are next heated in turn, transferring their  $H_2$  gas to the high pressure sorbent bed. The high pressure sorbent bed is then heated again to pressurize the  $H_2$  storage tank to its operating pressure.

Also during BETSCE startup, mechanical cryocoolers pre-chill the cryostat thermal storage device to 60-70 K. With startup conditioning sequences completed, BETSCE is ready to enter its operating cycle. Cooldown is initiated by releasing pressurized  $H_2$  gas from the storage tank to the fast absorption sorbent bed via the cryostat, whose pre-chilled thermal storage device, heat exchangers, and Joule-Thomson valve produce liquid  $H_2$  at 26-28 K in the cold head reservoir. Next, solid  $H_2$  at  $\leq 11$  K is produced by vacuum pumping the cold head reservoir.



about  $2.6 \times 10^{-4}$  MPa (2 torr) with the low pressure sorbent bed. Under simulated infrared sensor heat load and continued vacuum pumping the solid H<sub>2</sub> sublimates and is adsorbed by the low pressure sorbent bed. Then to recharge the system, hydrogen is returned to the tank by sequentially heating the three sorbent beds as before. The cycle repeats about every 12 to 14 hours. In each cycle, pre-planned variations of event timing are introduced to fully map operating characteristics and microgravity effects.

Table II summarizes some key experiment design and performance parameters.

### SUBSYSTEM HARDWARE DESIGN

The BETSCE Sorbent Bed Assembly comprises radiator panels, a fast absorption sorbent bed, a high pressure sorbent bed, and a low pressure sorbent bed. Design implementation of the three beds is tailored to meet performance requirements. See Figure 5. The high pressure bed pumps hydrogen to moderate pressures ( $\leq 10.3$  MPa, 1495 psia, when the tank temperature is 300 K) when heated. The fast absorption sorbent bed adsorbs large quantities of hydrogen rapidly [6]. The fast absorption and high pressure bed sorbent material is lanthanum-nickel-tin (LaNi<sub>4.8</sub>Sn<sub>0.2</sub>) hydride. The low pressure bed sorbent bed, designed to absorb hydrogen at moderate vacuum levels, contains zirconium-nickel (ZrNi) hydride.

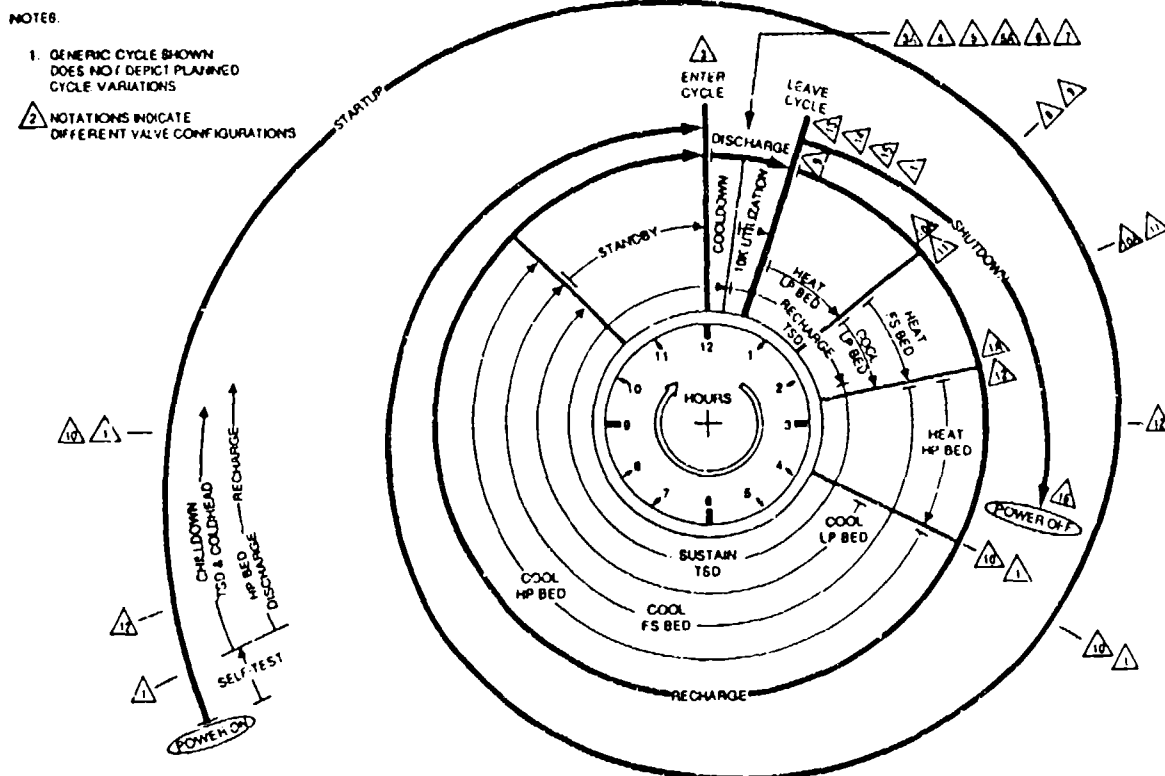


Figure 4. BETSCE operating sequence.

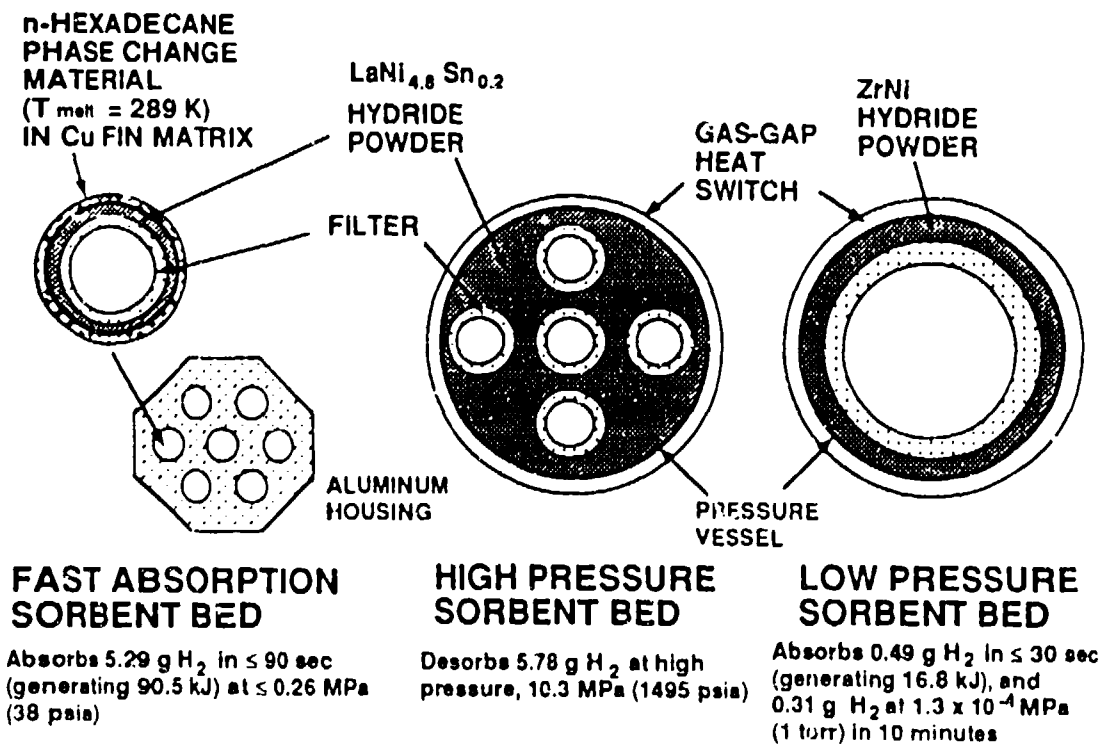


Figure 5. BETSCE Sorbent Bed Assembly.

Table II. Nominal Design and Performance Parameters

<b>Cooldown from 60 K to 27 K:</b>		
Time		$\leq 90$ seconds
Initial storage tank pressure (1358 psia at 0°C)		9.36 MPa
Final storage tank pressure (1030 psia at 0°C)		7.10 MPa
H <sub>2</sub> gas depleted from storage tank		6.09 g
LH <sub>2</sub> produced in cold head reservoir		0.50 g
H <sub>2</sub> gas absorbed by Fast Absorption Sorbent Bed		5.29 g
Energy dissipated by Fast Absorption Sorbent Bed		90.5 KJ
<b>Cooldown from 27 K to <math>\leq 11</math> K:</b>		
Time		$\leq 30$ seconds
SH <sub>2</sub> produced in cold head reservoir		0.31 g
H <sub>2</sub> gas absorbed by Low-Pressure Sorbent Bed		0.49 g
Energy dissipated by Low-Pressure Sorbent Bed		16.8 KJ
<b>Steady-state operation at <math>\leq 11</math> K:</b>		
Time		10 minutes
Cold head heat Load:		
I <sup>2</sup> R simulated detector heat load (100 mW)		250 mW
Conductive & radiative parasitics ( $\leq 150$ mW)		
Sublimated H <sub>2</sub> gas absorbed by Low-Pressure Sorbent Bed		0.31 g
Energy dissipated in Low-Pressure Sorbent Bed		10.6 KJ
<b>Recycle Parameters:</b>		
Heater power to each sorbent bed		180 W
Total heating time for 3 beds		3.9 hours
Total energy to desorb beds/ recharge storage tank		2.6 MJ
Total time-averaged desorption power over 24 hours		29.3 W

Besides hydride sorbent material, each sorbent bed contains heater elements, a heat sink/radiator, and either a gas-gap heat switch or a thermal capacitor. The hydride powders are enclosed in cylindrical pressure containers. Multiple cartridge-type heaters are brazed to the outside of the pressure containers. Surrounding the high pressure and low pressure beds' hydride containers are 3.8 mm (0.150-inch) wide vacuum spaces that function as gas-gap heat switches. These gaps may be filled with helium gas at a pressure of about  $1.3 \times 10^{-3}$  MPa (10 torr) on command, to provide conductive paths between the hydrides and heat sinks/ radiators. When the beds are subsequently heated to recharge the system, the gaps are evacuated to the vacuum of space to provide thermal isolation. The low pressure sorbent bed is heated to about 600 K to desorb the hydrogen at about 0.21 MPa ( $3^{(1)}$  psia) to transfer it to the high pressure bed. Then the high pressure bed is heated to 540 K to desorb the hydrogen at about 10.3 MPa (1495 psia when the tank temperature is 300 K) to recharge the storage tank.

The fast absorption sorbent bed consists of seven separate hydride containers located within an aluminum housing. Surrounding each hydride container is an aluminum chamber filled with n-hexadecane, a paraffin phase change material (PCM) that acts as a thermal capacitor, in a copper heat transfer enhancement matrix containing 15.7 fins per centimeter. As 5.29 g of hydrogen are absorbed by the fast absorption sorbent bed in about 80 seconds, the 90.5 KJ given off by the exothermic hydride reaction melts the PCM. Thus, the hydride temperature remains fairly isothermal at about 20 K above the PCM phase transition temperature of 289 K, allowing the hydrogen absorption pressure to remain at about 0.26 MPa (38 psia) in the fast absorption sorbent bed, which corresponds to about 0.39 MPa (57 psia) in the cryostat assembly cold head reservoir. To recharge the system, the fast absorption sorbent bed is then heated to about 360 K to desorb the hydrogen at about 0.41 MPa (60 psia), transferring the hydrogen to the high pressure sorbent bed. Then, as the radiator cools the n-hexadecane PCM to below 289 K it again solidifies.

The BETSCE Cryostat Assembly comprises the thermal storage device (TSD), mechanical cryocoolers, cryogen reservoir, heat exchangers, Joule-Thomson valve, outer shell, and associated piping. See Figures 2 and 3. The TSD is a 2.0-kg aluminum block cold sink. It is supported inside an evacuated cryostat outer shell that is vented to space by motorized valve V1 whenever BETSCE is operating. Heat is removed from the TSD by mechanical cryocoolers. When chilled to 60-65 K, the TSD is available to support the hydrogen cycle. In the initial stage of the cooldown cycle, hydrogen gas circulated past the TSD raises the TSD temperature by about 10 K.

The mechanical cryocoolers are split-Stirling rotary drive advanced tactical coolers manufactured by Hughes Electron Dynamics Division (Model No. 7044H). These coolers are identical to those used in the Cryogenic Heat Pipe Experiment (CRYOHP) planned for launch in 1992 aboard STS-53 [7], and the NASA Cryo System Flight Experiment planned for launch in 1994 [8]. BETSCE contains three of these mechanical cryocoolers; two are operated simultaneously, and the third provides redundancy.

The BETSCE Tank and Valve Assembly integrates 2 tanks, 11 valves, and associated pressurized piping into a single unit. This allows many of BETSCE's joints, seals, and pressure vessels to be intensively addressed and their performance verified before integration with the other flight equipment. The 11 normally-closed solenoid valves are activated by BETSCE Control Electronic Assembly drive circuits to produce the desired flows. See Figure 3.

The BETSCE Control Electronics Assembly directs the instrument through a series of pre-programmed sequences. Data on the status and performance of instrument components are acquired and stored in nonvolatile solid-state flash memory. Performance data are also downlinked to ground personnel so that experiment progress can be assessed. BETSCE can accept uplinked commands to modify sequences or configurations based on observed performance. All commands from the ground involve software, parameter adjustments, or valve configurations that have no safety implications. See Figure 2.

To measure and characterize the phenomena summarized in Table I, the BETSCE instrument contains an array of 96 sensors monitored by the Control Electronics Assembly. Temperatures are measured by an assortment of silicon diodes, platinum resistance thermometers (PRT's) and thermocouples. Other telemetry includes pressure sensors, and current and voltage monitors for determining electrical power consumed by heaters and mechanical cryocoolers.

The Control Electronics Assembly also provides power conditioning as needed of the  $28 \pm 4$  VDC supplied by the Shuttle. The strawman power and energy consumption profiles are shown in Figure 6.

### MISSION SCENARIO

Figure 7 summarizes the strawman mission timeline. On orbit, BETSCE is powered-on at the start of payload activities, and is capable of running continuously and operating autonomously for the full mission duration. When powered-on, BETSCE immediately does a self-check and status appraisal. In the event of power interruption, BETSCE will resume operation at the sequence where it left off.

Initially, the sorbent beds are sequentially heated to desorb their hydrogen and charge the storage tank. Simultaneously, BETSCE will vent the cryostat guard vacuum to space via valve V1 and turn on the 60 K mechanical cooler assembly, to begin pre-cooling the cryostat thermal storage device. These off-line conditioning sequences take about 18-24 hours. Then, BETSCE will execute an initial full cycle for evaluation, and a full check cycle incorporating any modifications that are necessary. Next, BETSCE will execute four conditioning cycles to establish repeatable cycle parameter data patterns. Data patterns are expected to approach the nominal 12-hour cycle in 3 or 4 cycles. See Figure 4. Additional cycles will be necessary if the data patterns have not stabilized by the fourth cycle.

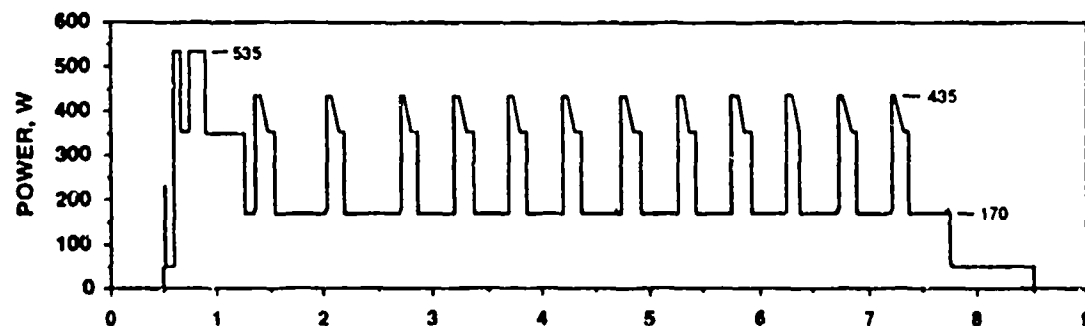
Following establishment of cycle repeatability, several utilization cycles follow, where various effects of parametric tuning are investigated. In one of these studies, it is planned to have a pressure release through calibrated orifices that bypass the cryostat to independently define sorbent bed performance. The one cycle per 12-hour period rate will be maintained. If mission duration and resources permit, additional cycles should be inserted to address any issues of opportunity that arise in the course of preplanned sequences.

Following the final sorption cycle, the mechanical coolers are shut down and the warmup of the thermal storage device and cold head is observed. While warmup is proceeding, hydrogen is returned to the sorbent beds until they are fully hydrided. Then BETSCE is configured for landing and powered-off.

### DATA ANALYSIS PLAN

The full data set will be downlinked in near-real time via the standard Shuttle communications data link, and archived. Experiment performance will be evaluated on the ground and parameter changes will be uplinked if necessary. After BETSCE is deintegrated from the Shuttle post-

## POWER PROFILE



## ENERGY CONSUMPTION

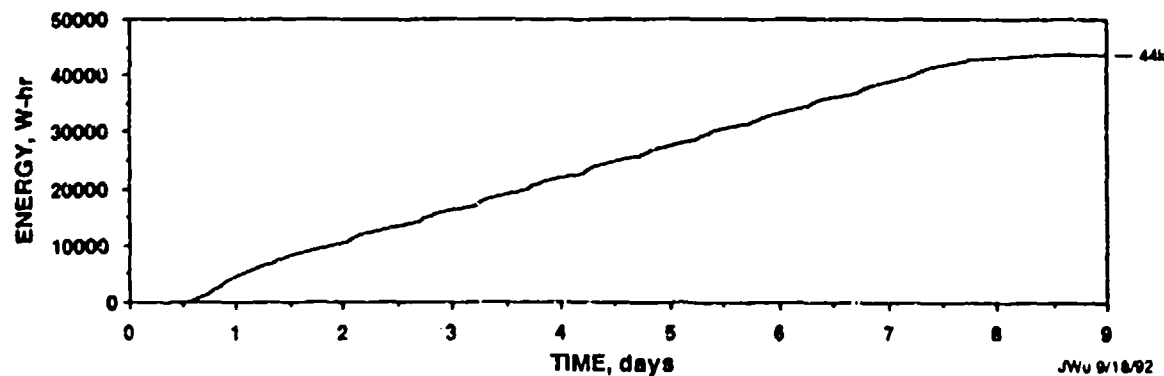


Figure 6. BETSCE strawman power and energy profiles.

FUNCTIONAL OBJECTIVE	DAY								
	1	2	3	4	5	6	7	8	9
Launch	■								
Startup	■	■							
Initial Cooldown/Recharge Cycle		■	■						
Modified Cooldown/Recharge Cycle			■	■					
Establish Nominal Cycle			■	■	■				
Establish Cycle Repeatability				■	■	■			
Multiple-Cooldown Cycle					■	■			
Sensitivity Study Test Cycles						■	■		
Upper-stage (<30 K) Test Cycle							■	■	
Hydride Bed Characterization Cycle								■	
Re-establish Nominal Cycle								■	■
Additional Sensitivity Study Tests									■
Shutdown									■
Return									■
Main Experiment					Extended Mission				

Figure 7. BETSCE strawman mission timeline.

flight, data will be retrieved from the on-board data storage device and again archived. After reduction and analysis, the microgravity spaceflight performance data will be compared and correlated with ground test data, and to analytical model predictions. Particular emphasis will be placed on gaining a quantitative understanding of the phenomena listed in Table I.

## SUMMARY AND CONCLUSIONS

The BETSCE offers the first opportunity to demonstrate the spaceflight performance of a sorption cryocooler. Extensive test data obtained from the 9 day mission will permit correlation of microgravity performance with ground test data and analytical model predictions. The spaceflight performance characterization database will aid in the design of future lightweight, efficient, periodic 10 K sorption coolers for Brilliant Eyes, as well as other infrared sensor cooling applications for surveillance, astronomy, planetary and earth observation satellite systems.

## ACKNOWLEDGEMENTS

The work described in this paper was carried out by the Jet Propulsion Laboratory (JPL), California Institute of Technology under contract with the National Aeronautics and Space Administration. The work was sponsored by the Brilliant Eyes program office, Strategic Defense Initiative Organization (SDIO), USAF Space and Missiles Systems Center (SMC). The authors wish to thank the entire BETSCE development team at JPL, Aerojet Electronics Systems Division, and APD Cryogenics for their technical contributions and commitment to this effort, and Dr. Donald Rapp for editing the manuscript. The support of Dr. Al Johnson in providing technical guidance and aiding the experiment requirements definition is also appreciated.

## REFERENCES

1. Johnson, A. L. and Jones, J. A., "Periodic 10 K Sorption Cooling," USA Patent No. TBD., 1992.
2. Johnson, A. L. and Jones, J. A., "Evolution of the 10 K Periodic Sorption Refrigerator Concept," 7th International Cryocoolers Conference, Santa Fe, NM, November 17-19, 1992.
3. Wu, J.-J., Bard, S., and Longworth, R., "10 K Sorption Cryocooler Proof-of-Principle Experiment," in preparation, 1993.
4. Bard, S., Fujita, T., Wade, L., Rodriguez, J., and Wu, J. J., "Development of a Periodic 10 K Sorption Cryocooler," 7th International Cryocoolers Conference, Santa Fe, NM, November 17-19, 1992.
5. London, J. R., Weissman, J. R. and McNeil, R. C., "Brilliant Eyes - A Technology Driver for Small Satellite Systems," Paper No. IAF-91-048, 42nd Congress of the International Astronautical Federation, Montreal, Canada, October 5-11, 1991.



6. Bowman, R., Freeman, B., Labor, D., Lynch, F., Marmaro, R., and Wade, L., "Evaluation of a Prototype Hydride Compressor for Periodic Sorption Cryocoolers," 7th International Cryocoolers Conference, Santa Fe, NM, November 17-19, 1992.
7. Beam, J., Brennan, P. J., and Bello, M., "Design and Performance of a Cryogenic Heat Pipe Experiment (CRYOHP)," Paper No. AIAA 92-2867, AIAA 27th Thermophysics Conference, Nashville, TN, July 6-8, 1992.
8. Russo, S., and Sugimura, R., "NASA Cryo System Flight Experiment (CSE)," 7th International Cryocoolers Conference, Santa Fe, NM, November 17-19, 1992.

# GAS ATOMIZED $\text{Er}_3\text{Ni}$ POWDER FOR CRYOCOOLER APPLICATIONS

I. E. ANDERSON, M. G. OSBORNE, H. TAKEYA, AND K. A. GSCHNEIDNER, JR.  
 AMES LABORATORY AND DEPARTMENT OF MATERIALS SCIENCE AND  
 ENGINEERING, IOWA STATE UNIVERSITY  
 AMES, IOWA 50011, USA

## ABSTRACT

Although  $\text{Er}_3\text{Ni}$  powder has become an important cryocooler regeneration material due to its significantly enhanced heat capacity at temperatures in the range of liquid He, an efficient method is still needed to produce commercial quantities of high quality  $\text{Er}_3\text{Ni}$  powder. A high pressure gas atomization (HPGA) approach was developed to produce uniform spherical powders of high purity  $\text{Er}_3\text{Ni}$  and 3 batches of about 1.3Kg each were prepared. The average yield of high quality spherical powders between 0.15 and 0.35mm was about 16% of the initial atomizer charge weight. Microstructural analysis of sectioned powder samples revealed single phase particles with some internal cracking but no evidence of an oxidized surface shell. Chemical analysis and x-ray diffraction measurements verified that single phase particles of the stoichiometric composition had been generated. Vacuum fusion measurements indicated that the powder contained 2600ppm of oxygen (by wt.). The heat capacity of a hot pressed, partially sintered  $\text{Er}_3\text{Ni}$  powder sample was measured from 2K to about 80K. The results indicated a maximum heat capacity of  $0.43 \text{ J/cm}^3\text{K}$  at about 7K. The heat capacity peak appears to be about  $0.04 \text{ J/cm}^3\text{K}$  higher than that reported by Sahashi et al. (1) and it is also narrower. Compared to the single peak for this sample, the Sahashi et al. (1) heat capacity peak has two maxima suggesting the existence of two phases in their material. In addition, our  $\text{Er}_3\text{Ni}$  powder has a larger heat capacity than Pb over the entire range of temperatures up to about 25K which should permit a lower final temperature for a cryocooler stage composed of this material.

## INTRODUCTION

$\text{Er}_3\text{Ni}$  powder has become an important cryocooler regeneration material due to its significantly enhanced heat capacity at temperatures in the range of liquid He. However, the pace of development of reliable magnetic refrigeration devices which utilize rare earth intermetallic (REI)

alloys as the heat exchanger bed material has been slowed by several problems associated with the characteristics of available alloy particulate. Most of these alloys have inherently poor mechanical properties, primarily poor fracture toughness. Only limited commercial sources of suitable powder of these alloys currently exist, typically supplying powder which is non-spherical, of low purity, and sized between about 0.1 to 0.3mm.

The most typical commercial practice involves mechanical grinding or crushing of cast alloys to size which produces irregular fragmented powders that are often partially fractured (2). Premature disintegration of this substandard particulate material generally occurs after a limited period of testing in a packed bed heat exchanger. The disintegration process causes the bed to shift and lose stability, creating a loose bed that promotes further particle attrition and dusting. The abrasive dust can also severely affect the lifetime of moving parts in the refrigeration unit (2).

An improved experimental technique, spark erosion, produces a yield of  $\text{Er}_3\text{Ni}$  powders that consists of both "shatters" and spheres (3). Recent research results reported by Ludeman (4) indicate that a drop tube atomization device with a fine diameter orifice and a high melt overpressure is capable of producing extremely high yields of REI alloy spheres, albeit at a low production rate. However, because the Raleigh disintegration process requires increasingly finer melt orifice sizes for finer powders and because of their tendency to freeze-off, this device appears to have a natural lower size limit of about 0.3mm for production of REI alloy powders. Recently, one commercial source has emerged for 0.3mm spheres (1) which are produced by a "Rotating Disk Process" method but uncertainty exists about its efficiency, adaptability for smaller size spheres, and suitability for higher melting point REI alloys.

To permit widespread development of advanced cryocooler designs that utilize this high performance material, an efficient method is needed to produce uniform spherical powders of high purity  $\text{Er}_3\text{Ni}$  in commercial quantities. A modified high pressure gas atomization (HPGA) technique has been demonstrated to be effective for production of rare earth-iron-boron permanent magnet alloy powders (5), a REI alloy of similar oxidation tendency, although in a much finer particle size. Because the modified HPGA technique already produces high purity spherical powders and includes provisions for powder surface passivation of REI alloys (5), the chief development needed for adapting HPGA for this application is a "detuning" of the atomization energy level (6) to produce significantly coarser powders.

## EXPERIMENTAL PROCEDURE

The starting materials used in this study were 99.8at.% pure Er bar, which had been prepared at the Materials Preparation Center, Ames Laboratory, and 99.9at.% pure Ni shot which was purchased from INCO. The major impurities in the Er in ppma (atomic) were: H - 828, C - 97, N - 60, O - 546, F - 246, Cl - 14, and Fe - 19 (all the remaining impurities present were < 10 ppma and most < 1 ppma). The major impurities in the Ni in ppma were: H - 330, C - 580, O - 107, Cl - 1, and Mn - 2 (all the remaining impurities present were < 1 ppma). Weighted amounts of Er and Ni were arc-melted on a water cooled Cu hearth in an inert atmosphere of Ar (99.998wt.% pure) and cast in 25g buttons. A total of about 3700g of alloy was prepared and split into three similar batches for atomization processing.

The high pressure gas atomization process incorporated a melting system with a high purity (99.55%), controlled porosity (21.0% porosity) alumina crucible, a high purity (99.8%), hard-fired alumina stopper rod, and a boron nitride (93% BN) pour tube. Based on an estimated liquidus temperature of 900°C of the Er<sub>3</sub>Ni alloy composition (Er-10.47wt.%Ni), a melt pour temperature of 1100°C was selected to provide about 200°C of superheat for effective alloy homogenization and atomization. The melting and atomization chamber, as shown schematically in Figure 1, was evacuated initially to about  $6 \times 10^{-2}$  torr and, then, backfilled with ultra high purity (99.998%) Ar gas to a positive pressure (1.1atm) for the melting and atomization operations. The atomization nozzle (7) was operated at a gas pressure of 2.8MPa (400psig) with ultra high purity (99.998%) Ar gas utilizing a melt tip configuration designed to reduce the energy of disintegration process (6) to promote production of large (0.15 to 0.35mm) powder particles. In addition, an in-situ particle passivation process (5) was performed during the atomization of the powder to render the powder surfaces resistant to ambient environmental degradation.

Since initial screening of the atomizer yield resulted in both spherical powders and flattened "splat" flakes, a fluidized bed sorting technique was developed which utilized a 2.5cm diameter by 0.7m long separation tube with an upward flow of Ar. At a selected gas flow setting the splats were transported up and out of the top of the open separation tube with the spherical powder retained in the lower portion of the tube for collection after termination of the gas flow.

To characterize particle shape, loose powder was observed with SEM using a conducting adhesive mount. Microstructural analysis included optical microscopy and SEM of powder particle cross-sections in etched (2% nital) and unetched conditions to observe internal particle microstructure and

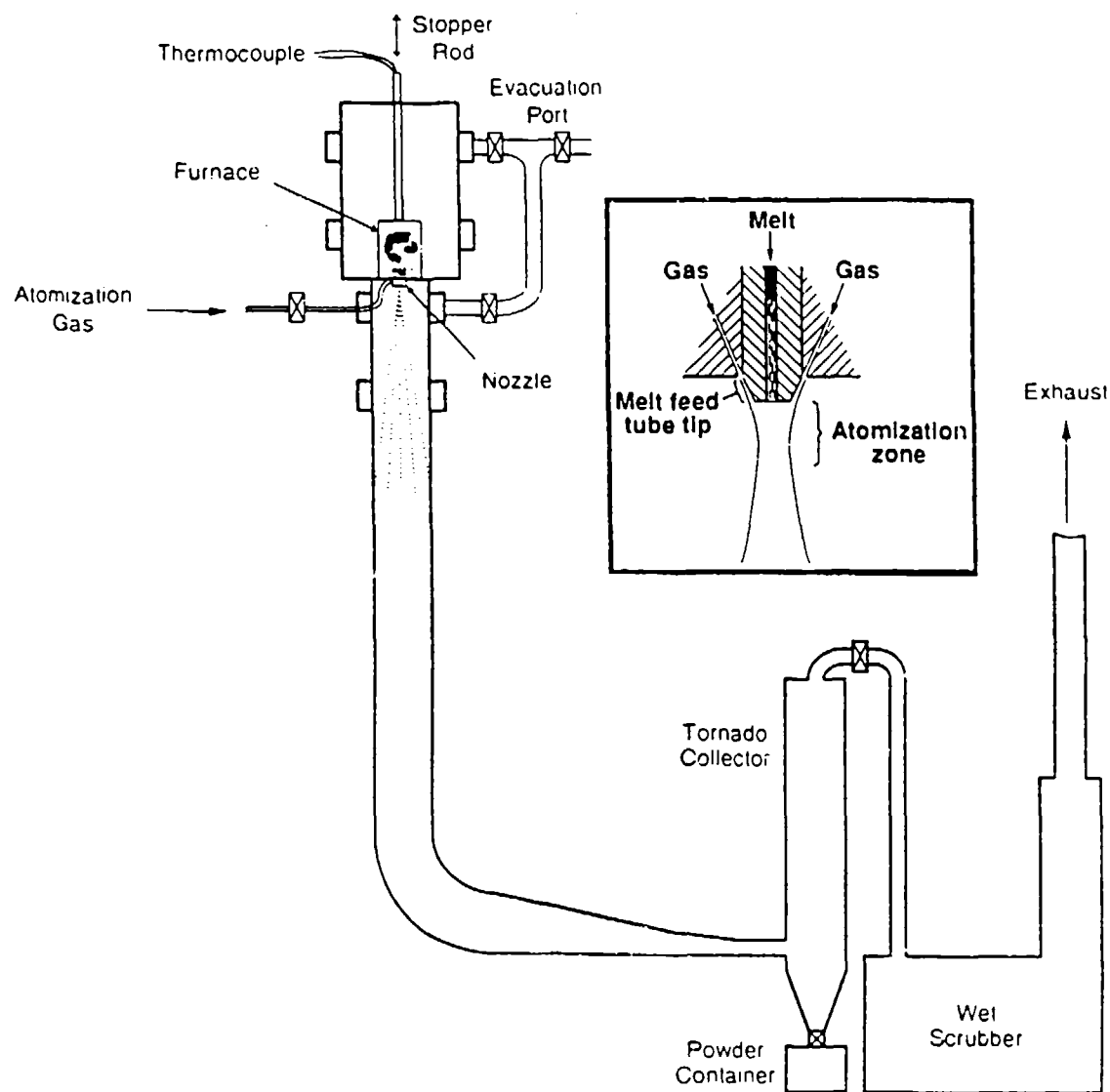


Figure 1. Schematic of high pressure gas atomization (HPGA) at the Ames Laboratory, with inset sketch of nozzle/pour tube configuration.

porosity, respectively. Metallographic sample preparation of these samples involved epoxy mounting of the loose powders and standard grinding and polishing techniques.

Because the measurement fixture of the sub-ambient calorimeter required a sample shaped like a right circular cylinder rather than loose particulate, the spherical  $\text{Er}_3\text{Ni}$  powders were partially sintered into this shape. Powder that had been screened to  $0.212 < \text{dia.} < 0.300\text{mm}$  and sorted to remove flakes was poured into a cylindrical BN die cavity, 3mm dia. by 3mm height, which was fitted with a BN plunger. The plunger was weighted with a stainless steel block of about 500g. The powder sample and die assembly was loaded into a resistance furnace chamber and vacuum ( $5 \times 10^{-6}\text{torr}$ ) sintered at  $700^\circ\text{C}$  for 44hr. The partially sintered sample exhibited sufficient mechanical integrity to permit removal from the BN die and handling in the calorimeter.

The low temperature (2 to 80K) heat capacity was measured using an adiabatic heat-pulse type calorimeter (8). The accuracy of the heat capacity measurements is estimated to be within 1% of the reported value below 20K, within 2-5% between 20 and 60K, and within 5-10% above 60K, with the accuracy decreasing with increasing temperature in the range above 20K. The reproducibility from one run to another, however, is much better: less than or equal to 1% below 40K, 2% between 40 and 50K, 3% between 50 and 60K, and 4 to 5% above 60K.

## RESULTS

Uniform spherical powders of  $\text{Er}_3\text{Ni}$  were produced by a high pressure gas atomization (HPGA) approach in 3 batches of about 1.3Kg each. The average yield of high quality spherical powders between 0.15 and 0.35mm was about 16% of the initial atomizer charge weight. The typical shape and surface character of the HPGA powder is given in Figure 2 which shows powders screened to  $0.106 < \text{dia.} < 0.150\text{mm}$ . Occasional small singular "nubs" are commonly attached to the spheres, but no large clusters of "satellite" particles are observed, as Figure 2 indicates. It should be noted that a fairly large fraction of the as-atomized yield (approximately 10 to 20% by weight) consisted of splat flakes and that the flakes were removed by a fluidized bed separation method described above. Observations of the  $\text{Er}_3\text{Ni}$  atomization spray suggested that the wide spray cone which resulted from the detuned atomization parameters contributed to impingement of a large number of molten droplets on the narrow spray chamber wall, probably producing the splats found in the powder yield.

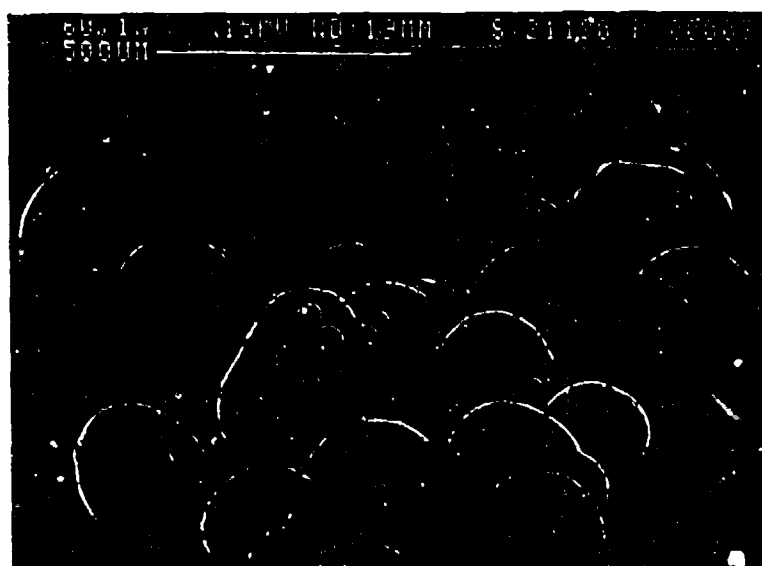


Figure 2. SEM micrograph of as-atomized  $\text{Er}_3\text{Ni}$  powder prepared by HPGA after screening to  $0.106 < \text{dia.} < 0.150\text{mm}$  and removal of flake particulate.

Microstructural analysis of sectioned and etched powder samples, represented by Figure 3 which shows  $0.212 < \text{dia.} < 0.300\text{mm}$  powders, revealed single phase particles with some internal cracking and a proportion (10 to 30%) containing large internal pores. Also, Figure 3 shows that the powder surfaces do not exhibit a thick exterior shell suggesting that the in-situ passivation treatment produces a surface film thinner than the SEM resolution limit. However, evidence of the passivation treatment effectiveness is provided by our recent observations of the lack of obvious degradation, typically in the form of a light colored oxide dust, of the HPGA powder surfaces even after extended exposure (nearly 2 years) in the ambient environment.

X-ray diffraction measurements indicated that single phase powders of the  $\text{Er}_3\text{Ni}$  compound (orthorhombic,  $\text{Pnma}$ ,  $\text{DO}_{11}$ ) had been generated by rapid solidification of the gas atomized particles. In spite of the complex Bragg diffraction pattern shown in Figure 4, a computer-aided comparison of the observed and calculated patterns, including both reflection positions and intensities, revealed excellent agreement. This suggests that the particles are single phase  $\text{Er}_3\text{Ni}$  within the resolution limit of the x-ray diffraction technique.

Chemical purity of the atomized powder which is another important characteristic that affects cryocooler performance was analyzed by atomic emission spectroscopy (AES), titrimetric titration, and vacuum fusion. The Er concentration of a random sample of as-atomized particulate was measured by both titration and AES, while the Ni concentration was measured only by AES. The results indicated that the nominal alloy composition, i.e., the initial composition charged into the atomizer crucible, was maintained in the resulting powder and that the final powder alloy stoichiometry was  $\text{Er}_{3.00}\text{Ni}$  within the resolution of the analysis techniques. Vacuum fusion measurements indicated that the powder contained 63ppmw of hydrogen, 67ppmw of nitrogen, and 2600ppmw of oxygen. The elevated oxygen content of the particulate is probably affected by the significant fraction of splat flakes in the random sample of the yield. Since the oxygen content is probably associated primarily with particulate surfaces, the contribution to total surface area of the splat flakes compared to the spherical powders is likely to be disproportionately large (by weight) and probably inflates the oxygen content of the total particulate yield.

The heat capacity of a hot pressed, partially sintered  $\text{Er}_3\text{Ni}$  powder sample was measured from 2 to about 80K. Figure 5 gives our  $\text{Er}_3\text{Ni}$  heat capacity results from 2 to 30K along with the Sahashi et al. (1) results for both  $\text{Er}_3\text{Ni}$  and Pb. The results of this study show a maximum heat capacity of  $0.43 \text{ J/cm}^3\text{K}$  at about 7K. The heat capacity of our  $\text{Er}_3\text{Ni}$  sample is somewhat higher than that reported by Sahashi et al. (1) from 5 to 25K, except in the 8 to 10K range just above the





Figure 3. SEM micrograph of as-atomized Er<sub>3</sub>Ni powder prepared by HPGA after screening to  $0.212 < \text{dia.} < 0.300\text{mm}$  and removal of flake particulate. Powder was encapsulated in epoxy, metallographically sectioned, and etched (2% nital) to reveal particulate microstructure.

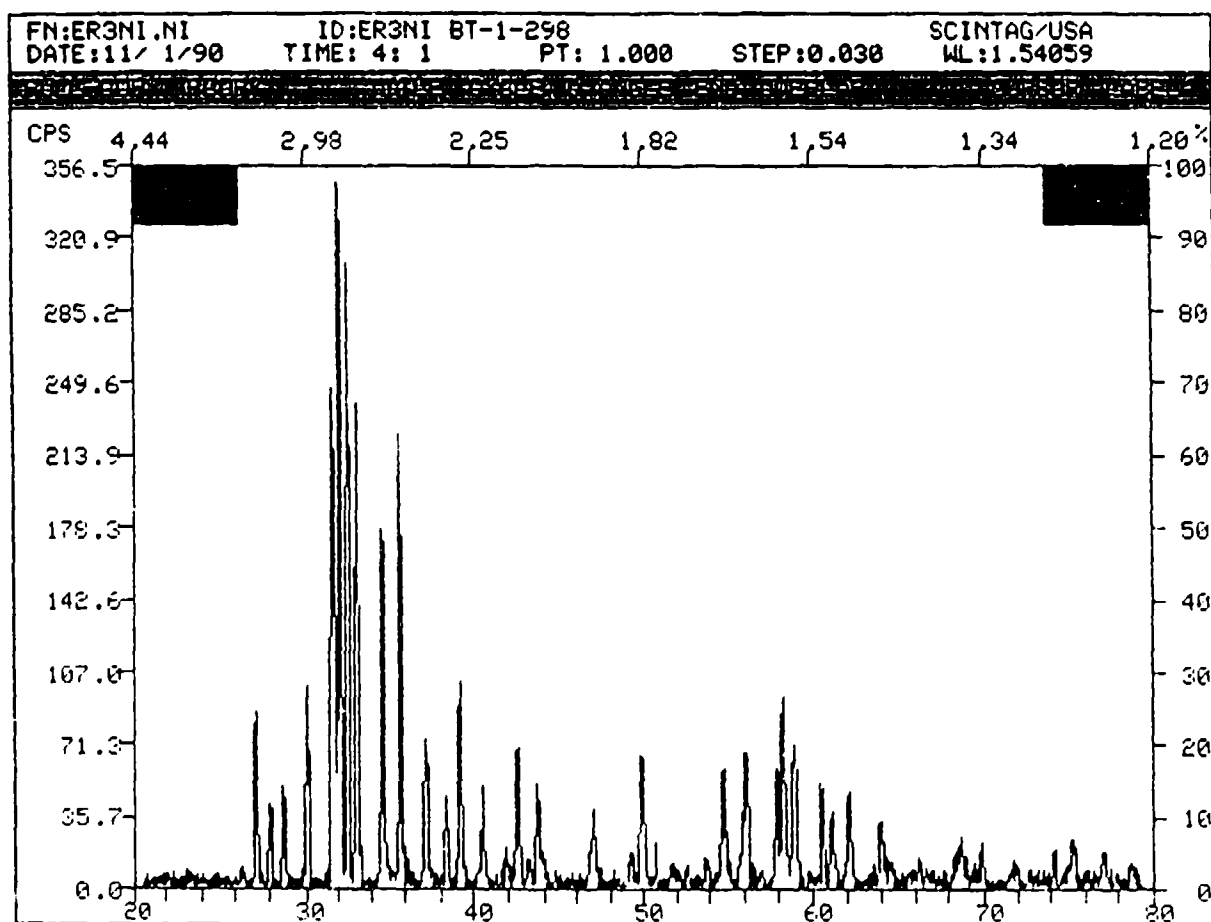


Figure 4. Results of x-ray diffraction analysis using Cu-K $\alpha$  radiation of a random sample of as-atomized Er<sub>3</sub>Ni powder prepared by HPGA, where the lower x-axis scale is in degrees 2 theta and the left y-axis scale is in arbitrary counts per second (CPS).

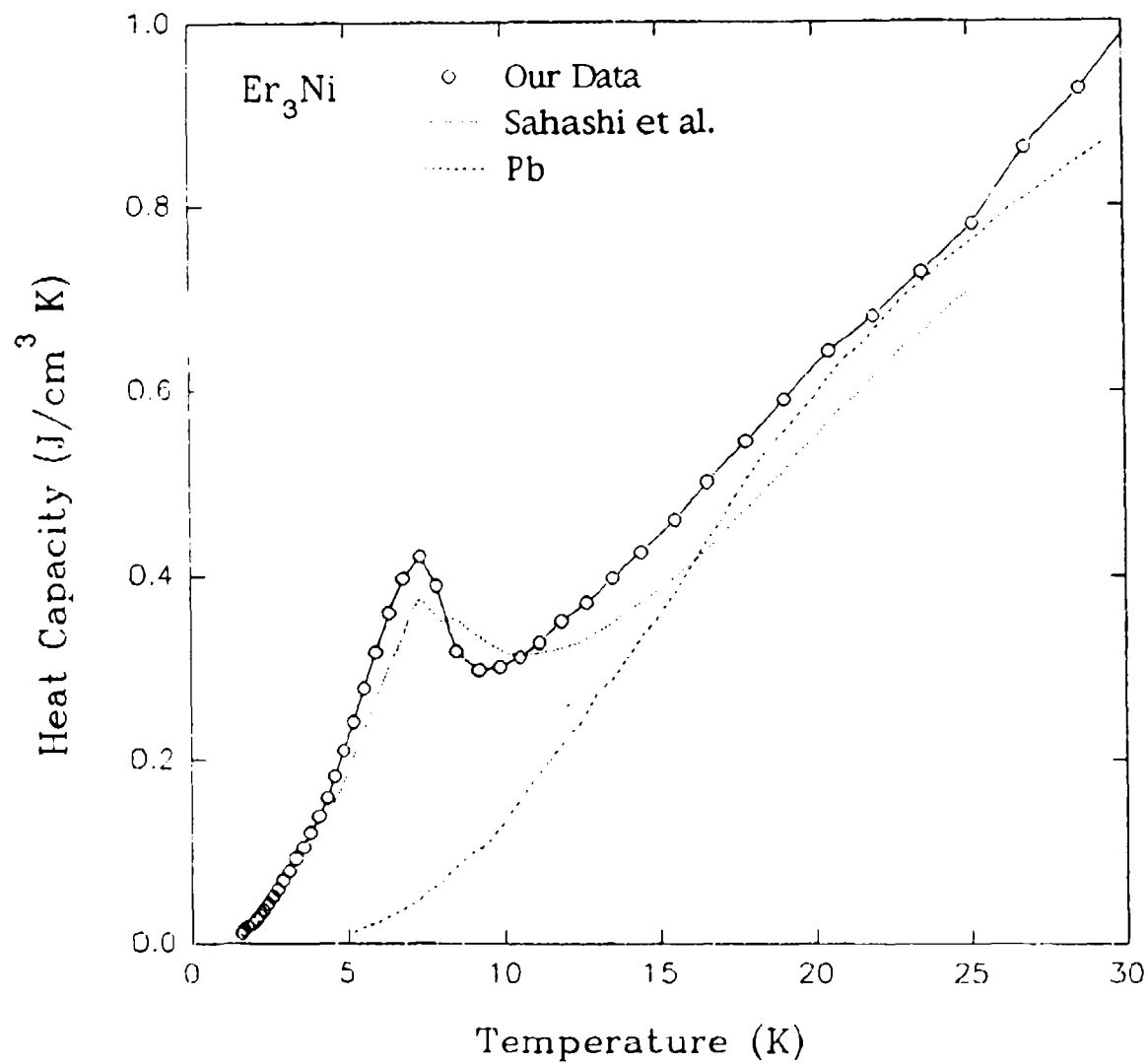


Figure 5. Low temperature portion of subambient (2 to 80K) calorimetry results for  $\text{Er}_3\text{Ni}$  alloy sample prepared from HPGA powder after screening to  $0.212 < \text{dia.} < 0.300\text{mm}$ , removal of flake particulate, and partial sintering. Also shown for comparison are the results that Sahashi et al. (1) reported for  $\text{Er}_3\text{Ni}$  and Pb.

antiferromagnetic ordering temperature. This is due to the broader heat capacity peak of the Sahashi et al. (1) sample. The heat capacity peak of our sample is about  $0.04 \text{ J/cm}^3\text{K}$  higher than that of Sahashi, et al. (1) and is also narrower.

## DISCUSSION

High pressure gas atomization (HPGA) experiments at the Ames Laboratory have yielded research quantities of  $\text{Er}_3\text{Ni}$ . These experiments resulted in 0.15 to 0.35mm spheres with an average yield of 16% of the original atomizer charge weight at a production rate of about 75g per second. Most of the remaining yield was splat flakes or finer powders. While the HPGA process yield of 16% spheres in the desired size range does not appear especially laudable, especially in light of the high cost of the alloy, our average yield is probably at least four times that of a competing gas atomization research program at NIST (2) which reported a 3% yield of both spheres and irregular particulate between 0.12 and 0.25mm.

Unfortunately, all gas atomized powders with diameters greater than about 0.075mm contain a fraction, usually about 10%, of particles with large central pores that arise from gas trapped during the atomization process. These hollow spheres are difficult to separate from the solid ones and can contribute to a reduction in total heat capacity of the packed bed. It is important to note that if the particle size requirements in new packed bed heat exchanger designs are decreased below 0.075mm, the HPGA process could produce significantly greater yields of solid spherical powders. Alternatively, a new atomization process under development at the Ames Laboratory (9) can produce internally sound spherical powders of large (0.15 to about 0.7mm) pure metals and alloys of transition metals. This centrifugal atomization into a rotating quench bath (CA/RQB) approach is currently being extended to REI alloys, including  $\text{Er}_3\text{Ni}$ , and the results of these experiments will be reported in the future.

In Figure 5, we also compare the results of our heat capacity measurements on  $\text{Er}_3\text{Ni}$  with those reported by Sahashi et al. (1) for  $\text{Er}_3\text{Ni}$  and for Pb. The sharper peak in our sample compared to that of the Sahashi et al. (1) sample indicates that our material is purer, either chemically or structurally, or both. Unfortunately, Sahashi et al. (1) do not report chemical analysis results which could be used for comparison of chemical purity. However, the double peak in the Sahashi et al. (1)  $\text{Er}_3\text{Ni}$  sample, taken by itself (in lieu of x-ray diffraction results), suggests that a second phase is present in their alloy. The presence of this second phase may also account for the fact that the heat capacity of their sample is smaller than ours over the 5 to 25K range. Furthermore, we

note that the heat capacity of our Er<sub>3</sub>Ni sample is larger than that of lead over the entire range of temperatures shown in Figure 5. This should permit a lower final temperature for a cryocooler stage composed of our material and also may allow for a shorter initial cooling time to a given temperature.

## SUMMARY

1. High pressure gas atomization (HPGA) is a viable technique for production of research quantities of spherical, passivated Er<sub>3</sub>Ni powders for cryocooler applications.
2. Chemical, structural, and calorimetric characterization of the HPGA powders indicates that single phase powders of the stoichiometric Er<sub>3</sub>Ni compound were produced without any significant level of contamination except possibly for oxygen.
3. As a result of the high quality of the HPGA Er<sub>3</sub>Ni, the calorimetric measurements revealed that the peak heat capacity of our sample at 7K exceeded all reported measurements of this alloy and is larger than that of lead from 2K to at least 30K which should permit a lower final temperature for a cryocooler stage composed of our material and also may allow for a shorter initial cooling time to a given temperature.

## ACKNOWLEDGMENTS

We wish to thank B. Beaudry and F. A. Schmidt for their valuable insight on the design of a compatible melting system for this alloy and R. L. Terpstra for his careful preparation of the atomization system for this difficult powder processing task. This work was funded partially by the U. S. Dept. of Energy through contract no. W-7405-Eng-82 from the Materials Science Division of Basic Energy Sciences.

## REFERENCES

1. M. Sahashi, Y. Tokai, T. Kuriyama, H. Nakagome, R. Li, M. Ogawa, and T. Hashimoto, *Advances in Cryogenic Engineering*, 35, Plenum Press, NY, NY, 1175(1990).
2. L. F. Aprigliano, G. Green, J. Chafe, L. O'Connor, F. Biancanello, and S. Ridder, *Advances in Cryogenic Engineering*, 37B, R. W. Fast, ed., Plenum Press, NY, NY, 1003(1992).
3. R. A. Ackermann, *Advances in Cryogenic Engineering*, 37B, R. W. Fast, ed., Plenum Press, NY, NY, 981(1992).

4. E. M. Ludeman and C. B. Zimm, in Proceedings of the Cryogenic Engineering Conference, held in Huntsville, AL, (June 1991).
5. I. E. Anderson, R. L. Terpstra, and B. K. Lograsso, "Environmentally Stable Reactive Alloy Powders and Method of Making Same," U. S. Patent Application pending.
6. I. E. Anderson, R. S. Figliola, and H. M. Molnar, Materials Science and Engineering, A148, 101(1991).
7. I. E. Anderson, H. M. Molnar, and R. S. Figliola, U.S. Patent No. 5,125,574, issued June 30, 1992.
8. K. Ikeda, K. A. Gschneidner, Jr., B. J. Beaudry, and U. Atzmony, Phys. Rev., B25, 4604 (1982).
9. M. G. Osborne, I. E. Anderson, K. S. Funke, and J. D. Verhoeven, in Advances in Powder Metallurgy - 1992, J. M. Capus and R. M. German, eds., MPIF-APMI, Princeton, NJ, (in press).

## MAGNETIC NANOCOMPOSITES AS MAGNETIC REFRIGERANTS

R.D. SHULL, R.D. MCMICHAEL, J.J. RITTER, L.J. SWARTZENDRUBER,  
and L.H. BENNETT

MATERIALS SCIENCE AND ENGINEERING LABORATORY  
NATIONAL INSTITUTE OF STANDARDS AND TECHNOLOGY  
GAITHERSBURG, MD 20899

### I. INTRODUCTION

It has been found that materials possessing nanometer-scale dimensions, called nanocrystalline or nanostructured materials, may possess properties or property combinations which are different from those possessed by conventional materials having larger dimensions<sup>[1]</sup>. The unique properties of these new materials are a consequence of either the large volume percent of interfaces in the material or the reduction in size to less than that of the critical length scale appropriate to the particular property. For nanocomposites<sup>[2]</sup>, wherein the material is a composite of nanometer-scale species, the properties are different from, but related to, those of the individual constituents. Consequently, the properties of this subset of the class of nanostructured materials are sensitive to the volume fraction of its components. This additional degree of freedom is useful for the atomic engineering of materials with very specific properties since volume fraction is a relatively easy variable to control. For magnetic nanocomposites, a new bulk magnetic state, called superparamagnetism, may exist. This magnetic state only exists when the magnetic particles are very small. At the last cryocooler conference, this type of magnetic material was first suggested as a new type of refrigerant for magnetic refrigerators<sup>[3,4]</sup>. Theoretical reasons for this suggestion were presented which showed that enhanced magnetocaloric effects are potentially obtainable in this type of material at higher temperatures and lower fields than in paramagnetic refrigerants. Preliminary data was also presented at that conference for a 10%Fe+silica gel magnetic nanocomposite. The magnetocaloric effects in this dilute nanocomposite, although being significantly enhanced over that of pure bulk Fe at 70 K, were still small in magnitude. Since that initial announcement, an analysis of the losses, refrigeration quality factor, and power density of magnetic refrigerators using magnetic nanocomposites<sup>[5]</sup> showed that these materials represent a real potential as magnetic refrigerants. In the following section, the theoretical basis for the enhanced magnetocaloric effects in superparamagnetic and "super-ferromagnetic" (wherein the magnetic clusters are allowed to magnetically interact)

nanocomposites will be reviewed, including improvements on the theory<sup>[6-8]</sup> made since the last cryocooler conference. A new magnetocaloric effect measurement method developed in this laboratory<sup>[9]</sup> for the fast screening of material candidates is described and data measured on several new magnetic nanocomposites is reviewed showing the predicted enhancements. Included in the last section is a description of a new type of magnetic nanocomposite: one which is single phase crystallographically, but multiple phase magnetically. This new material, Fe-doped gadolinium gallium garnet (GGIG), possesses magnetocaloric effects at 15 K and 1 T which are larger than that for the presently used low temperature magnetic refrigerant gadolinium gallium garnet (GGG)<sup>[10]</sup>. GGIG also has sufficiently large magnetocaloric effects at higher temperatures to suggest potential applications at temperatures in excess of 20 K.

## II. MAGNETOCALORIC EFFECT

The change in internal energy ( $dU$ ) of a closed system with no volume change occurring may be expressed in terms of the incremental changes in the entropy ( $dS$ ) and magnetization ( $dM$ ) as follows:

$$dU = TdS + HdM \quad (1)$$

where  $T$  and  $H$  are respectively the temperature and applied magnetic field. From this exact differential, the following Maxwell relation may be derived relating the incremental entropy change accompanying an incremental change in magnetic field to the easily measurable quantities of magnetization and temperature:

$$\left(\frac{\partial S}{\partial H}\right)_T = \left(\frac{\partial M}{\partial T}\right)_H \quad (2)$$

Upon integrating over  $H$ , the total entropy change of the system upon the application of a magnetic field may be determined:

$$\Delta S = \int_0^H \left(\frac{\partial M}{\partial T}\right)_H dH \quad (3)$$

The magnetocaloric effect (defined as a temperature change) is just  $\Delta S$  multiplied by the temperature and divided by the heat capacity (at constant  $H$ ). For the purposes of this paper we will focus on variations in  $\Delta S$  instead of  $\Delta T$ , keeping in mind they are closely related.



**A. For Paramagnets:**

For the case of a paramagnet, the temperature and field dependence of  $M$  is described by the Langevin function<sup>[11]</sup>:

$$M = N\mu[\coth(\alpha) - (\frac{1}{\alpha})] \quad (4)$$

$$\alpha = \frac{\mu H}{k_B T}$$

where  $\mu$  and  $N$  are respectively the size and number of non-interacting magnetic moments in the system, and  $k_B$  is the Boltzmann constant. Substituting the equation 4 relationship into equation 3 and performing the integration, one obtains the following for the entropy change upon application of the field<sup>[6]</sup>:

$$\Delta S = Nk_B[1 - \alpha \coth(\alpha) + \ln(\frac{\sinh(\alpha)}{\alpha})] . \quad (5)$$

At low fields or high temperatures (well away from saturation),  $M$  follows the Curie Law and  $\Delta S$  reduces to the following simple expression<sup>[4]</sup>:

$$\Delta S = \frac{N\mu^2 H^2}{6k_B T^2} . \quad (6)$$

Because  $\Delta S$  diverges to very large values at low temperatures, adiabatic demagnetization refrigerators in this temperature range can be made using paramagnetic salts like chromic potassium alum<sup>[12]</sup> (for  $T < 1$  K) or gadolinium gallium garnet<sup>[13,14]</sup> (for  $1 \text{ K} < T < 20 \text{ K}$ ) as the refrigerant. Note, however, from equation 6 that  $\Delta S$  decreases as  $1/T$ . Therefore, at high temperatures the magnetocaloric effect in paramagnets is small, and they cease to be useful refrigerants.

**B. For Nanocomposites with No Interaction Between Magnetic Clusters:**

Operation of a magnetic refrigerator at higher temperatures than 20 K requires a refrigerant with a larger  $\Delta S$  value than obtainable with a paramagnet. One potential way to obtain the larger  $\Delta S$  values required for higher temperature magnetic refrigerator operation is to use magnetic nanocomposites possessing superparamagnetic behavior<sup>[4,6,9]</sup>.

Note from equation 6, that if  $\mu$  is made larger (and  $N$  is simultaneously made smaller to keep the saturation magnetization,  $N\mu$ , constant),  $\Delta S$  increases because of the squared dependence on  $\mu$  (and only linear dependence with  $N$ ). This is the same situation as grouping the  $N$  spins (each with a magnetic moment of  $\mu_s$ ) in the system together into " $n$ " clusters (i.e. each cluster having  $N/n$  magnetic spins). Using equation 6, one can show that  $\Delta S$  for this situation at low values of  $\mu H/k_B T$  is described by equation 7:

$$\Delta S_{\text{nano}} = \frac{n \left( \frac{N}{n} \mu_s \right)^2 H^2}{6 k_B T^2} \quad (7)$$

Since " $n$ " is much smaller than  $N$ , comparison of equations 7 and 6 (in equation 6,  $\mu = \mu_s$ ) shows that  $\Delta S_{\text{nano}}$  can be much larger than  $\Delta S$  for a paramagnet at low fields and high temperatures. This is the situation of a superparamagnetic nanocomposite where the atomic magnetic moments cluster to form fewer, but larger, independently acting magnetic moments. There is a limit to this enhancement, however. According to equation 5, at high fields or very low temperatures (when saturation is approached),  $\Delta S$  will decrease when  $\mu$  is increased further. In this regime  $M$  is no longer proportional to  $\mu^2$  (it approaches the constant value of the saturation magnetization), and the reduction in  $N$  factor upon clustering becomes more important by comparison. In fact there is a maximum in  $\Delta S$  with respect to variations in  $N\mu$ , as given in equation 5, at  $\alpha \equiv \alpha_{\text{max}} = \mu H/k_B T \approx 3.5$  [6]. This means that for the maximum magnetocaloric effect there is an optimum cluster size (i.e. an optimal value for  $\mu$ ) for any given temperature of operation and applied magnetic field. Figure 1 shows mean field theory calculations of  $\Delta S$  vs.  $T$  for a system of  $N$  spin-7/2 atoms (e.g. Gd atoms) isolated and clustered into various magnetic cluster sizes. The enhancements in  $\Delta S$  at lower fields and/or higher temperatures on clustering the spins is obvious. Note also the points of intersection of the various curves. At temperatures lower than these crossover points, the **smaller** cluster sizes are better. Superparamagnetic nanocomposites do not create new entropy; they just skew the available entropy to different field and temperature ranges not normally accessible to refrigeration systems using conventional materials.

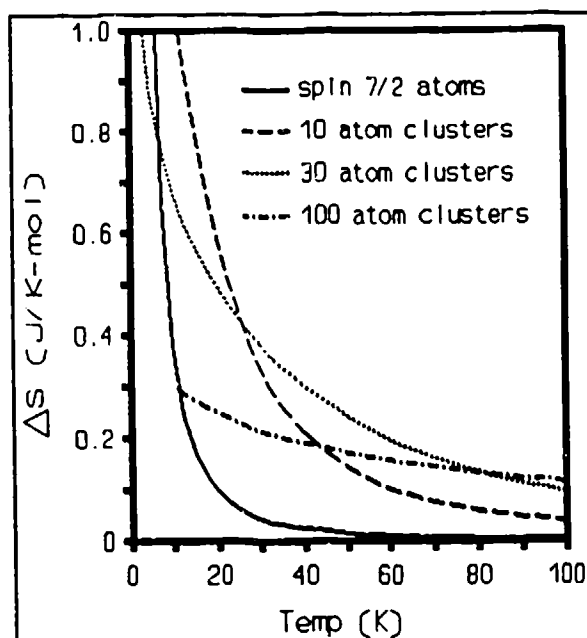


Figure 1. Calculated entropy change of a system of spin-7/2 atoms induced by the removal of a 800 kA/m field for individual spins (GGG) and for clusters of 10, 30, and 100 spins.

### C. For Ferromagnets:

In order to increase the operation temperature to very large values, ferromagnetic materials have historically been considered. In the case of a ferromagnet, examination of equation 3 indicates that the magnetocaloric effect would be small at temperatures much higher or much lower than the Curie temperature,  $T_C$ , since  $(dM/dT)_H$  is very small in those ranges. Accordingly, at  $T_C$  the magnetocaloric effect would be expected to be large. Above the Curie Point, the field and temperature dependence of the magnetization may be analyzed in the mean field approximation in a similar way as was done above for a paramagnet. The effect of the interaction between magnetic moments which occurs at temperatures below  $T_C$  is taken into account by replacing  $T$  in the above equations by  $T - T_C$  so that the parameter  $\alpha$  in equations 4 and 5 becomes

$$\alpha = \frac{\mu H}{k_B(T - T_C)} \quad (8)$$

For  $T > T_C$ , at low fields and high temperatures the entropy change on application of a magnetic field would be similar to that described in equation 6 for a paramagnet:

$$\Delta S = \frac{N\mu^2 H^2}{6k_B(T - T_C)^2} \quad (9)$$

In this case,  $\Delta S$  diverges to very large values as  $T$  approaches  $T_C$ . Consequently, near the Curie point ferromagnets are potentially useful as magnetic refrigerants. Below  $T_C$ , the magnetic spins are ordered in domains, but with an order which is incomplete at  $T_C$ . The magnetocaloric effect is proportional to the "disorder" within the domains at  $H=0$  (i.e. inversely with the spontaneous magnetization of the material below  $T_C$ ). As  $T$  decreases from  $T_C$ , the spin order within the domains increases, so  $\Delta S$  below  $T_C$  also decreases with  $T$ . Consequently,  $\Delta S$  for a ferromagnet is a sharply peaked function of  $T$  at the Curie point. Mean field theory calculations for  $\Delta S$  were performed as a function of  $T$  for a ferromagnet with a  $T_C$  near 300 K (e.g. Gd), and these are shown as the single atom curve in figure 2. Note in this figure the  $\Delta S$  systematics described above.

### D. For Nanocomposites with Interacting Clusters:

Magnetic nanocomposites may also be prepared so that the magnetic clusters interact with each other<sup>[15-16]</sup>. This situation describes the case of ferromagnetically-interacting

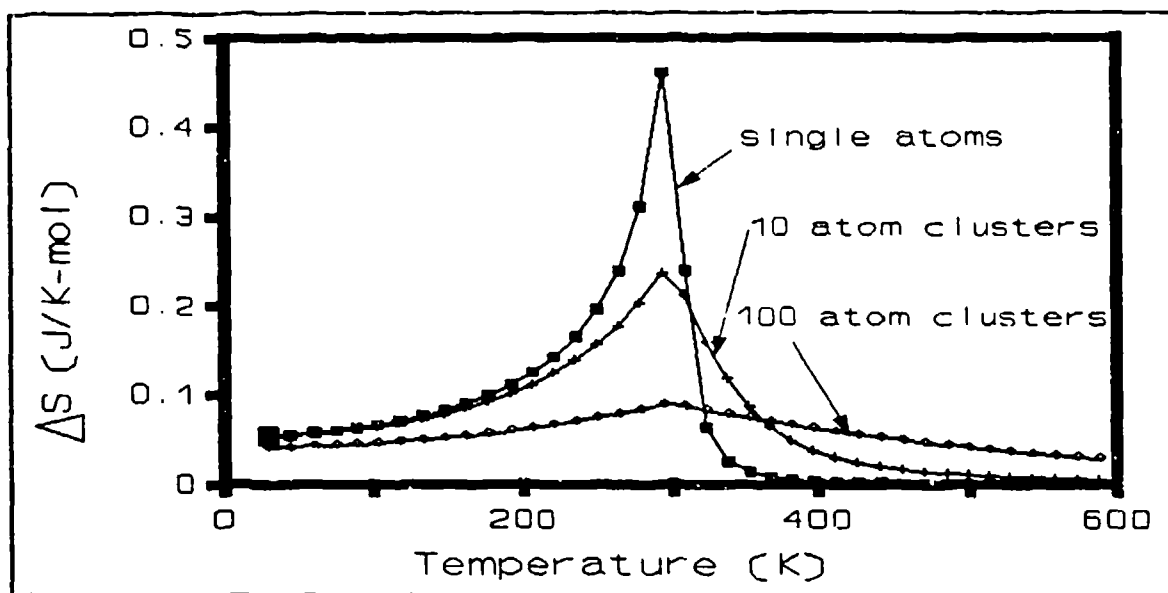


**Figure 2.** Calculated entropy change of a system of interacting spin-7/2 atoms (with  $T_i=300$  K) induced by the removal of an 800 kA/m field for individual atomic spins (Gd) and for clusters of 10 and 100 spins.

superparamagnetic clusters. Nanocomposites of this type will possess an effective interaction temperature,  $T_i$ , analogous to the Curie temperature of a ferromagnet, which describes the interaction between clusters. Below  $T_i$  there is long range magnetic order between the clusters, and above  $T_i$  the material is superparamagnetic. Some authors have referred to this case as "super-ferromagnetic"<sup>[17]</sup>. In this case, there is also an enhancement in  $\Delta S$  above  $T_i$  (compared to that of a ferromagnet with  $T_c=T_i$ ) at low fields as  $\mu N$  (the saturation magnetization) is kept constant while  $\mu$  is increased in magnitude<sup>[4,7]</sup>. In the low field/high temperature limit  $\Delta S$  (called  $\Delta S_{\text{superferro}}$  in this case) will be similar to that expressed in equation 9:

$$\Delta S_{\text{superferro}} = \frac{n [(N/n)\mu_s]^2 H^2}{6k_B (T-T_i)^2} \quad (10)$$

where "n" is the number of interacting clusters and  $\mu_s$  is the magnetic moment of an individual elemental atomic spin. For low fields and high temperatures, the factor  $n[(N/n)\mu_s]^2$  which appears in equation 10 may be much larger than the factor  $N\mu^2$  which appears in equation 9 (where  $\mu=\mu_s$ ). The same limit to these enhancements described above for the superparamagnetic materials occurs for the ferromagnetically-interacting superparamagnets. Maximum enhancements in  $\Delta S_{\text{superferro}}$  are expected when  $\mu_c H/k_B T \approx 3.5$ , where  $\mu_c = [N/n]\mu_s$  is defined as the cluster magnetic moment. For temperatures less than or equal to  $T_i$ , i.e. when magnetic saturation is approached,  $\Delta S$  is smaller when  $\mu$  is increased by clustering the atomic moments<sup>[17]</sup>. The mean field

theory calculations are shown in figure 2. More exact Monte Carlo calculations of  $\Delta S$  for ferromagnetically-interacting superparamagnetic clusters<sup>[7]</sup> above and below  $T_c$  confirm the mean field theory calculations. In both calculations, the entropy change for a given applied field is peaked around the critical temperature ( $T_c$  for a ferromagnet and  $T_1$  for the clustered magnet). In the case of clustered magnetic moments, as in a nanocomposite, figure 2 shows that  $\Delta S$  is also spread out over a broader temperature range. For some magnetic refrigerator designs the large breadth in  $\Delta S$  is important. Also, for refrigeration cycles using an active magnetic regenerator, the slope of the  $\Delta S$  vs.  $T$  relationship below  $T_c$  is particularly important for attaining high efficiency<sup>[18-20]</sup>. Magnetic nanocomposites with interacting clusters provide a means for selecting that slope. In addition, they also provide a means for selecting  $T_1$  and for providing enhanced  $\Delta S$  values at temperatures higher than  $T_1$ <sup>[7]</sup>. All these adjustments are possible without diluting or changing the magnetic spins in the system, unlike composite ferromagnet refrigerants<sup>[21-22]</sup>. Recent calculations for an active magnetic refrigerator substantiate the potential provided by nanocomposites for obtaining refrigeration with enhanced power density and lower magnetic fields<sup>[5]</sup>. Uniaxial magnetic anisotropy can also affect the peak magnitude, peak temperature, and breadth of  $\Delta S$ . For ferromagnetic refrigerants, optimal characteristics are obtained when the magnetic field is directed normal to the easy plane of magnetization<sup>[8]</sup>. If, however, one wished to employ superparamagnetic particles in their paramagnetic regime to obtain a broad  $\Delta S$  vs  $T$  curve, then the applied field should be parallel to the favored axis of magnetization<sup>[8]</sup>.

### III. ENTROPY CALCULATION FROM MAGNETIZATION DATA

Equation 3 relates the entropy change for the application of the magnetic field,  $H$ , in terms of the measurable quantities of  $M$ ,  $T$ , and  $H$ . If one measures the magnetization as a function of field at various temperatures, then the integral in equation 3 becomes just the area enclosed between any two isotherms divided by the temperature difference between the isotherms<sup>[9]</sup>:

$$\Delta S_i = \frac{1}{\Delta T_i} \int_0^H [M(T_{i+1}, H) - M(T_i, H)] dH \quad (11)$$

$$\Delta T_i = T_{i+1} - T_i .$$

Thus the magnetocaloric effect can be measured without calorimetry. This method was tested for gadolinium gallium garnet and compared to direct calculations for spin-7/2 atoms (i.e. a system of independent Gd atoms). The agreement between the measured

data using equation 11 and the calculated values was quite good (within 10%), thereby providing confidence in this method for determining  $\Delta S$ . Since magnetization data is much faster to measure than  $\Delta T$  and heat capacity data, this non-calorimetric method is a fast way to screen prospective magnetic refrigerants. In our laboratory, it has been especially valuable for assessing the utility of various magnetic nanocomposite processing methods, including co-precipitation, solution reduction, and metal-organo complex routes, for making magnetic refrigerants.

#### **IV. EXPERIMENTAL DATA**

Magnetic nanocomposites are usually prepared as a physical mixture of two distinctly different crystallographic phases (e.g. Fe + alumina<sup>[23]</sup>, Ni + silica<sup>[24]</sup>, and Fe<sub>3</sub>O<sub>4</sub> + silver<sup>[25]</sup>), one of which is ferromagnetic and one phase which is not magnetic. In the last cryocooler conference, we reported on some data for a 10%Fe+silica gel nanocomposite<sup>[4]</sup> which showed that this dilute superparamagnetic material possessed a magnetocaloric effect at 70 K which, although small, far exceeded that which pure Fe would have at that temperature. In fact, the dilute nanocomposite possessed an effect which was one quarter as large as the maximum effect possessed by pure Fe at its Curie temperature. These results were consistent with the enhancements predicted above for superparamagnetic nanocomposites. Subsequent investigation of the temperature and concentration dependence of  $\Delta S$  for the Fe+silica gel nanocomposites also provided consistent results with the predictions described above, but the magnetocaloric effects were still small<sup>[9]</sup>.

Recently, in our laboratory a magnetic nanocomposite of Gd magnetic clusters<sup>[26]</sup> in a garnet structure was prepared using a metal-organo complex process. Specifically, this type of magnetic nanocomposite was created by complexing the mixed nitrates of Gd and Fe with an excess of tartaric acid in water solution. The solvent was thermally removed ( $T \approx 300^\circ\text{C}$ ) and the nanocomposite was formed by treating the resultant precursors in air at  $950^\circ\text{C}$ . This process has the advantage that large amounts of material (in excess of several cubic centimeters) may be prepared relatively easily. This magnetic nanocomposite, however, is different from the ones previously examined (and described above) in the sense that it is a single crystallographic phase rather than a mixture of structurally different phases. The overall crystal structure of the nanocomposite was confirmed by x-ray diffraction to be that of a garnet, similar to the crystal structure of gadolinium gallium garnet (GGG), and with a stoichiometry of Gd<sub>3</sub>Ga<sub>5-x</sub>Fe<sub>x</sub>O<sub>12</sub> ( $x < 5$ ). In this nanocomposite, Fe atoms have substituted for Ga atoms in the lattice of GGG (Gd<sub>3</sub>Ga<sub>5</sub>O<sub>12</sub>). Concurrently, the field dependence of the magnetization for the Fe-doped

garnets (for  $x < 5$ ) near 20 K lost its linearity, indicating the loss of paramagnetism. Analysis of the magnetization of the  $\text{Gd}_3\text{Ga}_{5-x}\text{Fe}_x\text{O}_{12}$  ( $x < 5$ ) materials showed the paramagnetic state of GGG had been changed by the Fe addition to that indicative of small magnetic clusters in a non-magnetic or weakly magnetic matrix (earlier referred to as superparamagnetism). The iron-doped gadolinium gallium garnet (GGIG) is, therefore, comprised of at least two magnetically different regions (or phases) even though crystallographically it is only a single phase. It is believed that the superparamagnetic state formed in the GGIG nanocomposite is a consequence of the onset of ferromagnetic interactions between those Gd atoms which are near neighbors to the Fe atoms. This Gd-Gd interaction (absent in GGG) is possibly a magnetic superexchange-type interaction

via the Fe atom, as has been observed to occur between transition metal atoms in some transition metal alloys<sup>[27]</sup>. A schematic of the structure of the gadolinium gallium iron garnet magnetic nanocomposite is shown in figure 3. In this figure the magnetic clusters are pictorially represented by the atoms enclosed in the areas bounded by the dashed lines, and inside these areas the spins of the Gd atoms are aligned. The intermediate regions contain non-interacting (non-aligned) paramagnetic Gd atoms. This picture (which does not properly reflect the crystal symmetry) was drawn only for visualizing the correspondence between atomic position and magnetic state possessed by the various Gd atoms in this novel magnetic nanocomposite. Note, that in this type of nanocomposite, there is no dilution of magnetic material required for creating superparamagnetic behavior. Consequently, there is no loss in total magnetic-spin entropy, a problem with nanocomposites like the Fe+silica gel material where non-magnetic silica must be added to break up the Fe into small regions.

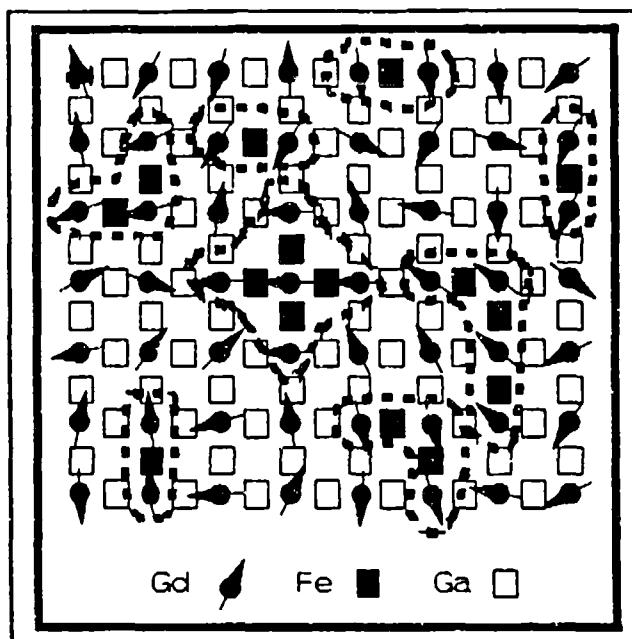


Figure 3. Schematic of the  $\text{Gd}_3\text{Ga}_{5-x}\text{Fe}_x\text{O}_{12}$  magnetic nanocomposite structure showing atomic positions, spin directions (via arrows) of the Gd atoms and the locations of magnetic clusters (dashed lines).

As an experimental test of the above predictions for enhanced magnetocaloric effects in magnetic nanocomposites, the magnetization as a function of  $H$  and  $T$  were measured for several  $\text{Gd}_3\text{Ga}_{5-x}\text{Fe}_x\text{O}_{12}$  (GGIG) samples with  $x < 5$  up to a field of 800 kA/m (1 tesla) between 4.2 K and 100 K. Calculation of the entropy change,  $\Delta S$ , for these materials upon a field change of 800 kA/m as a function of temperature was performed according

to the method described in equation 11 and compared to that measured for GGG. The results are shown in figure 4<sup>[10]</sup>. Note that as Fe is substituted for Ga in the nanocomposite,  $\Delta S$  systematically increases as more magnetic clusters are formed, in accordance with the  $\Delta S$ -enhancement predictions of equation 7. Maximum enhancements occur when half the Ga atoms are substituted by Fe. Further Fe addition was found to result in a decrease in the  $\Delta S$  enhancements over GGG. The optimal  $\Delta S$  enhancement behavior would be expected according to the predictions of equation 7, if the optimal cluster size for this field and temperature range is attained at the  $x=2.5$  composition. We argue that this proof of the earlier theoretical predictions should be used as motivation for an accelerated effort in the development of magnetic nanocomposite refrigerants. Furthermore, note from figure 4 that when half the Ga atoms are replaced by Fe atoms ( $x=2.5$ ),  $\Delta S$  was enhanced over that for GGG at all temperatures greater than 7 K. At 15 K, the GGIG nanocomposite possessed a  $\Delta S$  value at 800 kA/m (1 tesla) 3.4 times larger than that for GGG, the best present magnetic refrigerant at this temperature. At 20 K, the  $x=2.5$  GGIG possessed a  $\Delta S$  value 4.5 times larger than that of GGG. In fact, the  $\text{Gd}_3\text{Ga}_{2.5}\text{Fe}_{2.5}\text{O}_{12}$  nanocomposite possessed a  $\Delta S$  value at temperatures in excess of 70 K that was larger than that possessed by GGG at 15 K, the present maximum refrigeration temperature using GGG. This nanocomposite does not possess a remanent magnetization, and, therefore, no hysteretic losses during field cycling.

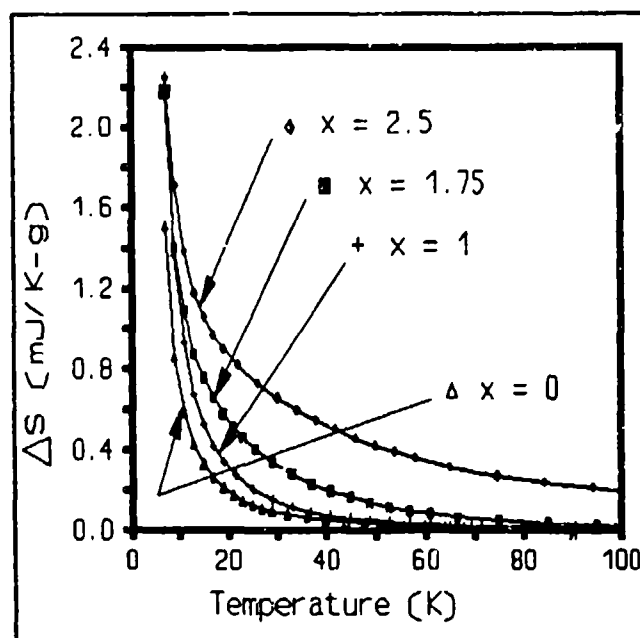


Figure 4. Measured entropy change vs  $T$  for a field change of 800 kA/m for GGG ( $x=0$ ) and the GGIG magnetic nanocomposites containing 1, 1.75, and 2.5 atomic % Fe.

## V. CONCLUSIONS

Magnetic refrigeration, which used to be restricted to  $T < 1$  K in one-shot adiabatic demagnetization refrigerators, is a viable technology at higher temperatures. Paramagnetic refrigerants are restricted to low temperature applications, while ferromagnetic refrigerants and nanocomposite refrigerants hold the promise for high



temperature refrigerators. Previous theoretical predictions for enhanced magnetocaloric effects in superparamagnetic nanocomposites have been substantiated by measurements on a new magnetic nanocomposite,  $\text{Gd}_3\text{Ga}_{3-x}\text{Fe}_x\text{O}_{12}$  ( $x < 5$ ). This nanocomposite even has potential applications as a substitute refrigerant for GGG in the  $7 \text{ K} < T < 20 \text{ K}$  temperature range, and perhaps at temperatures as high as 40 K. It has also been shown that magnetocaloric entropy changes can be calculated from the temperature and magnetic field dependence of the magnetization. This provides a fast method for screening potential magnetic refrigerants.

## VI. REFERENCES

1. "Cluster-Assembled Nanophase Materials", R.W. Siegel, *Annu. Rev. Mater. Sci.* **21** (1991) 559.
2. "Granular Metal Films", B. Abeles, *Appl. Solid State Sci.* **6** (1976) 1;  
"Nanocomposite Magnetic Materials", Shull, R. D. and Bennett, L. H., *J. Nanostructured Materials* **1**, No. 1 (1992) 83.
3. Patent Pending
4. R. D. Shull, L. J. Swartzendruber, and L. H. Bennett, *Proceedings of the Sixth International Cryocoolers Conference* (David Taylor Research Center Publ. #DTRC-91/002, Annapolis, MD, 1991), p. 231.
5. "Numerical Study of Magnetic Refrigeration Including Consideration of Magnetic Nanocomposites", C. Carpentis, *Proceedings of the 18th International Congress of Refrigeration*, Montreal (1991).
6. "Magnetocaloric Effect in Superparamagnets", R.D. McMichael, R.D. Shull, L.J. Swartzendruber, L.H. Bennett, and R.E. Watson, *J. Mag. & Magn. Mat.* **111**, No. 1-2 (1992) 29.
7. "Monte Carlo and Mean Field Calculations of the Magnetocaloric Effect of Ferromagnetically Interacting Clusters", L.H. Bennett, R. McMichael, L.J. Swartzendruber, R.D. Shull, and R.E. Watson, *J. Magnetism & Magnetic Materials* **104-107** (1992) 1094.
8. "The Magnetocaloric Effect: Role of Anisotropy", L.H. Bennett, R.D. McMichael, R.D. Shull, and L.J. Swartzendruber, to be published in the *J. Appl. Phys.* (April, 1993).
9. "Magnetocaloric Effect in Fine Magnetic Particle Systems," R.D. Shull, R.D. McMichael, L.J. Swartzendruber, and L.H. Bennett, Magnetic Properties of Fine Particles, edited by J.L. Dormann and D. Fiorani, Elsevier Publ., Amsterdam, (1992) p. 161.
10. "Enhanced Magnetocaloric Effect in  $\text{Gd}_3\text{Ga}_{3-x}\text{Fe}_x\text{O}_{12}$ ", R.D. McMichael, J.J. Ritter, and R.D. Shull, to be published in the *J. Appl. Phys.* (April, 1993).

11. B. D. Cullity, Introduction to Magnetic Materials (Addison-Wesley Publ. Co., Reading, MA, 1974), p. 94.
12. B. Bleaney, Proc. Roy. Soc. A204, 203 (1950).
13. T. Hashimoto, Advances in Cryogenic Engineering 32, 261 (1986).
14. T. Hashimoto, T. Yazawa, R. Li, T. Kuzuhara, K. Matsumoto, H. Nakagome, M. Takahashi, M. Sahashi, K. Inomata, A. Tomokiyo, and H. Yayama, Advances in Cryogenic Engineering 33, 733 (1988).
15. R. D. Shull, J. J. Ritter, A. J. Shapiro, L. J. Swartzendruber, and L. H. Bennett, Multicomponent Ultrafine Microstructures, MRS Symposium Proceedings 132 (North Holland Pub. Co., N.Y., 1988), p. 179.
16. R. D. Shull and J. J. Ritter, Physical Phenomena in Granular Materials, MRS Symposium Proceedings 195 (North Holland Pub. Co., N.Y., 1990), p. 435.
17. "Mössbauer Studies of Isolated and Interacting Ultrafine Magnetic Particles", S. MØrup, Magnetic Properties of Fine Particles, edited by J.L. Dormann and D. Fiorani, Elsevier Publ., Amsterdam, (1992) p. 125.
18. J. L. Smith, Y. Iwasa, and F. J. Cogswell, Advances in Cryogenic Engineering 35, 1157 (1990).
19. A. J. DeGregoria, Advances in Cryogenic Engineering 37, 867 (1992).
20. J. A. Barclay, Proceedings of the 18th International Congress of Refrigeration, Montreal (1991).
21. T. Hashimoto, M. Ogawa, A. Hayashi, M. Makino, R. Li, and K. Aoki, Advances in Cryogenic Engineering 37, 859 (1992).
22. T. Hashimoto, K. Matsumoto, T. Kurihara, T. Numazawa, A. Tomokiyo, H. Yayama, T. Goto, S. Todo, and M. Sahashi, Advances in Cryogenic Engineering 32, 279 (1986).
23. J. L. Dormann, L. Bessais, and D. Fiorani, J. Phys. C: Solid State Phys. 21, 2015 (1988).
24. J. P. Bilisoly, U.S. Patent No. 2496265 (Feb. 7, 1950).
25. R. D. Shull, U. Atzmony, A. J. Shapiro, L. J. Swartzendruber, L. H. Bennett, W. L. Green, and K. Moorjani, J. Appl. Phys. 63, 4261 (1988).
26. Patent Pending
27. A. Arrott and H. Sato, Phys. Rev. 114, 1420 (1959).

## ENTHALPY FLOW TRANSITION LOSSES IN REGENERATIVE CRYOCOOLERS

PETER KITTEL  
 Technology Development Branch  
 Space Projects Division  
 NASA, Ames Research Center  
 Moffett Field, CA 94035-1000

ABSTRACT

In regenerative cryocoolers, enthalpy flow is characterized by an oscillating temperature within the working fluid. When there are changes in enthalpy flow, the amplitude of the temperature oscillation also changes. This is an irreversible process that generates entropy. Thus, this process is a loss mechanism. Such losses occur at the transition between heat exchangers (isothermal regions) and adiabatic regions.

This paper presents a generalized method of calculating these losses. For a sinusoidal temperature variation, the fractional loss per cycle is

$$(\pi x \cos \phi)^{-1} \int_0^{2\pi} \left\{ \frac{1 + x \sin \theta}{\alpha x + 1} - \ln \left( \frac{1 + x \sin \theta}{\alpha x + 1} \right) - 1 \right\} \sin(\theta - \phi) d\theta$$

where  $x$  is the ratio of the temperature oscillation amplitude to the average temperature,  $\alpha$  is ratio of the change in the mean temperature at the transition to the temperature oscillation amplitude, and  $\phi$  is the phase angle between the mass flow and the temperature oscillation.

Approximate solutions are also developed for cases relevant to pulse tube and Stirling cryocoolers.

INTRODUCTION

Enthalpy flow analysis has become a useful tool in understanding how regenerative cryocoolers work.<sup>1</sup> Finite enthalpy flows occur in adiabatic regions of coolers and in regions with poor heat transfer between the working fluid and the surroundings. Regions with finite enthalpy flow include the pulse tube in pulse tube coolers, the expansion space in Stirling and G-M coolers that are operating too fast for isothermal expansion, and between a valveless compressor and the aftercooler.

Enthalpy flow analysis has mostly been used to analyze the gross cooling power. However this technique may also be used to quantify losses within coolers. This paper discusses a loss that occurs when there is a change in enthalpy flow, in particular, when the enthalpy flow changes

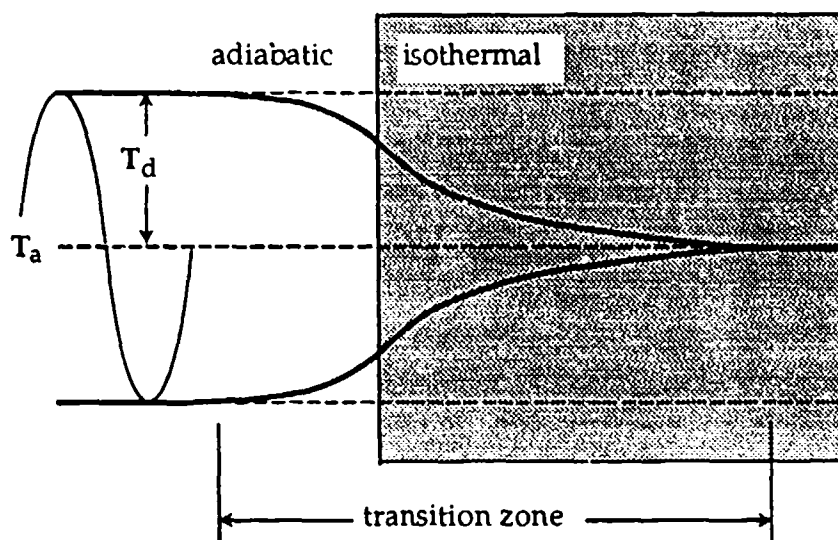


Figure 1. Representation of the change in the amplitude of the temperature oscillation at a transition from a finite enthalpy flow to isothermal flow. The amplitude changes from  $T_d$  to 0. In this example the mean temperature  $T_a$  does not change.

ween a finite value and zero. This is shown pictorially in Figure 1. Such transitions may be found at the junction of heat exchangers and adiabatic sections.

In regions with enthalpy flow the local temperature,  $T$ , and mass flow,  $\dot{m}$ , of the working fluid oscillate. The enthalpy flow per cycle is given by

$$H_d = C_p \int_0^{2\pi/\omega} \dot{m} T \, dt \quad (1)$$

On entering an isothermal section, the enthalpy flow goes to zero, because the amplitude,  $T_d$ , of the temperature oscillation goes to zero. The transition occurs over a finite distance in a transition zone. In this zone gas elements undergo a temperature change from  $T$  to  $T_a$ , the mean temperature. The time it takes for this transition is small compared to the cycle time ( $2\pi/\omega$ ). This is the same as saying that the displacement of a gas element during a cycle is large compared to the length of the transition zone. Thus, we may treat the process as quasi-static. During the time it takes for an element of gas to cross the transition zone,  $\dot{m}$  and the pressure,  $P$ , do not change and  $T$  in the adiabatic section does not change. However, while crossing the transition zone, the temperature of the gas element changes. The temperature change is not caused work being done because, on the time scale of crossing the transition zone,  $P$  and  $\dot{m}$  are constant. Thus, the temperature change is caused by transferring heat to or from the surroundings. The rate heat is transferred by an incremental change in temperature,  $d\tau$ , of the gas element is

$$d\dot{Q} = C_p \dot{m} d\tau \quad (2)$$

(Positive heat flow is from the heat exchanger to the gas.) The total heat transferred by an element of gas is

$$dQ = C_p \dot{m} \left( \int_T^{T_a} d\tau \right) dt \quad (3)$$

The net heat transfer per cycle is found by integrating over one cycle:

$$Q = -C_p \int_0^{2\pi/\omega} \dot{m} (T - T_a) dt = -H_d \quad (4)$$

This is the expected result since for infinitesimal processes  $dH = dQ + V dP$  and  $dP = 0$  for this process.

However the process is not reversible. During the incremental process described above the heat flows across a temperature difference. Thus entropy is produced. The rate entropy changes is

$$d\dot{S} = C_p \left| \dot{m} \left\{ \frac{1}{T_a} - \frac{1}{\tau} \right\} d\tau \right| \quad (5)$$

where  $\tau$  is the instantaneous temperature of an element of gas within the transition zone and the absolute value sign is a reflection of the second law of thermodynamics, that  $dS \geq 0$  for all processes. The entropy change within the transition zone is found by integrating eq. (5) over the complete temperature change:

$$dS = C_p \left| \dot{m} \left( \int_{T_a}^T \left\{ \frac{1}{T_a} - \frac{1}{\tau} \right\} d\tau \right) \right| dt \quad (6)$$

In a more generalized case the mean temperature is different in the two regions. This is depicted in figure 2 where the mean temperature changes from  $T_a$  in the adiabatic region to  $(T_a + T_b)$  in the isothermal region. This situation is representative of the expander in regenerative coolers and of the flow between a compressor and its aftercooler. Equation (6) may be easily rewritten for this situation:

$$dS = C_p \left| \dot{m} \left( \int_{T_a+T_b}^T \left\{ \frac{1}{T_a + T_b} - \frac{1}{\tau} \right\} d\tau \right) \right| dt \quad (7)$$

Similarly eq. (4) may be rewritten as

$$Q = -C_p \int_0^{2\pi/\omega} \dot{m} [T - (T_a + T_b)] dt = -H_d \quad (8)$$

Equation (7) may be integrated over a cycle to yield the entropy produced per cycle:

$$\Delta S = C_p \int_0^{2\pi/\omega} \left| \dot{m} \left( \int_{T_a+T_b}^T \left\{ \frac{1}{T_a + T_b} - \frac{1}{\tau} \right\} d\tau \right) \right| dt \quad (9)$$

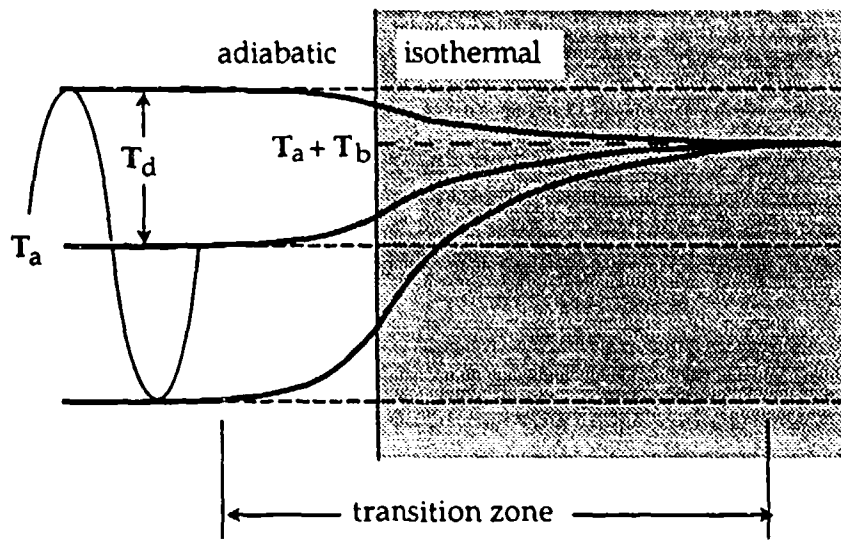


Figure 2. Representation of the change in temperature amplitude at a generalized transition from a finite enthalpy flow to isothermal flow. The amplitude changes from  $T_d$  to 0. The mean temperature changes from  $T_a$  in the adiabatic region to  $(T_a + T_b)$  in the isothermal region.

This entropy is produced by an irreversible process, the flow of heat across a temperature gradient. The enthalpy change during a process can be expressed as  $dH = T dS + V dP$ . Here, there is no pressure loss. Thus, the irreversible entropy reduces the enthalpy flow available for refrigeration. I.e., a portion of the heat transfer, eq. (8), is the result of this entropy production and is not available for cooling an external load. The lost enthalpy is  $T_a \Delta S$ . The fractional enthalpy lost per cycle is

$$\eta = T_a \Delta S / H_d \quad (10)$$

For simplicity we will assume that the temperature and mass flow are sinusoidal:

$$T = T_a + T_d \sin(\omega t) \quad (11)$$

$$\dot{m} = \dot{m}_d \sin(\omega t - \phi) \quad (12)$$

where the subscripts a and d refer to the mean and dynamic components,  $\omega$  is the frequency and  $\phi$  is the phase shift. Substituting eqs. (8), (9), (11), and (12) into eq. (10) and integrating over  $\tau$  results in :

$$\eta = (\pi x \cos \phi)^{-1} \int_0^{2\pi} \left\{ \frac{1 + x \sin \theta}{\alpha x + 1} - \ln \left( \frac{1 + x \sin \theta}{\alpha x + 1} \right) - 1 \right\} \sin(\theta - \phi) d\theta \quad (13)$$

where  $x = T_d / T_a$ ,  $\alpha = T_b / T_d$ , and  $\theta = \omega t$ . The variables  $x$ ,  $\alpha$ , and  $\phi$  are constrained to the following ranges by physical considerations:  $0 \leq x \leq 1$ ,  $-1 \leq \alpha x$ , and  $-\pi/2 < \phi < \pi/2$ .

(The loss, eq. (10), uses  $T_a$  as the reference temperature. This temperature was chosen because it is the mean temperature of the gas and it is the gas that carries the enthalpy flow. However, in cooler analysis it is more common to use the temperature of the isothermal sections,  $(T_a + T_b)$ , as the reference temperature. In this case one can define a loss:  $\eta^* = (T_a + T_b)\Delta S / H_d$  where  $\eta^* = \eta(T_a + T_b) / T_a = \eta(\alpha x + 1)$ . This paper will deal with  $\eta$  rather than  $\eta^*$ .)

### APPROXIMATE SOLUTION

The integrand of eq. (13) is shown in figure 3. This is not a simple function to integrate in closed form. Fortunately, there are ways of approximating it. It is also possible to numerically integrate eq. (13).

A lower limit,  $\eta_l$ , to eq. (13) can be found by making use of the relation:  $\int |I| d\theta \geq |\int I d\theta|$ . These two integrals are equal when  $I$  does not change sign over the range of integration; i.e.,  $I \geq 0$  or  $I \leq 0$  throughout the integration range. Here

$$I = \left\{ \frac{1 + x \sin \theta}{\alpha x + 1} - \ln \left( \frac{1 + x \sin \theta}{\alpha x + 1} \right) - 1 \right\} \sin(\theta - \phi) \quad (14)$$

Thus,

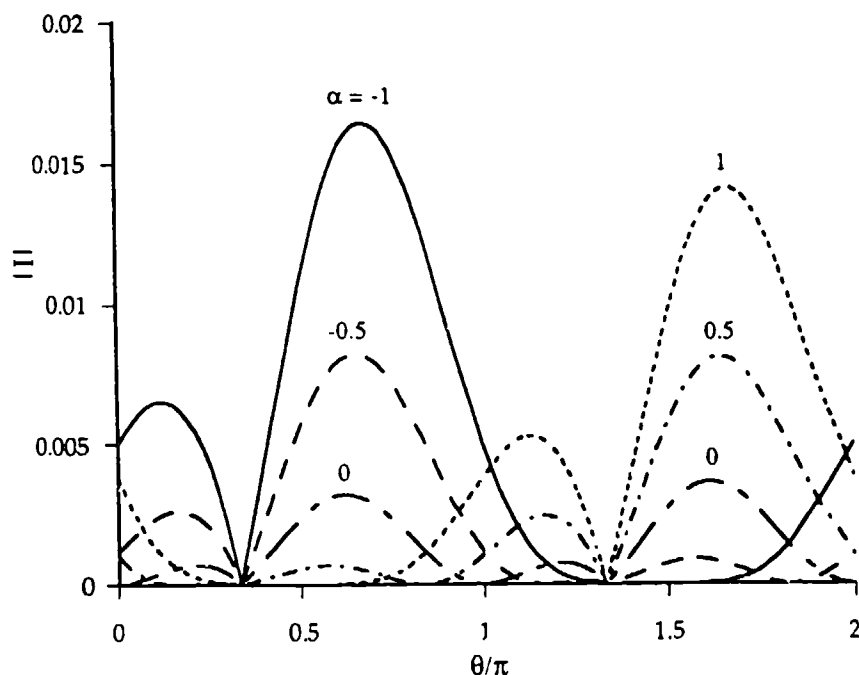


Figure 3. Plot of  $|I(x, \alpha, \theta, \phi)|$ , where  $I$  is given by eq. (14), for  $x = 0.1$ ,  $\phi = \pi/3$ , and five values of  $\alpha$  between -1 and 1.

$$\eta \geq \eta_\ell = (\pi x \cos \phi)^{-1} \left| \int_0^{2\pi} \left\{ \frac{1+x \sin \theta}{\alpha x + 1} - \ln \left( \frac{1+x \sin \theta}{\alpha x + 1} \right) - 1 \right\} \sin(\theta - \phi) d\theta \right| \quad (15)$$

An approximate form of  $\eta_\ell$  can be found by expanding the logarithmic term in eq. (15) as a power series in  $x$  and keeping the lowest order term. This results in

$$\begin{aligned} \eta_\ell &\approx \eta' = |\alpha| x (\alpha x + 1)^{-1} \\ &= |T_b| (T_a + T_b)^{-1} \end{aligned} \quad (16)$$

This approximation is the same as saying that the heat transfer process nominally involves the irreversible transport of heat from  $T_a$  to  $T_a + T_b$ ; which generates entropy:

$S = Q [T_a^{-1} - (T_a + T_b)^{-1}]$ . The same result can be reached by approximating the  $1/\tau$  term in eq. (7) by  $1/T_a$ . However eq. (16) is derived, it is only an approximate lower limit. It does not have the  $\phi$  dependence that is explicitly contained in eq. (13). Nor does it adequately predict the behavior near  $\alpha = 0$ . Equation (7) and, therefore, eq. (13) are clearly not 0 at  $\alpha = 0$ , yet eq. (16) is.

Another approach is to find an approximate closed form solution of eq. (13) in the limit of small  $x$  and  $\alpha$ . The integral in eq. (13) can be written as  $\int |I| d\theta$ . This integral may be rewritten, since  $(\alpha x + 1) \geq 0$ , as  $\int |I| d\theta = (\alpha x + 1)^{-1} \int |J| d\theta$  where

$$J = (\alpha x + 1) I = \left\{ x \sin \theta - \alpha x - (\alpha x + 1) \ln \left( \frac{1 + x \sin \theta}{\alpha x + 1} \right) \right\} \sin(\theta - \phi) \quad (17)$$

This can be expanded in a Taylor series of  $x$ . Keeping the lowest order term results in

$$J \approx \frac{1}{2} (\alpha - \sin \theta)^2 x^2 \sin(\theta - \phi) \quad (18)$$

The function  $|J|$  may be integrated by first dividing it into segments where  $J \geq 0$  or  $J \leq 0$  and then integrating each segment separately. These regions are illustrated in figure 4. The boundaries

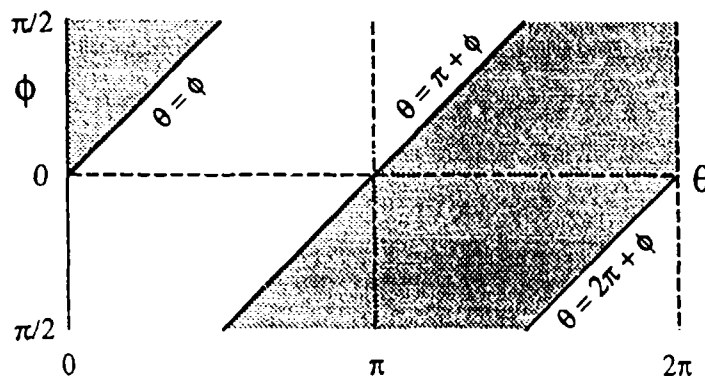


Figure 4. Regions in  $(\theta, \phi)$  space where eq. (18) is positive (unshaded) or negative (shaded).



between the  $J \geq 0$  and  $J \leq 0$  segments only depend on  $\theta$  and  $\phi$ .

Integrating  $|J(x, \alpha, \theta, \phi)|$  over  $\theta$  in this piecewise fashion yields

$$\eta = \eta'' = \left( \frac{1}{3} \cos(2\phi) + 2\alpha^2 + 1 \right) \frac{x}{\pi(\alpha x + 1) \cos \phi} \quad (18)$$

### COMPARISON TO NUMERICAL SOLUTION

It is possible to solve eq. (13) by numerical integration. Figure 5 shows such a solution for  $x = 0.1$ . The solution has a broad central region (where  $\alpha$  and  $\phi$  are small) in which  $\eta$  is slowly varying. At  $(\phi = 0, \alpha = 0)$   $\eta$  has a value of about  $4x/3\pi$  for a loss of about 4.2% when  $x = 0.1$ . Outside of this region,  $\eta$  increases rapidly. Figures 6, 7, and 8 show comparisons between  $\eta$  and the approximations,  $\eta'$  and  $\eta''$ . These comparisons are done around several operating conditions that are representative of conditions that might occur in coolers:  $\phi = 0$ ,  $x = 0.1$ , and  $\alpha = -1, 0$ , and  $1$ .

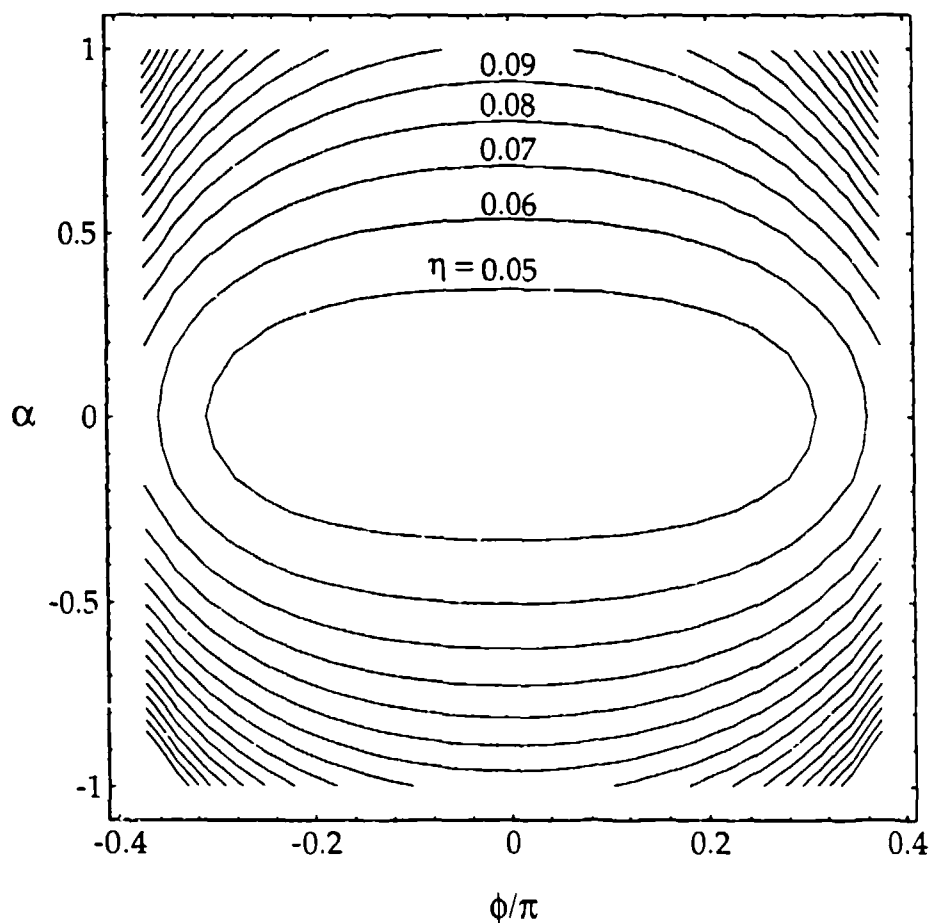


Figure 5. Contours of constant loss,  $\eta$ , in  $(\phi, \alpha)$  space for  $x = 0.1$ . The contours are 0.01 apart.

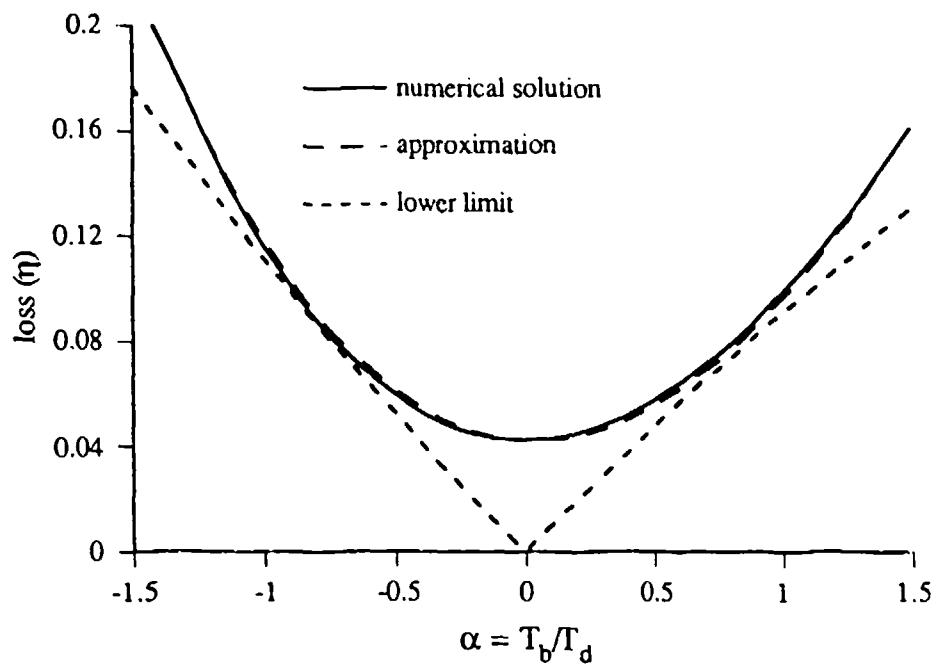


Figure 6. Comparison as a function of  $\alpha$  of the approximate lower limit,  $\eta'$ , and the approximation,  $\eta''$ , with the numerical solution of  $\eta$  for  $x = 0.1$  and  $\phi = 0$ .

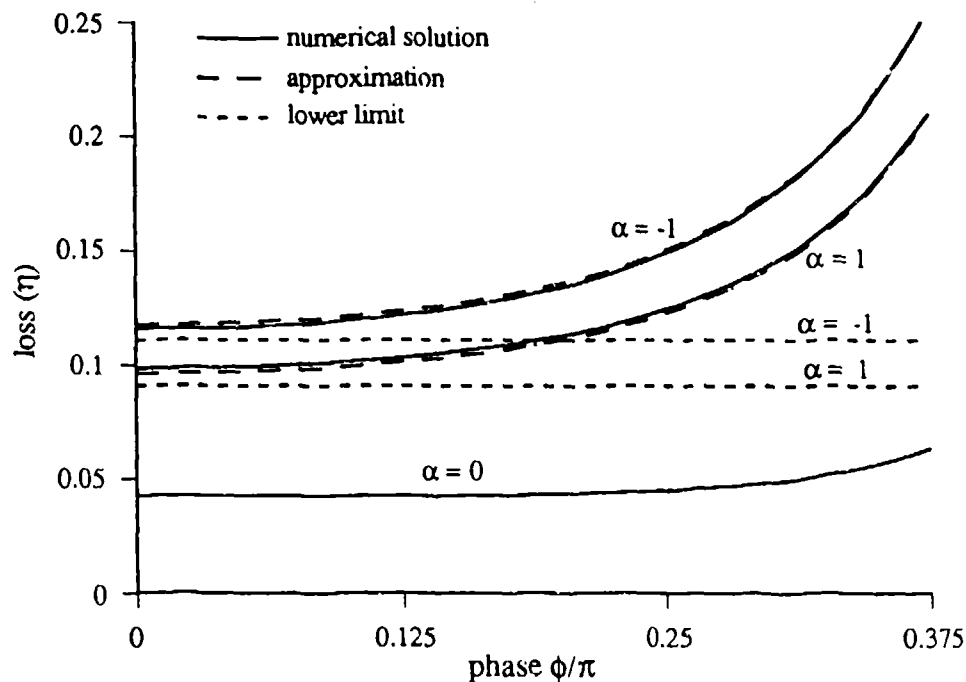


Figure 7. Comparison as a function of phase,  $\phi$ , of the approximate lower limit,  $\eta'$ , and the approximation,  $\eta''$ , with the numerical solution of  $\eta$  for  $x = 0.1$  and  $\alpha = -1, 0$ , and  $1$ . For  $\alpha = 0$ ,  $\eta$  and  $\eta''$  are indistinguishable on this scale and  $\eta' = 0$ .

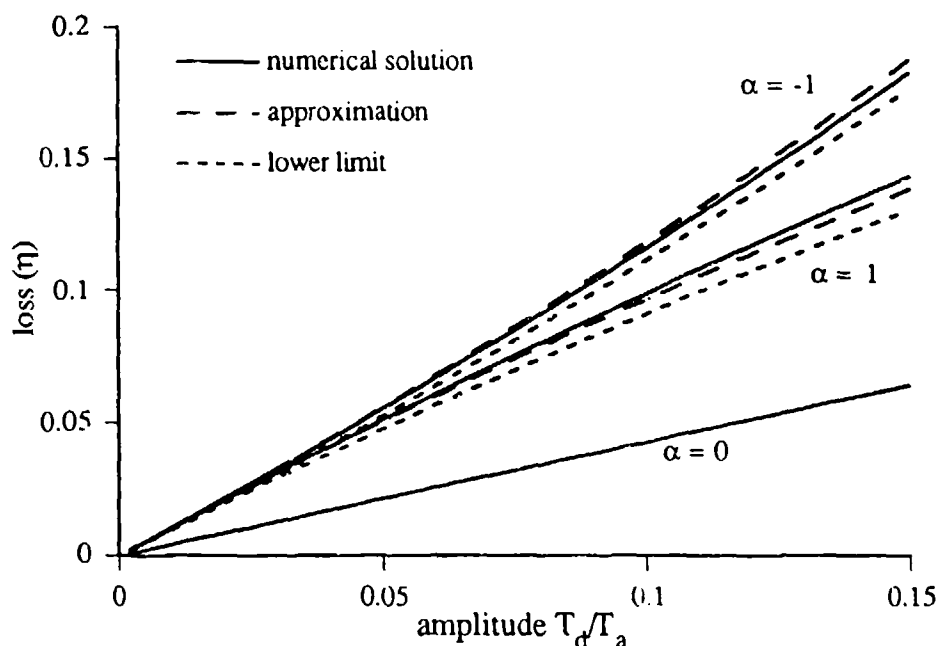


Figure 8. Comparison as a function of amplitude,  $x = T_d/T_a$ , of the approximate lower limit,  $\eta'$ , and the approximation,  $\eta''$ , with the numerical solution of  $\eta$  for  $\phi = 0$  and  $\alpha = -1, 0$ , and  $1$ . For  $\alpha = 0$ ,  $\eta$  and  $\eta''$  are indistinguishable on this scale and  $\eta' = 0$ .

The approximate lower limit,  $\eta'$ , behaves as was expected from the earlier discussion. It is not a good approximation. It does not have a phase dependence nor does it adequately predict the behavior for small  $\alpha$  or for large  $\alpha$ . It is only a good predictor for  $\phi \sim 0$  and  $0.5 \leq |\alpha| \leq 1$ . The approximation  $\eta''$  is a far better predictor. It tracks the  $\phi$  and  $x$  dependence of  $\eta$  over the range of interest. The errors are insignificant.

## DISCUSSION

Table 1 gives values of  $x$  and  $\alpha$  that might be expected for coolers. For hot heat exchangers, the exchanger temperature is near the minimum gas temperature. For cold heat exchangers, the exchanger temperature is near the peak gas temperature. The total loss may be found by combining the individual losses using:  $\eta = 1 - \prod_i (1 - \eta_i)$ . For the case given in Table 1 the overall loss would be 50%. This may be compared to the model of Wang et al.<sup>2</sup> A 50% loss in gross cooling power almost completely accounts for the difference between the calculated and experimental results they present. Such good agreement may be just coincidental. The losses calculated in Table 1 assume sinusoidal waveforms; the real waveforms are not. An integration of eqs. (8) and (9) using the real

Table 1: Typical values

location	x	$\alpha$	$\phi$	$\eta$
compressor/aftercooler	0.1	-1	0	0.12
cold heat exchanger *	0.1	1	0	0.10
hot heat exchanger *	0.1	-1	0	0.12

\* estimated from ref. 2

waveforms would give a different result. Also, the values listed in Table 1 are only rough estimates. The data presented in the table are consistent with the published data but may not adequately describe the process. Furthermore, some of the enthalpy flow losses may be already included in their model. As will be discussed below, the loss at the hot heat exchanger should not be included in the overall loss. Excluding this would reduce the total loss from 30% to 20%.

In an ideal pulse tube, all of the enthalpy flow must be irreversibly dissipated at the hot heat exchanger.<sup>3</sup> The mechanism discussed in this paper can account for part of this dissipation. (Another source of loss at the hot end is the  $V dP$  work done in the orifice.) Since this total dissipation is inherent to pulse tubes, most models probably already account for it. In any case a loss in enthalpy flow at the hot end of a pulse tube does not reduce the cooling power.

The estimate of  $\eta$  found in Table 1 was based on calculated waveforms at the ends of the pulse tube. These waveforms are probably taken from within the transition zone. Therefore Table 1 probably under estimates the loss. To improve on this, we can take a look at the temperature profile in the pulse tube. This profile has been measured for a pulse tube.<sup>1</sup> Estimated parameters based on these measurements are summarized in Table 2

There is a difficulty in using this data in the enthalpy flow loss model. The model assumes that  $T_a$  is constant in the adiabatic region. Yet, in a real pulse tube  $T_a$  has a steep gradient. This is especially true near the hot end. We would like to use temperature estimates that are neither affected by the transition zone nor by this gradient. One method is to use the minimum (or maximum) value of  $T_a$ . This choice reduces the effect of the transition zone. However, since the minimum (or maximum) occurs away from the end, the estimate is still affected by the gradient. This results in underestimating  $\eta$ . Another choice is to extrapolate  $T_a$  from the central region near the minimum (or maximum) to the ends of the pulse tube. Both of these methods are used in Table 2.

Table 2: Pulse Tube Performance Parameters ‡

position	$T_d$	$T_a$	$T_a + T_b$	$\eta$
cold end *	10 K	185 K	200 K	0.09
†	9.7 K	180 K	200 K	0.15
hot end §	30 K	360 K	300 K	0.31
†	33-35 K	400-425 K	300 K	0.75-1.11

‡ estimated from ref. 1

\* using minimum reported  $T_a$ § using maximum reported  $T_a$ †  $T_a$  estimated by extrapolating to end of pulse tube $T_d$  estimated by assuming  $T_d/T_a$  is same for both cases

The two methods give about the same result ( $\eta \sim 12\%$ ) for the cold end loss. This loss is similar to the one found in Table 1.

The hot end loss is quite different. Using the extrapolated data, the loss is  $\sim 90\%$ . Thus, this accounts for a substantial portion of the required dissipation. It also accounts for the large overshoot of the gas temperature above the hot end heat exchanger, a trait of pulse tubes. Again, this good agreement between calculated and expected loss may just be fortuitous. At the hot end of a pulse tube the mass flow is small. Only a small fraction of the mass flow through at the regenerator makes it through the orifice at the hot end. The assumption that the time to cross the transition zone is  $\ll 2\pi/\omega$  is questionable. A gas element may not even traverse the transition zone at the hot end. It may only move through part of the zone during a cycle. Thus, some of the temperature change may due to changes in  $\dot{m}$  and  $P$ . Such changes are reversible and do not increase the entropy. Therefore, the loss calculated here is an upper limit for the mechanism discussed in this paper.

## SUMMARY

A method of calculating the losses caused by transitions in enthalpy flow has been developed in the convective limit. In this limit, the time an element of gas takes to cross the transition zone is  $\ll 2\pi/\omega$ . Equivalently, the displacement of a gas element during a cycle is  $\gg$  the length of the transition zone. Since, these conditions are not always met in a real cooler, the loss presented here

is an upper limit of the real loss from this mechanism. Additional losses from other mechanisms may also be present.

The losses caused by transitions in enthalpy flow are significant. Losses ~10% are typical for aftercoolers and cold heat exchangers in regenerative cryocoolers. Even greater losses can be expected at the hot end of the pulse tube where this transition loss accounts for a large part of the heat rejected. While the examples used here were for pulse tubes, other regenerative coolers have similar values of  $x$  and  $\alpha$  at their cold heat exchangers and in their compressors. Thus, they should have similar losses. For real coolers there is likely to be a significant deviation from these calculated results which comes from the real waveforms not being sinusoidal.<sup>1,2</sup>

## REFERENCES

1. P. J. Storch and R. Radebaugh, "Development and Experimental Test of an Analytic Model of the Orifice Pulse Tube Refrigerator," *Adv. Cryo. Engin.* **33** (1988) 851.
2. C. Wang, P. Wu, and Z. Chen, "Numerical Modeling of an Orifice Pulse Tube Refrigerator," *Cryogenics*, **32** (1992) 785.
3. P. Kittel, "Ideal Orifice Pulse Tube Refrigerator Performance," *Cryogenics*, **32** (1992) 843.

NEODYMIUM REGENERATOR TEST RESULTS IN A STANDARD  
GIFFORD-McMAHON REFRIGERATOR

James Chafe and Geoffrey Green  
NSWC / Carderock Division  
Annapolis, MD 21402

Richard C. Riedy  
Balzers  
Hudson, NH

**ABSTRACT**

This paper discusses modifications in the regenerators of a Gifford-McMahon cycle refrigerator and their effects on the cooling performance. This work has been undertaken to satisfy the United States Navy's need for a rugged and reliable low temperature (4 to 5 K) cryogenic refrigerator which would be used for superconductive electric drive ship-propulsion. This paper discusses the modification and operating performance of a regenerator in a commercially available Gifford-McMahon refrigerator. The regenerator was modified using neodymium and lead spheres. Test results show that the refrigerator will produce 0.5W of cooling power at 4.2K.

**INTRODUCTION**

The work reported in this paper is sponsored by the Office of Naval Technologies (ONT). It is part of an ongoing research and development effort focused on a superconductive electric drive propulsion system for Naval surface ships. A cryogenic refrigerator is needed to provide cooling to superconducting magnets used in motor and generators for Naval ships.

A superconducting propulsion system which can withstand the demands of long sea voyages and combat conditions requires an extremely rugged and reliable cryogenic refrigeration system. The Gifford-McMahon (G-M) cycle refrigerator is a possible candidate for such a refrigeration system because of its relative small size, simplicity, good reliability and ruggedness. A description of the G-M cycle refrigerator and its theory of operation is provided by Walker <sup>1</sup>.

In the recent past, some researchers have had some measure of success in modifying G-M cycle refrigerators so they can reach temperatures below 4.2 K.<sup>2,3</sup> This was done by using  $\text{Er}_3\text{Ni}$  in place of lead (Pb) in the low temperature stages of the refrigerators. The improved performance is attributed to the fact that  $\text{Er}_3\text{Ni}$  has a considerably higher heat capacity than lead at temperatures below 10 K. Figure 1 illustrates this fact. These low temperatures are important to the U.S. Naval superconducting propulsion program because they allow the use of conventional superconducting wire (i.e. NbTi) as opposed to more experimental superconductors such as  $\text{Nb}_3\text{Sn}$ .

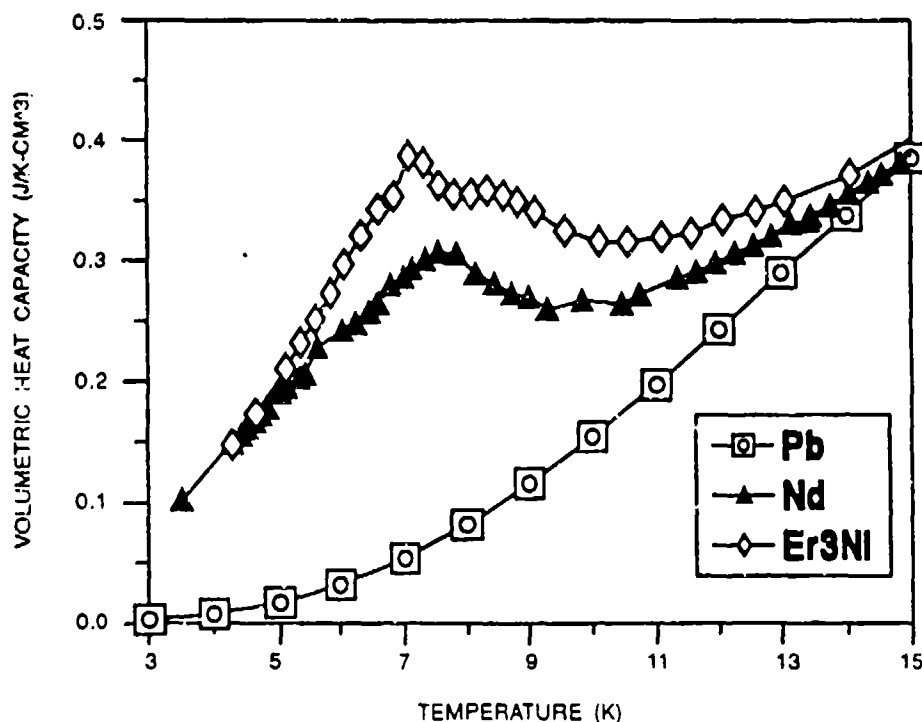


Fig 1 Volumetric heat capacities of Pb, Nd and  $\text{Er}_3\text{Ni}$ .<sup>4,5,6</sup>

The poor mechanical properties of  $\text{Er}_3\text{Ni}$  make it of limited usefulness to the U.S. Navy due to their requirements of shock and vibration tolerance and high reliability.  $\text{Er}_3\text{Ni}$  exhibits a very brittle nature which causes the material to fracture and eventually break down to a point



where it might damage the refrigerator. In addition, this material has proven to be rather difficult to form into the spherical powder most often used for low temperature regenerators. Most of the powders produced are irregularly shaped and the spheres were often found to be hollow. Most likely with some development work, this manufacturing problem could be solved.

This study looks at using neodymium (Nd) as a substitute for  $\text{Er}_3\text{Ni}$ . Neodymium is a pure rare-earth metal which has good ductility (thus it is not fracture prone) and a commercial process is available to form the material into spheres. Neodymium also shows high heat capacity at temperatures below 10 K (fig. 1), although not quite as high as  $\text{Er}_3\text{Ni}$ .

## **APPARATUS**

A standard cryogenic refrigeration system was used in this research. The system was a KelCool™ Model UCH 130 Cryogenic Helium Refrigerator manufactured by Balzers, of Hudson NH. Modifications of the refrigerator were primarily limited to altering the matrix materials used in the regenerators.

A radiation shield was placed in thermal contact with the first stage cooling station to provide shielding for the second stage. The instrumentation used consisted primarily of diodes used for temperature measurements.

### **REFRIGERATOR**

The KelCool™ Model UCH 130 is a two stage Gifford-McMahon cycle refrigerator. Both stages of this device have their regenerators located within their respective displacers. This is in contrast to some designs which have stationary regenerators and separate moving displacers<sup>7</sup>. Figure 2 is a sketch of the apparatus and fig. 3 is a photograph of the actual device. Its overall length is about two feet (0.6 m) and it weighs about 31 lb. (14 kg).

The displacers of this refrigerator are driven by a scotch-yoke mechanism which is in turn driven by a stepper motor. The refrigerator normally operates at 144 cycles per minute (cpm). However, the supplied control circuitry is capable of providing some variation in speed. The available speeds are 56, 72, 82, 96, 115, and 144 cpm. Additional circuitry could provide an even wider range of speeds. The helium compressor used with the UCH 130 is a 5 hp scroll type unit. The complete compressor module, including the drive motor control circuitry, nominally consumes 6.5 kW of power and pumps gas from a low pressure of about 60 psig to a high pressure of around 300 psig. A surge volume was added to the low pressure side of the compressor.

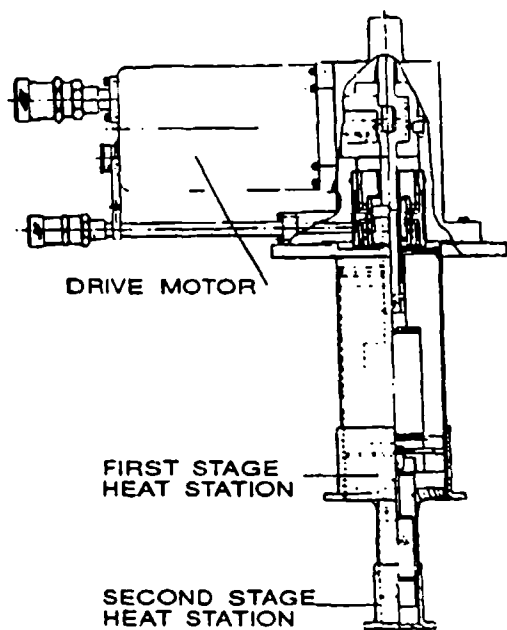


Fig 2. Sketch of the UCH 130

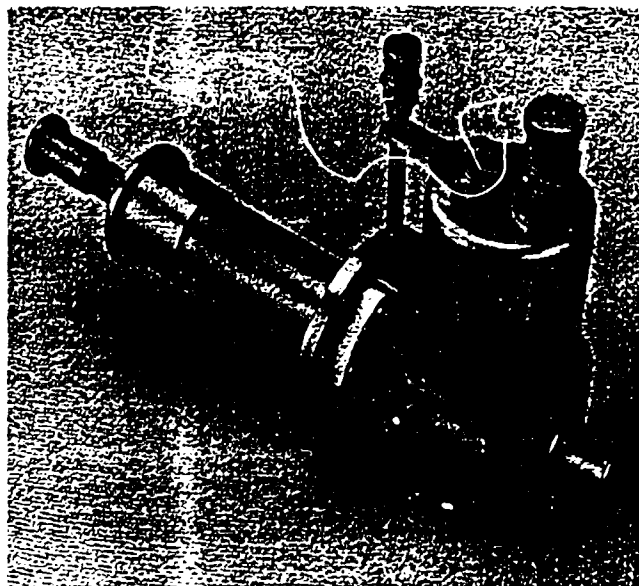


Fig 3. Photograph of the UCH 130

A standard UCH 130 achieves a nominal no load temperature of 6.5K. With no load on the first stage, it can produce 2.5 watts below 8 K and 5 watts below 10 K. Figure 4 is a load map for the standard UCH 130<sup>8</sup>.

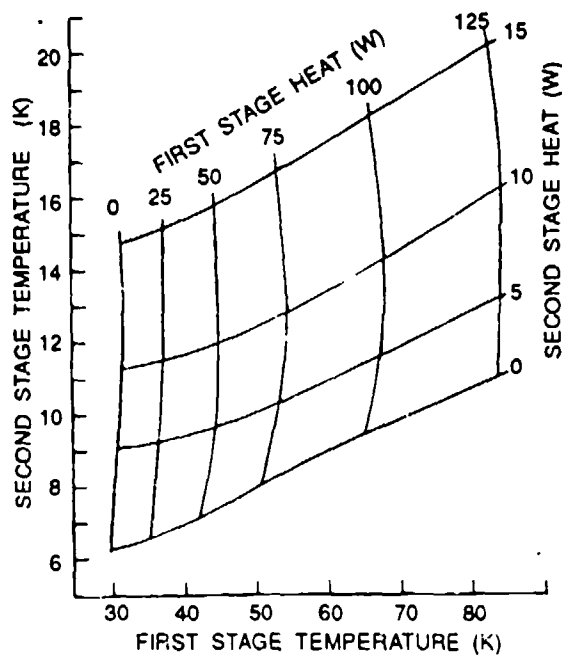


Fig. 4 Load map for the standard UCH 130.

## REGENERATOR

In addition to varying the speed of the drive motor and adding a surge volume to the compressor system, the only other changes made to the refrigerator were the alterations to the matrix material in the regenerators. The standard first stage regenerator uses a stack of phosphorus bronze screens. We constructed a modified first stage regenerator by substituting lead shot (110 g of spherical powder, 0.010 in. diameter) for a portion of the bronze screen stack. By doing this we felt the first stage would be able to achieve lower temperatures and produce more cooling power. We then constructed a modified second stage regenerator. The standard second stage regenerator only uses lead shot in the second stage. The modified regenerator uses approximately 50 % by volume lead spheres (0.010 in. diameter, approximately 100g) and 50 % neodymium spheres (0.006 to 0.009 in. diameter, approximately 50 g).

Both the modified regenerators were constructed with standard displacer/regenerator tubes and used the standard seal design. Thus the only changes made were the substitutions of the different materials into the regenerators.

## RESULTS

First, the refrigerator was operated with the modified first stage regenerator and the standard second stage regenerator. The no-load performance with this configuration is shown in fig. 5. This figure demonstrates that there was a 3 to 4 K decrease in the temperature of the first stage heat station. Although it is not shown in the figure, there was no significant change in the performance of the second stage.

Then tests were performed using both the modified first stage regenerator and the modified second stage regenerator. The no-load performance of this configuration is shown in fig. 6. As can be seen, the neodymium/lead regenerator produced temperatures dramatically lower than the standard 6.5 K (i.e. 3.1 K at the minimum drive motor speed of 56 cpm). The shape of the curve in fig. 6 indicates that a lower temperature might be possible if the speed of the motor was reduced even further.

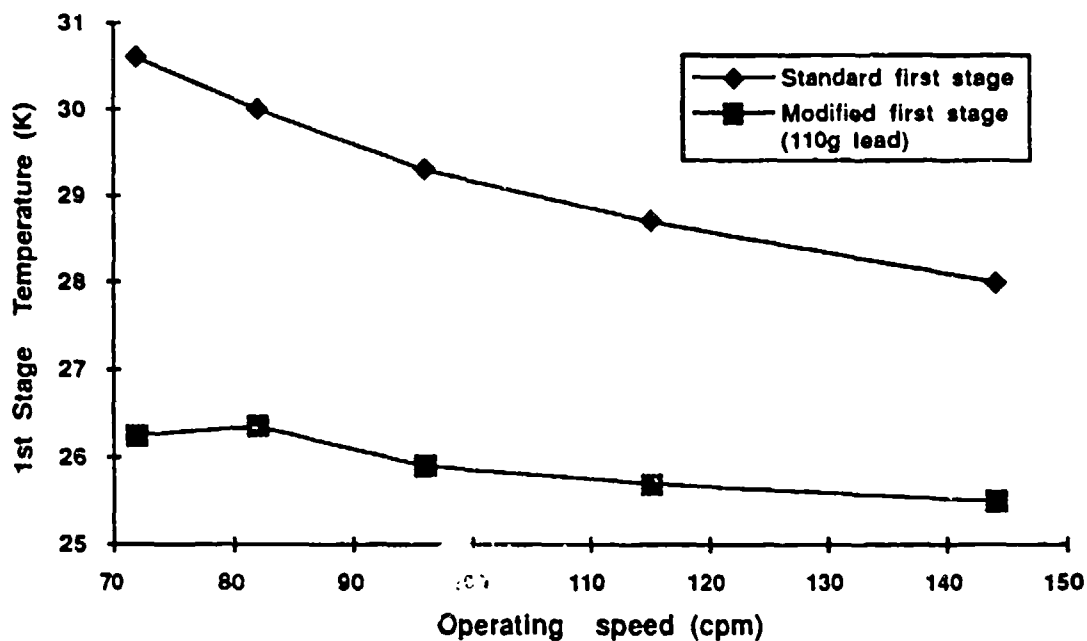


Fig 5. First stage no-load performance of the UCH 130 with standard and modified first stage regenerators.

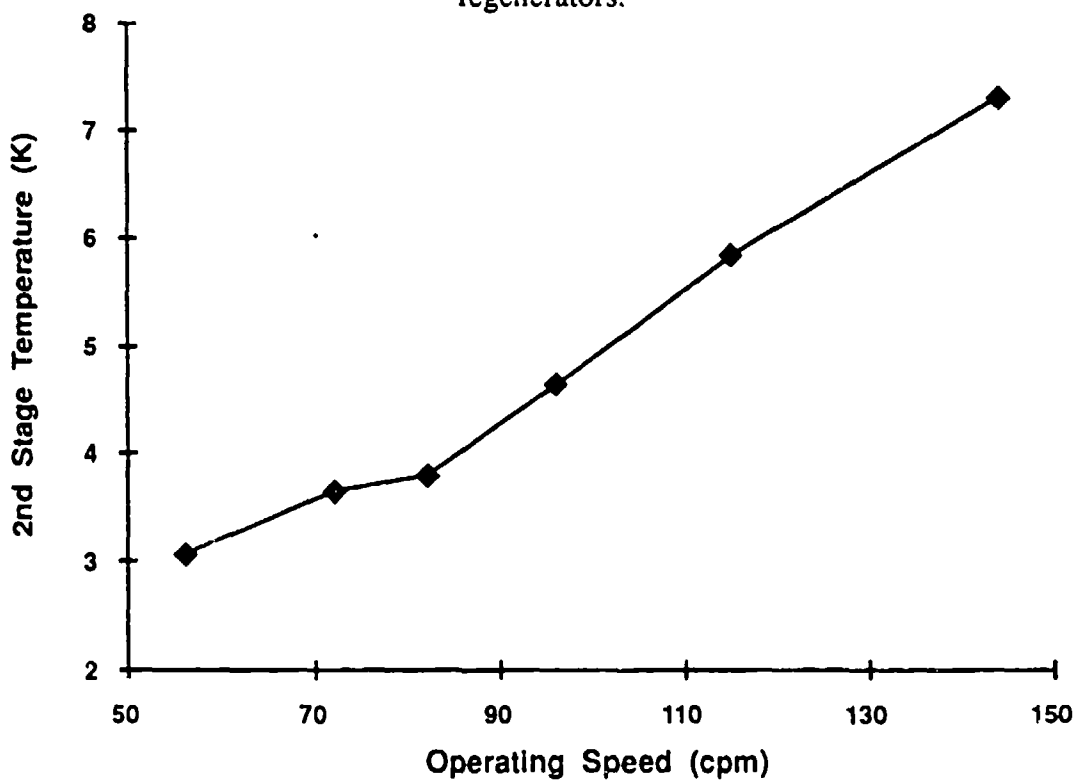


Fig. 6. Second stage no-load performance of the UCH 130 with the modified second stage regenerator.

Figure 7 compares the performance of the all lead regenerator to that of the neodymium/lead regenerator while under heat load. The second stage regenerator produced 0.5 W at 4.2 K and 5 W at 8 K. This is in comparison to a no-load temperature of 6.5 K and 2.5 W capacity at 8 K for the all lead regenerator.

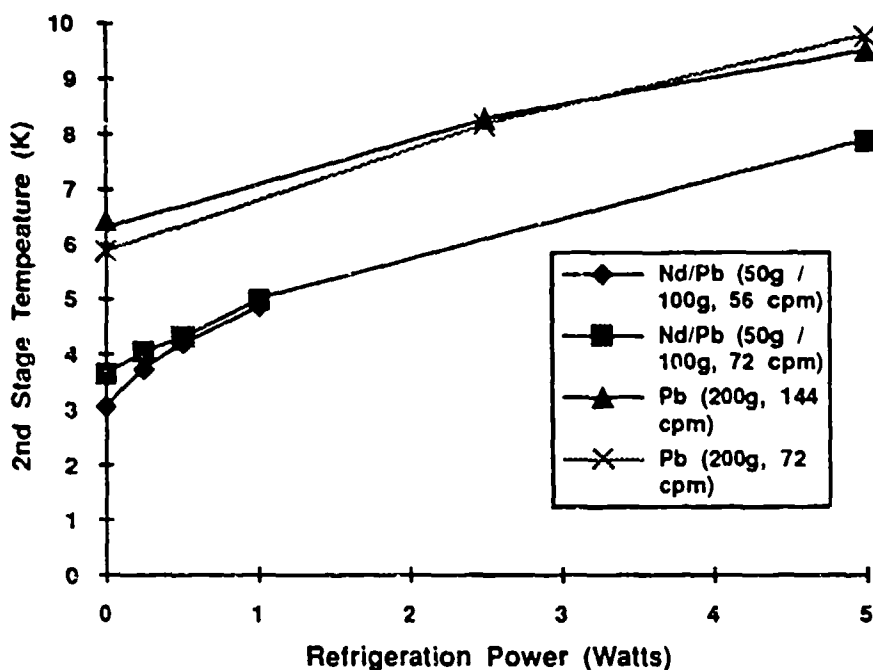


Fig. 7. Performance under heat load of the UCH 130 with the standard and modified second stage regenerators.

## CONCLUSIONS

The results of this work indicate that useful refrigeration may be obtained from a G-M refrigerator by using the high heat capacity material neodymium. By simply modifying the regenerator with 50 g of this matrix material in the second stage, the otherwise standard refrigerator was capable of producing 0.5 W of cooling power at 4.2 K.

While this kind of improvement has been demonstrated with  $\text{Er}_3\text{Ni}$ , neodymium has some advantages. First the mechanical properties of neodymium should allow for a much more rugged and reliable regenerator. Second, due to the fact that a well developed and understood commercial manufacturing process which yields a high percentage of useful spheres is available for neodymium, the overall cost to produce it is much lower than  $\text{Er}_3\text{Ni}$ .

As other researchers have found the optimum performance for high heat capacity low temperature regenerators is achieved at speeds lower than those used for standard regenerators. The exact reason why the slower speeds help improve performance is not fully understood and needs to be further investigated. Cold seal development also needs to be addressed in the future. Other regenerator configurations which would provide a more rugged and reliable system also need to be explored. Once these issues have been addressed, the development of a shipboard, 1 to 2 W, 4.2 K G-M refrigerator should be possible.

## References

- <sup>1</sup>G. Walker, "Cryocoolers, Part I: Fundamentals" Plenum Publishing Corp., New York (1983). pp. 245-261.
- <sup>2</sup>I. Kuriyama et al., Two-Stage GM Refrigerator with Er<sub>3</sub>Ni Regenerator for Helium Liquefaction, in : "Proceedings of the sixth International Cryocoolers Conference, Vol. II", Report # DTRC-91/002, David Taylor Research Center , Bethesda MD (1991), pg. 3.
- <sup>3</sup>T. Inaguchi et al, Two-Stage Gifford -McMahon cycle Cryocooler Operating at about 2 K, in: "Proceedings of the Sixth International Cryocoolers Conference, Vol. II", Report # DTRC-91/002, David Taylor Research Center, Bethesda MD (1991), pg. 25.
- <sup>4</sup>M. Sahashi et al, New Magnetic Material R<sub>3</sub>T System with Extremely Large Heat Capacities Used as Heat Regenerators, in: "Advances in Cryogenic Engineering", Vol. 35, Part B, Plenum Press, New York, (1989), pg. 1175.
- <sup>5</sup>C.B. Zimm et al, The Magnetocaloric Effect in Neodymium, in : "Advances in Cryogenic Engineering", Vol. 36, Part A, Plenum Press, New York, (1989), pg. 763.
- <sup>6</sup>R.J. Corruccini and J.J. Gniewek, "Specific Heats and Enthalpies of Technical Solids at Low Temperatures", NBS Monograph 21, (1960), p. 9.
- <sup>7</sup>J Chafe, G. Green, and P. Gifford, The Low Temperature Performance of a Three Stage Gifford-McMahon Cryocooler, in: "Advances in Cryogenic Engineering", Vol. 37, Part B, Plenum Press, New York, (1991), pg. 1011.
- <sup>8</sup>Operating Instructions for the KelCool™ model # UCH 130 Cryogenic Helium Refrigerator, Balzers, Hudson, New Hampshire, (1991), pg. 6

## SOLVAY REFRIGERATOR OPERATING AT HELIUM TEMPERATURES

Guobang Chen, Jianyao Zheng, Fagao Zhang, Jianping Yu, & Tao Sun  
Cryogenics Laboratory  
Zhejiang University, Hangzhou 310027, China

## ABSTRACT

The thermodynamic foundation of cryocoolers operating in liquid helium temperature region is described. Experimental results of a two-stage Solvay refrigerator utilizing magnetic rare-earth regenerative material are presented. The thermodynamic behavior of cryocoolers working at liquid helium temperature and the approach to improve the actual refrigerating capacity of a liquid helium refrigerator have been discussed.

## INTRODUCTION

In recent years, great advancement has been obtained to improve the efficiency of regenerative cryocoolers by using magnetic regenerative matrix with high magnetic entropy at low temperatures. The lowest refrigerating temperature of 2.4 K of a two-stage cryocooler has been reached, and a refrigerating capacity of 0.8 W at 4.2 K has been gained[1~3]. However, these experimental results are mostly obtained with mechanically driven G-M refrigerators, any tests using a cryocooler other than G-M type in this aspect have not been reported up to date. We have recently made some performance-improving tests with a two-stage Solvay refrigerator operating pneumatically and utilizing rare-earth compound  $\text{Er}_2\text{Ni}$  instead of lead(Pb) as the 2nd stage regenerative material. As a result, the no-load temperature of the 2nd stage is reduced below 4.2K from the original 11.5K.

## THERMODYNAMIC FOUNDATION

The importance of a regenerative cryocooler working with the aid of a regenerator should be that the regenerator matrix has a large specific heat and a suitable heat conductivity at the working temperatures. The specific heat of the matrix is always much larger than that of the working fluid. Once the heat capacity of the solid decreases to an extent closing to that of the working fluid, the regenerator becomes inefficient.

The temperature limitation of 6~8 K has not been broken through for a long time by using any commercial cryocoolers with Pb matrix due to the inefficiency of the regenerator at low temperatures. From thermodynamics phase diagram, the entropy of higher pressure helium is always less than that of the lower pressure one as long

as the temperature is higher than the  $\lambda$  point temperature, so a temperature decrement is always gained when the working fluid is expanding isentropically from a high pressure to a low one. Fig. 1(a) gives the phase diagram of helium in supercritical region, while Fig. 1(b) gives the theoretical temperature decrement

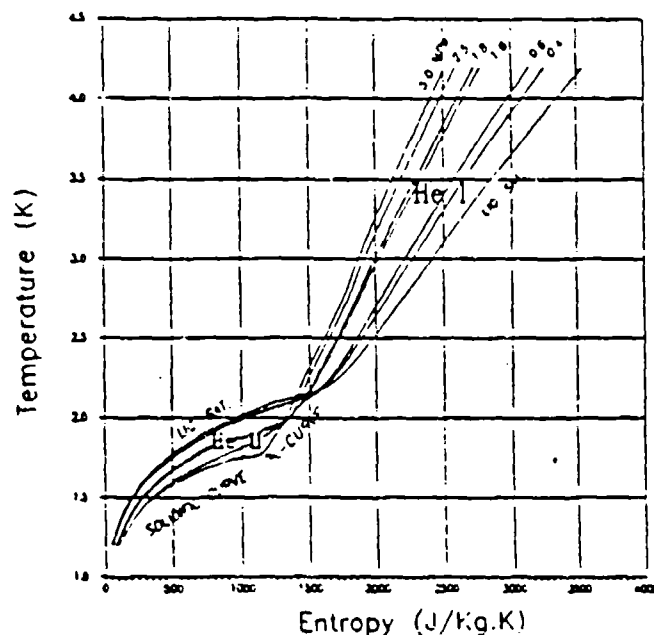


Fig.1(a) Phase diagram of helium in supercritical region

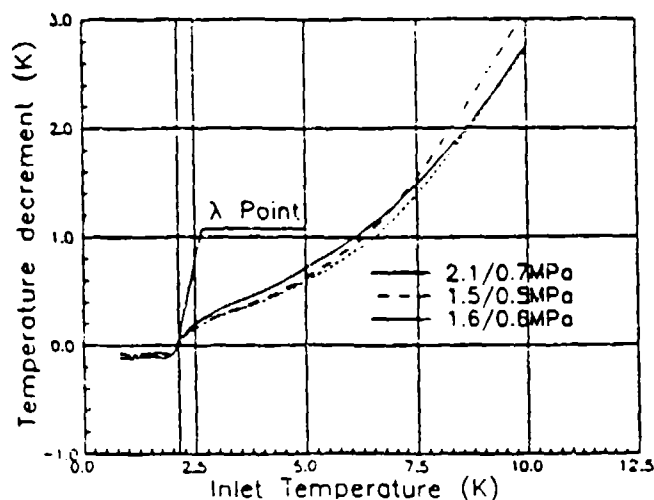


Fig.1(b) Theoretical temperature decrement of isentropical expand of helium in low temperature region



when helium is expanding isentropically in low temperature region. It's clear from Fig. 1 that the theoretical lowest refrigerating temperature of a cryocooler can be reached at 2 K region and is restricted by the  $\lambda$  line. Thus we know that it's possible to decrease the refrigerating temperature of cryocoolers to a temperature below liquid helium temperature (4.2 K).

### SOLVAY REFRIGERATOR

The prototype refrigerators reported that have been used for tests of magnetic regenerative material are all the G-M cycle cryocoolers, whose displacers are driven by a crank and connecting rod mechanism.

The refrigerator adopted in this paper is an improved two-stage Solvay cryocooler operated pneumatically. Fig. 2 shows the structure sketch of the refrigerator which consists of a transmission mechanism, a displacer, a cylinder and a vacuum insulating

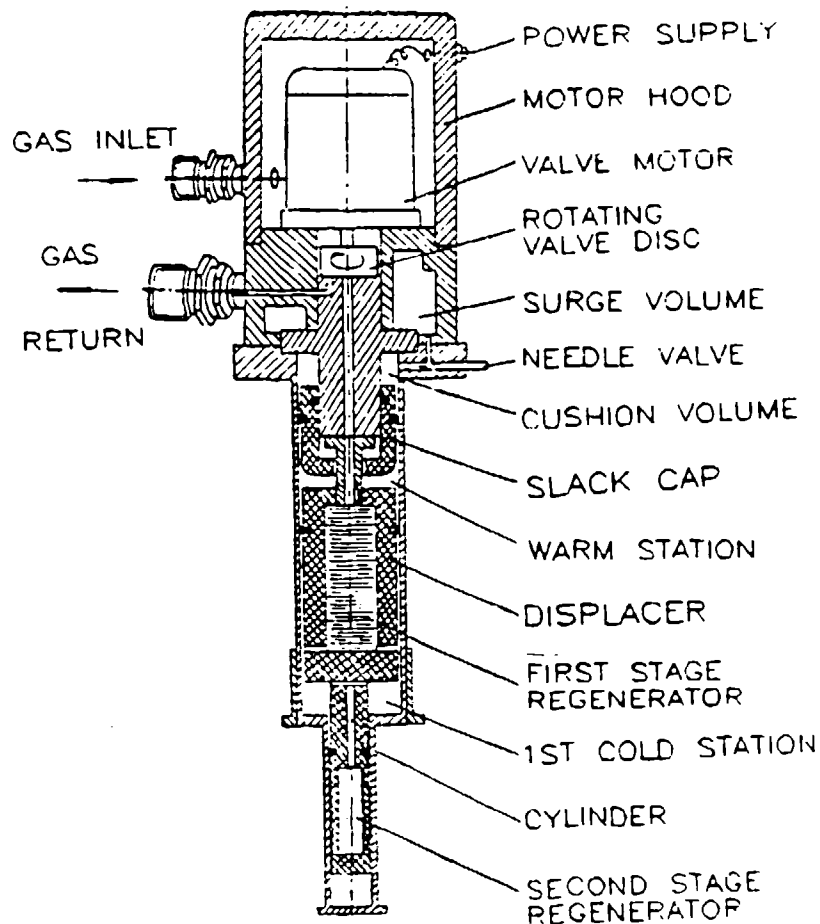


Fig.2 Sketch of a two-stage expander

housing. The transmission mechanism includes a rotating valve disc, a valve motor and a needle valve as well as a surge volume. The valve motor drives the rotating valve disc at a rotating speed of 60 rpm, making the displacer do reciprocating motion in the cylinder at a frequency of 120 cycles/min. The movement of the displacer is controlled by the surge volume and the needle valve.

The 1st regenerator was composed of stainless steel screen disks and the 2nd one was stacked by lead shots. In this case, the temperature of the first stage was about 28 K and the no-load temperature of the 2nd stage reached 11.5 K.

## TEST AND RESULT

$\text{Er}_2\text{Ni}$  was proved in a number of experiments[1~3] to be effective as a cryogenic regenerative material due to its greater specific heat than the traditional matrix Pb. In order to make tests using magnetic matrix  $\text{Er}_2\text{Ni}$ , we made another 2nd stage displacer, the dimension and material of which were the same as those of the original one. The only difference between them was that  $\text{Er}_2\text{Ni}$  grains were used instead of lead shots as the regenerative matrix of the new displacer. The 1st regenerator of the machine was kept unchanged, the matrix of which was still stainless steel screen disks simply.

The charging pressure of the machine was about 1.4 MPa. The intake and exhaust pressures of the compressor after starting were kept at 0.4~0.6 MPa and 1.7~1.8 MPa respectively. The temperature of the 2nd stage reached about 5 K in 90 minutes. Then we decreased down the power supply frequency of the motor gradually from 50 Hz. Finally, the 2nd stage of the refrigerator reached a temperature below 4.2 K at a frequency of 25~30 Hz (about 60~72 rpm) in 15 minutes. Fig. 3 shows the cool down curve of the machine. While reaching equilibrium, the temperature of the 1st stage was 25 K and the 2nd stage reached 2.8 K.

In addition, the effect of operating pressure on the refrigerating temperature has also been tested. The results show that the optimum intake pressure of the refrigerator is 1.8 MPa or so and the corresponding exhaust pressure is about 0.4~0.6 MPa. These values are lower than those reported in[3,4] that the highest pressure is about 2.0~2.2 MPa.

The working fluid helium of the Solvay refrigerator enters the 2nd regenerator at the state of about 1.8 MPa and 30 K (The first stage temperature), then it reaches a temperature of about 3 K (the corresponding pressure is about 0.5 MPa) in the 2nd expanding space. The state of helium has been get into the He I liquid state region. That is the working fluid in the 2nd stage regenerator enters the liquid phase region at the lower temperature end through the supercritical region from the compressed gas region, its working process is shown in Fig. 4. However, it is hardly observed any phenomena on the surveying instruments of the working fluid changing from the gas state to the liquid state, this may be caused by the fact that the density of helium varies continuously from 30 K to 3 K as shown in Fig. 5. The operating performance of the refrigerator is continuous and stable.

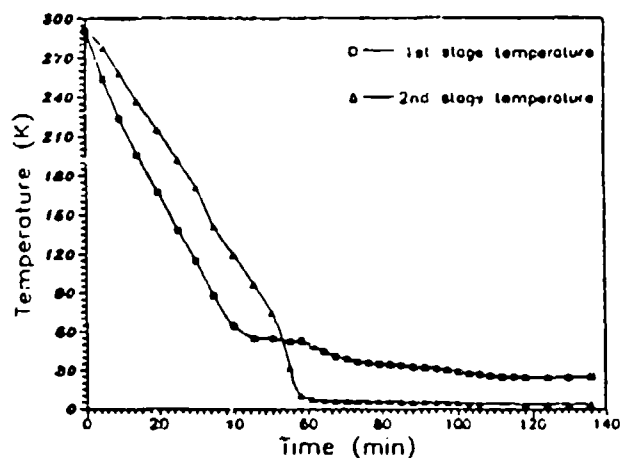


Fig.3 Cool down curve of the two-stage Solvay refrigerator

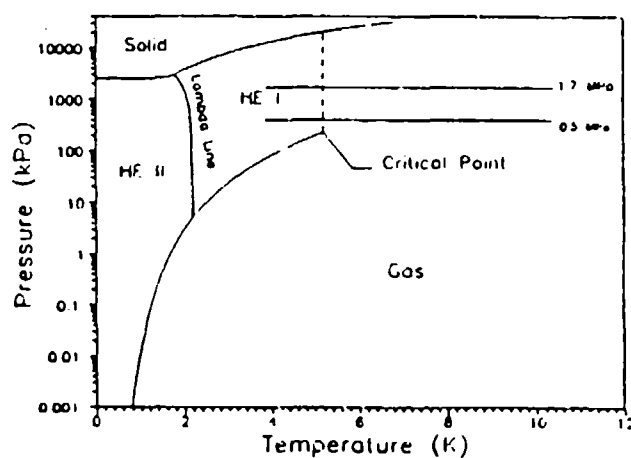


Fig.4 Working processes on P-T diagram

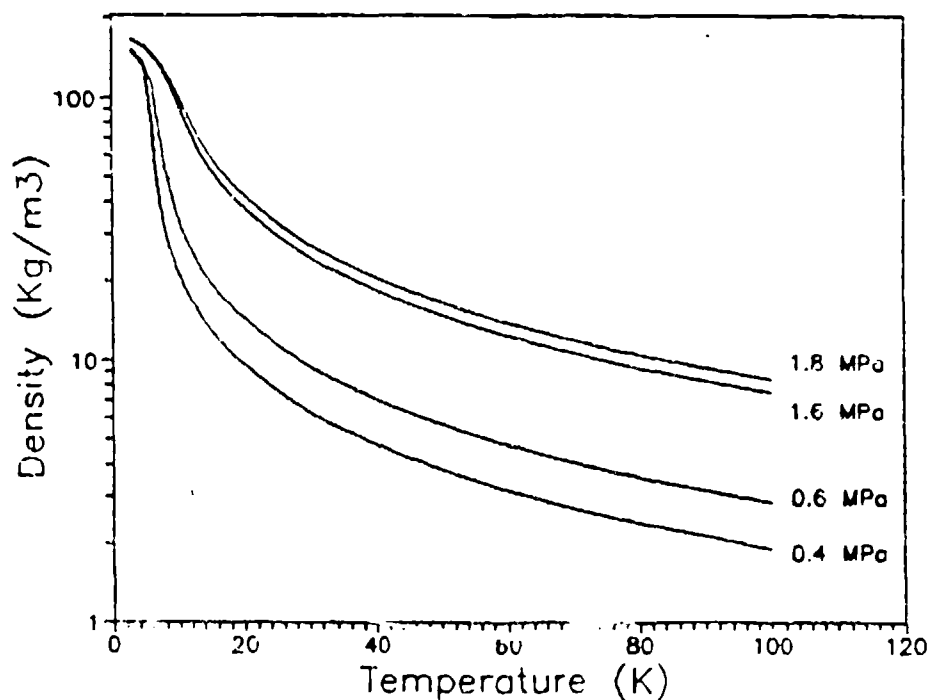


Fig.5 Density of helium in low temperature region

## DISCUSSION

Liquid helium refrigerator using magnetic regenerative material is composed of a gas compressor and a liquid expander. The thermodynamic behavior of such a refrigerator is rather complex. According to the first law of thermodynamics, the energy equilibrium in each working space is given by

$$dQ = du + pdv - d(mh)_{in} + d(mh)_{out} \quad (1)$$

The compressive or expansive process in the working space can be treated as an isothermal one because the rotating speed of the refrigerator is rather low. For a closing cycle, the internal energy  $\oint du = 0$ , so the theoretical refrigerating capacity per unit mass is

$$Q = \oint pdv - \oint d(mh)_{in} + \oint d(mh)_{out} = Q_c + Q_b \quad (2)$$

For an ideal gas, we have

$$Q_c = \oint pdv = (p_b - p_l)V \quad (3)$$

where  $p_b$  and  $p_l$  are the higher and the lower pressure respectively, and  $V$  is the volume of the cold space.

For a real gas, we have

$$Q = Q_c + \int_{T_l}^{T_b} (C_{p_{out}} - C_{p_{in}}) dT \quad (4)$$

where  $C_{p_{in}}$  and  $C_{p_{out}}$  are the specific heat of the working fluid at the entrance and the exit of the system respectively.

Fig. 6 gives a comparison for the refrigerating capacity of the real and ideal gas, where  $\eta$  equals to  $(Q_c + Q_b)/Q_c$  [5]. We can see from Fig. 6 that the theoretical refrigerating capacity is close to that of an ideal gas  $Q_c$  when the refrigerating temperature is higher than 20 K. The enthalpy changing of a real gas has a great influence upon the refrigerating capacity when the temperature is lower than 10 K. The theoretical refrigerating capacity is many times smaller than that of an ideal gas when the refrigerator operates in liquid region. Due to all kinds of heat losses of the cryocooler, the actual refrigerating capacity will be several times smaller than the theoretical one.

Thus it can be seen that it is the key to increase the actual refrigerating capacity that we must try to further improve the regenerative efficiency of the cryocooler operating in liquid helium temperature region. We should go on finding a magnetic rare-earth compound of higher heat capacity and larger heat penetration depth as the regenerative material in liquid helium region so as to increase the cooling capacity. It is suggested to increase the length of the 2nd stage regenerator properly with the permission of pressure drop to increase the mass of the regenerative material and further decrease the temperature difference between helium and the matrix grains. At the same time, it is also proposed to use smaller grains or mixing fill with grains big and small to reduce the void rate of the regenerator, so as to avoid compressive heat giving out to the remain gas in the cold space during high pressure charging process. It is estimated that the Simon compressive process makes the regenerator a temperature rise of 0.35K on condition that the void rate

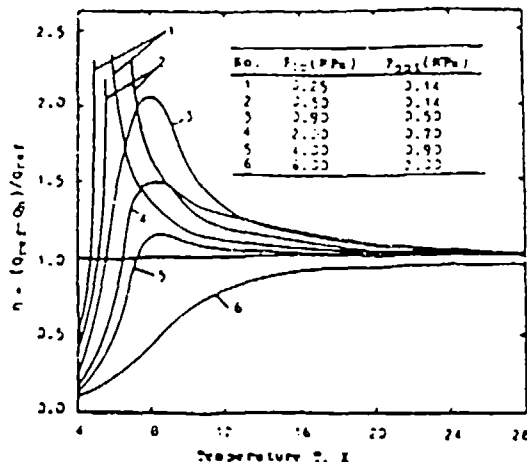


Fig.6 Refrigerating capacity of real and ideal gas

of the regenerator is 0.37. This means that the isothermal Simon refrigerating capacity will be canceled out one half[5].

### CONCLUSION

The refrigerating temperature of a two-stage Solvay refrigerator has been reduced in 3 K temperature region from the original 11.5 K by using magnetic compound  $\text{Er}_2\text{Ni}$  as the regenerative matrix of the 2nd stage instead of the traditional Pb.

The key to improve the refrigerating capacity of a cryocooler is the selection of magnetic rare-earth material of large specific heat and thermal penetration depth, the increment of the length of the low temperature regenerator and the adaption of finer matrix grains or the mixing fill of grains big or small.

### ACKNOWLEDGEMENT

This work was cooperated with Zhenshi Tao, Yi Long, Liang Zhang, and Peiyi Wu.

### REFERENCES

1. Kyriyama, T. et al. In: Proceedings of the International Conference of Cryogenics and Refrigeration, Hangzhou, China (1989) 91-96
2. Kyriyama, T. et al., High efficient two-stage G-M refrigerator with magnetic material in the liquid helium temperature region Adv. Cryo. Eng. (1990) 35 1261-1269
3. Inaguchi, T. et al., In: Proceedings of the 6th international Cryocoolers Conference, (1990) 25-36
4. Guobang, Chen et al., In: the 14th International Cryogenic Engineering Conference, Kiev, (1992)
5. Guobang, Chen et al., In: Proceedings of the 12th International Cryogenic Engineering Conference, Southampton, UK (1988) 571-576
6. C.S. Hong, Discussion on Refrigerating Capacity of a Cryogenic G-M Refrigerator, 3rd National Cryogenic Engineering Conference(in Chinese).